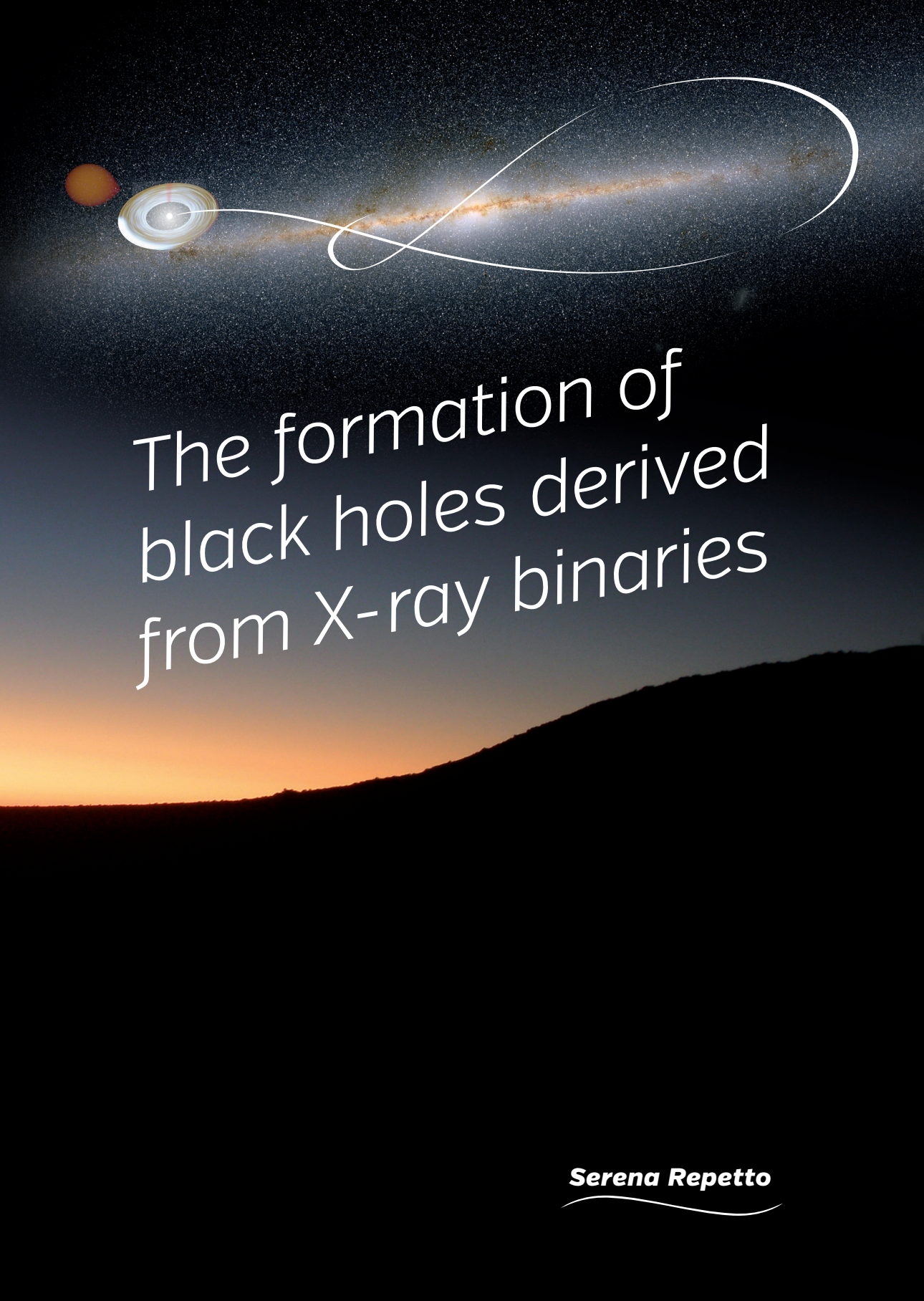

The formation of black holes derived from X-ray binaries

Serena Repetto

The formation of black holes derived from X-ray binaries

Proefschrift

ter verkrijging van de graad van doctor
aan de Radboud Universiteit Nijmegen
op gezag van de rector magnificus prof. dr. J.H.J.M. van Krieken,
volgens besluit van het college van decanen
in het openbaar te verdedigen op woensdag 28 september 2016
om 10:30 uur precies

door

Serena Repetto

geboren op 30 december 1985
te Savigliano (Italië)

PROMOTOR:	Prof. dr. G.A. Nelemans	(KU Leuven, België)
COPROMOTOR:	Dr. P. Jonker	
MANUSCRIPTCOMMISSIE:	Prof. dr. A. Fasolino	
	Prof. dr. M.B. Davies	(Lunds Universitet, Zweden)
	Dr. S.E. de Mink	(Universiteit van Amsterdam)
	Prof. dr. F.W.M. Verbunt	
	Dr. O.R. Pols	

The formation of black holes derived from X-ray binaries
Thesis, Radboud University Nijmegen
Illustrated; with bibliographic information and Dutch summary

Cover design by Buro Brouns
Cover elements: skyline from Paranal Observatory (Chile); rendering of a black hole X-ray binary made with the tool *BinSim*; an example of the orbit of a black hole X-ray binary in the Milky Way; the Milky Way in infrared light from 2MASS
Printed on Biotop paper by Ipskamp Nijmegen

This work was supported by the Netherlands Research School for Astronomy (NOVA)

Contact: repetto.serena@gmail.com

The formation of black holes derived from X-ray binaries

Doctoral Thesis

to obtain the degree of doctor
from Radboud University Nijmegen
on the authority of the Rector Magnificus prof. dr. J.H.J.M. van Krieken,
according to the decision of the Council of Deans
to be defended in public on Wednesday, September 28, 2016
at 10:30 hours

by

Serena Repetto

Born on December 30, 1985
in Savigliano (Italy)

Supervisor:	Prof. dr. G.A. Nelemans	(KU Leuven, Belgium)
Co-supervisor:	Dr. P. Jonker	
Doctoral Thesis Committee:	Prof. dr. A. Fasolino	
	Prof. dr. M.B. Davies	(Lund University, Sweden)
	Dr. S.E. de Mink	(University of Amsterdam)
	Prof. dr. F.W.M. Verbunt	
	Dr. O.R. Pols	

The formation of black holes derived from X-ray binaries
Thesis, Radboud University Nijmegen
Illustrated; with bibliographic information and Dutch summary

Cover design by Buro Brouns
Cover elements: skyline from Paranal Observatory (Chile); rendering of a black hole X-ray binary made with the tool *BinSim*; an example of the orbit of a black hole X-ray binary in the Milky Way; the Milky Way in infrared light from 2MASS
Printed on Biotop paper by Ipskamp Nijmegen

This work was supported by the Netherlands Research School for Astronomy (NOVA)

Contact: repetto.serena@gmail.com

"It has been said that Astronomy is a humbling and character-building experience. There is perhaps no better demonstration of the folly of human conceits than this distant image of our tiny world. To me, it underscores our responsibility to deal more kindly with one another, and to preserve and cherish the pale blue dot, the only home we've ever known".

- Carl Sagan -

Contents

Introduction 1
Astrophysical Black Holes . . . 1
Black Holes as end-points of stellar evolution . . . 3
Black Holes in X-ray binaries . . . 5
Dynamical measurement of Black Hole masses . . . 6
Orbits of Black Hole X-ray binaries . . . 8
Outline of the Thesis . . . 10
Methods . . . 12

1 Investigating stellar-mass black hole kicks 13
1.1 Introduction . . . 13
1.2 The Observed Binaries . . . 15
1.3 Integrating orbits within the Galaxy . . . 17
1.4 Kicks received by surviving binaries . . . 18
1.5 Binary Population Synthesis . . . 21
1.5.1 Statistics of the results . . . 24
1.6 Discussion . . . 25
1.7 Conclusions . . . 30
1.8 Acknowledgments . . . 31

2 The coupled effect of tides and stellar winds on the evolution of compact binaries 33
2.1 Introduction . . . 34
2.2 Model . . . 35
2.2.1 Tides coupled with Magnetic Braking . . . 35
2.2.2 Non-coupled methods . . . 37
2.2.3 Validation of the evolution code . . . 38
2.3 Binaries in our study . . . 39
2.3.1 Timescale considerations . . . 40
2.4 Results . . . 42

2.4.1 Black-hole low-mass X-ray binary . . . 42
2.4.2 Planetary system . . . 48
2.5 Wind Braking . . . 50
2.5.1 Tides coupled with wind braking . . . 51
2.5.2 Results . . . 53
2.6 Discussion . . . 57
2.6.1 On the quasi-equilibrium state . . . 59
2.6.2 An application to the neutron star high-mass X-ray binary Circinus X-1 . . . 59
2.6.3 Remarks on our results on the circularisation timescale and their consequences . . . 60
2.7 Conclusions . . . 61
2.8 Acknowledgments . . . 62

3 Constraining the formation of black holes in short-period Black-Hole Low-Mass X-ray Binaries 63
3.1 Introduction . . . 64
3.2 A short overview of the evolution of black-hole low-mass X-ray binaries . . . 65
3.2.1 Black hole formation and natal kicks at birth . . . 66
3.3 The Galactic population of short-period black-hole low-mass X-ray binaries . . . 67
3.3.1 Orbital properties . . . 67
3.3.2 Mass-radius relation . . . 68
3.3.3 Kinematical properties and Galactic positions . . . 70
3.4 A semi-analytical method to follow the evolution of short-period black-hole low-mass X-ray binaries . . . 73
3.4.1 Mass Transfer . . . 73
3.4.2 Detached evolution and black hole formation . . . 74
3.4.3 Supernova dynamics . . . 75
3.4.4 Monte Carlo calculation of black hole formation and detached evolution . . . 76
3.4.5 Observational biases on our sample . . . 77
3.5 Results . . . 79
3.5.1 Different models . . . 79
3.5.2 Lower limits on the natal kick and ejected mass . . . 79
3.5.3 Correlation natal kick VS mass of the black hole . . . 81
3.5.4 Initial orbital separation . . . 84
3.6 Discussion . . . 84
3.6.1 Zero ejected mass systems . . . 84
3.6.2 Standard systems . . . 85
3.6.3 High natal kick systems . . . 86
3.6.4 Effect of the uncertainty on the distance . . . 86
3.7 Conclusions . . . 88
3.8 Acknowledgments . . . 89
3.9 Appendix . . . 89
3.9.1 Fitting formulae for the maximal orbital separation . . . 89

4 The Galactic distribution of X-ray binaries and its implications for compact object formation and natal kicks 91
4.1 Introduction . . . 91
4.2 Intermezzo . . . 93
4.2.1 On the estimate of the peculiar velocity at birth . . . 93
4.2.2 Effect of a different choice of the Galactic potential with an application to the observed black hole X-ray binaries . . . 97
4.3 A Binary Population Synthesis of black hole and neutron star X-ray binaries . . . 99
4.3.1 Observational samples . . . 101
4.4 Results of the Binary Population Synthesis . . . 103
4.4.1 The expected vertical distribution of black hole and neutron star X-ray binaries . . . 103
4.4.2 The influence of the orbital separation distribution of the binary progenitors . . . 104
4.4.3 Comparison with observations: black hole X-ray binaries . . . 104
4.4.4 Comparison with observations: neutron star X-ray binaries . . . 108
4.5 Discussion . . . 111
4.5.1 A note on our Kolmogorov-Smirnov test . . . 113
4.6 Conclusions . . . 113
4.7 Acknowledgments . . . 114

5 Follow-up observations of the Galactic Bulge Survey source CX1004: a candidate Black Hole X-ray Binary 115
5.1 Introduction . . . 116
5.2 CX1004 . . . 117
5.3 Observations and data reduction . . . 117
5.3.1 Spectroscopic data . . . 117
5.3.2 Photometric data . . . 118
5.3.3 MOSAIC-II . . . 118
5.3.4 OGLE . . . 118
5.3.5 VVV . . . 118
5.3.6 DECam . . . 119
5.3.7 FORS2 . . . 119
5.4 Data Analysis and Results . . . 121
5.4.1 Radial Velocities from photospheric lines . . . 121
5.4.2 Spectral classification and rotational broadening . . . 121
5.4.3 Study of the emission lines . . . 122
5.4.4 Reanalysis of the VIMOS and GMOS data . . . 124
5.4.5 Testing the interloper hypothesis: positional offsets of CX1004 . . . 126
5.4.6 I-band and K-band counterparts . . . 127
5.4.7 OGLE light curve . . . 128
5.4.8 DECam light curve . . . 128
5.4.9 Reddening and distance to the interloper star and to the X-ray source . . . 129
5.5 Discussion . . . 131
5.5.1 CX1004 in the context of the known black hole transients . . . 131

5.5.2 A triple system . . . 132
5.6 Conclusions . . . 132
5.7 Acknowledgments . . . 133

Bibliography **135**

Summary **145**
Chapter I: A preliminary study of black hole natal kicks . . . 145
Chapter II: Tides coupled with magnetic braking . . . 146
Chapter III: Backtracing the evolution of black hole X-ray binaries . . . 146
Chapter IV: Neutron star formation VS black hole formation . . . 147
Chapter V: A new candidate black hole X-ray binary . . . 148
Conclusion & future prospects . . . 148

Samenvatting **149**
Introductie . . . 149
Dit proefschrift . . . 151
Hoofdstuk I: Een voorstudie over de *natal kicks* van zwarte gaten . . . 151
Hoofdstuk II: Het gekoppelde effect van getijden en stellaire winden . . . 152
Hoofdstuk III : Het terug in de tijd volgen van de evolutie van *black hole X-ray binaries* . . . 153
Hoofdstuk IV: De Galactische verdeling van de *X-ray binaries* en de gevolgen daarvan voor de vorming van compacte objecten . . . 154
Hoofdstuk V: Een nieuwe kandidaat zwart gat in de Melkweg . . . 154

Riepilogo **155**
Introduzione . . . 155
Questa tesi . . . 157
Capitolo I: Uno studio preliminare dei *kicks* ricevuti dai buchi neri alla nascita . . . 158
Capitolo II: L'effetto accoppiato di maree e venti stellari . . . 158
Capitolo III: Tracciando indietro nel tempo l'evoluzione delle binarie X contenenti un buco nero 159
Capitolo IV: La distribuzione galattica delle binarie X e le associate implicazioni per la formazione degli oggetti compatti . . . 159
Capitolo V: Un nuovo candidato buco nero nella nostra galassia . . . 160

Curriculum vitæ **161**

List of publications **163**
Refereed publications . . . 163
Publications in preparation . . . 164

Acknowledgments **165**

Ringraziamenti **169**

Introduction

It is hard to think of practical applications of the black hole.
Because practical applications are so remote,
many people assume we should not be interested.
But this quest to understand the world is what defines us as human beings.
– Yuri Milner –

Astrophysical black-hole candidates provide the most abundant, and possibly the only, evidence for the existence of black holes in nature.
– Luciano Rezzolla[1] –

Black Holes from an astronomer's perspective

In the 1960's, black holes (hereafter BHs) went from the realm of intriguing theoretical predictions of Einstein's theory of General Relativity to detectable Astrophysical sources. It was the boom era for X-ray astronomy and more and more extra-solar X-ray sources were being discovered, with the aid of rocket-borne instrumentations. The first identified *cosmic* X-ray source was Scorpius X-1 (Giacconi et al. 1962), which was later proved to be a binary system formed by a very compact and dead star, a neutron star (NS), and a star similar in mass and radius to our Sun. Bowyer et al. 1965, through the geiger detectors mounted on the Aerobee rocket, discovered a strong X-ray point-source which they named *Cygnus X-1*, after the constellation which hosted its projected position on the sky. The X-ray emission was later understood as being the signature of matter accreting onto a compact object. In the optical band, the X-ray location coincided with the emission from a massive star whose Doppler-shifted spectral lines allowed to weigh the object responsible for the X-ray emission. The compact object was found to have a mass above a few times the mass of the Sun (Webster & Murdin 1972; Bolton 1972), which is the upper limit for a stable NS, and had to be confined to a very compact region of space: a BH indeed.

Going back in time a little, in 1915, the same year when Einstein introduced General Relativity, Karl Schwarzschild, solving Einstein's field equations in vacuum for the gravitational field outside a spher-

[1] Extract from "Astrophysical Black Holes", Vol. 905 of "Lecture Notes in Physics".

ical distribution of mass, found a solution which hosted a singularity at its centre. Such singularity could not be removed by any change of coordinates: at $r = 0$ the curvature scalars, which are invariant under coordinate transformations, diverged to infinity. The term *black hole* was coined by John Archibald Wheeler in 1967: he made the link between the singularity found as a solution to Einstein's field equations and stellar objects collapsed under their own gravity.

On a curious note, the existence of objects from which light cannot escape was already predicted in the 18th century independently by John Michell and Pierre Simon Laplace from classical Newtonian-dynamics: they referred to these objects as *dark stars*. Based on energy conservation arguments, they speculated about the existence of objects either extremely massive or extremely small with escape speeds in excess of the speed of light. Within the formalism of General Relativity, the BH is defined as an object whose gravity is so strong that it curves the spacetime in such a way that no trajectories are possible to the outside world for radii smaller than a characteristic radius, the *Schwarzschild radius*: $R_{\rm Sch} = 2GM/c^2 \approx 3M/M_\odot$ km (where G is the gravitational constant, M the BH mass, c the light speed, $M_\odot$ the mass of the Sun).

The subject of this Thesis are *stellar-mass BHs*, with a mass much smaller than that of their cousins super-massive ones: around ten solar masses versus one hundred to one million solar masses. Given that they are black by definition, BHs can only be detected *indirectly*, either tracing the Keplerian orbit of stars revolving around them, or when they are accreting from a companion star, or via gas accretion on to supermassive BHs and the related phenomenology of quasars. In the first case, the BH gravitational sphere of influence projected on to the sky has to be large (like for a supermassive BH), and the observational time window long. Astronomers have computed the orbital solution of *S-stars* (those stars within the innermost arcsecond from the Galactic centre) in order to weigh the supermassive BH at the centre of our Galaxy (Ghez et al. 2008; Gillessen et al. 2009). Stellar-mass BHs are typically detected in the X-ray band when they are actively accreting from a companion star (a BH X-ray binary). Alternative ways of detecting BHs are the use of *gravitational microlensing*, which has so far produced weak candidates (Wyrzykowski et al. 2016), and the relation between the radio and X-ray luminosity of an accreting compact object (Maccarone & Knigge 2007). The latter has allowed to identify a few BH candidates in Galactic globular clusters (e.g. Strader et al. 2012) and one BH candidate in the field of our Galaxy (Tetarenko et al. 2016a).

The newly-born gravitational-wave (GW) era (Abbott et al. 2016) has opened up the possibility of *directly* detecting BHs (and in vacuum), when they are swirling around each other in a cosmic dance which terminates in the merger of the two and ring-down of the horizon of the newly formed BH. Up to date, the Laser Interferometer Gravitational Wave Observatory (LIGO) has detected two sources of gravitational waves from merging BHs and one candidate (The LIGO Scientific Collaboration et al. 2016).

The ultimate proof for the existence of the BH event horizon will be probably reached within a decade with the imaging of the shadow casted by a supermassive BH (Falcke et al. 2000). In the near future, Gaia will potentially provide us with the possibility of resolving the motion of stars around Galactic stellar-mass BHs, through orbital phase-resolved astrometry (Miller-Jones 2014).

The accretion signature in the X-ray band has allowed astronomers to discover tens of stellar-mass BHs in the Milky Way and a handful in outer galaxies (Remillard & McClintock 2006). We show these BHs as a bubble plot in Figure 1, together with those detected through the GW emission of their

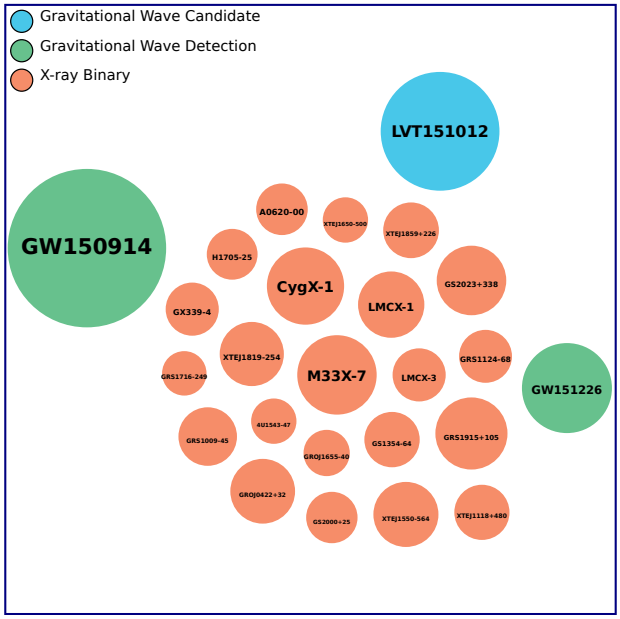

FIGURE 1: All known (Galactic and extra-Galactic) stellar-mass BHs, plotted as a bubble plot, detected either via the gravitational wave emission from their progenitor BH binary or via the signatures of accretion from a stellar companion. The circle area is proportional to the BH mass; in the GW-merger case, the mass is that of the resulting BH after the merger. Credits: Chris North on behalf of the LIGO Scientific Collaboration

progenitor BH binary[2].

Black Holes as end-points of stellar evolution

Stars spend most of their life burning hydrogen into helium in their core in a phase called *main-sequence* (MS). Those stars with an initial mass M_i larger than $\approx$ 20 times the mass of the Sun are thought to leave behind a BH[3] either when they explode as a core-collapse supernova (SN type II or Ib/c) or possibly when they implode through direct collapse (Fryer & Kalogera 2001). Stars are in balance between their self-gravity, which pushes inward, and the gradient of the thermal pressure, which pushes outward. Such thermal pressure is the product of the nuclear burning which takes place in the core. Massive stars burn light elements (hydrogen and helium) all the way to heavy elements, in a sequential chain of nuclear fusion reactions until iron is produced and which shapes the star into a typical onion-like structure. The central core of the star is composed mainly of iron, the shell around mainly of silicon, then oxygen, carbon, helium, and the outer one of hydrogen. The fusion of two nuclei with a mass lighter than iron (which, along with nickel, has the largest binding energy per nucleon) releases energy (a so-called *exothermic* nuclear reaction); instead, the fusion of iron costs energy. Hence, when iron is produced, there is no source of energy to counteract the star's self-gravity as no nuclear fusion is occurring and the star is doomed to collapse: the iron-core starts contracting. At some point, the core becomes so hot and dense that the iron dissociates (via *photodissociation*) and electrons are captured onto free protons (via *electron capture*) forming neutrons. The core, which

[2]See https://gravity.astro.cf.ac.uk/plotgw/bhbubble.html
[3]Throughout our work, we will refer to stellar-mass BHs simply as BHs for brevity.

was initially supported by the thermal and *electron-degeneracy pressure*, loses its support and starts free in-falling. Stars with a mass between $\approx 20 - 40\ M_\odot$ give birth to a BH most probably via an intermediate stage of NS formation. The free-fall collapse is halted when the core reaches nuclear density; at this point, it is the *neutron-degeneracy pressure* that sustains the core. The collapsing outer material bounces back against the incompressible nuclear matter. Such an overly-packed sphere made up of neutrons, so called *proto NS*, is what is soon to become a NS. While the shock moves outward, its density decreases, allowing neutrino to escape depriving the shock of its energy. In the meantime, the in-falling outer material has not yet realised the bounce, and it keeps falling inwards, causing a further deceleration and then a stalling of the shock propagation outwards. Various possible ways of reviving this shock have been suggested, such as neutrino heating (Fryer & Kusenko 2006), the *Rayleigh-Taylor instability* in the convective region right below the shock (Belczynski et al. 2012), or the *standing accretion shock instability* (Blondin et al. 2003). The revival of the shock casts the material outwards in the surrounding interstellar medium in what we observe as a SN type II. The time-lapse between the collapse and the launch of the explosion is very short: of the order of a few seconds. If some of the ejecta material does not have sufficient kinetic energy to overcome the gravitational pull from the NS, it falls back onto the NS and, if a critical mass is reached (the *Tolman-Oppenheimer-Volkoff limit* of $\approx 3\ M_\odot$), the NS collapses into a BH. If the progenitor is more massive than $\approx 40\ M_\odot$, the core-collapse is most likely not halted and the star is thought to collapse directly into a BH. In this case, the BH forms *in the dark*, with no SN explosion (i.e. no baryonic ejected mass).

Within the model for BH formation we just described, there are still many open questions, and which are the main trigger of this Thesis: how much mass is ejected at BH formation and what is the magnitude of the velocity BHs receive when formed (the so called *natal kick*, NK)? NSs are well-known to receive such kicks (Cordes et al. 1993; Lyne & Lorimer 1994; Hartman 1997); whereas, to date, the sample of confirmed BHs with a measured space velocity is too small for deriving a conclusive BH NK distribution (Miller-Jones 2014). On the theoretical side, there are two types of BH NKs: (i) kicks imparted intrinsically to the BH, and (ii) kicks received as an effect of the NK imparted to the NS that forms a BH through fallback. The intrinsic kicks could be caused either by asymmetric GW emission during the core collapse (Bonnell & Pringle 1995), or by asymmetric flux of those neutrinos which get to escape before all the collapsing material falls inside the event horizon (Gourgoulhon & Haensel 1993). There are two main processes which are thought to cause NS NKs and are therefore relevant for BH formation via fallback: either asymmetries in the SN ejecta (*ejecta-driven*, also called *hydrodynamical* NKs), or asymmetries in the neutrino flux (*neutrino-driven* NKs). In the fallback scenario, and if the NK is caused by asymmetries in the SN ejecta, the BH would receive a reduced NK. Just by conserving linear momentum, we expect reduced NKs to be of the order of $V_{\rm NK,BH} = (M_{\rm NS}/M_{\rm BH})V_{\rm NK,NS}$, leading the BH to receive an NK of the order of tens km/s. If this scenario is correct, we should find a correlation between the mass of the BH and the NK: the larger the fallback mass, the larger the BH mass, the lower the NK. We wish to highlight, however, that Janka 2013 suggests that BHs could be accelerated to the same velocity as NSs, even in a fallback scenario, due to the anisotropic gravitational pull from the asymmetrically expelled ejecta.

Black Holes in X-ray binaries

The focus of this Thesis are BHs accreting mass from a stellar companion in a binary system, a *black hole X-ray binary* (BH-XRB). We consider BH-XRBs that form from primordial massive binaries in the field of our Galaxy, whereas we leave the subject of BH-XRBs formed via dynamical encounters in globular clusters to later studies. The primordial binary is composed of a massive star with a (low-mass) companion. Typical orbital separations which allow a Sun-like star to overfill its Roche lobe radius[4] and transfer mass to a BH are of the order of a few tens of solar radii, whereas the binary must have been much wider (hundreds to thousands of solar radii) in the past in order to accommodate the BH progenitor during its nuclear expansion along the giant branch. The *common envelope*, suggested by Paczynski 1976 when modelling the evolution of close binaries harbouring a white dwarf (WD) and by van den Heuvel & de Loore 1973 when modelling the evolution of massive binaries, provides a means to shrink the progenitor binary down by a factor of hundreds. When the massive star expands and overfills its Roche lobe, the mass-transfer onto the companion is dynamically unstable, resulting in the envelope engulfing both stars: the common envelope. Through friction and consequent heating of the envelope, the orbital-energy reservoir is partially dumped into the envelope, the companion star spirals in, and the envelope is ejected, leaving a companion star in orbit around the naked helium core, which later collapses into a BH. From this moment on, the binary path bifurcates into two directions, depending on whether the orbital period is short or long. Short-orbital period binaries evolve to shorter and shorter periods via the coupling between tides and magnetic braking (which is the loss of angular momentum in a magnetic stellar wind; Verbunt & Zwaan 1981. In this case, the companion star overfills its Roche lobe and starts mass-transfer to the BH while being on the MS. Long orbital-period binaries start mass-transfer when the companion star expands during its own nuclear evolution along the red-giant branch. The basic traits of this evolution have been suggested for the first time by van den Heuvel & Habets 1984 who applied this evolutionary scenario to the extra-Galactic BH-XRB LMC X-3, and they represent the standard theory for the evolution of a primordial binary into a BH-XRB (see e.g. de Kool et al. 1987; Portegies Zwart et al. 1997; Tauris & van den Heuvel 2006).

Either through shrinking of the binary orbit due to loss of orbital angular momentum or through the nuclear expansion of the companion star, at some point the radius of the star will overfill the Roche lobe radius: this triggers the flow of gas from the star towards the BH. The inflowing material has net angular momentum, thus it cannot accrete directly on to the BH. It forms instead an accretion disc where matter is compressed and heated to temperatures of $\approx 10^7$ Kelvin (Shakura & Sunyaev 1973): the binary is visible in the X-ray band and becomes what we know as BH-XRB. While angular momentum moves outwards, matter falls inwards as it is accreted onto the BH. In Figure 1, an artist impression of a BH-XRB is presented; the accretion disc around the BH is fed via the accretion stream originating from the companion star.

With more and more sensitive X-ray telescopes, the number of candidate BHs has steadily increased with time; Figure 3 shows in red the cumulative number of candidate BHs at a certain time. The current Galactic population amounts to 60 BH-XRB candidates (Corral-Santana et al. 2016; Tetarenko et al. 2016b).

[4]The Roche lobe radius is a characteristic radius that defines the region within which the gas is bound to the star only; it is a function of the orbital period and masses of the binary components.

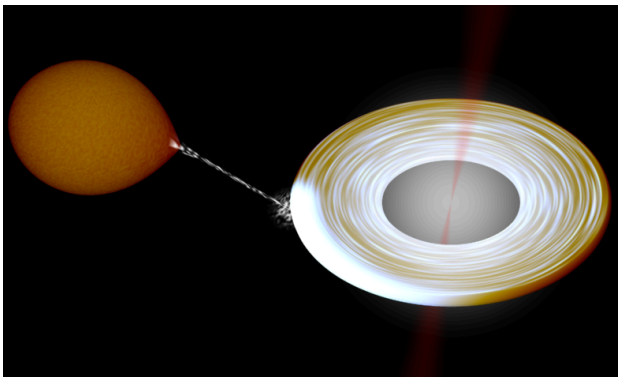

FIGURE 2: Artist impression of a BH-XRB; the accretion disc around the BH is fed via the accretion stream originating from the companion star. A jet launched in the vicinity of the BH is also visible.

Dynamical measurement of Black Hole masses

Tracking the motion of the companion star around the BH, it is possible to weigh the BH, therefore allowing for the full-confirmation of the BH nature against other types of compact objects: WDs and NSs, that are lower in mass. Just like any other classical gravitationally-bound system, the Keplerian velocity of the companion star orbiting around the BH is unequivocally determined by the masses of the objects ($M_{\rm BH}$, M_c) and the binary orbital period $P_{\rm orb}$. These three quantities combine in the *mass-function* (see e.g. Casares et al. 1992) which delivers a lower-limit for the BH mass from directly-observable quantities:

$$f(M) = \frac{P_{\rm orb} K_c^3}{2\pi G} = \frac{M_{\rm BH}^3 \sin^3 i}{(M_{\rm BH} + M_c)^2}; \quad (1)$$

where K_c is semi-amplitude of the radial velocity of the companion star projected onto the line of sight, M_c the mass of the companion star, i the inclination of the plane of the binary with respect to the line of sight. The velocity K_c is measured via periodic Doppler shifts of the photospheric absorption lines in the optical spectra of the companion star. In practice, K_c is obtained cross-correlating the photospheric absorption lines with those of a stellar template of the same spectral type. The periodicity arises due to the star's orbital period $P_{\rm orb}$; the orbital period can also be derived from periodic variations in the X-ray and/or optical light curve. If also the inclination i and the mass ratio between the two components $q = M_c/M_{\rm BH}$ are known, then the BH mass is measured, and we call it a *dynamical mass measurement*. The spectral type is determined using the *optimal subtraction* technique (Marsh et al. 1994; see *Chapter* V for a detailed description of this technique). The inclination can be determined either via ellipsoidal modulations in the optical light curve or, if the system has a high inclination ($i \gtrsim 70°$), via X-ray light-curve eclipses. The former relies on the fact that the shape of the companion star is distorted by the tidal torque, hence its projected surface area is not constant for the observer while the star revolves around the binary centre of mass. The higher the inclination of the binary, the larger the amplitude of the modulation. The mass ratio can be determined by measuring the rotational broadening ($V_{\rm rot} \sin i$) of the absorption lines in the companion star spectrum. Under the assumption that the companion star is synchronised with the orbit and that its radius equals the Roche lobe radius, it is possible to estimate the mass ratio q: $V_{\rm rot} \sin i / K_c \approx 0.462\ q^{1/3}(1+q)^{2/3}$ (Wade & Horne 1988). The rotational broadening $V_{\rm rot} \sin i$ is measured comparing the target spectrum with stellar templates with different rotational speeds, accounting for limb-darkening and instrumental broadening, and using

the χ^2-minimisation technique (see *Chapter* V for an application of this method).

The era of dynamical measurement of BH masses was boosted in the 1990's, with the advent of 10-m size telescopes, starting from the Keck telescope, which enabled the confirmation of BH candidates up to a magnitude of $R \sim 21 - 21.5$ (Filippenko et al. 1995a; Filippenko et al. 1995b).

The current Galactic population amounts to 18 objects with a dynamical measurement of the BH mass (Casares & Jonker 2014; Corral-Santana et al. 2016). Figure 3 shows in blue the cumulative number of dynamically-confirmed BHs at a certain time. Both from observational and theoretical arguments, it is possible to compute the expected number of BH-XRBs in our Galaxy. By convolving the number of detected sources with the sensitivity of X-ray monitors, more than $\sim 1300 - 3 \times 10^4$ BH-XRBs are expected (Romani 1998; Corral-Santana et al. 2016; Tetarenko et al. 2016a). From a theoretical standpoint, one can build synthetic populations of the binary progenitors of BH-XRBs and let them evolve in time, solving for all the physical processes involved; this also translates into an expected number of sources ($10^4 - 10^5$; Pfahl et al. 2003; Yungelson et al. 2006).

A typical BH-XRB is a transient system (BHT), which goes through cycles of outbursts and quiescence. The measurement of the radial velocity shift of the absorption lines, of the rotational broadening, and of the amplitude of the ellipsoidal modulations, are only achieved during the quiescent state, when the disc is emptied and most of the optical light in the system comes from the companion star. Even when a full orbital-solution of the radial velocity is not available, the recently established correlation between the full width at half maximum of the Hα line and K_c (Casares 2015) allows to estimate the mass function once the orbital period is known. Another useful correlation is the one that links the binary mass ratio q with the ratio of the double peak separation to the full width at half maximum of the Hα line (Casares 2016). These correlations will be used in *Chapter* V of this Thesis.

It is surprising that none of the BHTs currently known show optical or X-ray eclipses; for an isotropic distribution of the binary orientation along the line of sight, such eclipsing BHTs are expected. One suggestion is that the discovery of BHTs through their outburst in the X-ray intrinsically biases the detected systems towards mildly-inclined ones, with the higher-inclination ones being obscured behind the accretion disc rim (Narayan & McClintock 2005), or behind an inner disc torus (Corral-Santana et al. 2013). Another reason could be that being the typical companion stars to BH of low mass, their projected surface is small, and eclipses are allowed only for very high inclination, and they would be very short. In this respect, a great effort must be put into the detection of BHTs in the *quiescent* state, for example with dedicated surveys like the Galactic Bulge Survey of Jonker et al. 2011 or via the the aforementioned relation between the X-ray and radio luminosity of an accreting compact source.

Besides the confirmation of the BH nature against a WD or NS nature, there are other reasons why we are interested in BH masses:

- the BH mass gap.
  The observed distribution of BH and NS masses is not continuos and shows a gap between the highest NS mass and the lowest BH mass (between 2 and 5 solar masses; Özel et al. 2010). This can either be caused by systematics in the BH-mass measurements (Kreidberg et al. 2012) or by the physics of the SN explosion itself. In certain SN models, the SN happens either rapidly right after the bounce and it produces a NS, or the explosion is delayed, hence weaker, and produces heavier-mass BHs (Belczynski et al. 2012).

- The higher-end of the BH-mass spectrum depends on the strength of the stellar wind of the

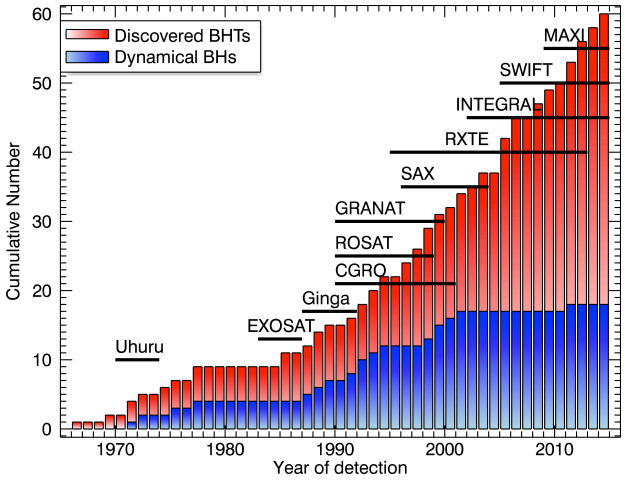

FIGURE 3: Cumulative histogram of discovered BHs (in red) as a function of time. The black lines show the lifetime of X-ray satellites. The blue histograms show the cumulative number of dynamical BHs, the ones with a dynamical measurement of their mass. Picture courtesy of J. M. Corral-Santana.

progenitor star.
After the common-envelope phase, the BH-XRB progenitor consists of the helium core and the companion star. Such helium star, which will core-collapse into a BH, undergoes strong wind mass loss in the *Wolf-Rayet* phase; depending on the strength of such winds, the maximum expected BH mass can decrease to a value of 10 $M_{\odot}$ (Fryer & Kalogera 2001).

- Calibrating the BH mass distribution as input for population synthesis studies.
  Clausen et al. 2015 have used the observed BH mass distribution in the attempt to calibrate the probability that a star will make a BH as a function of its initial mass, $P_{\rm BH}(M_i)$, to be used as input for binary population synthesis studies. They conclude that, to date, the observational constraints on $P_{\rm BH}(M_i)$ are too weak to make quantitative predictions about its nature, and that hence an increase in the number of BHs is needed.

- Increasing the number of BHs with measured space velocity, in order to investigate a possible correlation between BH mass and BH velocity, which is predicted in certain models of BH formation.
  So far, there is no clear correlation between the BH mass and the BH NK, the velocity which a BH can potentially acquire at birth (see *Chapter* III). Such a correlation is expected in a standard model for BH formation where the BH is formed via fallback onto the nascent NS: the larger the fallback mass, the larger the BH mass, the lower the NK.

Orbits of Black Hole X-ray binaries

The position and orbit of stars and binaries in the Milky Way can reveal much information about any initial velocity of these systems and hence about any NK that the BH possibly received at birth.

The distance to a BH-XRB is typically estimated from the apparent magnitude of the companion star, once its spectral type and the reddening towards the source are known. To date, there are only three BH-XRBs with a parallax distance (Cygnus X-1, V404 Cygni, and GRS 1915+105). The dynamical

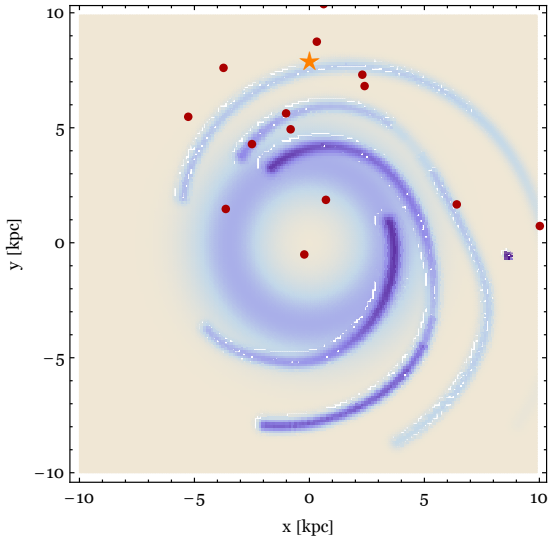

FIGURE 4: The distribution of BH-XRBs (filled circles) in the Galactic plane, in coordinates centered at the Galactic centre, together with a model for the spiral structure and the free-electron density according to Taylor & Cordes 1993. The Sun is indicated with a star.

BHs are located within 10 kpc from the Sun, as is shown in Figure 4 where we depict the dynamically confirmed BHs together with a model for the spiral arms. This is likely due to an observational bias: to confirm the BH nature, the compact object has to be weighted dynamically, introducing a bias towards sources not affected by high extinction and close enough that the low-mass companion is visible. Once the Galactic coordinates and distance to a BH-XRB are known, one can locate the binaries in the Galaxy, and look at their distribution in terms of the distance R from the Galactic centre and projected onto the Galactic plane, and the height above the Galactic plane z. Most massive stars resides in the disc of the Milky way, where there is continuous star formation, and they revolve around the Galactic centre with a velocity of approximately 200 km/s. If the BH-XRB acquires a *peculiar velocity* with respect to the Galactic rotation at some point during its evolution, and if this velocity is comparable in magnitude to the circular velocity, the orbit of the binary can drastically change. For instance, if this velocity has a significant component perpendicular to the Galactic plane, the binary will move away from its birth place and in the direction of the halo of the Galaxy in a so-called *box-orbit*, which is an oscillatory motion both in the z and R directions (see Figure 5). This trajectory is in contrast with a typical rotation in the Galactic disc.

The kinematics of the binary is strongly affected by the BH formation process if mass is lost in the SN; the instantaneous ejection of mass imparts a momentum-conserving recoil to the binary (the *mass-loss kick*). Furthermore, any velocity acquired at birth by the BH (the NK) adds up to the mass-loss kick, affecting the space velocity of the binary. From the offset of a BH-XRB above the Galactic plane, one can measure the velocity that the binary acquired at birth, and hence the NK (a method which we use in *Chapter* I, *Chapter* III, and *Chapter* IV). In this Thesis, in order to unravel how BHs form, we trace the binary evolution of BH-XRBs backward in time and we measure their space velocity at birth, which is the main topic of *Chapter* III. Another potential way to investigate the occurrence of a NK at birth is the detection of a misalignment between the BH spin and the orbital angular momentum. Since

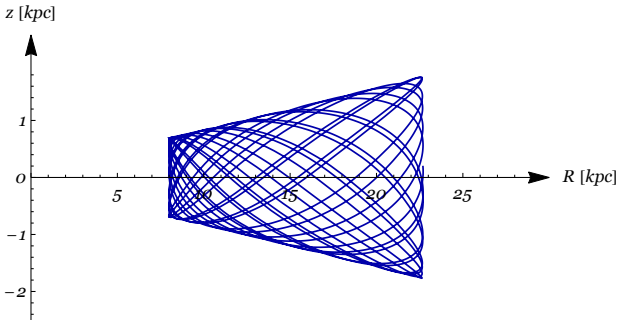

FIGURE 5: An example of a *box-orbit* in the Galactic potential; R is the distance from the Galactic centre projected on to the Galactic plane, z is the height above the Galactic plane.

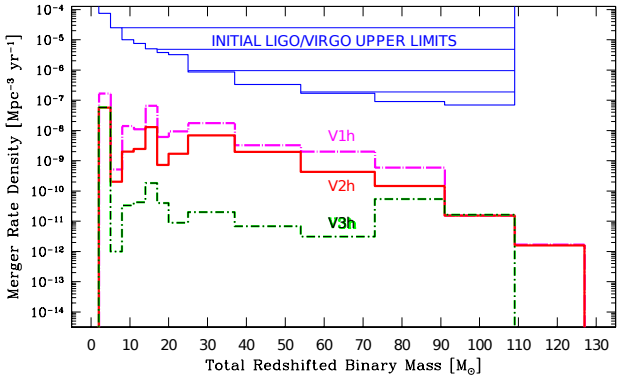

FIGURE 6: Merger rate density of double compact objects via the emission of gravitational waves for initial LIGO/Virgo. The green line corresponds to a model in which BHs receive a high NK at birth; in this case, the merger rate is drastically decreased. For details, see Belczynski et al. 2016b.

the tides acting on the BH are weak, the BH spin behaves as a gyroscope and it does not significantly change in time. This has been possible for the BH-XRB GROJ1655-40 (Martin et al. 2010), which has an observed misalignment between the jet axis (which is thought to coincide with the BH spin axis) and the disc plane.

Measuring BH NKs is not only essential for unraveling the physics of the SN explosion. There is another reason which has become compelling with the advent of the GW era: the GW merger rate of BH-BH and BH-NS binaries is a strong function of the BH NK distribution, and can vary by up to two orders of magnitude depending on whether BHs receive high or low NKs (Belczynski et al. 2016b). This can be seen in Figure 6, which shows the merger rate density of double compact objects via the emission of gravitational waves for initial LIGO/Virgo; the green line corresponds to BHs receiving a high NK at birth.

Outline of the Thesis

In this Thesis, we study XRBs hosting a BH, with the bulk of the work being computational. The main goal is to understand how BHs form, in particular in terms of how much mass is ejected at formation and how large the NK is they receive. The tool we use is the combination of the information we get from following the binary evolution of the systems backward in time, with the information we get from

the Galactic kinematics of the sources.

In *Chapter* I, we build a preliminary synthetic population of BH-XRBs, follow their Galactic trajectories, and compare their spatial distribution with that of the observed binaries. We find that high NKs are needed in order to explain the offset from the Galactic plane of the observed BH systems.

In *Chapter* II, we study the coupled effect of tides and magnetic braking on the evolution of different types of binary systems (BH and NS low- and high-mass XRBs; systems with a Jupiter-like planet orbiting close to a solar-type central star, so-called *hot Jupiters*). We find some interesting evolutionary outcomes of this coupling, such as the presence of a *pseudo-equilibrium* state for the stellar spin, and the *wind-braking* evolution in a high-mass XRB, which we successfully describe analytically. Furthermore, we find that simple timescale considerations, which rely on simplifying the coupling, do not provide an accurate description of the time evolution of the systems. This issue was explored previously for planetary systems, but not for BH nor NS systems.

In *Chapter* III, we consider the observed properties of a subset of BH-XRBs, those with a short orbital period, and find the possible combinations of NK and ejected mass at core-collapse which are consistent with the observed properties. We integrate the binary evolution of short-period BH-XRBs backward in time, from the current state of mass transfer to the moment the BH was formed, using the computational model for the coupling between magnetic braking and tides developed in *Chapter* II. The strength of this method is that we do not make any a priori assumption on the NK and ejected-mass distribution, and neither on the orbital period distribution of the binaries prior the SN. The information on the space velocity at birth which we get from the offset of the binaries above the Galactic plane, allows to further restrict the parameter space of the NK and ejected mass at BH formation. We find evidence for the occurrence of a high NK in two of the sources, and three BHs that could have formed with zero baryonic ejected mass and a non-zero NK. Further results of this study are: i) the lower limit on the NK does not depend on the details of the binary evolution; ii) given that BH binaries are typically close to the Sun, our observations are biased towards low NKs (less than 200 km/s); iii) we find no evidence for a correlation between NK and BH mass in the small subset of BH systems we considered.

In *Chapter* IV, we perform a detailed binary population synthesis of BH- and NS-XRBs to study the imprints that different compact object formation models have on the Galactic distribution of such binaries. We find that even in the case that BHs and NSs receive the same NK at birth, NSs would still show a larger scale height, which is in line with what is observed in the Galactic populations. When comparing the distribution of the synthetic BH-XRBs with that of the observed BH-XRBs, we find that a model in which at least some BHs receive a (relatively) high NK (≈ 100 km/s) fits the data best. We also thoroughly check the validity of the simple method we used for estimating the peculiar velocity at birth of a BH-XRB, and find that our analytical model offers a robust estimate in most of the cases.

In *Chapter* V, we embark on a project to try and increase the number of confirmed Galactic BHs. We present the optical spectroscopic and photometric follow-up of one of the X-ray sources discovered in the Galactic Bulge Survey of Jonker et al.: CX1004. The spectra show a wide double-peaked Hα emission line, which is a proxy for an accreting binary harbouring a BH. Surprisingly, the spectral absorption lines do not show evidence for any radial velocity shift, thus we deem it likely that we are actually observing not the companion star in the system, but rather an interloper star. We estimate the distance to the binary and to the interloper, and we constrain the spectral type of the donor star as a function of the binary distance.

Methods

In this Thesis, we make use of the methods of computational astrophysics and observational astronomy. On the computational side, we employ both numerical and analytical calculations. We learn and apply the techniques typical of binary population synthesis, a method which allows for the modelling of the birth and evolution of a large population of binaries, in order to compare the simulated population with the observed one. One technique which is widely used throughout this work is that of Monte Carlo methods, which enable the integration over of all possible values of physical parameters according to certain distribution functions. When numerically integrating differential equations (either with *Mathematica*, or *Python/C* codes), such as the ones describing the motion of a particle in a gravitational potential or the equations evolving the tidal torque acting on a star in a binary, we check the numerical accuracy of our codes using integral of motions. When possible, we combine the numerical modelling with analytical calculations, which can greatly simplify the description of certain phases of the evolution of a binary. On the observational side, we analyse optical images and spectra using the various tools available to the observational astronomer.

Chapter 1

Investigating stellar-mass black hole kicks

S. Repetto, M. B. Davies, S. Sigurdsson

MNRAS, Volume 425, Issue 4, 2012

Abstract

We investigate whether stellar-mass black holes have to receive natal kicks in order to explain the observed distribution of low-mass X-ray binaries containing black holes within our Galaxy. Such binaries are the product of binary evolution, where the massive primary has exploded forming a stellar-mass black hole, probably after a common envelope phase where the system contracted down to separations of order $10-30\ \mathrm{R}_{\odot}$. We perform population synthesis calculations of these binaries, applying both kicks due to supernova mass-loss and natal kicks to the newly-formed black hole. We then integrate the trajectories of the binary systems within the Galactic potential. We find that natal kicks are in fact necessary to reach the large distances above the Galactic plane achieved by some binaries. Further, we find that the distribution of natal kicks would seem to be similar to that of neutron stars, rather than one where the kick velocities are reduced by the ratio of black hole to neutron-star mass (i.e. where the kicks have the same momentum). This result is somewhat surprising; in many pictures of stellar-mass black-hole formation, one might have expected black holes to receive kicks having the same momentum (rather than the same speed) as those given to neutron stars.

1.1 Introduction

It has long been known that neutron stars receive kicks at birth in the range $\sim 200-400$ km/s (so called *natal kicks*), when they are formed in core-collapse supernovae, for example via proper motion studies of pulsars (Cordes et al. 1993, Lyne & Lorimer 1994). Whether stellar-mass black holes (for brevity, black holes hereafter) receive these kicks too is still a matter of debate. Black holes can be studied via interacting X-ray binaries which contain them. There are several known X-ray binaries

which are known to contain black holes or contain black hole candidates (Jonker & Nelemans 2004, Özel et al. 2010). In these systems, the massive primary has evolved to form a black hole via a core-collapse supernova and material is currently flowing from the lower-mass secondary (typically via Roche-lobe overflow) onto the black hole via an accretion disc (for a detailed review on the evolution of compact binaries see Tauris & van den Heuvel 2006). When the primary explodes as a supernova, the mass loss from the system can unbind the binary or at least give it a kick (as the mass lost has a net momentum in the rest frame of the binary). In addition, any natal kick received by the black hole will affect the orbital properties of the binary and its orbit within the Galaxy. By studying the orbit of a binary, or even its location within the Galaxy, one might obtain a limit on the range of allowed natal kicks. A number of studies have considered the motion of individual binaries within the Galaxy.

Brandt et al. 1995 considered GRO J1655–40 (Nova Sco) and concluded that a natal kick more easily accounted for the high space velocity of the binary.

Nelemans et al. 1999 studied Cygnus X-1 and concluding that a natal kick was not necessary to explain its space velocity.

Willems et al. 2005 considered GRO J1655–40 and suggested that although a natal kick is not formally required to produce the system as observed today, the inclusion of a (modest) natal kick more readily explains the system. They also placed an upper limit on the natal kick of $\simeq 210$ km/s.

Dhawan et al. 2007 considered GRS 1915+105. They concluded that any peculiar motion of the binary was more likely due to later scattering within the Galactic disc than a natal kick when the black hole formed.

The binary XTE J1118+480 is located at a very high latitude (1.5 kpc above the Galactic disc, see Remillard et al. 2000) and it has a high space velocity (Mirabel et al. 2001). Gualandris et al. 2005 concluded that for this system a black hole natal kick was *required*. More recently, Fragos et al. 2009 placed the value of the natal kick in the range 80 - 310 km/s.

Wong et al. 2010 considered Cygnus X-1. They found that in this case the black hole progenitor could have received a relatively small natal kick (few tens of km/s with an upper limit of 77 km/s). If the system originated in the Cyg OB3 association (Mirabel & Rodrigues 2003) , then the upper limit on a kick is reduced to 24 km/s.

In this Paper, we consider the population of black hole X-ray binaries as a whole (following the approach of White & van Paradijs 1996, Jonker & Nelemans 2004, Zuo et al. 2008) rather than consider the kinematics of an individual system. We synthesize a population of black-hole low-mass X-ray binaries (BH-LMXBs), using various natal kick distributions, and integrating the systems within the Galactic potential. We then compare their locations within the Galaxy to a catalogue of known black-hole X-ray binaries having measured distances (Özel et al. 2010).

The paper is arranged as follows. We review the current state of observations of X-ray binaries containing either neutron stars or black holes in Section 1.2. Our treatment of the motion of stars in the Galactic potential is given in Section 1.3. In Section 1.4 we review the effects of both natal and supernovae mass-loss kicks on binaries. In Section 1.5 we present the results of the binary population synthesis which we discuss in Section 5.5. The paper is concluded in Section 1.7.

Table 1.1: Observed properties of BH-LMXBs.

Name	l (deg)	b (deg)	d (kpc)	Δd (kpc)	R (kpc)	z (kpc)	Ref. (distance)
4U1543-47	330.0	+5.4	7.5	0.5	3.92	0.70	[1]
XTEJ1550-564	325.9	-1.8	4.4	0.5	5.0	-0.14	[2]
GROJ1655-40	345.0	+2.5	3.2	0.5	4.98	0.13	[3]
1659-487	338.9	-4.3	9.0	3.0	3.25	-0.67	[4]
1819.3-2525	6.8	-4.8	9.9	2.4	2.14	-0.82	[5]
GRS1915+105	45.4	-0.2	9.0	3.0	6.62	-0.03	[6]
GS2023+338	73.1	-2.1	2.39	0.14	7.65	-0.09	[7]
GROJ0422+32	166.0	-12.0	2.0	1.0	9.91	-0.41	[8]
A0620-003	210.0	-6.5	1.06	0.12	8.92	-0.12	[9]
GRS1009-45	275.9	+9.4	3.82	0.27	8.48	0.62	[10]
XTEJ1118+480	157.6	+62.3	1.7	0.1	8.73	1.50	[11]
1124-683	295.3	-7.1	5.89	0.26	7.63	-0.73	[10]
XTEJ1650-500	336.7	-3.4	2.6	0.7	5.71	-0.15	[12]
1705-250	358.2	+9.1	8.6	2.1	0.55	1.36	[13]
XTEJ1859+226	54.1	+8.6	8.0	3.0	7.23	1.20	[10]
GS2000+251	63.4	-3.0	2.7	0.7	7.21	-0.14	[13]

Notes: References (from Özel et al. 2010): [1] Orosz 2010 private communication, [2] Orosz et al. 2011b, [3] Hjellming & Rupen 1995, [4] Hynes 2005, [5] Orosz et al. 2001, [6] Fender et al. 1999, [7] Miller-Jones et al. 2009a, [8] Webb et al. 2000, [9] Cantrell et al. 2010, [10] Hynes 2005, [11] Gelino et al. 2006, [12] Homan et al. 1999, [13] Barret et al. 1996.

1.2 The Observed Binaries

In our Galaxy there are 16 dynamically confirmed black holes in LMXBs and 33 NS-LMXBs, whose distance and Galactic position is known; see respectively Özel et al. 2010, Jonker & Nelemans 2004, and references therein (in particular, Jonker & Nelemans consider only NSs not found in globular clusters). We present the binaries in Tables 1.1 and 1.2, along with their angular distribution, their distance from the Sun and their position, both in Galactic coordinates and in cylindrical ones (R refers to the radial distance from the Galactic centre and z refers to the distance from the Galactic plane). Concerning the black hole binaries, uncertainty on the distance is taken from Özel et al.; for the neutron star binaries, Jonker & Nelemans calculated the distance assuming two different Eddington peak fluxes, getting a maximum and a minimum value for the distance, of which we take the median value.

Using the values in Table 1.1 and Table 1.2, we plot the Galactic distribution of the binaries in Figure 1.1. In representing the observed system on the (R, z) plane we propagate the uncertainty on the distance into an uncertainty on R and on z, the corresponding range of values for R and z being represented as a solid line. The z-distribution of BH-LMXBs appears similar to the NS-LMXBs one (as

Table 1.2: Observed properties of NS-LMXBs.

Name	l (deg)	b (deg)	d (kpc)	Δd (kpc)	R (kpc)	z (kpc)	Ref. (distance)
EXO0748-676	279.98	-19.81	7.95	2.3	9.96	-2.70	[1]
2S0918-54	275.85	-3.84	5.05	1.5	9.0	-0.34	[2]
Cir X-1	322.12	0.04	9.15	2.7	5.67	0.00	[3]
4U1608-522	330.93	-0.85	3.3	1.0	5.36	-0.04	[4]
Sco X-1	350.09	23.78	2.8	0.3	5.49	1.13	[5]
4U1636-53	332.91	-4.82	4.3	1.2	4.62	-0.36	[6]
4U1658-298	353.83	7.27	9.85	2.9	2.01	1.25	[7]
4U1702-429	343.89	-1.32	6.2	1.8	2.67	-0.14	[8]
4U1705-44	343.32	-2.34	8.4	2.4	2.40	-0.34	[8]
XTEJ1710-281	356.36	6.92	17.3	5.0	9.20	2.08	[8]
SAXJ1712.6-3739	348.93	0.93	6.9	2.0	1.81	0.11	[9]
1H1715-321	354.13	3.06	6.0	1.8	2.13	0.32	[10]
RXJ1718.4-4029	347.28	-1.65	7.5	2.2	1.79	-0.21	[11]
4U1728-34	354.30	-0.15	5.3	1.6	2.78	-0.01	[12]
KS1731-260	1.07	3.65	6.2	1.8	1.81	0.39	[13]
4U1735-44	346.05	-6.99	9.4	2.8	2.48	-1.14	[8]
GRS1741.9-2853	359.96	0.13	7.75	2.3	0.25	0.01	[14]
2E1742.9-2929	359.56	-0.39	8.05	2.3	0.08	-0.05	[8]
SAXJ1747.0-2853	0.21	-0.24	8.75	2.5	0.75	-0.04	[15]
GX3+1	2.29	0.79	5.05	1.5	2.96	0.07	[16]
SAXJ1750.8-2900	0.45	-0.95	6.1	1.8	1.90	-0.10	[17]
SAXJ1752.3-3138	358.44	-2.64	9.25	2.7	1.26	-0.43	[18]
SAXJ1808.4-3658	355.38	-8.15	3.15	0.9	4.90	-0.45	[19]
SAXJ1810.8-2609	5.20	-3.43	5.95	1.7	2.15	-0.36	[20]
4U1812-12	18.06	2.38	4.0	1.2	4.38	0.17	[21]
XTEJ1814-338	358.75	-7.59	9.6	2.8	1.53	-1.27	[22]
GX17+2	16.43	1.28	13.95	4.1	6.67	0.31	[23]
SerX-1	36.12	4.84	11.1	3.2	6.59	0.94	[8]
Aq1X-1	35.72	-4.14	5.15	1.5	4.86	-0.37	[24]
4U1857+01	35.02	-3.71	8.75	2.5	5.08	-0.57	[25]
4U1916-053	31.36	-8.46	8.8	2.6	4.56	-1.29	[26]
XTEJ2123-058	46.48	-36.20	18.35	5.3	10.96	-10.83	[27]
Cyg X-2	87.33	-11.32	13.35	3.9	15.02	-2.62	[28]

Notes: [1] Gottwald et al. 1986, [2] Jonker et al. 2001, [3] Tennant et al. 1986, [4] Murakami et al. 1987, [5] Bradshaw et al. 1999, [6] Fujimoto et al. 1988, [7] Wijnands et al. 2002, [8] Galloway et al. 2001, [9] Cocchi et al. 2001a, [10] Tawara et al. 1984, [11] Kaptein et al. 2000, [12] Basinska et al. 1984, [13] Muno et al. 2000, [14] Jonker & Nelemans 2004, [15] Natalucci et al. 2000, [16] Kuulkers et al. 2002, [17] Kaaret et al. 2002, [18] Cocchi et al. 2001b, [19] in't Zand et al. 2001, [20] Natalucci et al. 2000, [21] Cocchi et al. 2000, [22] Strohmayer et al. 2003, [23] Kuulkers et al. 2002, [24] Jonker & Nelemans 2004, [25] Chevalier & Ilovaisky 1990, [26] Galloway et al. 2001, [27] Homan et al. 1999, [28] Smale 1998.

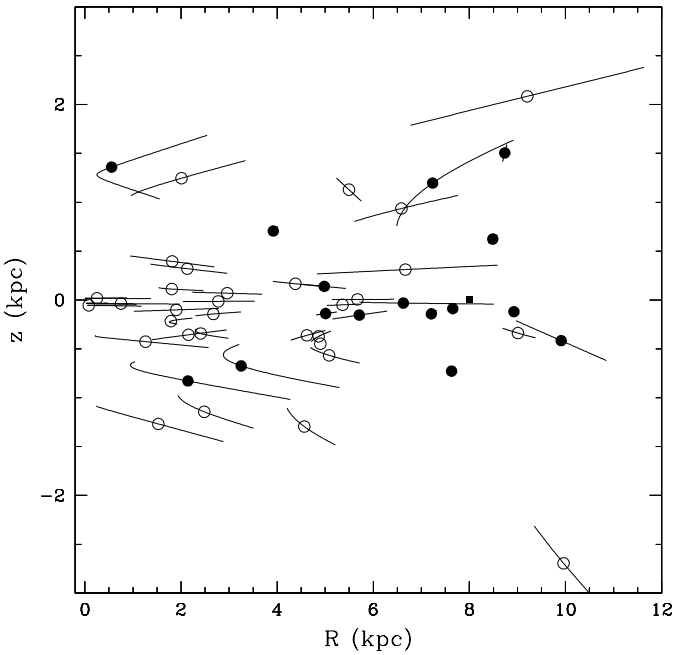

Figure 1.1: Galactic distribution of NS-LMXBs (open circles) and BH-LMXBs (filled circles). The radial distance from the Galactic centre is $R = \sqrt{x^2 + y^2}$, where x and y are the cartesian coordinates in the Galactic plane, whereas the distance from the plane of the Galaxy is $z = d \sin b$. Two neutron star binaries fall off the figure: XTEJ2123-058 and CygX-2. Solid lines account for the uncertainty of the distance from the Sun for each binary. The Sun is indicated as a square.

already pointed out by Jonker & Nelemans 2004, who calculated the rms z for the two samples); the *Kolmogorov-Smirnov* probability P for the two distributions to be the same is indeed convincing: $P \sim 0.81$ (that increases to 0.85 if binaries located at $z > 2.0$ kpc are excluded from the test). Concerning the R distribution, we may observe that NS-LMXBs seem to be more concentrated towards the Galactic centre with respect to the BH-LMXBs. This is very likely an observational bias, as already suggested by Jonker & Nelemans 2004, since the BH binaries that we consider are those for which a dynamical measurement of the BH mass exists, and this biases the binaries towards those closer to us.

1.3 Integrating orbits within the Galaxy

In this section, we will give a short overview of how the orbital trajectories within the Galaxy are calculated. For the Galactic potential, we make use of the model proposed by Paczynski 1990. The potential is modelled as the superposition of three components due to the disc ($\Phi_{\rm d}$), the spheroid ($\Phi_{\rm s}$) and the halo ($\Phi_{\rm h}$), as given below

$$\Phi_{\rm d}(R,z) = -\frac{GM_{\rm d}}{\sqrt{R^2 + \left(a_{\rm d} + \sqrt{z^2 + b_{\rm d}^2}\right)^2}} \tag{1.1}$$

where $a_{\rm d} = 3.7$ kpc, $b_{\rm d} = 0.20$ kpc, and $M_{\rm d} = 8.07 \times 10^{10} {\rm M}_{\odot}$.

$$\Phi_{\rm s}(R,z) = -\frac{GM_{\rm s}}{\sqrt{R^2 + \left(a_{\rm s} + \sqrt{z^2 + b_{\rm s}^2}\right)^2}} \tag{1.2}$$

where $a_{\rm s} = 0.0$ kpc, $b_{\rm s} = 0.277$ kpc, and $M_{\rm s} = 1.12 \times 10^{10}{\rm M}_{\odot}$.

$$\Phi_{\rm h}(r) = \frac{GM_{\rm c}}{r_{\rm c}}\left[\frac{1}{2}\ln\left(1 + \frac{r^2}{r_{\rm c}^2}\right) + \frac{r_{\rm c}}{r}\arctan\left(\frac{r}{r_{\rm c}}\right)\right] \tag{1.3}$$

where $r_{\rm c} = 6.0$ kpc and $M_{\rm c} = 5.0 \times 10^{10}{\rm M}_{\odot}$.

When integrating the trajectory of a binary within the Galaxy, we make use of the cylindrical symmetry of the potential. The equations of motion which are thus integrated are given below

$$\frac{dR}{dt} = v_R, \qquad \frac{dv_R}{dt} = -\left(\frac{\partial\Phi}{\partial R}\right)_z + \frac{j_z^2}{R^3} \tag{1.4}$$

$$\frac{dz}{dt} = v_z, \qquad \frac{dv_z}{dt} = -\left(\frac{\partial\Phi}{\partial z}\right)_R \tag{1.5}$$

where R and z are the cylindrical coordinates of the binary, j_z is the z-component of the angular momentum of the binary, and $\Phi = \Phi_{\rm d} + \Phi_{\rm s} + \Phi_{\rm h}$.

It will turn out that typical kick velocities that the binary receives when the primary explodes as a supernova are comparable to the circular orbital speed in the Galaxy ($\sim$ 200 km/s). This implies that kicks can significantly affect the trajectory of the binary within the Galaxy. We can get an idea of the maximum z reached by the binary as a function of the initial peculiar velocity. We integrate the equations of motion of the binary for ~ 10 Gyrs (which is the typical main sequence MS-time of a sun-like star), using a 4th-order Runge-Kutta integrator developed by SR, and assuming the system was born right in the Galactic plane with a peculiar velocity perpendicular to the plane $v_{\perp}$. We perform the integration for different values of the velocity ($v_{\perp} = 20$, 40, 100, 200 km/s) and of the initial position $R_{t=0}$ over the plane, writing down the maximum z reached over the trajectory (see Figure 1.2). We see how z_{max} is a rather strong function of the initial position: for a fixed value of $v_{\perp}$, $z_{\rm max}$ gets smaller as the binary gets deeper in the potential well (i.e. smaller values of $R_{t=0}$). It is clear from this figure that binary kick speeds in excess of 200 km/s will be required in at least some of the observed systems shown in Figure 1.

1.4 Kicks received by surviving binaries

In this section we consider the effects of the supernova explosion on the binary. We will see how the rapid mass loss from the supernova alone could impart a kick on some systems whilst breaking others up. In addition, any kick imparted to the neutron star or black hole on its formation (i.e. a natal kick) will also play a role, both in adding to the overall kick received by the binary, and in some cases ensuring that the binary remains bound.

It is important to note that a *conspiracy of three velocities* will have an important role; namely the coincidence that the following three speeds are comparable: the speed of a circular orbit in the Galaxy, the typical orbital speed within a tight stellar binary when the primary explodes as a supernova, and

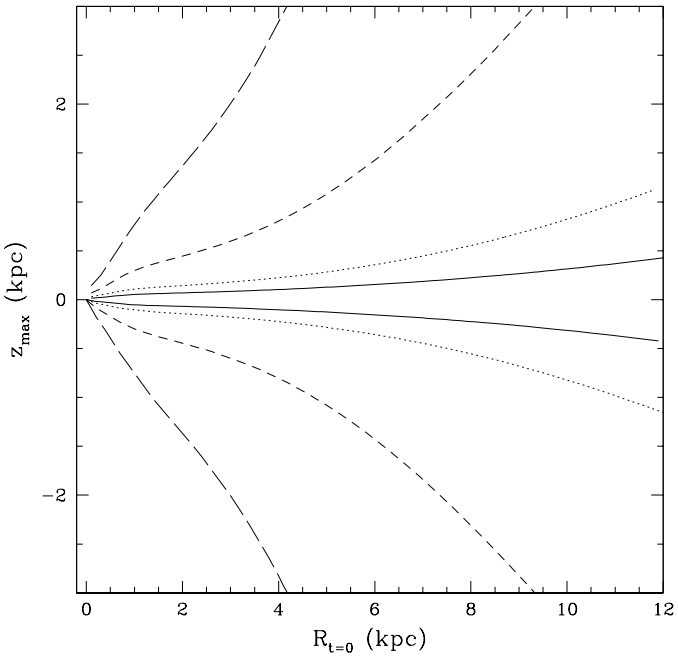

FIGURE 1.2: Maximum z reached by a binary over its trajectory. The object has been kicked perpendicularly to the Galactic plane, for four different magnitudes of the kick ($v_\perp = 20, 40, 100, 200$ km/s).

the characteristic kick speed the binary receives. This coincidence implies that kicks will significantly affect the orbit of the binary within the Galaxy.

We begin by considering the case of zero natal kick. In other words, where any kick is due solely to the rapid mass loss occurring during the supernova explosion. We will refer to this as the mass-loss kick $V_{\rm mlk}$ (also called *Blaauw kick*, Blaauw 1961), which is given by the expression below

$$V_{\rm mlk} = \frac{\Delta M}{M'} \frac{M_2}{M} \sqrt{\frac{GM}{a}} \tag{1.6}$$

where M is the total mass of the binary at the point of the supernova explosion, M' is the total mass of the binary after the supernova explosion, ΔM is the mass lost during the supernova explosion (i.e. $\Delta M = M - M'$), M_2 is the mass of the secondary, and a is the binary semi-major axis at the moment of the supernova explosion.

$V_{\rm mlk}$ can't be too large, since the binary must remain bound after the supernova: the mass loss must be less than half of the initial mass. If we agree on a common envelope phase having shrunk the binary down to an orbital separation of $\sim 10\ {\rm R}_\odot$, the resulting typical mass loss kicks for BH-LMXBs are of the order of $20 - 40$ km/s (for NS-LMXBs they are typically higher). Looking at figure 1.2, we immediately realise how kicks of this size cannot make the highest-z black hole binaries: in the optimal case of $V_{\rm mlk} \simeq 40$ km/s perpendicular to the Galactic plane, the maximum z reached over the trajectory never exceeds 1 kpc (however, we do see binaries in the halo of our Galaxy at larger values of z, see table 1.1).

We consider now the case where the neutron star or black hole produced in the supernova receives a natal kick. If we assume the orientation of the natal kick is random with respect to the orbital plane,

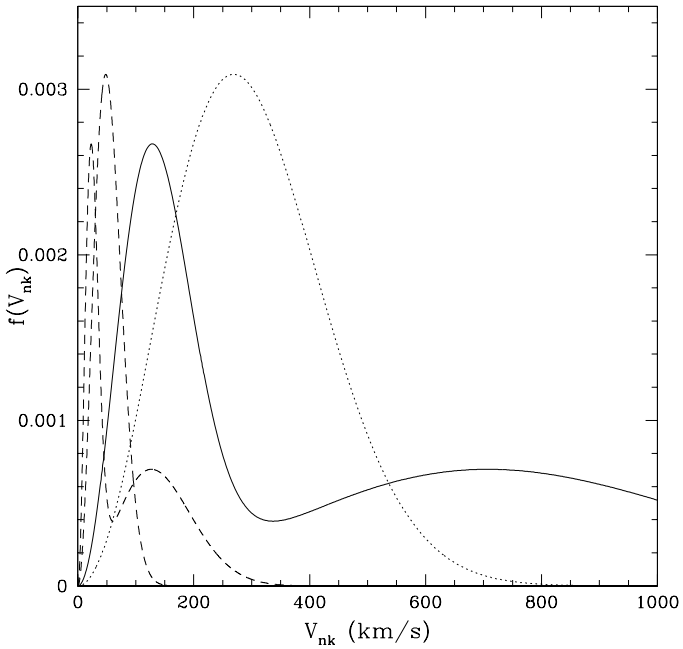

FIGURE 1.3: Natal Kick distributions used in our binary population synthesis calculations. Solid line corresponds to Arzoumanian distribution, dotted line to Hansen & Phinney and the two dashed lines to these two distributions but with kick speeds reduced, assuming that the momentum imparted to the black hole is the same as the momentum imparted to the neutron star.

the natal kick $V_{\rm nk}$ combines with the mass loss kick $V_{\rm mlk}$ as given below:

$$V_{\rm k} = \sqrt{\left(\frac{M_{\rm bh}}{M'}\right)^2 V_{\rm nk}^2 + V_{\rm mlk}^2 - 2\frac{M_{\rm bh}}{M'} V_{\rm nk,x} V_{\rm mlk}} \tag{1.7}$$

where we have chosen the x axis aligned with the orbital speed of the BH progenitor and the y axis along the line connecting the two stars at the moment of the supernova explosion.

Many distributions to model neutron star natal kicks have been proposed. For example, Hansen & Phinney 1997 modelled the natal kick as a Maxwellian distribution peaked at 300 km/s. To solve the retention problem in globular clusters as well as the low eccentricity of a subclass of Be X-ray binaries, two-peak distributions have also been proposed where one peak occurs at a somewhat lower velocity (Pfahl et al. 2002a, Pfahl et al. 2002b).

We consider two different natal kick distributions here: one is the Hansen & Phinney distribution, the other is a bimodal distribution proposed by Arzoumanian et al. 2002 which has a lower peak at $\sim$ 100 km/s and the higher peak at $\sim$ 700 km/s. We also consider modified versions of the above two distributions, which we term momentum-conserving kicks MCKs, where we assume that the momentum imparted on a black hole is the same as the momentum given to a neutron star using the two distributions. Thus the kick velocities will be reduced: $V_{\rm nk,bh} = (M_{\rm ns}/M_{\rm bh})V_{\rm nk,ns}$. For example, a 7 $M_\odot$ black hole receives a natal kick reduced by a factor of 5: for a neutron-star natal kick of 300 km/s, the black hole would receive a smaller kick of only 60 km/s. We show in figure 1.3 the natal kick distributions which we use.

It is important to recall that a large fraction of binaries are broken up when the primary explodes as a supernova.

Table 1.3: Fraction of systems that stay bound after the SN.

Fraction of bound systems		
	BH	NS
Hansen	58%	30%
	56%[a]	35%[a]
	64%[b]	3%[b]
Bimodal	54%	29%
	56%[a]	30%[a]
	52%[b]	10%[b]
Hansen MCK	99%	-
Bimodal MCK	95%	-

Notes: [a] For a NK lying in the orbital plane. [b] For a NK perpendicular to the orbital plane.

Considering a population of binaries where $M_1 = 11$ $\mathrm{M}_\odot$, $M_2 = 1.5$ $\mathrm{M}_\odot$, $M_{bh} = 7.8$ $\mathrm{M}_\odot$, $a = 10$ $\mathrm{R}_\odot$ (M_1 is the mass of the progenitor of the black hole, M_2 is the companion star and a is the pre-SN orbital separation), we impart the BH of each binary a NK drawn randomly from each of our four distributions. The fraction of systems remaining bound for each of the kick distributions is shown in Table 1.3. We also include the case where a 1.4 $\mathrm{M}_\odot$ neutron star is produced instead of a black hole (taking as the progenitor mass 3.5 $\mathrm{M}_\odot$). A larger fraction of binaries remain bound for binaries containing black holes rather than neutron stars owing to the greater binding mass.

We show in figure 1.4 the distribution of kick velocities for BH-LMXBs that we obtain drawing from each of the four natal kick distributions. One should in particular note how the kick velocities for the momentum conserving kicks are typically lower than ~ 100 km/s.

1.5 Binary Population Synthesis

In this section we discuss the calculation of the synthetic population of black hole low-mass X-ray binaries. We produce a population of BH-LMXBs considering their formation within the Galactic disc at a range of radii. For each binary, we randomly draw the black hole natal kick, considering five different natal kick distributions (including a zero natal kick) and give this kick a random direction which we then add to the mass-loss kick due to the supernova to produce the total kick speed of the binary V_k. The gained velocity will be added randomly to the circular velocity of the binary within the Galaxy. Each system is then integrated forward in time within the Galactic potential for $\sim 3 \times 10^9$ yr (which is the MS-time of the 1.5 $\mathrm{M}_\odot$ companion), and its position is noted at random times over the trajectory. We are thus able to produce an entire population of BH-LMXBs given the initial distribution of progenitor systems in the Galactic disc, their binary properties (separation and stellar masses) and the natal kick distributions for the black holes formed.

We populate the disc of the Galaxy assuming the disc distribution of binaries to be proportional to the surface density of stars $\Sigma(R) \sim \Sigma_0 e^{-R/R_\mathrm{d}}$, with a maximum distance from the Galactic centre of

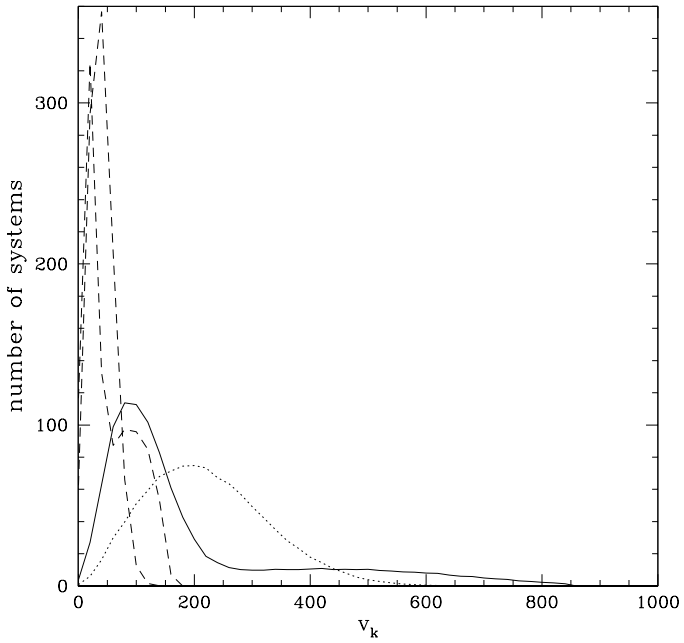

FIGURE 1.4: Peculiar velocity gained by the binary after an asymmetric supernova. Natal kicks have been drawn from Arzoumanian distribution (solid line), Hansen & Phinney distribution (dotted line), whereas the dashed lines correspond to the MCKs. The total number of systems for each curve has been normalised to 1000 and only systems that stay bound after the SN are represented.

$R_{max} = 10$ kpc. We chose $R_{\rm d}$ to be the length scale of the thin disc of the Galaxy, where the progenitor systems are thought to be produced, $R_{\rm d} \sim 2.6$ kpc (McMillan 2011). Concerning the z-distribution of the binaries, we model it as an exponential with scale height ~ 0.167 kpc (Binney & Tremaine 2008).

The population is formed by 100 binaries with the following parameters: $M_1 = 11$ M$_\odot$, $M_2 = 1.5$ M$_\odot$, $M_{\rm bh} = 7.8$ M$_\odot$, $a = 10$ R$_\odot$ (M_1 is the mass of the progenitor of the black hole, M_2 is the companion star and a is the pre-SN orbital separation). For the black hole mass, we choose the average mass of stellar black holes in the Galaxy (see Özel et al. 2010); for the initial orbital separation, our choice is guided by the typical results of common envelope evolution considered in detailed binary evolution calculations for progenitor systems. We choose a typical mass loss in the supernova explosion of ~ 3 M$_\odot$ (see Fryer & Kalogera 2001), which delivers an associated mass-loss kick of ~ 20 km/s.

In addition, the black hole receives a natal kick drawn from one of the following five distributions: 1) a natal kick of zero km/s; 2) one drawn from the Hansen & Phinney distribution (Hansen & Phinney 1997); 3) one drawn from the bimodal distribution of Arzoumanian et al. 2002; 4) as 2) but with the kick speed multiplied by the factor $M_{\rm ns}/M_{\rm bh}$; and 5) as 3) but with the kick speed multiplied by the factor $M_{\rm ns}/M_{\rm bh}$.

We plot the positions of the 100 binaries -at random times of the trajectory- in Galactic cylindrical coordinates for zero black-hole natal kicks in Figure 1.5 and for the other four natal kick distributions in Figure 1.6. From Figure 1.5 it is clear that it is impossible to place BH-LMXBs seen at larger values of z when the black holes receive zero natal kicks. Either the Hansen & Phinney or the Arzoumanian distributions appear to fit the observed distribution of BH-LMXBs, whereas those produced by natal kick distributions with velocities reduced by a factor of $M_{\rm bh}/M_{\rm ns}$ (bottom panels in Figure 1.6) appear to produce distributions which are more concentrated on lower values of z.

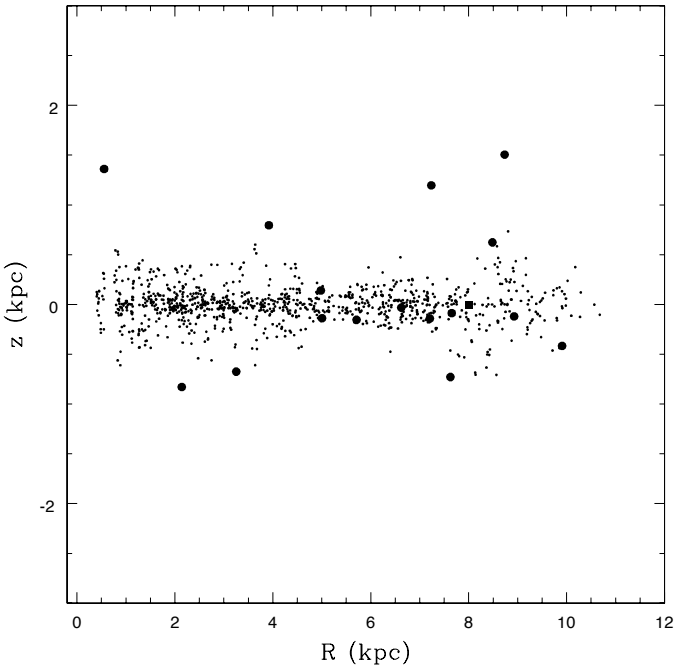

Figure 1.5: Binary population synthesis for a sample of BH-LMXBs. No natal kick has been imparted to the BH. Smaller dots correspond to the synthetic population, bigger ones to the observed binaries and the position of the Sun is denoted with a square.

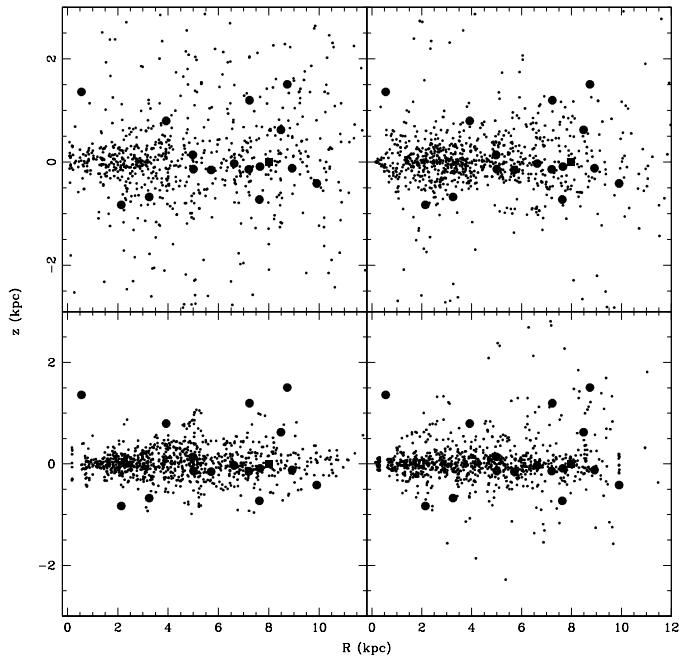

Figure 1.6: Binary population synthesis for a sample of BH-LMXBs. Natal kicks have been drawn from Hansen & Phinney (top left) distribution, a bimodal distribution (top right), whereas the bottom figures correspond to the reduced natal kicks. Smaller dots correspond to the synthetic population, bigger ones to the observed binaries and the position of the Sun is denoted with a square.

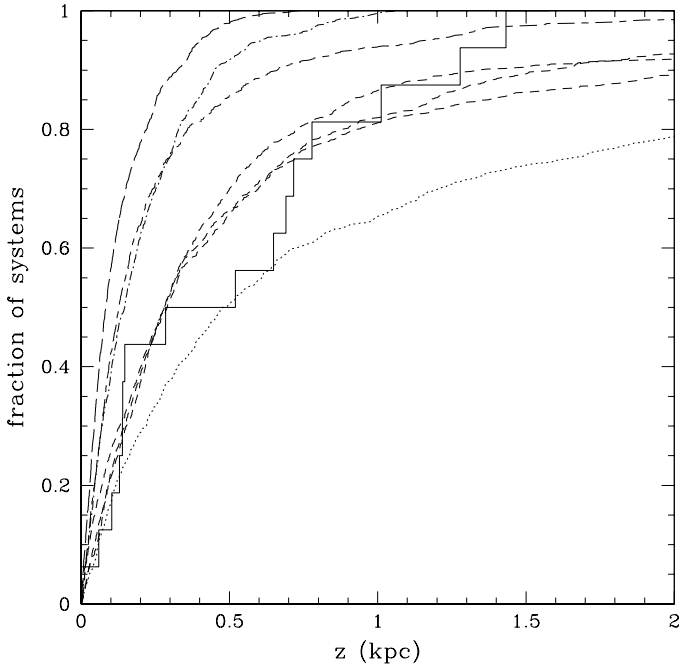

FIGURE 1.7: Cumulatives which show the fraction of BH-LMXBs versus the distance from the Galactic plane, for the four different natal kicks (dotted line is for an Hansen & Phinney NK, dotted-dashed line is for a reduced Hansen & Phinney NK, short-long-dashed is for a reduced Arzoumanian NK, whereas a zero NK scenario corresponds to the long-dashed line). For the Arzoumanian NK, we tested two additional scenarios, a NK lying in the orbital plane and a NK perpendicular to it (see the three short-dashed lines). Cumulatives are to be compared with the observed one (solid line).

1.5.1 Statistics of the results

In order to quantify the results of the BPS, we show in figure 1.7 the fraction of binaries that at some time over the trajectory are located at a distance z from the Galactic plane less than a certain value. We include in the plot the results of the BPS for which no NK has been imparted to the black hole.

It is evident how the mass-loss kicks alone cannot account for the z-distribution of the observed binaries. A reduced Hansen & Phinney NK cannot make the binaries that are located at $z \gtrsim 1$ kpc; in particular, the percentage of binaries that get to z higher than 1 kpc is only the 0.5%. With a reduced Arzoumanian NK the percentage gets higher ($\sim 6\%$), though the fit remains unsatisfactory (see table 1.4). It then turns out to be very difficult, with a momentum conserving kick, to reproduce the binaries XTEJ118+480, 1705-250, XTEJ1859+226, which are located respectively at $z = 1.5$, 1.36, 1.20 kpc. Section 5.5 is dedicated to the detailed study of these sources.

We are aware that the integration time we chose ($\sim 3 \times 10^9$ years) might be higher than the actual age of some of the observed binaries, particularly those whose mass transfer is driven by angular momentum losses, or those with a relatively massive companion star ($M_2 \sim 3$ M$_\odot$, see the updated catalogue Ritter & Kolb 2003). We then carry out other two synthesises for the BH-LMXBs, integrating their trajectories for $\sim 10^8$ years and for $\sim 5 \times 10^8$ years. In the first integration, the percentage of binaries that reach z higher than 1 kpc is 0% for a reduced Hansen & Phinney NK and 1% for an Arzoumanian reduced NK. In the second integration, the percentages are respectively are 0.2% and

2.2%. Concerning the KS-test, the resulting probabilities get 1 or 2 order of magnitudes lower when choosing a reduced integration time; this is easily explained, since the binary doesn't live long enough to be seen at high z.

We wonder whether a larger mass-loss kick would affect our conclusions. Referring to equation 4.3, we see that the mass-loss kick increases either in the case of a larger mass-loss, or a more compact initial binary, or a larger companion mass. It is believed that in the SN event the Helium star loses no more than $3 - 4$ $M_\odot$ (before exploding as a SN, the Helium star suffers from strong WR winds after the common envelope phase, see for example Fryer & Kalogera 2001). Concerning the initial orbital separation, there is a limiting minimum value for which either one or both of the two stars fill their Roche lobe. The following parameters, $M_1 = 11$ $M_\odot$, $M_2 = 3.0$ $M_\odot$, $M_{\rm bh} = 7.8$ $M_\odot$, $a = 6$ $R_\odot$, give a recoil velocity $V_{\rm mlk}$ of ~ 40 km/s. We then perform two synthesises in which we fix the mass loss kick to ~ 40 km/s, testing the two types of reduced natal kicks. The corresponding KS probabilities remain unsatisfactory: 2×10^{-3} for a reduced Hansen NK, and 2×10^{-2} for a reduced bimodal NK. We shall also stress that the integration time for these two synthesises has been set to $\sim 3 \times 10^9$ years; decreasing the integration time would make the KS probabilities even lower.

We perform a BPS for NS-LMXBs as well (binary parameters chosen: $M_1 = 3.5$ $M_\odot$, $M_2 = 1.0$ $M_\odot$, $M_{\rm ns} = 1.4$ $M_\odot$, $a = 7.0$ $R_\odot$): in Figure 1.8 results are shown. It is pretty clear that a bimodal distribution better fits the observed sample. This a strong case for neutron stars receiving a bimodal NK at birth. Previous studies, focused on NSs in Be X-ray binaries and double NS binaries (see works by Pfahl et al. 2002b and Wong et al. 2012), showed that at least some of the NSs should have received a lower kick at birth. We highlight our work as the first test of a bimodal distribution being a better fit to the Galactic position of NS low-mass X-ray binaries. When excluding from the test the observed NS binaries that are located at $z > 2$ kpc, the KS probability rises to 0.19; this is easily explained, since the change in normalisation shifts the simulated curve towards the observed one.

In table 1.4 KS probabilities for the different types of scenario are shown (the probabilities are reasonably accurate for our number of data points, see Teukolsky et al. 1993).

1.6 Discussion

We now aim at deriving the minimum natal kick required to place the observed BH-LMXBs in their current locations. Rather than considering the properties of a general progenitor binary system (i.e. stellar masses, black-hole mass, and binary separation), we use the observed properties for each known system, where possible, to more accurately calculate the mass-loss kick and the effect of any natal kick on the particular system (see Ritter & Kolb 2003 for an updated catalogue of LMXBs in the Galaxy).

For simplicity here, we consider a kick in the (optimal) direction perpendicular to the Galactic disc. We first compute, via conservation of energy, the minimum kick $V_\perp$ for the binary to reach the current position (R_0, z) after traveling in the Galactic potential, assuming the binary is born right over the Galactic plane at some radius R_0. Thus

$$\frac{1}{2}{V_\perp}^2 + \Phi\left(R_0, 0\right) = \Phi\left(R_0, z\right) \tag{1.8}$$

where Φ is the gravitational potential of the Galaxy.

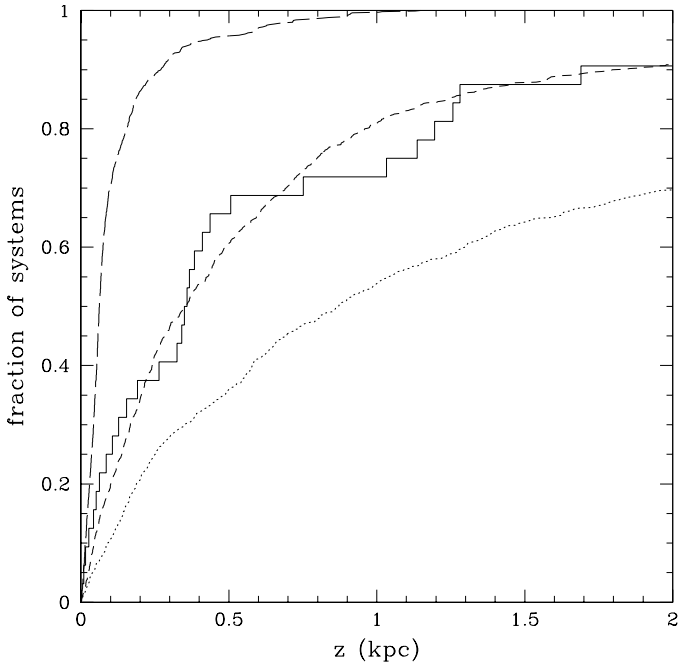

FIGURE 1.8: Cumulatives which show the fraction of NS-LMXBs versus the distance from the Galactic plane, for the four different natal kicks (dotted line is for an Hansen & Phinney natal kick, short-dashed line is for an Arzoumanian natal kick, whereas a zero natal kick scenario corresponds to the long-dashed line). Cumulatives are to be compared with the observed one (solid line).

TABLE 1.4: KS probabilities for the BPS.

KS probabilities		
	BH-BPS	NS-BPS
Integration time 3×10^9 years		
Hansen NK	0.20	2.6×10^{-3}
Bimodal NK	0.18	0.78
Hansen MCK	2×10^{-3}	-
Bimodal MCK	1×10^{-2}	-
zero NK	2×10^{-4}	5×10^9
Integration time 5×10^8 years		
Hansen MCK	7×10^{-4}	-
Bimodal MCK	5×10^{-3}	-
Integration time 10^8 years		
Hansen MCK	4×10^{-4}	-
Bimodal MCK	6×10^{-4}	-

We show in Table 3.3 the minimum perpendicular kick $V_\perp$ and minimum natal kick $V_{\rm nk}$ required for those BH-LMXB systems which have relatively well-constrained binary properties. One should understand that the natal kick value quoted in Table 5 is the absolute lower limit, assuming that the natal kick occurred in the perfectly optimal direction. In practice, the natal kick required will be much larger in many realisations (i.e. different kick directions for the natal and mass-loss kicks). For example, for many directions, the necessary natal kick to reproduce the current location of XTE J1118+480 is up to 300 km/s (as was also seen in Fragos et al. 2009).

The minimum peculiar velocity is normally greater than 80 km/s for binaries that are located at $z > 1$ kpc, or for binaries that are closer in towards the Galactic centre and at $z > 0.6$ kpc. Particularly, for systems that are located at $R \lesssim$ kpc from the Galactic centre, typical required velocities are greater than 100 km/s for the highest-z systems. These high velocities cannot evidently be accounted for by a mass-loss kick alone. In other words, the current location of at least some systems clearly requires the presence of a black hole natal kick broadly in the range $100 - 500$ km/s. For other systems, the current location could be reached with the black hole having received no natal kick. We note that our results are consistent with those found earlier (Nelemans et al. 1999, Jonker & Nelemans 2004, Willems et al. 2005, Dhawan et al. 2007, Fragos et al. 2009).

The system 1705-250 requires the largest minimum natal kick. This is because the system is located close to the Galactic centre and therefore has climbed out of a deeper potential well, assuming it was born at a comparable radius in the Galactic disc. As there is a strong radial dependence of the Galactic potential this close in, we compute the minimum peculiar velocity both launching the binary out of the disc at $R = 0.5$ kpc (the current location is at $R = 0.55$ kpc, $z = 1.36$ kpc) and $R = 2$ kpc. In the first case, we get $V_\perp \sim 400$ km/s, while in the second case a velocity $V_\perp \sim 250$ km/s is needed. These velocities require a minimum natal kick of 440 km/s and of 260 km/s respectively. Our results might have been affected by the choice of a spherically symmetric bulge (i.e. $a_{\rm s} = 0.0$ kpc, see equation 1.2 for the potential of the spheroid); we then take a *pseudobulge* with $a_{\rm s} = 1.0$ kpc. The resulting $V_\perp$ is ~ 320 km/s for $R = 0.5$ kpc and $V_\perp \sim 220$ km/s for $R = 2.0$ kpc. The associated minimum natal kicks are 340 and 230 km/s respectively. For both of the two model for the Galactic potential, the required velocities are larger than the largest velocities drawn from a reduced-velocity kick, from either the Hansen & Phinney or Arzoumanian kick distributions.

We may wonder whether our conclusions on the required minimum natal kick would be affected by a new estimation of the distance. For all of the previously mentioned four binaries, the distance has been derived from the estimation of the absolute magnitude of the companion (see respectively Orosz et al. 2002, Orosz et al. 2001, Gelino et al. 2006, Barret et al. 1996). Jonker & Nelemans 2004 observed that this method typically underestimates the distance. Also, we point out that any underestimation of the contribution of the disc to the observed magnitude of the companion star, would lead to an underestimation of the distance. To quantify the effect of a new estimation of BH binaries distance, we computed the minimum required natal kick, the distance being 10, 25, 50, 100 % larger than the nominal value. We perform the computation for our four candidates of BHs receiving the same NK as NSs. The required minimum NK decreases in all the cases except for XTEJ1118+480. This is easily explained since a larger distance would move the binary further out the Galactic potential well. The binaries 4U1543-47, 1819.3-2525, 1705-250 require a minimum natal kick of 45, 22, 92 km/s, respectively, when the distance is increased of the 100%. XTEJ1118+480 shows instead an increase of the minimum NK

up to ~ 100 km/s when the distance is multiplied by a factor of 2.

An alternative scenario for the formation of BH binaries would be via dynamical interactions in globular clusters (GCs). However, it is still uncertain whether BHs are retained in GCs or whether they follow a different dynamical evolution than NS binaries. So far, no BH X-ray binary has been found in Galactic globular clusters (Verbunt & Lewin 2006); the strongest BH candidate in a GC is the one found by Maccarone et al. 2007, in the Galaxy NGC 4472. The question whether black holes might be retained in a globular cluster has been largely discussed in the literature (e.g., Kulkarni et al. 1993, Sigurdsson & Hernquist 1993, Portegies Zwart & McMillan 2000, Miller & Hamilton 2002). It is generally thought that black holes would tend to decouple dynamically from the rest of the cluster and to segregate into the core, where they would form BH-BH binaries. Sequential dynamical interactions between these binaries and single BHs would lead to the ejection of the BHs from the cluster in a timescale shorter than $\sim 10^9$ years. In case one black hole survives in the cluster, it could potentially capture a stellar companion via two main mechanisms: tidal capture of a star by the BH or exchange interactions of the BH with a primordial binary (see Kalogera et al. 2004 and reference therein). Stars the BH is interacting with have a typical mass $\lesssim 1\ M_\odot$ at this stage of the life of the GC. It has been shown that the two-body tidal capture scenario between a NS and a low-mass star is likely to result in a merger (Davies et al. 1992, Kumar & Goodman 1996, McMillan et al. 1990, Rasio & Shapiro 1991). Specifically, Davies et al. 1992 showed that an encounter between a NS and a red-giant would result in a merger in some 70% of the cases, and some 50% for an encounter between a NS and a MS-star. For a BH, tidal forces are expected to be much larger, so that a merger becomes even more likely. Regarding the exchange interaction scenario, we find it unlikely that the resulting BH-MS star binary will get a large kick in subsequent dynamical encounters for the binary to be expelled from the cluster. Nevertheless, in the optimistic case that the binary managed to be ejected from the cluster with a velocity comparable to the escape speed of the cluster, we may compute the resulting overall distribution of Galactic BH binaries. We assume the binaries to be born in a spheroid of 20 kpc radius around the Galactic centre, taking the halo distribution of Dehnen & Binney 1998. We then kick the binaries with a velocity of 45 km/s and we follow their motion in the Galactic potential for $\sim 3\times10^9$. The resulting KS test gives probabilities lower than 8×10^{-7}, even when we double the BH binaries distance. This result is not surprising since we rarely get any binaries in the disc when assuming that all binaries are born in GCs. It could be that this mechanism would work for the BH binaries found at the highest z. However, at least in the case of XTE J1118+480 there are strong arguments for rejecting a GC origin. Gualandris et al. 2005 estimated the age of the system, using stellar evolution calculations, to be between 2 and 5 Gyr, rendering a globular cluster origin unlikely. González Hernández et al. 2008 performed a detailed chemical analysis of the optical star. Starting from different initial metallicities of the companion, they calculated the expected abundances after contamination from SN nucleosynthesis products and were able to rule out a halo origin for this BH binary. Additionally, Fragos et al. 2009 claimed that the surface metallicity of the donor star right before the onset of RLO might have been even higher than the observed one, which would make the argument for a disc origin stronger. A natal kick seems to be required for this system and one which exceeds the range of kicks obtained from either the Hansen & Phinney or Arzoumanian distributions with a reduction by the ratio of black hole to neutron star masses.

From table 3.3 we see that natal kicks exceeding 70 km/s are required for several systems: 4U1543-47, 1819.3-2525, XTEJ1118+480 and 1705-250. These binaries provide us with evidence that *black*

holes receive natal kicks of the same size as those received by neutron stars. One might have expected the black hole natal kicks to carry the same momentum as those for neutron stars if, for example, a neutron star formed first (and having received a kick) and then a black hole formed later as a result of fall-back material within the supernova. In particular, the magnitude of the natal kick imparted to the BH depends on the competition between two timescales: the fall-back timescale τ_{fb} and the timescale of the mechanism leading to the natal kick τ_{nk}. If $\tau_{fb} > \tau_{nk}$, we expect the fall-back material not to receive the same natal kick has the proto neutron star; the BH natal kick will then be reduced by the ratio M_{ns}/M_{bh}. In case $\tau_{fb} \lesssim \tau_{nk}$, we expect the BH to receive a full natal kick. From our simulations it seems that at least in some of the cases the fall-back material received the same NK as the proto-NS. Our result, already strongly suggested in the overall distribution of z seen in the binary population synthesis, is surprising. However, one should note the large natal kick speeds obtained by the black hole in some of the supernova simulations performed by Fragos et al. 2009.

We would also like to point out the recent measurement of the distance of the BH candidate MAXI J1659-152 (Jonker et al. 2012). Taking the medium value for the distance in the allowed range $d = 6 \pm 2$ kpc, we derive a distance from the Galactic plane of $z \sim 1.7$ kpc. This candidate would add to the number of BH binaries found at large distance from the plane of the Galaxy (see also Kuulkers et al. 2013), thus likely enlarging the sample of strong candidates for BHs receiving large kicks.

A number of mechanisms have been suggested for natal kicks received by neutron stars, some of which will also apply to black holes, especially those forming through the subsequent fall-back of material onto a proto neutron star. Suggested kick mechanisms include two main scenarios: hydrodynamically-driven kicks and neutrino-driven kicks. The former can either be caused by asymmetries in the convective motions under the stalled shock (see Herant et al. 1994, Burrows et al. 1995, Janka & Mueller 1996, and the recent work by Nordhaus et al. 2012) or by over-stable oscillation modes of the progenitor core (Goldreich et al. 1997). The latter are produced by asymmetries in the neutrino flux in a strong magnetic field (Arras & Lai 1999, Lai & Qian 1998). Electromagnetically-driven kicks, instead, act once the neutron star has formed: the off-centre rotating dipole impart the neutron star a kick (Harrison & Tademaru 1975, Lai et al. 2001). For a review of neutron star natal kicks, see Lai 2003. Alternatively, if the core is rotating extremely rapidly it may form a central object surrounded by a massive disc on collapse, which may in turn fragment possibly producing a second compact object orbiting close to the central black hole or neutron star. This secondary will rapidly spiral-in towards the primary. If the secondary is a neutron star, then it may transfer mass to the primary until it reaches the minimum mass for a neutron star at which point it will explode potentially giving the primary a kick (Colpi & Wasserman 2002, Davies et al. 2002). In case both objects are black holes, then a merger kick may result from the asymmetric emission of gravitational waves (see Church et al. 2012, Xing et al. 1994, Rasio & Shapiro 1991, Ruffert & Janka 2001). In both cases, the kick received can be several hundreds km/s. Or else, when the disc on collapse forms directly around a BH, it might release its energy as a powerful jet: if this jets happens to be one-sided, it might impart a kick to the central BH, as suggested by Barkov & Komissarov 2010. The BH-BH merger scenario might be tested via BH spin measurement. Evidence of highly rotating BHs comes from the properties of X-ray spectra of Galactic BH binaries (see for example Zhang et al. 1997, Laor 1991 and also Fender et al. 2010). Ruling out the accretion of matter from a low-mass companion as origin of the BH spin (see McClintock et al. 2006), a BH-BH merger might well fit in this scenario. Herrmann et al. 2007 estimated the recoil velocity for

TABLE 1.5: $V_\perp$ necessary to get to the observed position, and corresponding minimum natal kick $V_{\rm nk}$ [a].

Name	$V_\perp$ (km/s)	$V_{\rm nk}$ (km/s)	R (kpc)	z (kpc)
3 4U1543-47	95	80	3.92	0.70
XTEJ1550-564	22	10	5.0	-0.14
GROJ1655-40	36	0	4.98	0.13
1659-487	113	-	3.25	-0.67
1819.3-2525	160	190	2.14	-0.82
GRS1915+105	5	0	6.62	-0.03
GS2023+338	10	0	7.65	-0.09
GROJ0422+32	25	10	9.91	-0.41
A0620-003	10	0	8.92	-0.12
GRS1009-45	40	15	8.48	0.62
XTEJ1118+480	80	70	8.73	1.50
1124-683	50	40	7.63	-0.73
XTEJ1650-500	20	-	5.71	-0.15
1705-250	420	450	0.55	1.36
XTEJ1859+226	80	-	7.23	1.20
GS2000+251	15	0	7.21	-0.14

NOTES: [a] For BH-LMXBs that lack strong observational constraints, we are unable to calculate accurately $V_{\rm nk}$ so leave it blank here.

two coalescing BHs of equal mass and opposite and equal spin. The recoil velocity reaches ~ 470 km/s in the extreme case. Merritt et al. 2004 considered the case of two BHs of unequal mass; they calculated a maximum recoil velocity of 450 km/s for a mass ratio q in the range $0.2 - 0.4$.

1.7 Conclusions

In this Paper, we have considered the distribution of low-mass X-ray binaries containing black holes (BH-LMXBs) within the Galaxy as a function of the distribution of natal kicks given to the black holes. We have synthesised a BH-LMXB population by forming systems randomly throughout the Galactic disc, weighted by stellar surface density of the disc. We have given each binary a mass-loss kick due to the supernova explosion of the primary and added to this kick a black hole natal kick drawn from one of five kick distributions: 1) a natal kick of zero km/s; 2) one drawn from the Hansen & Phinney distribution (Hansen & Phinney 1997); 3) one drawn from the bimodal distribution of Arzoumanian et al. 2002; 4) as 2) but with the kick speed multiplied by the factor $M_{\rm ns}/M_{\rm bh}$; and 5) as 3) but with the kick speed multiplied by the factor $M_{\rm ns}/M_{\rm bh}$. We have added the two kicks together with random directions and combined (randomly) with the original orbital velocity within the Galaxy. The trajectory of each binary has then been integrated within the Galaxy.

A number of observed BH-LMXBs are found in excess of 1 kpc from the Galactic disc. By comparing our synthesised population to the observed systems, we show that the hypothesis that black holes only

rarely receive a natal kick is ruled out at very high significance. The computed distribution is most similar to the observed distribution when the black hole natal kicks are drawn from the same velocity distribution as for neutron stars. Although we are unable to rule out that black holes receive smaller kicks than neutron stars, in a number of cases the required natal kick is very likely to exceed the maximum possible kicks in the reduced-velocity distributions (i.e. distributions 4 and 5 above).

1.8 Acknowledgments

This work was supported by the Swedish Research Council (grants 2008–4089 and 2011–3991). We thank the anonymous referee for helpful comments that improved our paper. SR is thankful to the University of Pavia for the Erasmus grant and Andrea De Luca for helpful suggestions. MBD and SS gratefully acknowledge the hospitality of the Aspen Center for Physics.

Chapter 2

The coupled effect of tides and stellar winds on the evolution of compact binaries

S. Repetto, G. Nelemans

MNRAS, Volume 444, Issue 1, 2014

Abstract

We follow the evolution of compact binaries under the coupled effect of tides and stellar winds until the onset of Roche-lobe overflow. These binaries contain a compact object (either a black-hole, a neutron-star, or a planet) and a stellar component. We integrate the full set of tidal equations, which are based on Hut's model for tidal evolution, and we couple them with the angular momentum loss in a stellar wind. Our aim is twofold. Firstly, we wish to highlight some interesting evolutionary outcomes of the coupling. When tides are coupled with a non-massive stellar wind, one interesting outcome is that in certain types of binaries, the stellar spin tends to reach a quasi-equilibrium state, where the effect of tides and wind are counteracting each other. When tides are coupled with a massive wind, we parametrise the evolution in terms of the decoupling radius, at which the wind decouples from the star. Even for small decoupling radii this *wind braking* can drive systems on the main sequence to Roche-lobe overflow that otherwise would fail to do so. Our second aim is to inspect whether simple timescale considerations are a good description of the evolution of the systems. We find that simple timescale considerations, which rely on neglecting the coupling between tides and stellar winds, do not accurately represent the true evolution of compact binaries. The outcome of the coupled evolution of the rotational and orbital elements can strongly differ from simple timescale considerations, as already pointed out by Barker & Ogilvie 2009 in the case of short-period planetary systems.

2.1 Introduction

Just like the Earth and the Moon, stars in binaries raise tidal bulges on each other. Tidal interaction is an important ingredient in binary evolution, and, on secular timescales, it can drive the evolution of the system. Tidal interaction between two bodies dissipates energy, and induces exchange of angular momentum between the orbit and the spin of the components. See Zahn 2008 for a recent comprehensive review on tidal theory in binaries.

We study tidal interaction in binaries formed by a stellar component and a companion which can be approximated as a point mass, i.e. neutron star (NS), black-hole (BH) or planet. Unless the spin angular momentum of the stellar component exceeds $1/3$ of the orbital angular momentum, the binary orbital and rotational elements evolve in time, and the binary is pushed towards the lowest-energy configuration, on a timescale which depends on the strength of the tidal interaction. This configuration corresponds to a stable solution for the evolution (Alexander 1973, Darwin 1879, Hut 1980). The equilibrium is characterised by circularity, tidal locking of the two components (synchronisation), and alignment of the stellar spin with respect to the orbital spin. However, an equilibrium solution does not exist in case there is a sink of angular momentum in the system. A possible sink is any stellar wind which carries away angular momentum. One type of angular-momentum loss we consider is *magnetic braking* (MB, see Parker 1958, Weber & Davis 1967, Verbunt & Zwaan 1981), the loss of angular momentum in a magnetic stellar wind from a low-mass star. The stellar wind, being anchored to the magnetic field lines, is forced to corotate out to large stellar radii, causing large amount of angular momentum being lost from the star and consequently from the orbit, thanks to the tidal coupling. Tides, counteracting the effect of magnetic braking, induce a secular spiral-in of the two stars, driving systems- that would otherwise remain detached- to Roche-lobe overflow (RLO).

Tidal evolution is to be considered in all of those systems which acquire a certain degree of eccentricity and/or asynchronism at some point in their evolution. For instance, progenitors of black-hole and neutron-star X-ray binaries, systems containing a star and a planet, or binaries in globular clusters. Tides are also important in one of the possible models for long gamma-ray bursts, in which the black-hole progenitor that undergoes core-collapse is required to be a fast rotator. A way of enhancing the rotation of the progenitor is through synchronisation with the orbital motion (see for example Church et al. 2012).

The coupling between tides and magnetic braking in the progenitors of black-hole low-mass X-ray binaries (BH-LMXBs) and neutron-star X-ray binaries (NS-LMXBs) has often been neglected in the past; typically, one assumes that the binary rapidly circularises and synchronises; once synchronisation is achieved, every bit of angular momentum that is lost from the star, is also lost from the orbit. We aim at investigating whether this model is a good description of the evolution of the systems. In order to do so, we numerically integrate the full set of tidal equations, coupled with magnetic braking, until the Roche-lobe overflow configuration. We then compare our results with the estimates provided by the non-coupled method. We do the same for binaries containing a low-mass star with a planetary companion. We will extend our model to binaries where the stellar companion is of high mass, and we will see how the evolutionary equations need to be modified.

The effect of the coupling between tides and magnetic braking on the evolution of short-period extrasolar planetary systems was studied by Barker & Ogilvie 2009 (hereafter, BO2009). They found that neglecting magnetic braking in this type of systems results in a very different outcome of the

evolution. And in particular, they concluded that it is essential to consider the coupled evolution of the rotational and orbital elements, a conclusion which was previously pointed-out by Jackson et al. 2008, who also focused on the orbital evolution of planetary systems.

This paper is divided into 6 sections: in section 2.2 we present our model and we validate our code, in section 2.3 we show the binaries we study and we make some predictions of the evolution from simple timescale considerations, in section 4.4 and 2.5 we show our results, and in section 2.6 and 2.7 we discuss our results and we draw our conclusions.

2.2 Model

2.2.1 Tides coupled with Magnetic Braking

Magnetic braking is the loss of angular momentum in the stellar wind of a main-sequence magnetic star. Low-mass stars ($0.3 \lesssim M_\star \lesssim 1.5$ M$_\odot$) have radiative cores and convective envelopes, where magnetic fields are thought to be amplified by dynamo processes. Thanks to the corotation of the magnetic field lines out to large distances from the star, any stellar wind takes away large amounts of angular momentum, even if the mass-loss is negligible. The braking is responsible for the slow rotation of most cool and old stars, like the Sun. From Skumanich's empirical law (Skumanich 1972) that describes the dependence of the equatorial velocity on age for main-sequence G stars, the spin-down is obtained as:

$$\frac{d\omega_\star}{dt} = -\gamma_{\rm MB} {\rm R}_\star^2 \omega_\star^3 \tag{2.1}$$

where $\gamma_{\rm MB}$ is measured as $\approx 5 \times 10^{-29} {\rm s/cm}^2$, R$_\star$ is the radius of the star, and $\omega_\star$ its spin frequency. For the radius of the star, we use the mass-radius relation of a ZAMS-star as in Tout et al. 1996. (Note that the star can grow by up to a factor of 2 on the main sequence). For a review on the different prescriptions of magnetic braking see Knigge et al. 2011.

The star is doomed to lose its rotation within its MS-lifetime, unless it is tidally coupled to a companion: the rotational angular momentum reservoir of the star is constantly being refuelled by the tidal torque.

We follow the Hut 1981 description of tidal interaction, in which tides have small deviations in magnitude and direction from their equilibrium shape, and where dynamical effects are neglected. In this model, the deviation of tides in magnitude and direction is parametrised in terms of a constant and small time-lag τ. Orbital elements can therefore be assumed to vary slowly within an orbital period, and their change can be computed through averages along the orbit of the tidal potential.

We extend Hut's equations, valid in the small-angle approximation, to arbitrary inclinations of the stellar spin with the orbital spin, using the same orbit-averaged approach. We note that the tidal model by Hut 1981 was first extended to the case of arbitrary inclinations by Eggleton et al. 1998.

Taking a binary with semi-major axis a, spin frequency of the star $\omega_\star$, eccentricity e, and inclination of the rotational angular momentum with respect to the orbital angular momentum i, we write the tidal equations for the evolution of the rotational and orbital elements, adding the magnetic braking term of equation 2.1:

$$\frac{da}{dt} = -6\left(\frac{K}{T}\right)_i q(1+q)\left(\frac{R_\star}{a}\right)^8 \frac{a}{(1-e^2)^{15/2}} \left[f_1(e^2) - (1-e^2)^{3/2} f_2(e^2)\frac{\omega_\star \cos i}{\omega_{\rm orb}}\right] \tag{2.2}$$

$$\frac{de}{dt} = -27\left(\frac{K}{T}\right)_i q(1+q)\left(\frac{R_\star}{a}\right)^8 \frac{e}{(1-e^2)^{13/2}} \left[f_3(e^2) - \frac{11}{8}(1-e^2)^{3/2} f_4(e^2)\frac{\omega_\star \cos i}{\omega_{\rm orb}}\right] \tag{2.3}$$

$$\frac{d\omega_\star}{dt} = 3\left(\frac{K}{T}\right)_i \frac{q^2}{k^2}\left(\frac{R_\star}{a}\right)^6 \frac{\omega_{\rm orb}}{(1-e^2)^6}\left[f_2(e^2)\cos i - \frac{1}{4}\frac{\omega_\star}{\omega_{\rm orb}} (1-e^2)^{3/2}(3+\cos 2i) f_5(e^2)\right] - \gamma_{\rm MB} R_\star^2 \omega_\star^3 \tag{2.4}$$

$$\frac{di}{dt} = -3\left(\frac{K}{T}\right)_i \frac{q^2}{k^2}\left(\frac{R_\star}{a}\right)^6 \frac{\sin i}{(1-e^2)^6}\frac{\omega_{\rm orb}}{\omega_\star}\left[f_2(e^2) - \frac{f_5(e^2)}{2} \times \left(\frac{\omega_\star \cos i\,(1-e^2)^{3/2}}{\omega_{\rm orb}} + \frac{R_\star^2 a\,\omega_\star^2 k^2 (1-e^2)}{M_{\rm comp} G}\right)\right] \tag{2.5}$$

where $M_{\rm comp}$ is the mass of the compact companion, $M_\star$ the mass of the star, q the mass-ratio $M_{\rm comp}/M_\star$, and the functions $f_i(e^2)$ are polynomials in e^2 as in Hut 1981. For the radius of gyration k, we use the fitting formula given in de Mink et al. 2013, which is based on the detailed stellar evolution models of Pols et al. 1998, and which gives the mass-dependence of k.

The calibration factors $\{K/T\}_{i=c,r}$ measure the strength of the dissipation of the tidal flow. K is the apsidal motion constant, which takes into account the central condensation of the star (Lecar et al. 1976). T is a typical timescale on which significant changes in the orbit take place through tidal evolution; in units of the orbital period, T is the inverse of the tidal time-lag τ. In his derivation, Hut considers a constant time-lag τ. However, it has been later argued whether this was the appropriate choice. The time-lag should in fact be compared with typical relaxation time of the process responsible for the dissipation. The source of dissipation depends on the type of star which undergoes tidal deformations (see Zahn 1977).

Low mass stars have convective envelopes and it is believed that turbulent convection is responsible for the dissipation. When viscosity results from turbulence, the natural relaxation time is the eddy-turnover timescale $\tau_{\rm conv}$. This may be longer than the orbital period, in which case the efficiency of the dissipation should be reduced. The efficiency should then be dependent on the tidal forcing frequency (see Goldreich & Nicholson 1977, Zahn 1989, Ivanov & Papaloizou 2004).

Two scalings have been proposed for the viscosity due to the turbulent convection. Zahn 1966 assumes a linear scaling with the tidal forcing frequency. He expresses $f_{\rm conv}$, the fraction of the convective cells which contribute to the damping, as:

$$f_{\rm conv} = \min\left[1, \left(\frac{P_{\rm tid}}{2\tau_{\rm conv}}\right)\right] \tag{2.6}$$

where $P_{\rm tid}$ is the tidal forcing period, given by:

$$\frac{1}{P_{\rm tid}} = \left| \frac{1}{P_{\rm orb}} - \frac{1}{P_\star} \right| \tag{2.7}$$

For high tidal-forcing frequency (i.e. when $P_{\rm tid} \ll \tau_{\rm conv}$) the efficiency of momentum transfer by the largest convective cells is reduced. Instead, Goldreich & Nicholson 1977 suggested a quadratic dependence:

$$f_{\rm conv} = \min\left[1, \left(\frac{P_{\rm tid}}{2\tau_{\rm conv}}\right)^2\right] \tag{2.8}$$

There is a long-standing uncertainty regarding which scaling is correct, with some numerical simulations of turbulent viscosity in a convection zone favouring a linear scaling (Penev et al. 2007), while others favouring a quadratic scaling (Ogilvie & Lesur 2012).

The question of tidal dissipation in a convective shell is still "Achille's heel of tidal theory", as Zahn 2008 wrote, and it goes beyond the scope of this Paper. We choose $f_{\rm conv}$ as in eq. 2.8. In this we follow the approach by Hurley et al. 2002, Belczynski et al. 2008 and Valsecchi & Rasio 2014, who express the calibration factor for a convective envelope as:

$$\left(\frac{K}{T}\right)_c = \frac{2}{21}\frac{f_{\rm conv}}{\tau_{\rm conv}}\frac{M_{\rm env}}{M_\star}\ [\mathrm{yr}^{-1}] \tag{2.9}$$

where $M_{\rm env}$ is the mass in the convective envelope.

Zahn's prescription seem to be in better in agreement with observations of tidal circularisation times for binaries containing a giant star (Verbunt & Phinney 1995). A more recent work by Belczynski et al. 2008, showed the need for multiplying $f_{\rm conv}$ in eq. 2.8 by 50, to match the observed circularisation period of close binary stars. However, due to general uncertainties on tidal calibration for a convective envelope, we find our model a reasonable place to start.

Another uncertainty is whether and how the time-lag should depend on the misalignment between the stellar spin and the orbital angular momentum. There is not yet agreement on this (Adrian Barker, priv. communication), and we prefer not to add additional parameters to our model.

High-mass stars have radiative envelopes, and tidal motions are assumed to be dissipated via radiative damping of the stellar g-modes. In this case the calibration factor is (Hurley et al. 2002, Belczynski et al. 2008):

$$\left(\frac{K}{T}\right)_r = 1.9782 \times 10^4 \frac{M_\star R_\star^2}{a^5}\,(1+q)^{5/6}\,E_2\ [\mathrm{yr}^{-1}] \tag{2.10}$$

where E_2 is a second-order parameter which measures the coupling between the tidal potential and the gravity mode (Zahn 1975); we fit it to the values given by Zahn 1975:

$$E_2 = 1.58313 \times 10^{-9} M_\star^{2.84} \tag{2.11}$$

(see also Hurley et al. 2002).

2.2.2 Non-coupled methods

One way of following the evolution of a binary system in which tidal friction and magnetic braking are both operating, is to assume synchronisation and to circularise the binary instantaneously or on a certain circularisation timescale, neglecting the spin of the star. The new semi-major axis is then

$a_{\rm circ} = a(1-e^2)$. This choice appears reasonable when dealing with systems in which the angular momentum stored in the tidally-deformed component is small (i.e. the moment of inertia of the star is small). Tidal interaction conserves the total angular momentum $J_{\rm tot} = J_{\rm orb} + J_\star$. Neglecting $J_\star$, conservation of $J_{\rm orb}$ gives $a_{\rm circ} = a(1-e^2)$. Afterwards, the tidal torque counteracts the effect of the magnetic spin-down, bringing angular momentum from the orbit back into the star. It is then reasonable to assume that every bit of angular momentum which is lost from the star, is also lost from the orbit (i.e. $\dot{J}_{\rm orb} = \dot{J}_\star$, see Verbunt & Zwaan 1981). The rate of angular momentum loss in the stellar wind is:

$$\frac{dJ_\star}{dt} = k^2 M_2 R_\star^2 \frac{d\omega_\star}{dt} \tag{2.12}$$

where we have neglected the change in radius and mass of the star, for the mass-loss being negligible (typically, $|\dot{M}_\star| \sim 10^{-14}$ M$_\odot$ /yr for a Sun-like star). Using $\dot{a}/a = 2\dot{J}_{\rm orb}/J_{\rm orb} = 2\dot{J}_\star/J_{\rm orb}$ and equation 2.1, and assuming $\omega_\star = \omega_{\rm orb}$, the semi-major axis decay rate is:

$$\frac{da}{dt} = -\frac{2\gamma_{\rm MB} k^2 R_\star^4 G M^2}{M_{\rm comp}} \frac{1}{a^4} \tag{2.13}$$

where M is the total mass of the binary. We will call this approach *non-coupled* method.

Our approach instead is to numerically-integrate the full set of tidal equations coupled with the magnetic spin-down (eqs. 2.2-2.3-2.4-2.5). In section 4.4 we present the results of this integration for some illustrative binaries, showing how they differ from the results in the non-coupled method. A particular stress will be given to circularisation timescales. Some previous works used these timescales as a simple way of depicting the evolution of compact binaries. It turns out that the true evolution of the eccentricity can highly differ from the exponential decay implied by the choice of a circularisation timescale as $e/\dot{e}$.

2.2.3 Validation of the evolution code

For small values of the inclination, our tidal equations for an eccentric and non-coplanar binary recover the equations in Hut 1981. In contrast to the BO2009 equations, we write down explicitly the tidal equations for $(a, e, \omega_\star, i)$ in the case of a non-circular and non-coplanar orbit. BO2009 choose instead of constant time-lag τ like in Hut's model, a constant Q', where Q' is a re-parametrisation of the tidal calibration factor Q. The factor Q, also called *quality factor*, is a dimensionless quantity used mainly in planetary studies for characterising the efficiency of tidal dissipation. BO2009 take $Q' = 10^6$ (see also Ogilvie & Lin 2007). We recover the equations 4, 5, 6 in BO2009 for a circular and non-coplanar orbit, when replacing K/T in our equations with $\frac{3}{2Q'}\frac{1}{\omega_{\rm orb}}\frac{GM_\star}{R_\star^3}$.

In order to validate our code, we reproduce some of the results presented by BO2009. Figure 2.1 is a phase-portrait plot, showing the evolution in the plane ($\tilde{n}$, $\tilde{\Omega}$) of coplanar and circular systems with varying initial conditions. The variables $\tilde{n}$ and $\tilde{\Omega}$ are re-parametrisation of the orbital frequency and the stellar spin frequency respectively, which have been normalised to the orbital frequency at the stellar surface, together with a constant factor (see BO2009 for details). In integrating our evolutionary equations, we have replaced our tidal calibration factor K/T with $\frac{3}{2Q'}\frac{1}{\omega_{\rm orb}}\frac{GM_\star}{R_\star^3}$, and we have used BO2009 calibration for magnetic braking ($\gamma_{\rm MB}$ in our model is 0.4 times smaller than $\gamma_{\rm MB}$ in BO2009). Figure 2.1 coincides with the top plot in fig.1 of BO2009. Once magnetic braking spins down the star below corotation ($\tilde{\Omega} < \tilde{n}$) the orbit undergoes tidally-induced decay.

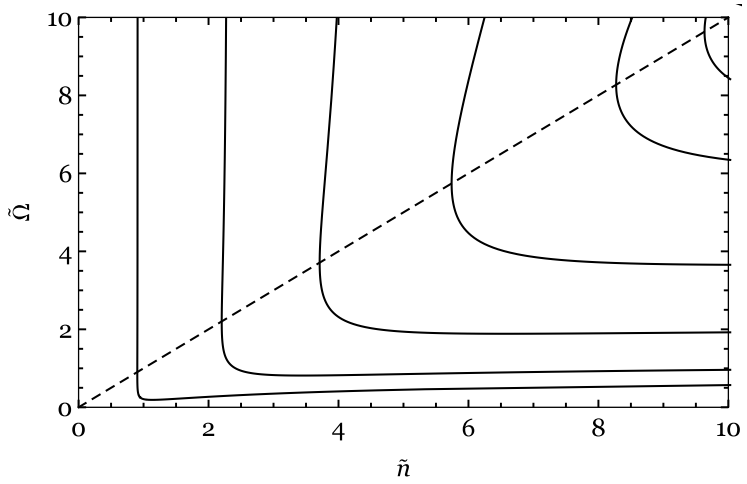

FIGURE 2.1: Evolution of a coplanar and circular planetary system with varying initial conditions in the plane $(\tilde{n}, \tilde{\Omega})$ (solid lines). The diagonal line corresponds to corotation $\tilde{\Omega} = \tilde{n}$.

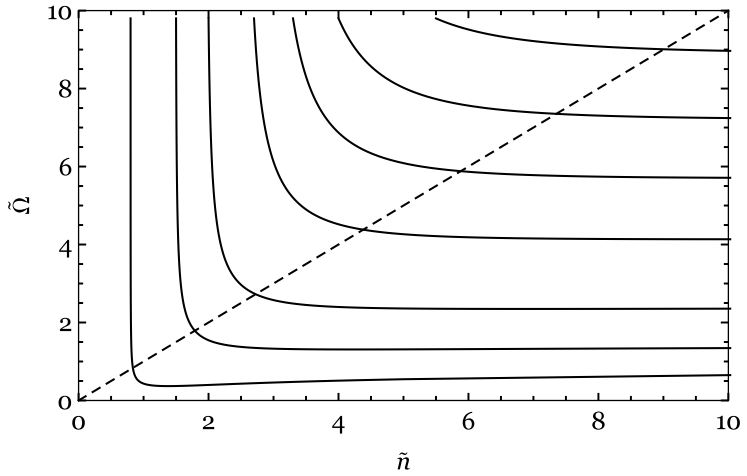

FIGURE 2.2: Evolution of a circular and non-coplanar ($i = 90°$) planetary system with varying initial conditions in the plane $(\tilde{n}, \tilde{\Omega})$ (solid lines). The diagonal line corresponds to corotation $\tilde{\Omega} = \tilde{n}$.

We also integrate our evolutionary equations for a set of planetary systems with circular and non-coplanar orbit ($i = 90°$), and we show the corresponding solutions in the phase-portrait plot of figure 2.2. The overall evolution is similar to the one in figure 2.1, the only difference being that system with $\tilde{\Omega} \cos i < \tilde{n}$ undergo orbital decay while still being outside corotation. This plot is identical to the top plot in fig.3 in BO2009.

2.3 Binaries in our study

We present the binaries we consider in our study in figure 2.3. The most extreme ones are binaries in which the magnetic wind from a low-mass star is coupled with the tidal friction between the star and its compact companion. The companion is either a black-hole, or a Hot Jupiter, which is a planet with mass similar to Jupiter at a distance less than 0.1 AU from its host star.

We will also extend our model to a case in which the star is of high-mass instead (see section 2.5). The companion is either a neutron star, a black-hole, or, in a more exotic scenario, a white dwarf (WD).

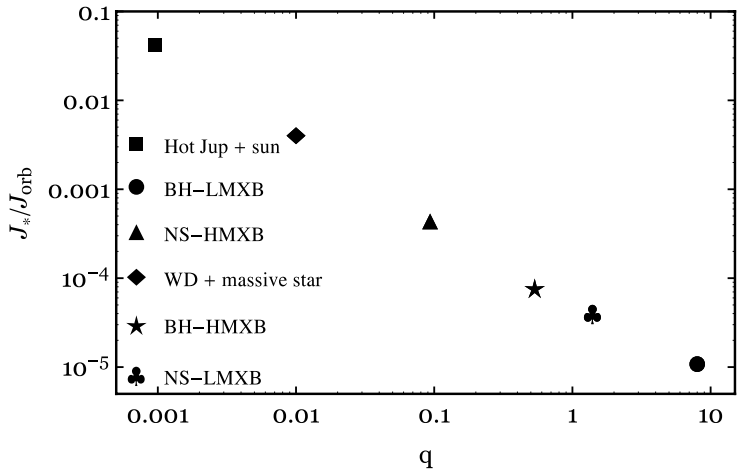

FIGURE 2.3: Different types of compact binaries as a function of the ratio $J_\star/J_{\rm orb}$ between the rotational and the orbital angular momentum and as a function of the binary mass ratio q.

Together these systems span a wide range of mass ratios, ranging from $q = 0.001 - 10$.

We will refer to a binary containing a black hole or a neutron star as a black-hole X-ray binary of high or low mass (BH-HMXB/BH-LMXB), or a neutron-star high/low-mass X-ray binary (NS-HMXB/NS-LMXB), where low and high refer to the mass of the companion. We point out though that these terms commonly refer to the mass-transfer phase, which is one of the evolutionary stages experienced by these binaries. What we deal with instead are systems on their way of becoming X-ray binaries, that is, we study the secular phase before mass-transfer sets in.

2.3.1 Timescale considerations

Before going into the details of the numerical integration of the coupled equations 2.2-2.3 -2.4 -2.5, we wish to make some predictions on the evolution of the systems based on simple timescale considerations[1].

The binaries in our study are presented in figure 2.3 in terms of their mass-ratio q and the ratio $\eta = J_\star/J_{\rm orb}$. $J_{\rm orb}$ is calculated for a circular orbit with $a = 2\ a_{\rm RLO}$. $a_{\rm RLO}$ is the orbital separation at which the system undergoes RLO, i.e. $a_{\rm RLO} = R_\star/f(1/q)$, where $f(q)$ is a function of the mass-ratio as in Eggleton 1983. $J_\star$ is calculated for a slow-spinning star with $\omega_\star = 10^{-3}\ \omega_{\rm break}$, where $\omega_{\rm break}$ is the break-up frequency $\sqrt{GM_\star/R_\star^3}$. The ratio η is then larger for faster-spinning star. It is an indicator for how much angular momentum is stored in the star compared to how much is stored in the orbit. A larger η, like in the planetary system case, implies that tides will more easily bring changes to the orbit than to the spin. If the orbit is sufficiently close, the planetary system suffers a significant tidal decay, while the tidal change of the stellar spin is much less significant. The opposite happens in a BH-LMXB, where tides easily affect the stellar spin.

The larger the mass-ratio, the smaller the timescale on which tides cause significant changes to the orbital and rotational elements, as can be seen from the dependence on the mass-ratio of the tidal

[1] As a note, throughout the paper we will indicate the timescale of a certain event with τ, whereas t will indicate the time of occurrence of the same event in our integration.

equations 2.2-2.3-2.4-2.5. Hence tides are much more efficient in a BH-LMXB than in a planetary system.

We can obtain a rule of thumb for determining which systems will first circularise rather than synchronise. The circularisation timescale can be estimated as $e/\dot{e}$ where $\dot{e}$ is as in equation 2.3, and assuming $e \approx 0$ and $\omega_\star = \omega_{\rm orb}$ (Hurley et al. 2002):

$$\frac{1}{\tau_{\rm circ}} = \frac{21}{2}\left(\frac{K}{T}\right)_{\rm c} q\,(1+q)\left(\frac{R_\star}{a}\right)^8 \tag{2.14}$$

The synchronisation timescale for a circular orbit is calculated as (Hurley et al. 2002):

$$\frac{1}{\tau_{\rm sync}} = \left|\frac{\dot{\omega}_{\star|\rm tid}}{\omega_\star - \omega_{\rm orb}}\right| = 3\left(\frac{K}{T}\right)\frac{q^2}{k^2}\left(\frac{R_\star}{a}\right)^6 \tag{2.15}$$

Then $\tau_{\rm circ} < \tau_{\rm sync}$ when:

$$\frac{kR_\star}{a} > \sqrt{\frac{6}{21}\frac{q}{1+q}} \tag{2.16}$$

where the star can be modelled as a rigid sphere of radius $kR_\star$. Taking $a = 2\ a_{\rm RLO}$, the criteria is satisfied for two of the types of binaries we showed in figure 2.3: the planetary system and the binary consisting of a white-dwarf and a massive star. In all the other cases, we expect the first phase of the evolution of the binary to be driven by changes in the stellar spin rather than the orbit.

In our model the spin is being affected both by tides and by magnetic braking; we compare their typical timescales.

The MB spin-down timescale is calculated as:

$$\frac{1}{\tau_{\rm MB}} = \frac{\dot{\omega}_{\star|\rm MB}}{\omega_\star} \tag{2.17}$$

where $\dot{\omega}_{\star|\rm MB}$ is as in equation 2.1. In figure 2.4, we show the synchronisation timescale and the circularisation timescale for a binary composed of a low-mass star ($M_\star = 1\ {\rm M}_\odot$), as a function of the compact companion mass (solid black and solid grey line). Timescales are calculated using equations 2.14 and 2.15. The orbital separation is taken to be $a = 2\ a_{\rm RLO}$ and the star is spinning with $\omega = 0.9\ \omega_{\rm break}$. We also show the MS-lifetime, the MB spin-down timescale for a star spinning at $0.9\ \omega_{\rm break}$, the MB spin-down timescale for a star spinning at $\omega_{\rm eq}$, and for a star spinning at $10^{-5}\ \omega_{\rm break}$.

The quasi-equilibrium frequency $\omega_{\rm eq}$ is the frequency at which MB and tidal torque are balancing each other (i.e. $|\dot{\omega}_{\star,\rm MB}| = |\dot{\omega}_{\star,\rm tid}|$, see section 4.4 for further details). It has been calculated for an orbit with $a = 2\ a_{\rm RLO}$ and $e = 0.1$.

For low mass-ratios, tides are weak. Consequently, magnetic braking spins-down the star below corotation ($\omega_\star < \omega_{\rm orb}$), and tides won't manage to synchronise the spin frequency to the orbital frequency within a MS-lifetime. This is what happens in the planetary-system case. Instead, in a BH-LMXB tides and magnetic braking tend to reach a quasi-equilibrium state in which they balance each other.

Concerning the circularisation timescale, it is typically shorter than the synchronisation timescale for $q < 0.05$, like in the planetary system case.

When tides and magnetic braking are coupled, we can use this figure to predict the evolution of the binary. If a star is initially spinning at $0.9\ \omega_{\rm break}$, $\tau_{\rm MB}$ is shorter than $\tau_{\rm sync}$. This means that in the first phase of the evolution MB spins down the star, until the timescale on which tides act on the spin becomes comparable to the MB timescale, and tides start playing a role.

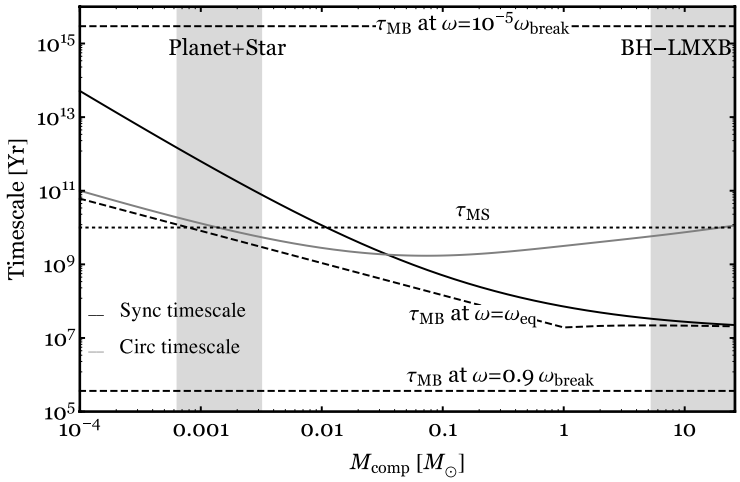

FIGURE 2.4: The solid black line and the solid grey line show respectively the synchronisation and circularisation timescale for a binary with $a = 2\ a_{\rm RLO}$ composed of a sun-like star and a companion of mass $M_{\rm comp}$. The dotted line shows the MS-lifetime, whereas the dashed lines show the MB spin-down timescale for $\omega_\star = 0.9\ \omega_{\rm break}$, the MB spin-down timescale for $\omega_\star = \omega_{\rm eq}$ (see text for details on $\omega_{\rm eq}$), and for $\omega_\star = 10^{-5}\ \omega_{\rm break}$.

2.4 Results

2.4.1 Black-hole low-mass X-ray binary

The orbit of a black-hole low-mass X-ray binary is typically eccentric right after the formation of the black-hole. The eccentricity is the result of the mass ejection and/or possibly the natal kick in the supernova which gives birth to the black hole. In addition, any component of the natal kick perpendicular to the orbital plane will result in a misalignment between the orbital spin and the stellar spin. The most effective way of shrinking a BH-LMXB down to the RLO configuration is a coupling between the magnetic wind from the low-mass star and tidal friction, whereas gravitational wave emission can be neglected for the typical initial orbital separations ($a \approx 10\ R_\odot$).

Previous binary population synthesis (BPS) works on the evolution of BH-LMXBs have neglected the coupling between the stellar spin and the orbital spin, following the evolution of the binaries according to what we call the non-coupled method (see for example Kalogera 1999 and Yungelson et al. 2006). This has been done for NS-LMXBs too, see for example Pylyser & Savonije 1988 and Ma & Li 2009. This choice was motivated by the fact that the rotational angular momentum is small compared to the orbital angular momentum. Also, the tidal evolution of the misalignment between the spin of the star and the orbital spin has usually been neglected.

2.4.1.1 An illustrative example of the evolution in the coplanar case

We integrate the tidal equations 2.2, 2.3, 2.4, 2.5 for an illustrative system formed by a black hole of mass $M_{\rm BH} = 8\ M_\odot$ and a star of mass $M_\star = 1\ M_\odot$, until the RLO configuration is reached ($a_{\rm RLO} \approx 4\ {\rm R}_\odot$). The rotational angular momentum is small compared to the orbital one (see figure 2.3), thus we expect the system to rapidly reach the synchronous state.

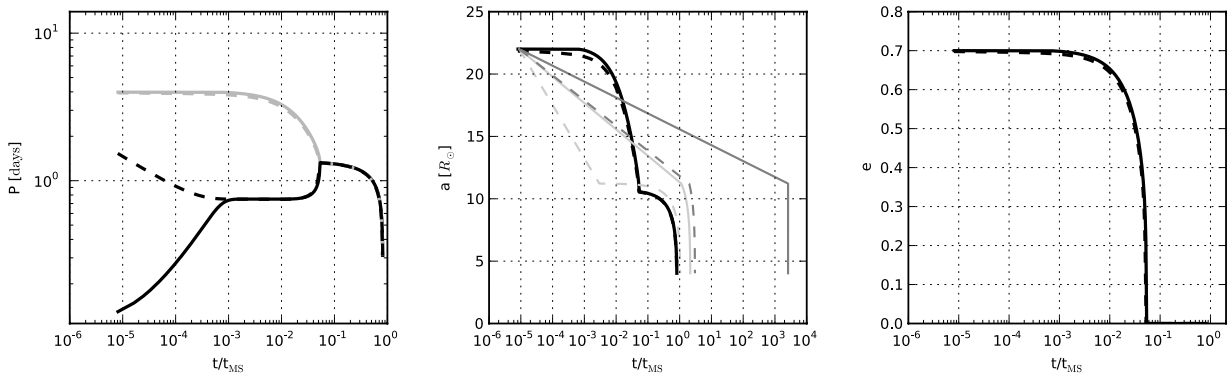

FIGURE 2.5: Evolution of a coplanar and eccentric BH-LMXB under the effect of tides and magnetic braking. The binary is composed of a black-hole of mass $8\ M_\odot$ and a one solar-mass star. Initial orbital parameters are $a = 22\ R_\odot$, $e = 0.7$, $i = 0$. We consider both a high-spinning star ($\omega_\star = 0.9\ \omega_{\rm break}$) and a low-spinning star ($\omega_\star = 10^{-5}\ \omega_{\rm break}$). In all the three panels, the solid lines correspond to the high-spin, the dashed lines to low-spin. The left panel shows the evolution of the stellar rotation period in black and of the orbital period in grey. The middle panel shows the evolution of the orbital separation, whereas the right one represents the evolution of the eccentricity. In the centre panel, the two thick black lines represent the evolution of the orbital separation in our integration. The thin dark-grey lines represent the evolution of the orbital separation in the non-coupled method when taking $\tau_{\rm circ} = (e/\dot{e})|_{\rm e\approx 0, \omega_\star = \omega_{\rm orb}}$; thin light-grey lines when taking $\tau_{\rm circ} = e/\dot{e}$.

In figure 2.5 we show the evolution for initial orbital parameters $a = 22\ R_\odot$, $e = 0.7$ and $i = 0$. Concerning the spin of the star, we consider both a star spinning at $\omega_\star = 0.9\ \omega_{\rm break}$ (see solid thick lines), and at $\omega_\star = 10^{-5}\ \omega_{\rm break}$ (dashed thick lines).

Either via magnetic spin-down (high-spin case) or via tidal spin-up (low-spin case), the spin frequency converges to $\omega_{\rm eq}$, where $\omega_{\rm eq}$ is the spin-frequency such that $|\dot{\omega}_{\star,\rm MB}| = |\dot{\omega}_{\star,\rm tid}|$ (plateau in the left panel in figure 2.5). The approach of this *quasi-equilibrium* state [2] is allowed by the fact that both $\dot{\omega}_{\star,\rm MB}$ and $\dot{\omega}_{\star,\rm tid}$ depend on the stellar spin (see equations 2.1 and 2.4).

Both solutions reach the quasi-equilibrium state $\omega_{\rm eq}$ on a similar timescale, which is very short ($\approx 10^{-3}\ t_{\rm MS}$), therefore no significant changes in the orbit take place during this phase. Afterwards, the orbit circularises and the spin synchronises to the orbital frequency. We note that the time for the orbit to become circular is non-negligible ($t_{\rm circ} \sim 6 \times 10^{-2}\ t_{\rm MS}$). Once synchronisation and circularisation are achieved, every bit of angular momentum which is lost from the star in the wind, is also lost from the orbit. The two components effectively approach each other until RLO, and equation 2.13 describes well the evolution of the system. During this phase of the evolution, tides and magnetic braking are perfectively counteracting each-other, i.e. $\dot{\omega}_\star|_{\rm MB} = \dot{\omega}_\star|_{\rm tid}$.

2.4.1.2 Comparison with non-coupled methods

We also compare the results of our integration with the estimates of the non-coupled method, both for the low-spinning case and the high-spinning case. The results are presented in the centre panel of figure 2.5, where we show the evolution of the semi-major axis in the non-coupled method. We

[2] We call it *quasi-equilibrium* state due to the fact that the orbital properties are still evolving.

take two types of circularisation timescale; one as in equation 2.14 (dark grey lines), and one given by $\tau_{\rm circ} = e/\dot{e}$ (light grey lines). Solid lines are for the high spinning case and dashed lines for the low spinning case. The circularised orbital separation is overestimated in both scenarios, since changes in the orbit once the binary reaches the quasi-equilibrium state, are neglected in non-coupled methods. As a consequence, the age of the binary at the RLO configuration is overestimated. When taking $\tau_{\rm circ} = e/\dot{e}$, it is overestimated by a factor of ≈ 2.6 in the high-spin case, and by ≈ 1.3 in the low-spin case. The time it takes to reach circularisation in our integration is $t_{\rm circ} \approx 0.06\ t_{\rm MS}$. The ratio $t_{\rm circ}/\tau_{\rm circ}$ when taking $\tau_{\rm circ} = e/\dot{e}$, is 0.05 in the high-spin case, and 20 in the low-spinning case. With $\tau_{\rm circ}$ as in equation 2.14, the ratio is 2×10^{-5} and 0.03 respectively.

A better estimate of the time it takes to reach circularisation would arise taking a star spinning at half the break-frequency in the calculation of $e/\dot{e}$ (see for details figure 2.7).

This illustrative example highlights the importance, at least in the first phase of the evolution (before circularisation is achieved), of considering the coupled evolution of the rotational and orbital element.

2.4.1.3 An illustrative example of the evolution in the misaligned case

Misalignment has usually been neglected, and we wonder whether it brings significant changes to the orbital evolution. Due to the small angular momentum stored in the star ($J_\star/J_{\rm orb} \ll 1$), we expect the tidal torque to easily affect $J_\star$. That is, we expect the stellar spin to rapidly align and synchronise with the orbital spin.

In figure 2.6 we show a representative illustration of the evolution of a BH-LMXB with initial orbital parameters $a = 9\ R_\odot$, $e = 0.5$, with the star in a retrograde orbit around the black hole ($i = 120^\circ$) and spinning at $0.9\ \omega_{\rm break}$. Once magnetic braking has spun-down the star sufficiently, the spin aligns with the orbital angular momentum. This can be seen in the right panel in the figure, which shows how steeply the inclination decreases once the spin of the star has become negligible. An interesting difference with respect to the evolution in the coplanar case, is the initial decay of the orbital separation of a retrograde orbit. This is due to the fact that $\omega_\star \cos i < \omega_{\rm orb}$. In the retrograde case, or in any case when the previous condition is satisfied, there is a first phase in which tides and magnetic braking are simultaneously at work. In the coplanar case, instead, the first phase of the evolution is dominated either by tides or by magnetic braking, that act in opposite directions.

In case magnetic braking is not present, the star would align, but on a longer timescale. This is due to the fact that magnetic braking is much more efficient than tides in spinning down the initially high-spinning star. Once the star has been spun-down, the spin rapidly aligns. For the binary configuration we've just showed the ratio between the time at which the spin aligns in the magnetic braking case and in the tides-only case is ≈ 0.6.

2.4.1.4 Population study

As a more general diagnostic of the discrepancy between the coupled and the non-coupled method, we now do a population study, investigating how both the orbital separation at the time the binary circularises and the time it takes to reach circularisation, change over the population. In the non coupled method, the two quantities just mentioned are given by $a_{\rm circ} = a(1-e^2)$ and $\tau_{\rm circ} = e/\dot{e}$.

The initial values e_0 of the eccentricity are taken from a grid which spans the interval $[0.001, 0.901]$.

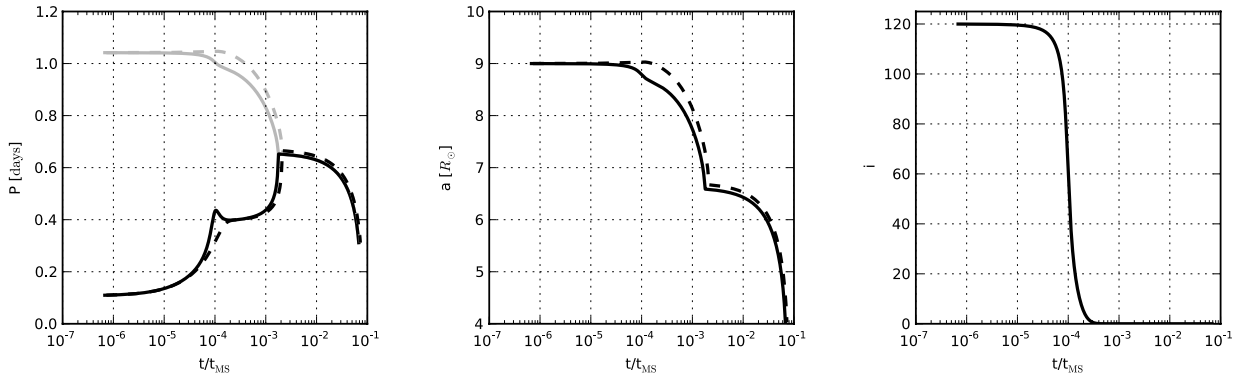

FIGURE 2.6: Evolution of a misaligned and eccentric BH-LMXB under the effect of tides and magnetic braking. The binary contains a black-hole of mass $8\ M_\odot$ and a one solar-mass star. Initial orbital parameters are $a = 9\ R_\odot$, $e = 0.5$, $i = 120°$. The left panel show the evolution of the rotation period of the star (black solid line) and of the orbital period (grey solid line). The middle panel shows the evolution of the orbital separation (solid black line). The right panel shows the evolution of the eccentricity (solid black line). The dashed lines in all of the three panels correspond to the evolution of a BH-LMXB with the same initial condition for ($\omega_\star$, a, e), but with no misalignment between the spin and the orbit.

For each value of the eccentricity, we draw uniform values a_0 for the orbital separation in the interval $[a_{\rm min}(e), a_{\rm max}(e)]$. $a_{\rm min}(e) = a_{\rm RLO}/(1-e)$ is the orbital separation at which the system undergoes RLO at periastro; $a_{\rm max}(e)$ is the maximal orbital separation such that the system undergoes RLO within the MS-lifetime. We draw uniform values $\omega_{\star,0}$ for the stellar spin in the interval $[0, \omega_{\rm break}]$, and uniform values i_0 in $[0°, 180°]$.

For each initial condition $(a_0, e_0, \omega_{\star,0}, i_0)$, we integrate the tidal equations coupled with magnetic braking and we study the properties of 1000 solutions which undergo RLO within the MS-lifetime. We calculate the ratio between the value in the coupled method and the value in the non-coupled method of the previously mentioned variables as a function of the eccentricity. We show the results in figure 2.11 and figure 2.7.

For each value of the eccentricity there is a range of values for $t_{\rm circ}/\tau_{\rm circ}$. The spread in the values at a fixed eccentricity is mainly caused by different initial spin frequencies. This was already seen in figure 2.5, where taking either a low-spinning star or a high spinning star, under-estimates or over-estimates $t_{\rm circ}$.

To show how the spread in the ratio $t_{\rm circ}/\tau_{\rm circ}$ is reduced when fixing the initial spin of the star, we show in figure 2.7 the ratio $t_{\rm circ}/\tau_{\rm circ}$ when the initial spin is chosen to be $\omega_\star = 1/2\ \omega_{\rm break}$ (dark grey shaded area). When we fix instead the orbital separation at birth (as an example, we take the average value between $a_{\rm min}(e)$ and $a_{\rm max}(e)$), the spread is conserved (light grey shaded area).

We also calculate the ratio $t_{\rm circ}/\tau_{\rm circ}$ when taking for $\tau_{\rm circ}$ the expression in equation 2.14, see figure 2.8. The decrease in the ratio is caused by the dependence of $\tau_{\rm circ}$ on the orbital separation, which increases with increasing eccentricities, and $\tau_{\rm circ}$ increases accordingly.

Concerning the ratio between the orbital separation at $e = 0$ in our integration ($a_{e=0}$) and $a_{\rm circ} = a(1-e^2)$, it is typically less than 1. This is due to the fact that as soon as magnetic braking has spun-down the star sufficiently, tides start removing angular momentum from the orbit, before synchronisation is achieved. This effect is neglected in the non-coupled method. The decrease of the ratio

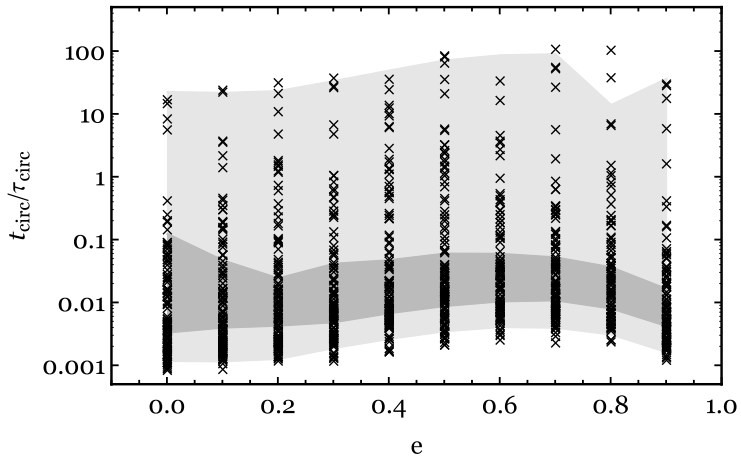

FIGURE 2.7: Ratio between the time it takes to reach circularisation in the coupled and non-coupled method for 1000 black-hole low-mass X-ray binaries undergoing RLO within the MS-lifetime, when taking $\tau_{\rm circ} = e/\dot{e}$. The light grey shaded area is for a fixed initial orbital separation, and the darker grey area is for a fixed initial stellar spin.

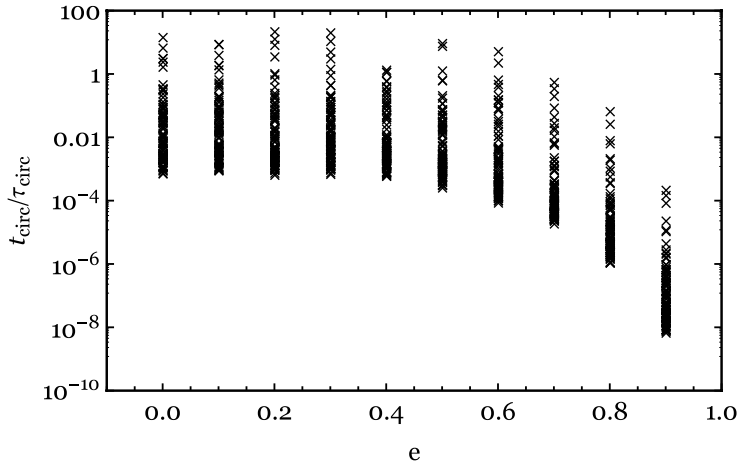

FIGURE 2.8: Ratio between the time it takes to reach circularisation in the coupled and non-coupled method for 1000 black-hole low-mass X-ray binaries undergoing RLO within the MS-lifetime, when taking $\tau_{\rm circ}$ as in eq. 2.14.

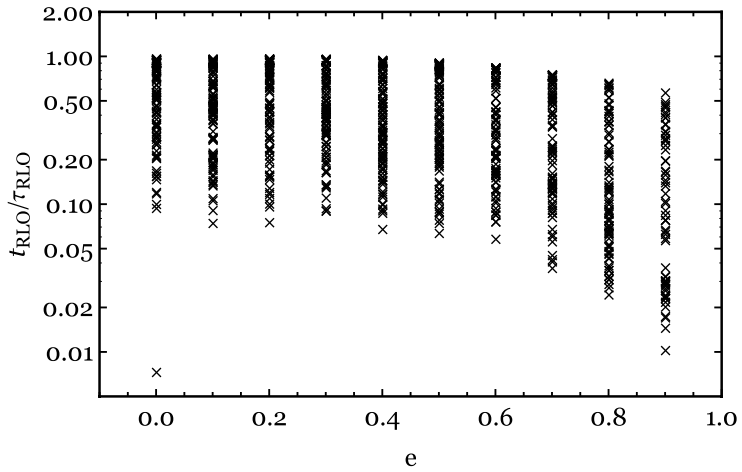

FIGURE 2.9: Ratio between the time it takes to reach RLO in the coupled and non-coupled method for 1000 black-hole low-mass X-ray binaries undergoing RLO within the MS-lifetime. In the non coupled method, we take $\tau_{\rm RLO}$ as $\tau_{\rm circ} + t_{\rm VZ}$ (see text for details).

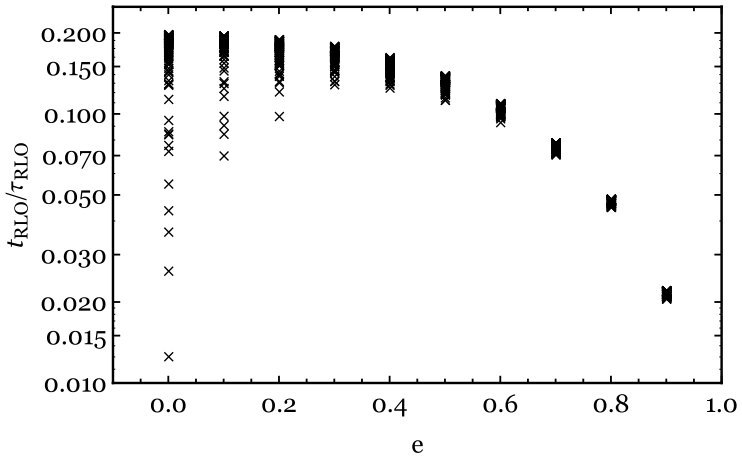

FIGURE 2.10: Ratio between the time it takes to reach RLO in the coupled and non-coupled method for 1000 black-hole low-mass X-ray binaries undergoing RLO within the MS-lifetime. In the non coupled method, we take $\tau_{\rm RLO}$ as $\tau_{\rm VZ}$ (see text for details).

with the eccentricity, is a consequence of the $a_{\rm circ}$ dependence on $(1 - e^2)$.

We also calculate the ratio between the time it takes to reach the RLO configuration in our integration ($t_{\rm RLO}$) and the estimated value for it in the non-coupled method ($\tau_{\rm RLO}$). In the non-coupled method, we calculate $\tau_{\rm RLO}$ in two ways. One as $\tau_{\rm circ} + t_{\rm VZ}$, the other as $\tau_{\rm VZ}$. In the first way we integrate the equation 2.13 taking as initial condition $a_{\rm circ} = a(1 - e^2)$; this gives $t_{\rm VZ}$. We then calculate $\tau_{\rm RLO}$ as $\tau_{\rm circ} + t_{\rm VZ}$, where $\tau_{\rm circ} = e/\dot{e}$. The other way relies on assuming instantaneous circularisation and taking $\tau_{\rm RLO} = \tau_{\rm VZ}$, where $\tau_{\rm VZ}$ is $a/\dot{a}$ with $\dot{a}$ as in equation 2.13, and again we use $a_{\rm circ} = a(1-e^2)$ when calculating $\tau_{\rm VZ}$. This way of estimating $\tau_{\rm RLO}$ has been mostly used in previous BPS works on the evolution of binaries hosting a black-hole or a neutron star. We show the respective outcomes in figures 2.9 and 2.10. The decrease in the ratio which appears in figure 2.10 is due to the fact that for higher eccentricities, both $a_{\rm min}$ and $a_{\rm max}$ increase; $\tau_{\rm VZ}$ increases accordingly. When choosing $\tau_{\rm RLO}$ as $\tau_{\rm circ} + t_{\rm VZ}$, the ratio is constrained to be in the interval $(0.1 - 1)$, so we find this way of calculating $\tau_{\rm RLO}$ a better estimate than when $\tau_{\rm RLO} = \tau_{\rm VZ}$.

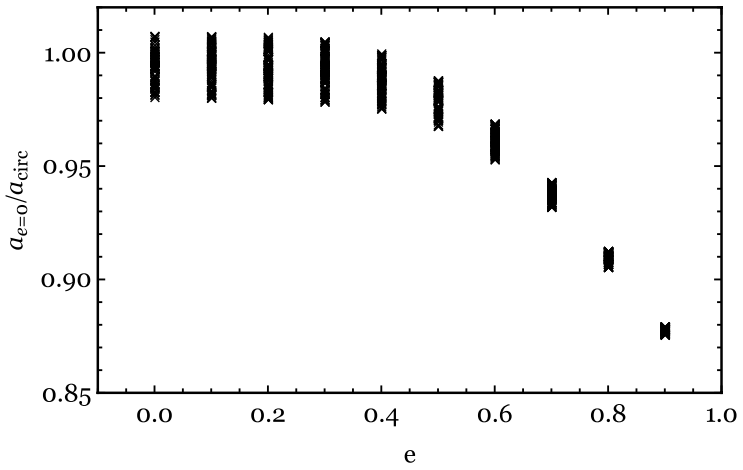

FIGURE 2.11: Ratio between the orbital separation at $e = 0$ and $a_{\rm circ}$ for 1000 black-hole low-mass X-ray binaries undergoing RLO within the MS-lifetime.

2.4.2 Planetary system

We follow the evolution of a planetary system as well, composed of a Sun-like star and a Hot Jupiter.

2.4.2.1 An illustrative example of the evolution in the coplanar case

We show an illustration of the evolution until the planet fills its Roche-lobe (at $a_{\rm RLO} \approx 2$ R$_\odot$) in figure 2.12. The initial configuration is $a = 4\ R_\odot$, $e = 0.2$, $i = 0$, and we again consider the two cases of a high-spinning star ($0.9\ \omega_{\rm break}$) and a low-spinning star ($10^{-5}\ \omega_{\rm break}$).

In the high-spinning case, magnetic braking pushes $\omega_\star$ below corotation, and Hut's stability condition is recovered within a short timescale. Below corotation, tides are too inefficient for synchronising the spin within the main-sequence lifetime. The same result was found by BO2009 (see their figure 3). The difference is that we use a different calibration factor causing tides in our model to be weaker. This is shown expressing the tidal calibration factor K/T as $\frac{3}{2Q'}\frac{1}{\omega_{\rm orb}}\frac{GM_\star}{R_\star^3}$. This leads to $K/T \approx 7 \times 10^{-9}$ for the chosen initial conditions and $Q' = 10^6$, whereas in our model $K/T \approx 10^{-11}$, for every value of the initial spin. The weaker tides cause magnetic braking to spin down the star even more significantly below corotation.

In the BH-LMXB case, a condition in which $\dot{\omega}_{\star,\rm MB} = \dot{\omega}_{\star,\rm tid}$ is reached. This does not happen in the planetary case. The planetary system typically goes through one or two main evolutionary phases, each driven either by magnetic braking or by the tidal torque. In the high spin case, the first phase is driven by MB until the spin finds its-self below corotation, at which point the evolution is driven by the tidal interaction. In the low-spin case, the whole evolution is driven by tides. This overall behaviour of the solution persists in case the calibration factor is the one in BO2009. The stellar spin does not converge to the quasi-equilibrium characterised by $\omega_\star = \omega_{\rm eq}$. In both tidal models, $\omega_{\rm eq}$ is much smaller than typical $\omega_{\rm eq}$ in BH-LMXBs (the corresponding $P_{\star,\rm eq}$ is ≈ 21 days -see dotted line in the left panel of figure 2.12- and ≈ 3 days in BO2009 model for tides). We will further comments on the absence or presence of the quasi-equilibrium state in section 2.6.1. The only difference between the evolution in our model and in BO2009 one, is that in the low-spinning case, the time it takes for tides to significantly spin-up the star is shorter.

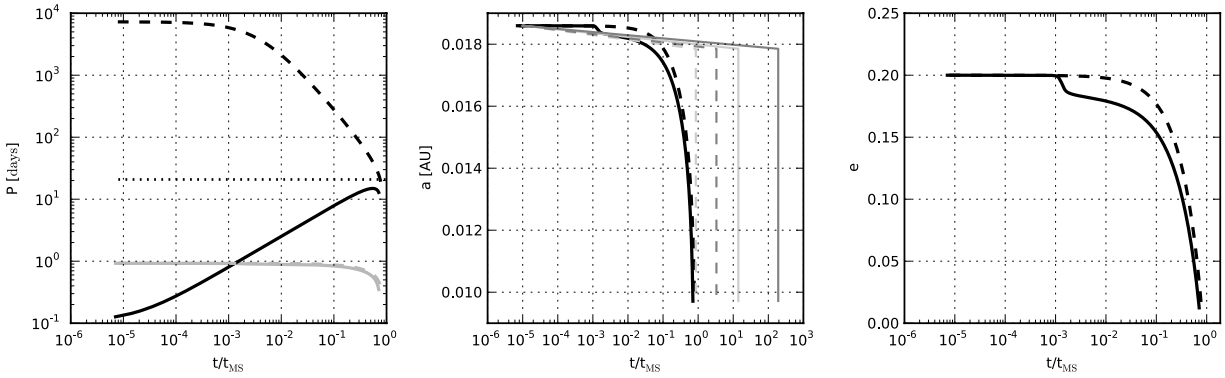

FIGURE 2.12: Evolution of an eccentric and coplanar planetary system under the effect of tides and magnetic braking. The system contains a Hot-Jupiter and a sun-like star. Initial orbital parameters are $a = 4\ R_\odot$, $e = 0.2$, $i = 0$. We consider both a high-spinning star ($\omega_\star = 0.9\ \omega_{\rm break}$) and a low-spinning star ($\omega_\star = 10^{-5}\ \omega_{\rm break}$). In all panels, solid lines correspond to high-spin, dashed lines to low-spin. In the left panel, the grey lines represent the evolution of the orbital period, the black lines of the stellar period. The dotted line in the same panel represents the value of $\omega_{\rm eq}$ (see text for details). In the centre panel, the two thick lines represent the evolution of the orbital separation in our integration. In the same panel, the thin dark-grey lines represent the evolution of the orbital separation in the non-coupled method when taking $\tau_{\rm circ} = (e/\dot{e})|_{\rm e\approx 0, \omega_\star = \omega_{\rm orb}}$; light-grey lines when taking $\tau_{\rm circ} = e/\dot{e}$. The right panel shows the evolution of the eccentricity.

In the high-spin case, once $\omega_\star$ has been brought by MB below corotation (at $\rm t \approx 10^{-3}\ t_{MS}$), tides start removing angular momentum from the orbit, the binary shrinks, and the solution approaches the low-spinning solution, since the star now spins too slowly for magnetic braking to be effective.

In both cases of a high-spinning star and a low-spinning star, tides more easily bring changes to the orbit than to the star, due to the high ratio $J_\star/J_{\rm orb}$ (see figure 2.3), and in neither case the RLO-configuration is synchronous, due to low mass-ratio, unlike the BH-LMXB case.

In the middle panel of figure 2.12 we also show the evolution in the non-coupled method, when taking $\tau_{\rm circ} = e/\dot{e}$ (thin light-grey lines), and $\tau_{\rm circ} = (e/\dot{e})|_{\rm e\approx 0, \omega_\star = \omega_{\rm orb}}$ (thin dark-grey lines). Neglecting the spin of the star results in a different evolution: the circularisation timescale is overestimated. At these large values of $J_\star/J_{\rm orb}$, it is essential to follow the coupled evolution of the orbital and rotational elements.

2.4.2.2 An illustrative example of the evolution in the misaligned case

Due to the high ratio $J_\star/J_{\rm orb}$, we expect tides to be inefficient in washing away any initial misalignment. In figure 2.13, we show the evolution of the planetary system for an initial configuration $a = 3\ \rm R_\odot$, $e = 0$, $i = 160°$. The rate of alignment is larger in the low-spin case, whereas in the high-spin case, the star rotational angular momentum is too large for being affected by the tidal torque, and the system reaches RLO while being in a non-coplanar configuration. We might wonder what would happen to a retrograde orbit in the absence of magnetic braking. Taking the semi-major axis decay rate for a misaligned orbit (equation 2.2) and considering a circular case, the i-dependence of $\dot{a}$ can be written

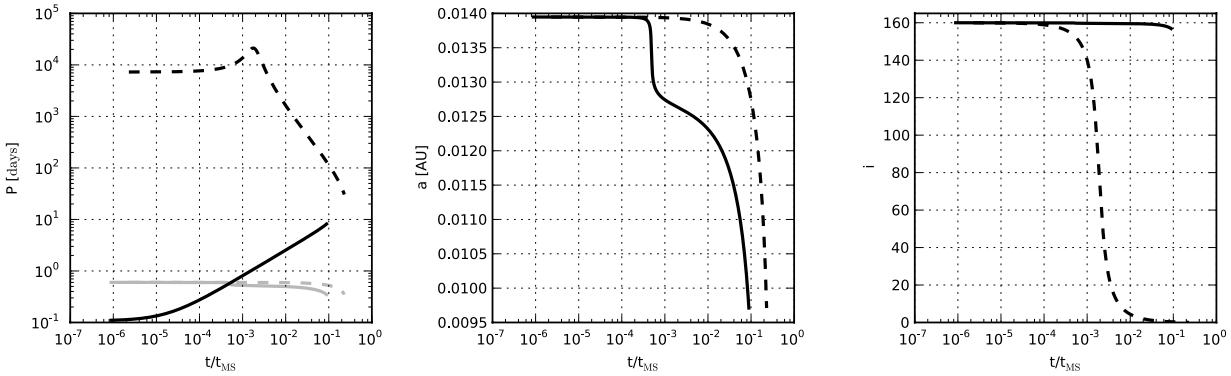

FIGURE 2.13: Evolution of an eccentric and misaligned planetary system under the effect of tides and magnetic braking. The system consists of a Hot-Jupiter and a sun-like star. Initial orbital parameters are $a = 3\ R_\odot$, $e = 0$, $i = 160°$. We consider both a high-spinning star ($\omega_\star = 0.9\ \omega_{\rm break}$) and a low-spinning star ($\omega_\star = 10^{-5}\ \omega_{\rm break}$). In all panels, solid lines correspond to high-spin, dashed lines to low-spin. In the left panel, the grey lines represent the evolution of the orbital period, the black lines of the stellar period. In the centre panel, we show the evolution of the orbital separation. The right panel shows the evolution of the misalignment angle.

as:

$$\frac{da}{dt} \propto -\left(1 + \frac{\omega_\star |\cos i|}{\omega_{\rm orb}}\right) \tag{2.18}$$

The orbit would undergo an initial decay, with a larger rate for larger inclinations. This is an interesting way of shrinking the orbital separation, though the initial orbital separation has to be already comparable to $a_{\rm RLO}$ for RLO to happen on the MS. For example, for the case of an initial misalignment of $160°$, the maximum initial orbital separation is $\approx 1.5\ a_{\rm RLO}$. The same orbital decay due to $\omega_\star \cos i < \omega_{\rm orb}$ happens in a BH-LMXB. In this case however, the system always reaches alignment and synchronisation within the MS-lifetime for sufficiently tight initial orbits, since the tidal torque is much larger.

2.4.2.3 Population study

We do a population study for the planetary system too, drawing the initial conditions in the same way as we did for the BH-LMXB case (see figures 2.14 and 2.15). In the non-coupled method, $\tau_{\rm circ}$ is again $e/\dot{e}$.

Again we see that $a_{\rm circ}$ typically overestimates the actual orbital separation at $e = 0$. Concerning the ratio of the timescales, it spans a range of $\approx [10^{-2}\text{-}1]$. This is consistent with the example of figure 2.12.

2.5 Wind Braking

While most low-mass stars are magnetic, due to the dynamo processes undergoing in their convective envelopes, only a fraction of intermediate/high-mass stars show magnetic fields. This fraction is smaller than about 15% of the total population, see Donati & Landstreet 2009. When the massive star is magnetic, the stellar wind becomes an analogue of the magnetic-wind in a low-mass star, the only difference being that mass loss is non-negligible anymore. We will take into account the effect of the

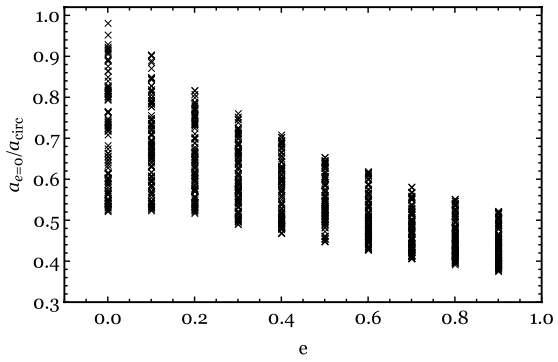

Figure 2.14: Ratio between the orbital separation at $e = 0$ and $a_{\rm circ}$ for 1000 planetary systems undergoing RLO within the MS-lifetime.

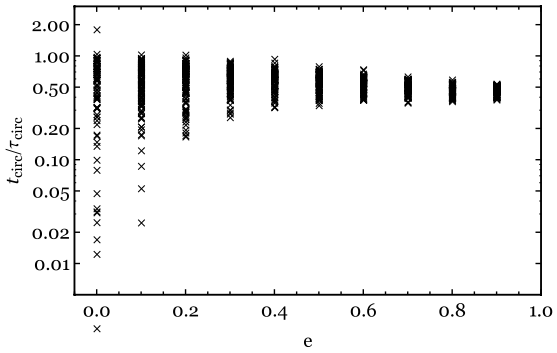

Figure 2.15: Ratio between the time it takes to reach circularisation in the coupled and non-coupled method for 1000 planetary systems undergoing RLO within the MS-lifetime.

mass-loss on the binary evolution adding a mass-loss term both in the orbital separation rate and in the spin-frequency rate. We will show that neglecting the spin-down rate due to the mass-loss leads to a different evolution.

2.5.1 Tides coupled with wind braking

Mass loss in a stellar wind removes angular momentum from a rotating star. We assume that the wind is radial and isotropic; the wind can hence be modelled as a spherical shell decoupling from the star at a certain *decoupling radius* $r_{\rm d}$. If the star is non magnetic, $r_{\rm d}$ is the radius of the star $R_\star$; whereas if it is magnetic, $r_{\rm d}$ is the magnetospheric radius $r_{\rm M}$, i.e. the radius out to which the material corotates with the star.

Expressing the decoupling radius in terms of the stellar radius as $r_{\rm d} = \gamma R_\star$, the rate of angular momentum lost is then:

$$\frac{d\vec{J}_\star}{dt} = \frac{2}{3}\dot{M}_\star \omega_\star \gamma^2 R_\star^2 \vec{e}_\omega \tag{2.19}$$

where $\omega_\star$ is the rotational frequency of the star. This expression coincides with the the well-known prescription for the angular-momentum loss in a stellar wind by Weber & Davis 1967, when parametrising the Alfven radius in terms of the stellar radius. It is valid both for a stellar wind decoupling at the stellar surface ($r_d = R_\star$), and for a wind which is forced to corotate out to r_d by a purely radial magnetic field. For a different field geometry this expression becomes:

$$\frac{d\vec{J}_\star}{dt} = \frac{2}{3}\dot{M}_\star \omega_\star R_\star^2 \gamma^n \vec{e}_\omega \tag{2.20}$$

recovering the purely-radial field configuration for $n = 2$ (Kawaler 1988).

We assume that the wind decouples from the binary at $r_{\rm d}$, without further interaction with the binary components. This is the so-called *fast-wind* approximation, motivated by the fact that typical wind speeds are larger than typical orbital speeds. In a neutron-star high-mass X-ray binary containing a NS of 1.4 $M_\odot$ and a 15 $M_\odot$ star, $v_{\rm orb} < 600$ km/s for $a > a_{\rm RLO}$. Taking as wind-velocity $v_{\rm wind}$ the escape-velocity from the star, we obtain $v_{\rm wind} \approx 1000$ km/s.

To obtain the spin-down rate, we use the mass-radius relation for a ZAMS star, and we assume that the radius of gyration does not change during the evolution on the MS:

$$\frac{d\omega_\star}{dt} = -\frac{\omega_\star}{M_\star}\dot{M}_\star - \frac{2\omega_\star}{R_\star}\frac{dR_\star}{dM_\star}\dot{M}_\star + \frac{2}{3}\frac{\dot{M}_\star {r_d}^2 \omega_\star}{k^2 M_\star R_\star^2} \tag{2.21}$$

If the star is in a binary, the wind won't take away rotational angular momentum only, but orbital angular momentum as well. This effect adds up to the tidal effect on the orbital separation as a non-negative term $-a\dot{M}_\star/M$ in the orbital separation rate.

The full evolutionary equations for an eccentric and misaligned binary system under the coupled effect of tides and a massive stellar wind are equations 2.2, 2.3, 2.4, 2.5, to which we add the term in equation 2.21 and the term:

$$\frac{da}{dt} = -\frac{\dot{M}_\star}{M}a \tag{2.22}$$

and we use the calibration factor $(K/T)_\mathrm{r}$ for a radiative envelope.

The mass-loss for a sun-like star on the MS is negligible, thus we can neglect the term in eq. 2.22. The mass-loss effect on the spin-down rate is reduced to the third term in equation 2.21. Even if the mass-loss is small, this term can be significant, when the decoupling radius is large ($r_\mathrm{d} \approx 20$ R$_\odot$ for the Sun). The magnetic-braking law 2.1 is empirical, and it can be recovered through MHD-theory coupled with theoretical studies of the dynamo process. Kawaler 1988 studied the angular momentum loss in low-mass stars and showed that Skumanich's law is recovered taking $n = 3/2$ in equation 2.20 and neglecting the change in mass and radius of the star.

The mass-loss in a fast isotropic wind always widens the orbit of a binary formed by point-like components, due to the decrease in binding energy. However, if the mass-losing star suffers from tidal deformation, the tides-induced torque can prevent the widening thanks to the redistribution of angular momentum. When $\omega_\star < \omega_\mathrm{eq,tid}$, where

$$\omega_\mathrm{eq,tid} = f_2\left(e^2\right)\omega_\mathrm{orb}\left[\frac{1}{f_5\left(e^2\right)\left(1-e^2\right)^{3/2}}\right], \tag{2.23}$$

the tidal torque term in the spin rate is positive (see equation 2.4). This means that tides bring angular momentum from the orbit to the star, counteracting the effect of the mass loss. We note that $\omega_\mathrm{eq,tid}$ is alternatively referred to as *pseudo-synchronisation* frequency, the synchronisation frequency on an eccentric orbit (see Hut 1981). This is an *instantaneous*-equilibrium spin frequency, since orbital properties are still evolving. When the orbit is circular, this pseudo-synchronisation frequency coincides with the orbital frequency.

In the next paragraph, we will estimate for which value of γ the effect of the tidal torque in decreasing the orbital separation is stronger than the effect of the orbital angular momentum loss in increasing it.

A few of the previous works on the evolution of HMXBs have integrated the tidal equations coupled with the angular momentum loss in the wind (see for example Wong et al. 2012). What we do differently, is to include in our set of equations the misalignment between the spin of the orbit and the stellar spin, and to parametrise the angular momentum loss in the wind in terms of γ, following the orbital evolution in a semi-analytical way and highlighting some interesting outcomes of the coupling between tides and a massive stellar wind.

2.5.2 Results

2.5.2.1 Timescale considerations

Let's assume we have a synchronised, circular and coplanar orbit. The orbital separation changes due to the loss of orbital angular momentum (term of equation 2.22). It also changes due the tidal redistribution of angular momentum. The star loses rotational angular momentum in the wind, and the tidal torque counteracts this effect. The effect of the tidal torque on the orbital separation can then be found from $\dot{J}_{\rm orb} = \dot{J}_\star$, which gives the orbital separation decay rate:

$$\left.\frac{da}{dt}\right|_{\rm tid} = -\frac{4}{3}\frac{|\dot{M}_\star|\gamma^2 R_\star^2 M}{M_{\rm comp} M_\star a} \tag{2.24}$$

Taking the ratio between $\dot{a}|_{\rm ML}$ and $\dot{a}|_{\rm tid}$, we get:

$$\frac{\left.\frac{da}{dt}\right|_{\rm tid}}{\left.\frac{da}{dt}\right|_{\rm ML}} = \frac{4}{3}\left(\frac{\gamma R_\star}{a_2}\right)^2 q \tag{2.25}$$

where a_2 is the distance of the star from the binary centre-of-mass, $a_2 = (M_{\rm comp}/M)a$. The effect of the loss of $J_{\rm orb}$ is larger when the star is further away from the centre-of-mass (i.e. the larger a_2 is). Whereas the effect of the tidal torque is larger the larger the decoupling radius is (due to $J_\star$-loss being larger), and/or the larger is the mass-ratio (due to the tidal torque dependence on q).

We define $\gamma_{\rm min}$ as γ such that the condition $\left.\frac{da}{dt}\right|_{\rm tid} = \left.\frac{da}{dt}\right|_{\rm ML}$ is met. The tidal torque is more effective than the orbital angular momentum loss in changing the orbital separation for $\gamma > \gamma_{\rm min}$:

$$\gamma_{\rm min}(q,\eta) = \sqrt{\frac{3}{4q}}\frac{q}{1+q}\frac{\eta}{f(1/q)} \tag{2.26}$$

where we parametrised the orbital separation in terms of the RLO-separation, $a = \eta a_{\rm RLO}$.

For a NS-HMXB composed of a 1.4 $M_\odot$ NS and a 15 $M_\odot$ companion[3], the mass ratio is $q \approx 0.09$, and taking $\eta = 2$, we find $\gamma_{\rm min} \approx 0.83$. For the illustrative integration showed in figure 2.18, $\eta = 1.5$, and the corresponding $\gamma_{\rm min}$ is ≈ 0.6. This means that *wind-braking*[4] wins over the mass-loss effect for every value of gamma. This remains valid when the companion mass spans a range of $[10 - 50]\ M_\odot$ in mass.

For a BH-HMXB composed of a 8 $M_\odot$ BH and a 15 $M_\odot$ companion, $q \approx 0.53$. We calculate $\gamma_{\rm min}(q,2) \approx 1.9$ and $\gamma_{\rm min}(q,1.5) \approx 1.6$. The latter $\gamma_{\rm min}$ corresponds to the initial conditions of figure 2.19. For smaller γ, we expect the orbital separation to grow in time (see dotted line in figure 2.19). As another example we calculate the minimum gamma for the BH-HMXB Cygnus X-1. Its component masses are $M_\star \approx 19\ M_\odot$ and $M_{\rm comp} \approx 15\ M_\odot$ (Orosz et al. 2011a). The correspondent $\gamma_{\rm min}$ for $\eta = 2$ is ≈ 2.

In case wind braking is effective in shrinking the orbit, we wonder for which values of mass-loss in the wind and of γ, the binary is shrunk down to RLO within the MS-lifetime. The spin-down timescale

[3] There are at least 3 known NS-HMXBs with similar component masses, see van Kerkwijk et al. 1995, van der Meer et al. 2005, Val Baker et al. 2005.

[4] We name "wind braking" (WB) the shrinking of the semi-major axis due to the tidal counteracting effect on the loss of rotational angular momentum, in analogy with magnetic braking.

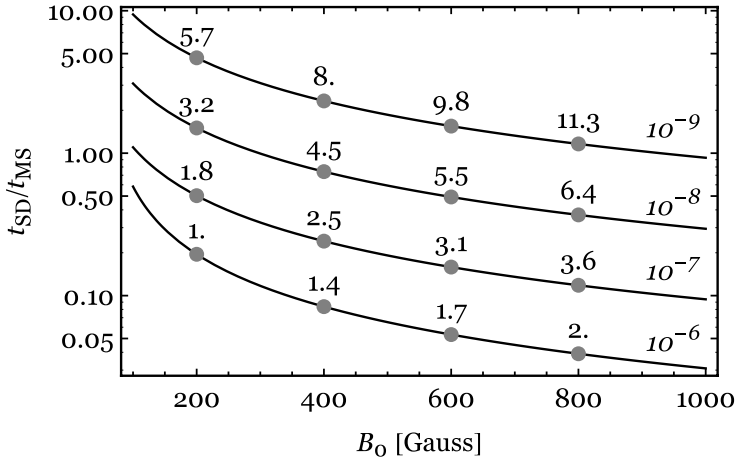

FIGURE 2.16: Ratio between the spin-down timescale and the MS-lifetime for a star of mass 15 $M_\odot$, as a function of the stellar surface magnetic field for different mass losses, $|\dot{M}_\star| = \left\{10^{-9}, 10^{-8}, 10^{-7}, 10^{-6}\right\}$ $M_\odot$ /yr. Values of γ as a function of B_0 and $\dot{M}_\star$ are indicated along the curves.

due to the angular momentum loss in the wind is:

$$\frac{1}{\tau_{SD}} = \frac{|\dot{\omega}_{\star|SD}|}{\omega_\star} \tag{2.27}$$

where $\dot{\omega}_{\star|SD}$ is as in equation 2.21. The spin-down timescale is then a function of the mass-loss and of the decoupling radius. If the star is magnetic, we use the fact that the decoupling radius can be defined as the distance from the star at which the ram pressure of the flow and the magnetic pressure are balancing each other. Justham et al. 2006 show that:

$$r_d \sim B_0^{1/2} R_\star^{13/8} |\dot{M}_\star|^{-1/4} (GM_\star)^{-1/8} \tag{2.28}$$

where B_0 is the surface stellar magnetic field. We use this expression for r_d in order to rewrite the spin-down timescale 2.27 in terms of B_0 and of $\dot{M}_\star$. We are interested in those combinations of $\dot{M}_\star$ and B_0 for which the star is sufficiently spun-down on the MS.

In figure 2.16 we show the ratio between the spin-down timescale and the MS-lifetime for a star of mass 15 $M_\odot$ ($\tau_{MS} \approx 1.15 \times 10^7$ years) as a function of the stellar surface magnetic field. Different curves are presented for different wind mass-losses. Mass-losses are chosen as:

$$|\dot{M}_\star| = \left\{10^{-9}, 10^{-8}, 10^{-7}, 10^{-6}\right\} \; M_\odot \; /\mathrm{yr}.$$

For larger B_0, the ratio decreases, since a stronger field guarantees the corotation of the field lines out to large distances from the star, where the rotational angular momentum carried away by the wind is larger. For the same magnetic field, the spin-down timescale is smaller for larger mass-loss, since a higher mass-loss brings away a larger angular momentum. Along the curves we also indicate the value of $\gamma = r_d/R_\star$ for that combination of B_0 and $\dot{M}_\star$. For the same field strength at the surface B_0, the decoupling radius is larger for a smaller mass loss. This is due to the fact, that for a smaller ram pressure (smaller $\dot{M}_\star$), the balancing magnetic pressure ($\sim B_0^2/r_d^6$) is smaller; if the surface B-field is fixed, the decoupling radius has therefore to be larger.

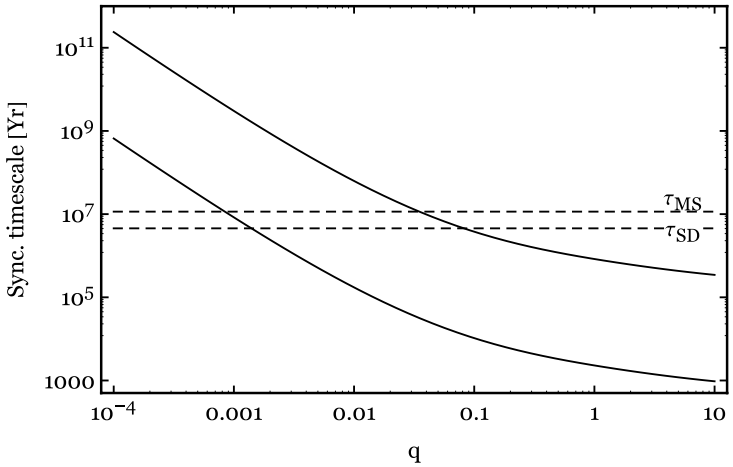

Figure 2.17: Synchronisation timescales for a binary composed of a 15 $M_\odot$ star as a function of the binary mass-ratio q, both for an orbital separation $a = a_{\rm RLO}$ and $a = 2\,a_{\rm RLO}$. The horizontal dashed lines show the spin-down timescale and the MS-lifetime. The spin-down timescale has been computed for $\gamma = 2$ and $\dot{M}_\star = -10^{-7}$ $M_\odot$ /yr.

Typical magnetic fields of the subset of magnetic O-B stars and of Ap-Bp stars are of the order of hundreds to thousands Gauss (Donati & Landstreet 2009). We compute their typical main-sequence wind mass-loss using the fitting formula by Nieuwenhuijzen & de Jager 1990, who parametrize the wind-mass loss in terms of the luminosity, the mass and the radius of the star. Evolving a star with a ZAMS mass of 15 $M_\odot$, with the SSE code by Hurley et al. 2000 embedded in the Astrophysics Multipurpose Software Environment AMUSE (Portegies Zwart et al. 2009), we extract the luminosity and radius of the star. We find a wind mass-loss in the range $10^{-8} - 10^{-7}$ $M_\odot$ /yr on the MS.

As an example, for a decoupling radius $\gamma = 2$ and a mass-loss $|\dot{M}_\star| = 10^{-7}$ $M_\odot$ /yr, we obtain an estimate for the required stellar magnetic field of ~ 250 Gauss. For these values of B and $\dot{M}_\star$, we expect the binary to shrink down to RLO.

In figure 2.17 we show the synchronisation timescales calculated using eq. 2.15 for a binary formed by a star of mass 15 $M_\odot$ as a function of the mass-ratio q, both for an orbital separation $a = a_{\rm RLO}$ and $a = 2\,a_{\rm RLO}$. The assumptions we make on the decoupling radius and the mass-loss rate are $\gamma = 2$ and $\dot{M}_\star = -10^{-7}$ $M_\odot$ /yr which, as can be seen in figure 2.16, allow for a short spin-down timescale ($\tau_{\rm SD}/\tau_{\rm MS} \approx 0.3$). For our cases of interest of a NS-HMXB ($q \approx 0.1$) and of a BH-HMXB ($q \approx 0.5$), $\tau_{\rm sync}$ is short, hence we expect the binaries to rapidly reach the synchronous state.

2.5.2.2 Wind braking in NS-HMXBs and BH-HMXBs

We integrate the coupled equations of section 2.5.1 for a binary composed of a neutron star of mass 1.4 $M_\odot$ and a 15 $M_\odot$ star, with an orbital separation $a = 14$ $R_\odot$ and eccentricity $e = 0.2$.

We take different combination for the mass-loss rate and the decoupling radius:

$$\{|\dot{m}|,\gamma\} = \left\{\left\{10^{-7}, 2\right\}, \left\{10^{-8}, 2\right\}, \left\{10^{-7}, 1\right\}\right\}$$

(where $\dot{m}$ is the mass-loss rate in solar masses per year). For each of these three combinations, we also calculate the evolution when neglecting the mass-loss terms in the spin-frequency rate (terms in eq. 2.21), which we call *standard* model. Concerning the spin frequency, we take a star rotating at 20%

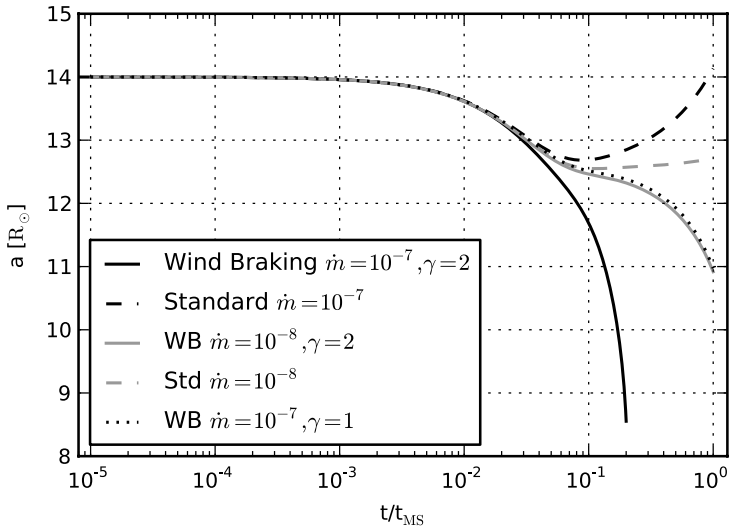

FIGURE 2.18: Evolution of a NS-HMXB under the effect of tides and a massive stellar wind (solid lines). Masses of the components are $M_\star = 15\,\mathrm{M}_\odot$ and $M_{\rm comp} = 1.4\,\mathrm{M}_\odot$. Initial orbital parameters are $a = 14\ \mathrm{R}_\odot$, $e = 0.2$, $\omega_\star = 0.2\ \omega_{\rm break}$. We also show the evolution in the standard scenario, when the mass-loss has an effect on the orbital separation only (dashed lines).

of its break-up frequency, which is a typical lower-limit on the natal rotating speed of a high-mass star (see Donati & Landstreet 2009). The associated ratio $\omega_\star/\omega_{\rm eq,tid}$ is ≈ 0.7. We must point out that this is valid in the assumption that the binary evolution prior and during the compact object formation does not affect the stellar spin. Anyhow, what is important for our study, is to compare the initial $\omega_\star$ with $\omega_{\rm eq,tid}$ of equation 2.23. Initial conditions with $\omega_\star > \omega_{\rm eq,tid}$ are of no interest, since the binary widens, preventing RLO.

We show in figure 2.18 the outcome of the evolution. The first phase of the evolution is driven by tides, until synchronisation is achieved (at $t \approx 6\times10^{-2}\ t_{\rm MS}$). At this moment, the different prescriptions on the decoupling radius and on the mass-loss rate start playing a role. When dealing with WB, the evolution is faster for a larger mass-loss. If the mass-loss is too small, the binary does not reach RLO within the MS-lifetime. If the wind-braking spin-down is not taken into account, the orbital separation increases once the synchronous state is achieved, as expected due the positive wind-mass loss term in the orbital separation rate. For the wind-braking solutions, once synchronisation is achieved, the tidal torque replenishes the rotational angular momentum reservoir of the star, counteracting the spin-down effect of the wind, and removing angular momentum from the orbit: this is exactly what happens in the magnetic braking case.

We also note how the two solutions with $\{|\dot{m}|,\gamma\} = \{10^{-7},1\}$ and $\{|\dot{m}|,\gamma\} = \{10^{-8},2\}$ only slightly differ from each other. This is due to the degeneracy in $\dot{m}$ and γ. The spin-down timescale is $\tau_{\rm SD} \approx 2\tau_{\rm MS}$ and $\tau_{\rm SD} \approx 4\tau_{\rm MS}$ for the two choices respectively.

Solving the coupled equations for different values of the initial stellar spin, we note that if the initial spin is too low, tides won't manage to synchronise the star on the evolutionary timescale. What happens is that the orbit keeps shrinking due to the tidal torque only, and there is no appreciable difference between the tides-only solution and the WB-solution. The initial binary configuration $(a, e, \omega_\star)$ which gives rise to an evolution of the wind-braking type, satisfies three properties. The stellar spin is less

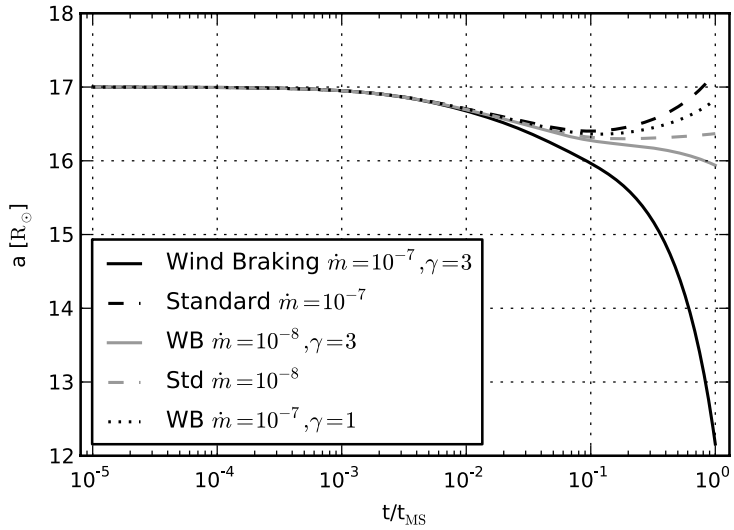

FIGURE 2.19: Evolution of a BH-HMXB under the effect of tides and a massive stellar wind (solid lines). Masses of the components are $M_\star = 15$ M$_\odot$ and $M_{\rm comp} = 8$ M$_\odot$. Initial orbital parameters are $a = 17$ R$_\odot$, $e = 0.2$, $\omega_\star = 0.2\ \omega_{\rm break}$. We also show the evolution in the standard scenario, when the mass-loss has an effect on the orbital separation only (dashed lines).

than $\omega_{\rm eq,tid}$. The configuration allows for tides to synchronise the spin within the MS-lifetime. Lastly, it allows the wind to significantly remove angular momentum from the orbit bringing the system to RLO within the MS-lifetime.

We follow the evolution under tides and a massive stellar wind for a BH-HMXB as well. We take as initial orbital parameters $a = 17$ R$_\odot$, $e = 0.2$, and a star rotating at $0.2\ \omega_{\rm break}$. We show in figure 2.19 the result of the integration. We note how the solution with $\{|\dot{m}|, \gamma\} = \{10^{-7}, 1\}$ (dotted line) differs from the solution corresponding to the same pair $\{|\dot{m}|, \gamma\}$ for a NH-HMXB. This is due to the fact that $\gamma R_\star / a_2$ is smaller for a BH-HMXB since a_2 is larger; this means that the tidal effect on the orbital separation is smaller. This was expected, since $\gamma = 1$ is less than the minimum value for having wind-braking type solutions in a BH-HMXB of this type.

2.6 Discussion

In this section, we would like to comment on the calibration of magnetic braking and of tides that we chose. We also comment briefly on how our results on the evolution of a planetary system might change when considering the tides raised by the star on the planet as well.

1. The empirical Skumanich law was derived measuring the equatorial velocity of G-type MS-stars with rotational velocities between $1-30$ km/s. It is therefore arguable whether it is still applicable to fast rotators, like the ones in compact binaries where the star, being synchronised with the orbit, rotates at velocities of hundreds km/s. For this reason, *saturated* magnetic-braking laws have been suggested, in which the spin-down rate saturates once the star-frequency reaches a critical value (see Knigge et al. 2011, for reviewing the different MB-prescriptions). We adopt Ivanova & Taam 2003 prescription for MB in the formulation chosen by Ivanova & Kalogera

2006:

$$\dot{J}_{\star,\mathrm{MB}} = -K_j \left(\frac{R_\star}{R_\odot}\right)^4 \begin{cases} (\omega_\star/\omega_\odot)^3 & \text{for } \omega \leq \omega_\mathrm{x} \\ \omega_\star^{1.3}\omega_\mathrm{x}^{1.7}/\omega_\odot^3 & \text{for } \omega > \omega_\mathrm{x} \end{cases} \tag{2.29}$$

where $\omega_\odot \approx 3 \times 10^{-6}\mathrm{s}^{-1}$ is the angular velocity of the Sun, $K_j = 6 \times 10^{30}$ dyn cm, and the critical angular velocity is $\omega_x = 10\ \omega_\odot$. From this law, the spin-down rate $\dot{\omega}_\star$ is derived.

We integrate the tidal equations coupled with the previous MB-prescription for the BH-LMXB shown in figure 2.5, taking a star spinning at $0.9\ \omega_\mathrm{break}$, a value which is much larger than the critical angular frequency ω_x, thus the spin-down rate scales as $\omega_\star^{1.3}$. In this prescription magnetic braking is much less efficient than in the Verbunt & Zwaan 1981 prescription, hence the binary does not reach RLO within the MS-lifetime ($a \approx 5\ a_\mathrm{RLO}$ at $t = t_\mathrm{MS}$). In the first phase of the evolution, MB spins down the star while tides lead to a slight widening of the orbit, unlike what happens in our formulation. In this case too $\omega_\star$ converges to ω_eq, which corresponds to the value at which $\dot{\omega}_{\star,\mathrm{MB}} = \dot{\omega}_{\star,\mathrm{tid}}$. After that, the binary shrinks thanks to the coupling tides-MB, however much less significantly than when using Verbunt & Zwaan 1981 prescription for MB.

2. There is a factor $\approx 10^5$ between the timescales in our model and the timescales computed according to BO2009 tidal model. This is due to the fact that K/T is a function of both $\omega_\star$ and ω_orb, through the tidal pumping timescale, whereas the calibration factor in BO2009, is a function of ω_orb only. When $\omega_\star$ and ω_orb differs strongly (like in the case when $\omega_\star = 0.9\ \omega_\mathrm{break}$) our tidal calibration factor is significantly reduced. Instead, when $\omega_\star \approx \omega_\mathrm{orb}$, the ratio between the two tidal calibration factors is $1 - 2$ for every mass ratio, leading to similar timescales.

3. We wonder whether our results are a function of the tidal calibration we choose. In the BH-LMXB case, a different tidal calibration factor will affect the time it takes for reaching the circular and synchronised configuration. However, since this timescale is very short compared to the MS-lifetime, independently of the chosen calibration, we expect no appreciable difference when taking a different tidal calibration factor. Once synchronisation is achieved, the evolution of the system is well described by equation 2.13, that is, the calibration of tides does not play a role anymore. Integrating the tidal equations according to BO2009 model for tides and coupling them with magnetic braking, we note that when the star is initially high-spinning, the orbital separation increases initially, that is in the first phase of the evolution tides and MB are both at work; this will lead to a larger circularised orbital separation, but the final outcome of the evolution of a BH-LMXB is not significantly affected. As a more quantitative test, we use the maximal initial orbital separation a_max such that the BH-LMXB reaches RLO within the MS-lifetime; the ratio between a_max in our model and a_max in BO2009 model of tides, is ≈ 1, for all values of the initial eccentricity.

   In the planetary system case, the situation is different. A high-spinning star is typically spun-down below corotation. At this point, MB has a negligible effect, unlike the tidal interaction, and, if the initial configuration is close enough, tides bring the system towards RLO. The stronger tides are, the faster the evolution towards RLO. Looking at the maximal initial orbital separation so that the planetary system reaches RLO within the MS-lifetime, the ratio between a_max in our model and a_max in BO2009 model of tides, is $\approx 0.3 - 0.4$.

4. When applying our model to the planetary case, we only considered the tide raised by the planet on the star, and not the tide raised by the star on the planet. Since the angular momentum stored in the planet is much less than the orbital angular momentum, due to the compactness of the planet, we expect the planet to rapidly synchronise with the orbit. If tides in the planet are included, we expect circularisation to be reached faster, due to eccentricity damping effect of the tide in the planet (see BO2009 and Rasio et al. 1996). Matsumura et al. 2010 followed the evolution of a Hot Jupiter in an eccentric and misaligned orbit around its host star, accounting for both the tide in the star and in the planet. The stellar tide largely dominates the evolution of the orbital separation and obliquity. Instead, both the tide in the planet and in the star contribute to the damping of the eccentricity, and depending on the planet tidal quality factor, circularisation can be achieved without a significant orbital decay. We expect our main conclusions on the inadequacy of timescale considerations to be preserved, as already predicted by Jackson et al. 2008, who accounted for the tide in the planet.

2.6.1 On the quasi-equilibrium state

The concept of *quasi-equilibrium state* for the spin of the stellar component in a binary, was already introduced by Dobbs-Dixon et al. 2004, for the case of a planetary system containing a star and a Hot Jupiter. At the quasi-equilibrium, the rate of angular momentum loss in the stellar wind is balanced by the rate at which the star gains angular momentum from the orbit as the planet attempts to spin-up the star. The authors give an upper limit for the angular momentum loss in the stellar wind, such that this quasi-equilibrium can be achieved. We use a similar approach, and we calculate the maximum spin-down rate due to MB such that the quasi-equilibrium can be achieved. In order to find $\omega_{\rm eq}$, we put $\dot{\omega} = 0$ in equation 2.4, and we take a circular and coplanar orbit. We obtain:

$$\omega_{\rm eq} = \omega_{\rm orb} - \frac{1}{3}\frac{1}{K/T}\frac{k^2}{q^2}\left(\frac{a}{R_\star}\right)^6 |\dot{\omega}_{\rm MB}| \tag{2.30}$$

where a and $\omega_{\rm orb}$ are the orbital separation and the orbital frequency at the quasi-equilibrium state. This quasi-equilibrium spin value is attainable provided that:

$$|\dot{\omega}_{\rm MB}| < \frac{9}{2Q'}\frac{q^2}{k^2}\frac{GM_\star R_\star^3}{a^6} = \dot{\omega}_{\rm max} \tag{2.31}$$

We note that we have chosen the calibration factor as in BO2009, that is we have replaced K/T with $\frac{3}{2Q'}\frac{1}{\omega_{\rm orb}}\frac{GM_\star}{R_\star^3}$, so that the equation $\dot{\omega} = 0$ could be solvable analytically in terms of $\omega_{\rm eq}$. Condition 2.31 is typically not fulfilled in a planetary system, whereas it is fulfilled in a BH-LMXB (see figure 2.20). This is consistent with our results in section 4.4.

2.6.2 An application to the neutron star high-mass X-ray binary Circinus X-1

One way of testing the calibration of tides, is to look at young and detached high-mass X-ray binaries, which still did not have time to circularise. In detached systems, any orbital decay or boost could be directly associated with the tidal interaction between the two components. Such a study was performed by Belczynski et al. 2008 for LMC X-4, a NS-HMXB. The observed orbital decay of the source, $P/\dot{P} \approx 10^6$ years, is consistent with an orbital decay driven by the tidal torque when using the calibration factor in equation 2.10.

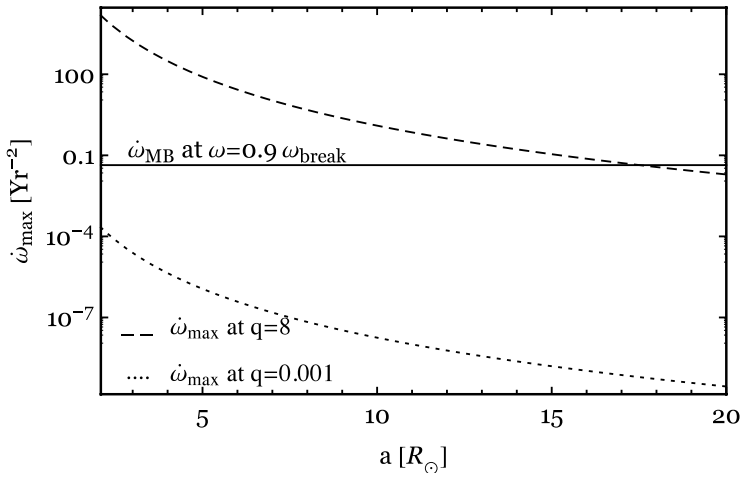

FIGURE 2.20: Values of $\dot{\omega}_{\rm max}$ such that the system can reach the quasi-equilibrium state, as a function of the orbital separation, and calculated for a mass ratio $q = 8$ and for $q = 0.001$. Horizontal lines correspond to the spin-down rate due to MB.

Another possible example is Circinus X-1, the youngest known X-ray binary. An upper limit on its age of $t < 4600$ years has been placed by Heinz et al. 2013, through X-ray studies of its natal supernova remnant. The X-ray emission is thought to be caused by RLO at periastro, hence this binary is semi-detached, unlike LMC X-4. X-ray dip timing shows the binary is undergoing orbital decay (Parkinson et al. 2003 and Clarkson et al. 2004), with $P/\dot{P}$ measured to be ~ 3000 yr. The current orbital parameters are $e \approx 0.45$ and $P_{\rm orb} \approx 16.68$ days. Jonker et al. 2007 constrained the radius of the companion star by ensuring the neutron star does not go through the companion at periastro. The surface gravity gives in turn the mass. We use $M_\star = 10\ M_\odot$ and $R_\star \approx 39\ R_\odot$ for the mass and radius of the high-mass star, and $M_{\rm comp} = 1.4\ M_\odot$ for the mass of the neutron star. These initial conditions allow us to compute the current timescales for the change in the orbital period $P/\dot{P} = (2/3)a/\dot{a}$, using the tidal equations in our model. The only uncertainty is the spin of the companion. When $\omega_\star$ is smaller than $\omega_{\rm eq,tid}$, tidal interaction results in a decay of the orbit. For these initial orbital parameters, $\omega_{\rm eq,tid} \approx 1.25\ \omega_{\rm break}$. The calculated timescales are $\approx 9 \times 10^3$ years and $\approx 2 \times 10^4$ years, for $\omega_\star$ varying from 0 and 0.9 $\omega_{\rm break}$. One possibility is that tides are more efficient than the ones in our model, by a factor of ≈ 3 when taking a non-rotating star. Alternatively, the observed orbital decay is either induced by the mass-transfer itself, or an additional spin-orbit coupling is responsible for it, as suggested by Heinz et al. 2013.

2.6.3 Remarks on our results on the circularisation timescale and their consequences

1. There is a variety of papers in the literature which base their description of the evolution of compact binaries on timescale considerations (see for example, Kalogera 1999, Yungelson et al. 2006, Pylyser & Savonije 1988, Ma & Li 2009). Since citing all of them does not seem like a sensible choice, we rather show an example of how timescale considerations could fail. Janssen & van Kerkwijk 2005 study a compact binary formed by a pulsar and a low-mass star. The observed eccentricity is $e \lesssim 0.005$, while the initial eccentricity is constrained to be $e \sim 0.7$. The authors assume an exponential decay of the eccentricity when dealing with the circularisation

of the binary. We instead integrated our equations to solve for the evolution of the eccentricity of this system. We obtain $t_{\rm circ} = 2 \times 10^9$ yr and $\tau_{\rm circ} = 6 \times 10^7$ yr for a low-spinning star, and $t_{\rm circ} = 4 \times 10^9$ yr and $\tau_{\rm circ} = 2 \times 10^{10}$ yr, for a high-spinning star. This result highlights the inadequacy of timescale considerations when studying the evolution of individual systems.

2. We would also like to point out that some of the currently used BPS codes might treat tidal interaction using timescale arguments or assuming instantaneous circularisation (see for example, Portegies Zwart & Verbunt 1996). However, our population models for the progenitors of BH-LMXBs show that the population of BH-LMXBs (i.e. the number of systems that start mass transfer on the MS) might not be very different, also given the large uncertainties in the calibration factor.

2.7 Conclusions

1. The evolution of a binary formed by a point-mass and a star can be solved relatively easily for arbitrary mass-loss, eccentricity, and inclination via coupled differential equations. In this way we can easily investigate how the evolution changes as a function of the binary mass-ratio and of the ratio $J_\star/J_{\rm orb}$.

2. When tides are coupled with magnetic braking the evolution of a BH-LMXB can be separated into two main phases. The first one is driven either by tides or by magnetic braking, depending on how fast the star is initially rotating. In both cases, the outcome of the first phase of the evolution is that the spin of the star converges to a quasi-equilibrium value at which $|\dot{\omega}_{\star,\rm MB}| = |\dot{\omega}_{\star,\rm tid}|$: the effect of the tidal torque and of magnetic braking are balancing each other. From this moment on, every piece of angular momentum lost from the star is subtracted from the orbit.

3. In a planetary system instead, tides are too weak, and an initially-high stellar spin is typically brought below corotation. From this point on, the evolution coincides with the evolution in the low-spin case. Unlike the BH-LMXB case, the binary does not reach the quasi-equilibrium state. If the star is initially high-spinning and highly inclined with respect to the orbital angular momentum, the RLO configuration is typically non-coplanar.

4. Models which neglect the coupling between tides and winds do not accurately represent the true evolution of compact binaries. The simple estimate $\tau_{\rm circ}$ is not a good approximation for the actual change of e over time, because it does not account for the change in the orbital separation due to changes in the stellar spin. Nor for the fact that $\dot{e}$ typically increases during the evolution, due to decrease of the semi-major axis, whereas in the estimate $e/\dot{e}$ the orbital separation a is assumed to be constant. Furthermore, neglecting the spin leads to an overestimate of the semi-major axis at circularisation. It is then essential to consider the coupled evolution of rotational and orbital elements in order to accurately model the evolution of compact binaries. This was already showed previously by Jackson et al. 2008 and Barker & Ogilvie 2009, for the planetary system case.

5. We have implemented an easy model to follow the evolution of a HMXB under the coupled effect of tides and winds. For particular choices of decoupling radius and mass-loss, wind braking in a high-mass X-ray binary behaves as magnetic braking in a low-mass X-ray binary. The values

of decoupling radii and mass-losses which allow for a wind braking-type solution, are consistent with typical magnetic fields and typical mass-losses of high-mass stars.

2.8 Acknowledgments

We thank the anonymous referee whose comments greatly improved the Paper. SR is very grateful to Silvia Toonen for a careful and critical reading, which brought significant improvements to the manuscript. SR is thankful to Adrian Barker for a useful discussion on the calibration of tidal dissipation. The work of SR was supported by the Netherlands Research School for Astronomy (NOVA).

Chapter 3

Constraining the formation of black holes in short-period Black-Hole Low-Mass X-ray Binaries

S.Repetto, G. Nelemans

MNRAS, 453, Issue 3, 2015

Abstract

The formation of stellar mass black holes is still very uncertain. Two main uncertainties are the amount of mass ejected in the supernova event (if any) and the magnitude of the natal kick the black hole receives at birth (if any). Repetto et al. (2012), studying the position of Galactic X-ray binaries containing black holes, found evidence for black holes receiving high natal kicks at birth. In this Paper we extend that study, taking into account the previous binary evolution of the sources as well. The seven short-period black-hole X-ray binaries that we use, are compact binaries consisting of a low-mass star orbiting a black hole in a period less than 1 day. We trace their binary evolution backwards in time, from the current observed state of mass-transfer, to the moment the black hole was formed, and we add the extra information on the kinematics of the binaries. We find that several systems could be explained by no natal kick, just mass ejection, while for two systems (and possibly more) a high kick is required. So unless the latter have an alternative formation, such as within a globular cluster, we conclude that at least some black holes get high kicks. This challenges the standard picture that black hole kicks would be scaled down from neutron star kicks. Furthermore, we find that five systems could have formed with a non-zero natal kick but zero mass ejected (i.e. no supernova) at formation, as predicted by neutrino-driven natal kicks.

3.1 Introduction

Since the discovery of the first stellar-mass black hole (BH) in the Galactic X-ray source Cygnus X-1 (Bowyer et al. 1965), other BHs have been found. Stellar-mass[1] BHs have a mass between ~ 5 and 30 times the mass of the Sun, while the peak of the Galactic distribution is centered at 8 $M_{\odot}$ (Özel et al. 2010). Their Galactic population currently amounts to 17 dynamically confirmed BHs (Casares & Jonker 2014), and 31 BH candidates (Tetarenko, B.E. et al. 2015, in prep).

So far, the best way to detect BHs is when they are actively accreting from a stellar companion, whose matter falls in the gravitational field of the BH while forming an accretion disc. We wish to mention the recent discovery of a BH with a Be-type star as companion (Casares et al. 2014). This system, in which the accretion flow onto the BH is radiatively inefficient, opens-up the possibility of a new detection-window for BHs. In black-hole low-mass X-ray binaries (BH-LMXBs), a BH accretes matter from a star similar in mass to our Sun. At some point in the evolution of the progenitor of a BH-LMXB, the companion overfills its Roche lobe, either because of its own nuclear expansion, or due to shrinking of the orbit caused by angular momentum losses. The material hence escapes the gravitational pull from the star and forms an accretion disc around the BH, which is detectable in the X-ray band (Shakura & Sunyaev 1973).

Despite the strong evidence for the existence of BHs, the way they actually form is still a matter of great debate. It is generally accepted that BHs are formed from the gravitational collapse of a massive star, a star with a mass on the main sequence (MS) greater than $20-25$ $M_{\odot}$, and/or a core mass greater than 8 $M_{\odot}$, e.g. Fryer 1999, MacFadyen et al. 2001, Tauris & van den Heuvel 2006. In one scenario, massive BHs are thought to form by direct collapse, whereas the lightest ones via fallback onto the nascent neutron star (NS). Two main uncertainties are the size of the velocity the BH receives at birth (*natal kick*, NK), if any, and the amount of mass ejected at the moment of BH formation, if any. These are the questions we address in this Paper.

Measuring BH natal kicks is of great importance for a number of reasons. First of all, the magnitude of the NK is dependent upon the physical mechanism driving the kick. For instance, if BHs were discovered to receive high kicks, this would have important implications for the supernova (SN) mechanism. Theoretical calculations by Janka 2013 show that the momentum of the BH can grow with the fallback mass and lead to high kicks. Secondly, the velocity that BHs receive at birth affects the number of BHs which can be retained in a globular cluster (GC, Strader et al. 2012, Sippel & Hurley 2013, Morscher et al. 2015), as well as in a young stellar cluster (Goswami et al. 2014). Furthermore, the black hole NK distribution is an important ingredient in binary population synthesis (BPS) studies, for examples the ones which compute the gravitational wave (GW) merger rate of binaries harbouring BHs (see for example Lipunov et al. 1997 and Dominik et al. 2015). Additionally, the likelihood of discovering isolated (and nearby) BHs accreting from the interstellar medium (ISM) through radio signatures detectable by future surveys, is a function of the BH velocity relative to the ISM, hence of the NK (Fender et al. 2013).

In our first study of BH natal kicks (Repetto et al. 2012), we found evidence for BHs receiving *high* kicks, where *high* stands for kicks similar to those received by NSs (that is, hundreds of km/s). In that study, high NKs were needed in order to match the current out-of-the-plane distribution of BH X-ray binaries.

[1] Throughout this Paper, we will refer to stellar-mass BHs simply as BHs.

As currently observed binary properties (e.g., orbital period, masses, and position in the Galactic potential) are determined by the conditions present at the moment of BH formation, and therefore significantly affected by the magnitude of both the ejected mass and NK imparted, BH-LMXB systems are the optimal tool for shedding light on BH formation mechanisms.

In this Paper, we focus on a subset of BH-LMXBs, those ones with a short orbital period (less than 1 day). In these systems the current mass transfer phase is driven by angular momentum loss in the form of magnetic braking (MB). This study is complementary to the study of Repetto et al. 2012 (Paper I hereafter). Contrary to Paper I, which used a BPS approach to study the NK magnitude required to explain the current out-of-plane distribution of Galactic BH-LMXBs, in this Paper we use a detailed binary evolution approach, allowing us to take into account the current orbital parameters of each system. We trace the binary evolution of the seven short-period BH-LMXBs backwards in time until the moment the BH was formed. This allows us to set constraints on the mass ejected and the NK in terms of lower limits.

Previous works on BH natal kicks combined the study of the binary evolution of the systems with the information on the space velocity. A small NK has been found for GRO J1655-40 (Willems et al. 2005) and for Cygnus X-1 (Wong et al. 2012), whereas evidence for a high NK was found for XTE J1118+480 (Fragos et al. 2009). Evidence for a BH formed in a SN explosion comes from the chemical enrichment in the spectra of the companion to the BH in XTE J1118+480 (González Hernández et al. 2006), in GRO J1655-40 (Israelian et al. 1999), in 1A 0620-00 (González Hernández et al. 2004), in V4641 Sgr (Orosz et al. 2001), and in V404 Cyg (González Hernández et al. 2011). Whereas Cygnus X-1 was claimed to have formed without a SN (Mirabel & Rodrigues 2003).

The Paper is structured as follows: in Section 3.2 we give a brief overview of the evolution of BH-LMXBs and of what we know about BH formation, in Section 3.3 we show the properties of the observed systems. In Section 3.4 we describe our method to calculate the NK and mass ejected for the seven binaries, and in Section 4.4 the results. We end with a discussion and conclusion of our findings.

3.2 A short overview of the evolution of black-hole low-mass X-ray binaries

The standard formation scenario for a BH-LMXB is an extension of the formation scenario which explains low-mass X-ray binaries with a NS as accretor (van den Heuvel 1983). The primordial binary from which a neutron-star low-mass X-ray binary originates, is a binary with a very extreme mass ratio between the two components. In order to form a BH low-mass X-ray binary, one just needs to start with a more massive progenitor which will core-collapse into a BH, instead of a NS (Romani 1996, Portegies Zwart et al. 1997, Ergma & Fedorova 1998). The progenitor of a BH low-mass X-ray binary probably consists of a Sun-like star orbiting around a massive star (with a mass of $20-25\ M_{\odot}$). Typical orbital separations which allow a sun-like star to overfill its Roche lobe and transfer mass to a BH are of the order of $\sim 10\ R_{\odot}$. These separations are much smaller than the typical orbital separation that the progenitor of the BH-LMXB must have had in order to accommodate the progenitor of the BH during its nuclear expansion. Therefore, it is commonly accepted that the binary must have undergone a phase of common envelope (CE), which shrank the binary down by a factor of ~ 100 (Paczynski 1976). During the CE, the massive star is believed to lose its H-envelope; what is left, the Helium core, collapses into a BH. If the binary survives the event in which the BH forms, its further evolution can follow two

alternative paths. The evolution can be driven by the nuclear evolution of the stellar component, and the binary will undergo mass transfer when the star is large enough for some of its material to fall in the gravitational potential of the BH. At the current state, the companion star is thus an evolved star off the MS. Alternatively, the evolution can be driven by angular momentum losses from the binary and the two components get closer and closer to each other thanks to the coupled effect of tides and magnetic braking, until mass transfer sets in. The latter ones are the binaries we focus on in this study, where the companion star is a MS-star. For previous studies of the evolution of BH-LMXBs see e.g. Ergma & Fedorova 1998, Kalogera 1999, Podsiadlowski et al. 2003, Yungelson et al. 2006.

3.2.1 Black hole formation and natal kicks at birth

In the most common scenario of BH formation, higher mass BHs are thought to form via direct collapse of the progenitor star, lighter mass BHs via fallback onto the proto-NS (Fryer & Kalogera 2001, MacFadyen et al. 2001, Heger et al. 2003, Zhang et al. 2008). BH formation via fallback occurs in a successful but weak explosion, where some fraction of the ejecta does not have enough kinetic energy to escape the potential well of the proto NS. However, we wish to highlight that the occurrence of fallback is not agreed upon by the entire SN community. Some studies showed that the fallback requires a fine-tuning between the explosion energy and the envelope binding energy (see for example Dessart et al. 2010). Normally, either the SN is successful and leads to the formation of a NS, or it is unsuccessful and all the material collapses into a BH. The BH mass would therefore be equal to the mass of the collapsing Helium core (see Kochanek 2015 and Clausen et al. 2015).

A further source of uncertainty is whether BHs receive NKs at birth or not, and what the size of the NK would be. There are two types of BH natal kicks, kicks (i) imparted intrinsically to the BH, and (ii) received as an effect of the NK imparted to the NS that forms a BH through fallback. The intrinsic kicks could be caused either by asymmetric gravitational wave emission during the core-collapse (Bonnell & Pringle 1995), or by asymmetric flux of those neutrinos which get to escape before all the collapsing material falls inside the event horizon (Gourgoulhon & Haensel 1993). In either cases, there is no need for mass-ejection at BH formation.

There are two main processes which are thought to cause NS natal kicks and are therefore relevant for BH formation via fallback: either asymmetries in the SN ejecta (*ejecta-driven*, also called *hydrodynamical* NKs), or asymmetries in the neutrino flux (*neutrino-driven* NKs). Both of these two NK mechanisms have their own drawbacks (Fryer & Kusenko 2006). Only 1% of the collapse energy is in the ejecta, thus the hydrodynamics of the explosion has to develop a large degree of anisotropy to impart the NS a large NK. Instead, most of the energy and momentum liberated in the explosion are carried away by neutrino, hence only a small degree of asymmetry ($\sim 1\%$) in the neutrino flux is necessary to impart the NS a NK as high as hundreds km/s. However, this mechanism requires a strong magnetic field.

If the BH is formed via fallback onto the proto NS, the magnitude of the NK it receives depends on the competition between two timescales: the timescale for (some of) the material in the ejecta to fall back onto the nascent NS, $\tau_{\rm fb}$, and the timescale for the process which imparts the NS a NK, $\tau_{\rm NK}$. If $\tau_{\rm fb} > \tau_{\rm NK}$ we expect the BH to receive a reduced NK. If $\tau_{\rm fb} < \tau_{\rm NK}$, we expect the BH to receive a full NK. While hydrodynamic simulations by MacFadyen et al. 2001 show that fallback onto the NS happens within 100 s after core collapse, the timescale of NKs induced by neutrino emission and by

hydrodynamics in the ejecta is estimated to be $\tau_{\rm NK} \sim 10$ s and $\tau_{\rm NK} \sim 0.1$ s respectively (Lai et al. 2001). This indicates that, in the fallback scenario, the BH would receive a reduced NK.

Just by conserving linear momentum, we expect reduced NKs to be of the order of $V_{\rm NK,BH} \sim (M_{\rm NS}/M_{\rm BH})\, V_{\rm NK,NS}$, leading the BH to receive a NK of the order of tens km/s. If this scenario is correct, we should find a correlation between the mass of the BH and the NK: the larger the BH mass, the larger the fallback mass, the lower the NK. We wish to highlight, however, that Janka 2013 suggests BHs could be accelerated to the same velocity as NSs, even in a fallback-scenario, due to the anisotropic gravitational pull from the asymmetrically expelled ejecta. Thus, in this scenario, BHs would receive high kicks even when $\tau_{\rm fb} > \tau_{\rm NK}$, and the momentum of the BH would grow with the fallback mass.

For NSs there is both evidence for high and low kicks. The proper motion of isolated pulsars implies transverse velocities up to 1000 km/s, with a mean birth speed for young pulsars of ~ 400 km/s (Hobbs et al. 2005). On the other hand, few Galactic NS high-mass X-ray binaries seem to be more consistent with a low NK. These binaries have long periods and small eccentricities. Such a small eccentricity, being a prior of the eccentricity immediately after the SN explosion, requires a small NK, of the order of few tens km/s (Pfahl et al. 2002b). High NS natal kicks are thought to be produced in a standard core-collapse SN, whereas low NS natal kicks are thought to be produced in a less-energetic type of SN, an electron-capture SN from a low-mass star (Podsiadlowski et al. 2004). Such a low-mass star has little chance of forming a BH. When the collapsing core is low in mass, the explosion is thought to be so rapid that there is no time for large asymmetries to develop. Such a theoretical scenario is consistent with the results obtained tracing backwards the orbital properties of a few members of the Galactic population of double NS binaries (Wong et al. 2010). Few of them are consistent with a low-mass progenitor and a low NK at birth. The retention of NSs in GCs is another argument in favour of some NSs receiving low kicks (Pfahl et al. 2002a).

3.3 The Galactic population of short-period black-hole low-mass X-ray binaries

3.3.1 Orbital properties

In our Galaxy there are 13 BH-LMXBs with BH masses dynamically measured (Orosz et al. 2004, McClintock & Remillard 2006). Dynamical measurement of the BH mass is done tracing the Keplerian motion of the companion star. In this way, the BH mass can be determined once the orbital period, the radial velocity semi-amplitude of the companion star, the mass-ratio, and the inclination of the binary with respect to the line of sight, are known. The BH mass is a strong function of the inclination, hence it is the inclination the major contributor to any uncertainties in the BH mass. The inclination is typically determined fitting the ellipsoidal modulations in the optical light curve of the companion. The companion can be detected when the binary is in quiescence, i.e. when the accretion disc is under-luminous. Failure in accurately determining the contribution of the disc to the light curve, results in inaccurate BH mass determination. For an up-to-date overview of dynamical mass determinations in BHs, and the associated main sources of systematic errors, see Casares & Jonker 2014.

In Fig. 3.1 we show the orbital period $P_{\rm orb}$ of BH-LMXBs as a function of the mass of the companion $M_\star$. They fall in three categories: 10 short-period ($P_{\rm orb} \lesssim 1$ day) systems, of which 7 with $M_\star \lesssim$

1.5 $M_{\odot}$, and 3 systems with longer periods. Out of this sample, we only consider the short-period binaries with low-mass companions. We don't consider the binary with 1.5 day period as a short-period binary, since it contains a giant as a companion (Orosz et al. 2011b), so it is thought to evolve to longer periods.

The choice $P_{\rm orb} \lesssim 1$ day is motivated by the fact that binaries with longer periods are driven by the evolution of the donor, while only those with shorter periods are driven by magnetic braking and evolve towards smaller and smaller periods until the companion overfills its Roche lobe, while still being on the MS (see Yungelson et al. 2006). This defines a so-called bifurcation period $P_{\rm bif}$ (Tutukov et al. 1985, Pylyser & Savonije 1989), that is shown as the solid line in Fig. 3.1. We calculate $P_{\rm bif}$ as the the orbital period such that the magnetic braking time scale ($\tau_{\rm MB}$, calculated below in Section 3.4.2.1) is equal to the main-sequence life-time. The limit $M_{\star} \lesssim 1.5\ M_{\odot}$ is motivated by the fact that more massive donors are not thought to sustain a significant surface magnetic field, hence magnetic braking is not supposed to operate. We wish to mention that Justham et al. 2006 proposed that BH-LMXBs could descend from a population of intermediate-mass X-ray binaries with Ap/Bp-star companions. However, the spectral types predicted by the stellar evolutionary tracks are too hot for explaining the observed temperatures of companion stars in BH-LMXBs.

We indicate the dynamical properties of the seven short-period BH X-ray binaries in Table 3.1. We wish to note that GRS 1009-45 lacks strong constraints on the mass of the BH. This is due to the large uncertainty on the inclination of the system, and the BH-mass value given in Filippenko et al. 1999 is a lower-limit (see Casares & Jonker 2014). Another BH-LMXB whose observational properties are debated is GRO J0422+32. Reynolds et al. 2007 claimed that negligible contamination arising from the accretion disc was assumed in the estimate from Gelino & Harrison 2003. They estimate the contamination to the companion-star light curve due to the accretion disc, and they get a lower limit to the BH mass of $\sim 10.4\ M_{\odot}$. Although both the reported masses are probably biased, because of very large flickering amplitude in the light curves (Casares & Jonker 2014), we find the measurement by Gelino & Harrison 2003 as the most reliable one, because it is based on a database where the ellipsoidal modulation is best detected. Neglecting the disc contribution to the light curve would, in any case, underestimate the inclination, and consequently overestimate the BH mass, in strong contrast with the results of Reynolds et al. 2007.

3.3.2 Mass-radius relation

For our sample, the companion star is currently overfilling its Roche lobe. From the observed binary properties and inferred masses we can hence calculate the radius of the companion assuming $R_{\star} = R_{\rm L}$, where $R_{\rm L}$ is the Roche lobe radius of the companion star (Eggleton 1983). The results are plotted in Fig. 3.2 and can be compared to the radii of single main sequence stars shown as the solid lines. We compute such radii for single stars, both at the beginning and at the end of the MS, with the SSE code by Hurley et al. 2000 embedded in the Astrophysics Multipurpose Software Environment AMUSE (Portegies Zwart et al. 2009).

As is well known, stars in interacting binaries are typically somewhat larger than single stars. This can be caused by the fact that the star does not have time to relax back to its thermal equilibrium (Knigge et al. 2011). In case one component is a NS or BH the effect of X-ray irradiation, which heats up (hence bloats) the star, can play a role (Podsiadlowski 1991, Harpaz & Rappaport 1991). However,

Table 3.1: Dynamical properties of short-period black-hole low-mass X-ray binaries.

Source	$P_{\rm orb}$ [day]	$M_\star$ [$M_\odot$]	$M_{\rm BH}$ [$M_\odot$]	Ref.
XTE J1118+480	0.17	0.15-0.29	8.16-8.58	[1]
GRO J0422+32	0.21	0.15-0.77	3.02-4.92	[2]
GRS 1009-45	0.28	0.61^a	4.4^a	[3]
1A 0620-00	0.32	0.39-0.41	6.44-6.84	[4]
GS 2000+251	0.34	0.16-0.47	5.5-8.8	[5]
Nova Mus 91	0.43	0.68-0.81	6.35-7.55	[6]
H 1705-250	0.52	0.3-0.6	6.4-6.9	[7]

Notes: (a) This system lacks strong constraints on the component masses (see Text).
References: [1] González Hernández et al. 2012, [2] Gelino & Harrison 2003, [3] Filippenko et al. 1999, [4] González Hernández et al. 2014, [5] Ioannou et al. 2004, [6] Gelino et al. 2001, [7] Filippenko et al. 1997.

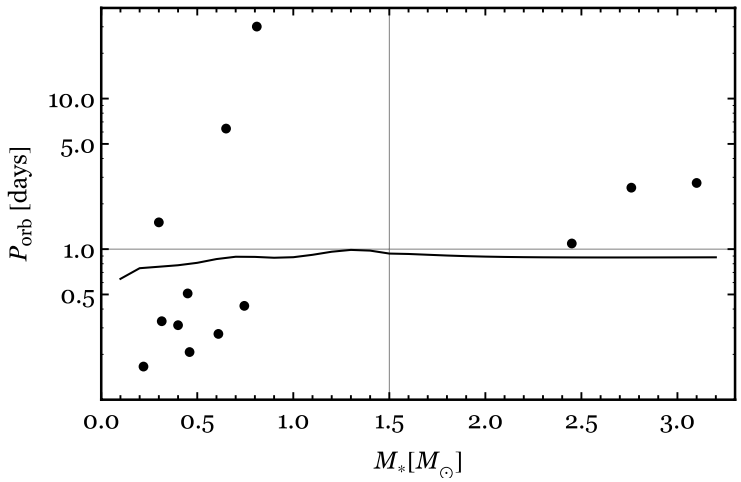

Figure 3.1: Black-hole low-mass X-ray binaries as a function of orbital period $P_{\rm orb}$ and companion mass $M_\star$. The solid line shows the bifurcation period. The sources in the bottom left of the plot are those we study in this work.

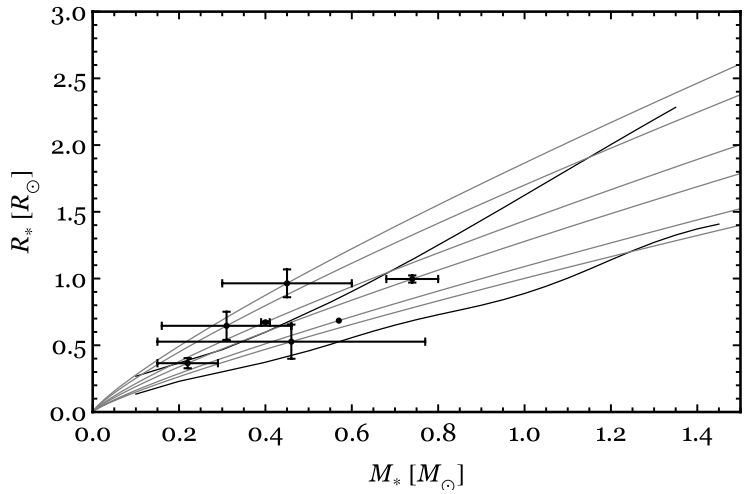

Figure 3.2: Radius and mass of the seven short-period black-hole low-mass X-ray binaries. The two black lines correspond to the radius of single stars at the beginning and at the end of the main sequence. The grey lines correspond to our fit of the mass-radius relation of the seven short-period BH low-mass X-ray binaries.

this effect is not thought to be significant in LMXBs in quiescent state.

In order to calculate the evolution of the binaries, it is needed to know their mass-radius relation, since we need to know how the star responds to the loss of mass during mass transfer. For interacting binaries with white dwarfs accretors (cataclysmic variables, CVs), it has been shown that a power-law fit to the mass-radius relation $R_\star \propto M_\star^\alpha$ is an adequate description (Knigge et al. 2011).

We therefore model the mass radius relation of the companion stars in BH-LMXBs as $\frac{R_\star}{R_\odot} = f\left(\frac{M_\star}{M_\odot}\right)^\alpha$. We thus assume the BH-binaries to all align on the same slope in the logM-logR diagram. We fit the short-period binaries with a mass-radius index of ~ 0.82. We use this common power-law index as a fixed parameter to fit the mass-radius relation for each system, that is, for finding f for each binary. In Fig. 3.2 we show such a common power-law index with the grey lines, to be compared with the mass-radius relation of single MS stars (solid black lines). For comparison, the mass-radius relation for CVs has been fitted by Knigge et al. 2011 with $\alpha_{\rm CV} = 0.69$.

3.3.3 Kinematical properties and Galactic positions

The final (and crucial) piece of information we will use to reconstruct the birth of the BH is the position of the binary in the Galaxy. Assuming that the binary is born in the Galactic plane and receives a kick in the SN explosion right perpendicular to the plane, it will then move on a straight line reaching a maximum height $z_{\rm max}$. Assuming that the binary's current height z above the plane is $z_{\rm max}$, this height gives a minimum peculiar velocity at birth $v_{\perp,\rm min}$ given the Galactic potential at the distance R from the Galactic center (Paper I). The velocity $v_{\perp,\rm min}$ is the minimum velocity at birth required for bringing the system from the plane to its current position above (or below) the plane. This velocity is calculated simply by conserving the energy along the trajectory in the Galactic potential:

$$v_{\perp,\rm min} = \sqrt{2[\Phi\left(R_0, z\right) - \Phi\left(R_0, 0\right)]},$$

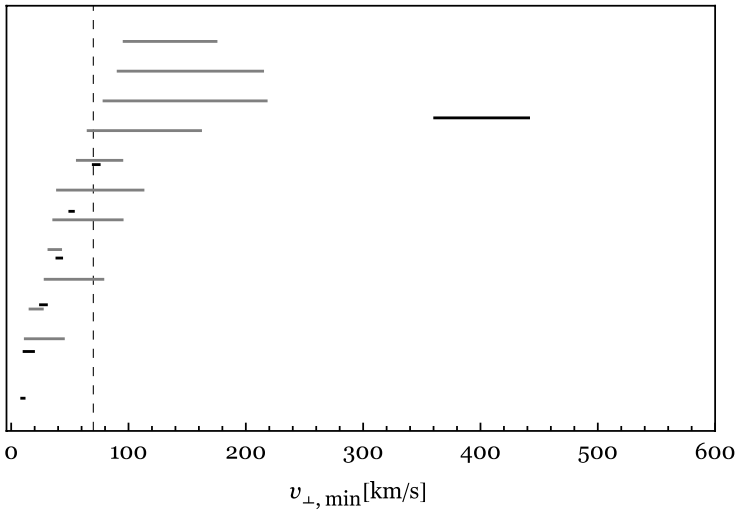

Figure 3.3: Range of possible values for the minimum peculiar velocity at birth of the short-period black hole X-ray binaries from Table 3.2. The solid lines indicate the systems belonging to our study. The grey lines indicate the BH candidates from Tetarenko, B.E. et al. 2015, in prep. The dashed vertical line indicates the lower limit on the peculiar velocity at birth for XTE J1118+480.

where $\Phi\,(R, z)$ is a model for the Galactic potential (Paczynski 1990) and R_0 is the observed projected distance of the binary from the Galactic centre.

In Table 3.2 we show the resulting values for $v_{\perp,\mathrm{min}}$ for our seven systems, as well as for the tentative BH candidates from Tetarenko, B.E. et al. 2015 (in prep). These BHs do not have a dynamical BH-mass estimate, but are likely BHs due to their spectral and timing properties (Tetarenko, B.E., priv. comm.). Of the sources contained in Tetarenko et al. catalogue, we select only the short-period ones. We show the range of possible values of $v_{\perp,\mathrm{min}}$ for every source in Fig. 3.3. It is interesting to note that there are 5 other sources whose minimum $v_\perp$ is very similar to the one of XTE J1118+480, which is one of the sources in our sample consistent with a high NK (see Sec. 5.5). Kuulkers et al. 2013 noted the similarities between XTE J1118+480, MAXI J1659-152 and Swift J1753.5-0127, pointing out their similar orbital period (few hrs) and the large scale height from the Galactic plane, suggesting that all three were kicked out of the Galactic plane, or possibly born in a GC (see also Shahbaz et al. 2013). We will suggest a similar interpretation for the remaining high peculiar velocity sources.

An estimate of the actual (rather than minimal) peculiar velocity received at birth can be obtained if the current 3D space velocity of the binary is measured. Integrating the trajectory of the binary backwards in time from the current initial conditions of the position and 3-D velocity, it is possible to infer the 3-D velocity at birth. The only system in our sample with measured both radial velocity and proper motion, and hence 3-D space velocity, is XTE J1118+480 (Miller-Jones 2014). Its Galactic trajectory has been integrated backwards by Fragos et al. 2009, giving a peculiar velocity at birth of $110 - 240$ km/s, which is consistent with our lower limit $v_{\perp,\mathrm{min}} \sim 70$ km/s.

Table 3.2: Kinematical properties of short-period black-hole low-mass X-ray binaries. The first group contains the binaries of this study. The second group contains the putative black hole candidates.

Source	distance [kpc]	z [kpc]	$v_{\perp,\min}$ [km/s]	Ref.
XTE J1118+480	1.62-1.82	1.43-1.61	70-75	[1]
GRO J0422+32	2.19-2.79	-[0.45-0.57]	25-30	[2]
GRS 1009-45	3.55-4.09	0.58-0.66	39-43	[3]
1A 0620-00	0.94-1.18	-[0.11-0.13]	9-11	[4]
GS 2000+251	2-3.4	-[0.10-0.18]	11-19	[5]
Nova Mus 91	5.63-6.15	-[0.69-0.76]	50-53	[6]
H 1705-250	6.5-10.7	1.02-1.68	361-441	[7]
MAXI J1305-704	2-8	-[0.26-1.06]	29-78	[8]
Swift J1357.2-0933	0.5Ð6.3	[0.38-4.83]	91-214	[9]
XTE J1650-500	1.9-3.3	-[0.11-0.20]	16-26	[10]
MAXI J1659-152	4.9-12.3	[1.39-3.50]	79-217	[11]
GRS 1716-249	2-2.8	[0.24 -0.34]	32-42	[12]
Swift J174510.8-262411	2-8	[0.05-0.19]	12-44	[8]
Swift J1753.5-0127	2-8	[0.42-1.69]	66-161	[8]
H 1755-338	4-9	-[0.34-0.77]	96-174	[13]
MAXI J1836-194	4-10	-[0.37-0.93]	39-112	[14]
XTE J1859+226	11-14	[1.65-2.09]	56-94	[15]
4U 1957+115	2-8	-[0.32-1.30]	36-94	[8]

Notes: References: [1] Gelino et al. 2006, [2] Gelino & Harrison 2003, [3] Gelino 2001, [4] Cantrell et al. 2010, [5] Barret et al. 1996, [6] Hynes 2005, [7] Remillard et al. 1996, [8] No acceptable estimates for the distance is available, so a distance of 5 ± 3 is assumed as done by Tetarenko, B.E. et al. 2015, in prep., [9] Shahbaz et al. 2013, [10] Homan et al. 2006, [11] Kuulkers et al. 2013, [12] della Valle et al. 1994, [13] Mason et al. 1985, [14] Russell et al. 2014, [15] Corral-Santana et al. 2011.

3.4 A semi-analytical method to follow the evolution of short-period black-hole low-mass X-ray binaries

In order to link the observed properties of BH-LMXBs with BH formation, we will have to take the evolution of the binary since the BH formation into account. We use a semi-analytical approach to simulate the evolution of each binary in our sample. We follow the evolution of the three stages the binary goes through (BH formation, detached phase, mass transfer), but in reverse order.

Tracing backwards in time the mass transfer phase, we obtain the orbital properties of the binary at the onset of the Roche Lobe Overflow (RLO), $a_{\rm RLO}, M_{\star,\rm RLO}, M_{\rm BH,RLO}$, where $a_{\rm RLO}$ is the orbital separation. These properties will be a function of the mass transferred to the BH and of the mass-radius relation of the companion, both parameters that we vary. We then use these to calculate the orbital evolution due to the coupled effect of tides and magnetic braking during the detached phases following the BH formation. This then defines a set of potential progenitor binaries and BH formation properties (NK and mass ejection) that are consistent with the currently observed properties of BH-LMXBs.

3.4.1 Mass Transfer

The evolution of long-period BH binaries is driven by the nuclear expansion of the donor. Assuming the orbital angular momentum is conserved, one can trace the mass-transfer backwards in terms of the mass transferred to the BH (see Miller-Jones et al. 2009b). We use a similar approach for dealing with the mass-transfer in short-period binaries, modelling it in an analytical way.

During Roche Lobe Overflow, the BH companion loses mass and its radius shrinks accordingly. Assuming that some type of orbital angular momentum loss always ensures the star is filling its Roche lobe, the shrinkage of the star induces a consequent shrinkage of the orbit. How much the orbit shrinks depends on the mass-radius relation $R_\star \sim M_\star^\alpha$ of the star. A similar approach was used for following the evolution of CVs by Knigge et al. 2011.

The rate at which the logarithm of the orbital separation a changes due to the combined effect of mass transfer, mass and angular momentum loss from the binary, is given by the following balance equation:

$$\frac{\dot{a}}{a} = 2\frac{\dot{J}_{\rm orb}}{J_{\rm orb}} - 2\frac{\dot{M}_{\rm BH}}{M_{\rm BH}} - 2\frac{\dot{M}_\star}{M_\star} + \frac{\dot{M}}{M}, \tag{3.1}$$

where M is the total mass of the binary and $J_{\rm orb}$ the orbital angular momentum. We reparametrize the balance equation 3.1 in terms of $M_\star$, eliminating time as a variable. Solving the corresponding equation, we obtain the orbital separation a and mass of the BH at any point in the past, as a function of $M_\star$ and α, when the mass transfer is conservative (i.e. $\dot{M}_{\rm BH} = -\dot{M}_\star$). When the mass transfer is non conservative, an additional parameter is β ($\dot{M}_{\rm BH} = -\beta\dot{M}_\star$), and we assume that the matter leaves the binary with the specific angular momentum of the BH. The resulting analytic formulae are

$$\frac{a}{a_{\rm cur}} = \left(\frac{M_\star}{M_{\star,\rm cur}}\right)^{-\frac{1}{3}+\alpha}, \tag{3.2}$$

for conservative mass transfer, and

$$\frac{a}{a_{\rm cur}} = \left(\frac{M_{\rm BH}}{M_{\rm BH,cur}}\right)^{2-\frac{2}{\beta}} \left(\frac{M_\star}{M_{\star,\rm cur}}\right)^{-\frac{1}{3}+\alpha} \left(\frac{M}{M_{\rm cur}}\right)^{-\frac{8}{3}}, \tag{3.3}$$

for non-conservative mass transfer. The cur-subscript indicates values at the current time.

The mass transfer is traced backwards in this way until the onset of mass transfer. In order to define this, we have to assume how much mass is transferred since the onset, ΔM, and this defines $M_{\star,\mathrm{RLO}} = M_{\star,\mathrm{cur}} + \Delta M$. In our standard model we assume $\Delta M = 1\ M_\odot$. We will vary our assumptions on the mass transfer, namely the amount of transferred mass and the mass-radius index, when performing our simulations in Section 4.4. A smaller transferred mass and/or a smaller mass-radius index, will make the orbital separation at the onset of RLO smaller.

3.4.2 Detached evolution and black hole formation

3.4.2.1 Coupling between tides and magnetic braking

To calculate the evolution during the detached phase preceding the mass transfer, we need to model the evolution of a system in which both tides and magnetic braking operate. Magnetic braking is the loss of angular momentum in a magnetic stellar wind (see Parker 1958, Weber & Davis 1967, Verbunt & Zwaan 1981). We refer to Repetto & Nelemans 2014 for details on the numerical method used to take into account the coupling between tides and magnetic braking. In short, after BH formation, the tidal torque circularises and synchronises the binary. From here, every bit of angular momentum lost from the star in its magnetic wind is also lost from the orbit, effectively shrinking the binary until the onset of RLO.

Our test-bed MB prescription was introduced by Verbunt & Zwaan 1981, and it gives the rate at which the star spins down $\dot{\omega}_\star$. This in turn gives the MB timescale, $\tau_{\mathrm{MB}} = J_{\mathrm{orb}}/\dot{J}_\star = J_{\mathrm{orb}}/I_\star\dot{\omega}_\star$, where $I_\star = k^2 M_\star R_\star^2$ is the moment of inertia of the star. Assuming the star is synchronised with the orbit ($\omega_\star = \omega_{\mathrm{orb}}$), one gets:

$$\tau_{\mathrm{MB}} = \frac{M_{\mathrm{BH}}}{M^2}\frac{1}{G\gamma_{\mathrm{MB}}k^2}\frac{a^5}{R_\star^4}, \tag{3.4}$$

where k is the gyration radius of the star and γ_{MB} is measured as $\approx 5\times10^{-29}\mathrm{s/cm}^2$.

For each of the seven binaries, we compute $a_{\max}$ such that RLO happens within the MS lifetime of the BH companion. The maximal orbital separation $a_{\max}$ is a function of the eccentricity of the binary right after the BH formation, and it depends on the MB calibration. The value of $a_{\max}$ varies only very little when taking a different calibration factor for tides, as shown in Repetto & Nelemans 2014.

We numerically fit $a_{\max}$ as a function of the eccentricity e and of the orbital separation at the onset of RLO, a_{RLO}:

$$a_{\max}(e, a_{\mathrm{RLO}}) = \alpha + \beta(1-\exp(\gamma e)) + \frac{\delta e}{e-\epsilon} \tag{3.5}$$

where $\alpha, \beta, \gamma, \delta, \epsilon$ are the parameters of the fit, and they depend on a_{RLO} (see Appendix).

We test two types of magnetic braking law: one from Verbunt & Zwaan 1981 (VZ, hereafter), and the other one from Ivanova & Taam 2003 (IT, hereafter). The tidal model is based on Hut 1981 and we use calibration factors as in Hurley et al. 2002.

We show $a_{\max}$ as a function of the eccentricity in Fig. 3.4 for the seven sources we are studying, when using a VZ-type of magnetic braking. The orbital separation of the RLO configuration a_{RLO} is computed using formula 3.2, tracing the mass transfer phase backwards in time from the current properties, until the companion-star mass increases to $1\ M_\odot$.

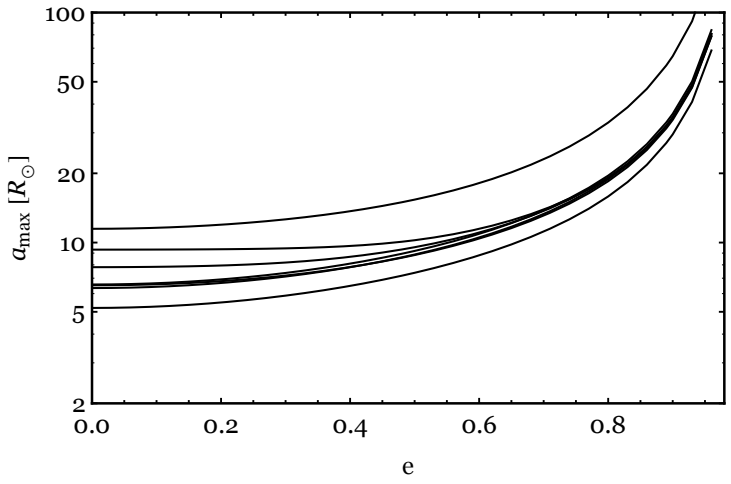

FIGURE 3.4: Maximal orbital separation right after black hole formation so that the star in short-period black-hole low-mass X-ray binaries fills its Roche Lobe within the main-sequence lifetime. From bottom to top, the curves are associated to the following sources: GRO J0422+32, 1A 0620-00 and Nova Mus 91 (overlapping curves), GRS 1009-45, GS 2000+251, H 1705-250, XTE J1118+480.

We wish to note that the orbital separation $a_{\max}$ is not affected by the rate at which the companion star is initially spinning. This is due to the fact that the angular momentum stored in the star is much less than the angular momentum stored in the orbit. The ratio between the value of $a_{\max}$ when taking a star initially spinning at $\omega_\star \approx 0.9\ \omega_{\rm break}$ and the value when the stellar spin is $\omega_\star \approx 10^{-6}\ {\rm s}^{-1}$, is between $1 - 1.5$ for every value of the eccentricity.

Another way of computing $a_{\max}$ is simply by requiring that $\tau_{\rm MB} \leq \tau_{\rm MS}$, as done for instance by Kalogera 1999. The orbital separation used for computing $\tau_{\rm MB}$ is the circularised orbital separation after BH formation. As an example, in the case of the binary XTE J1118+480, $a_{\max}$ computed using timescale considerations differs only little from $a_{\max}$ in our model, by 15% at most.

3.4.3 Supernova dynamics

The orbital configuration right after BH formation[2] can be determined univocally from the properties of the pre-BH-formation configuration through conservation of orbital energy and orbital angular momentum. An abundance of earlier studies deal with the effect of a SN explosion and possibly of a NK on the orbital configuration (see for example Blaauw 1961, Boersma 1961, Hills 1983, Kalogera 1996). In this way, one can compute the orbital elements $a_{\rm post}, e_{\rm post}$ knowing $a_{\rm pre}$, $e_{\rm pre}$, the magnitude and direction of the NK, and the amount of mass ejected from the collapsing star (mass which is assumed to leave the system instantaneously without further interacting with the binary). The effect of the NK and the mass ejected at BH formation combine together to give the total peculiar (also called *systemic*) velocity of the binary:

$$V_{\rm pec} = \sqrt{\left(\frac{M_{\rm BH}}{M'}\right)^2 V_{\rm NK}^2 + V_{\rm MLK}^2 - 2\frac{M_{\rm BH}}{M'} V_{\rm NK,x} V_{\rm MLK}}, \tag{3.6}$$

[2]Throughout the whole paper, we denote with *-pre* the binary configuration right before the BH formation, with *-post* the configuration right after.

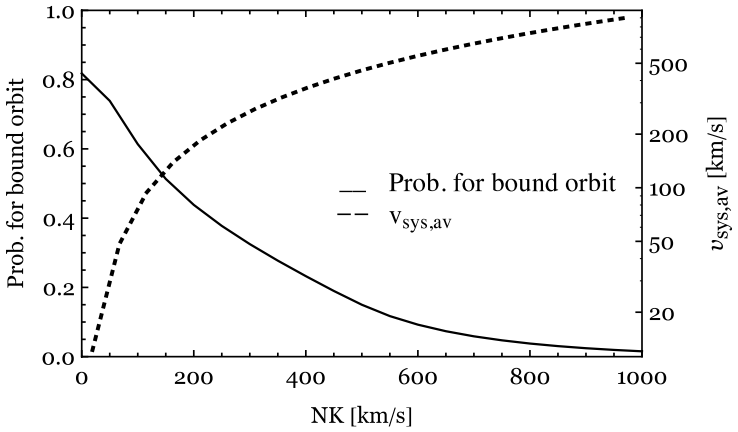

Figure 3.5: Probability for a binary containing a black hole of mass $8\ M_\odot$ and a companion with mass $1\ M_\odot$ of having survived the supernova event (solid line) as a function of the natal kick. The dashed line shows the averaged systemic velocity acquired by the binary in the supernova event.

where M' is the total mass after the binary has lost a mass $M_{\rm ej}$ in the SN, $V_{\rm NK}$ is the magnitude of the NK, $V_{\rm NK,x}$ its component along the orbital speed of the BH progenitor, and $V_{\rm MLK}$ is the *mass-loss kick*, the recoil the binary gets after a mass $M_{\rm ej}$ is lost, also known as *Blaauw kick* (Blaauw 1961):

$$V_{\rm MLK} = \frac{M_{\rm ej}}{M'}\frac{M_\star}{M}\sqrt{\frac{GM}{a}}, \tag{3.7}$$

where M is the total mass of the binary right before the SN.

In Fig. 3.5, we show the probability for the binary to stay bound in the SN event (solid line). This probability is calculated for a sample of binaries formed by a BH of mass $8\ M_\odot$ and a companion of mass $1\ M_\odot$, with randomised initial orbital separations and ejected mass, and random orientation of the NK. The probability is calculated as a function of the NK. We also show (dashed line) the average systemic velocity acquired by the binary in case it stays bound.

3.4.4 Monte Carlo calculation of black hole formation and detached evolution

Once we have the properties at RLO, we treat the BH formation phase with a Monte Carlo approach. We build a sample of 80×10^6 initial binaries formed by a companion of mass $M_{\star,\rm RLO}$ and the progenitor of the BH with mass $M_{\rm prog} = M_{\rm BH,RLO} + M_{\rm ej}$, where $M_{\rm ej}$ is drawn from a uniform distribution between 0 and $10\ M_\odot$. The orbital separation of the initial binary is drawn from a uniform distribution between a minimum value and $50\ R_\odot$, and the orbit is assumed to be synchronous and circular. The minimum value for the orbital separation is the value at which the Helium star and/or the companion overfill their Roche lobe. The Helium star ejects a mass equal to $M_{\rm ej}$, and what is left collapses into a BH, which receives a NK at formation drawn from a uniform distribution between 0 and 1000 km/s. The inclination of the NK with respect to the orbital plane is uniformly peaked over a sphere centered on the progenitor of the BH.

The motivation which lays behind our choice of the range for the initial orbital separation is statistics. Orbital separations larger than $50\ \rm R_\odot$ will only very rarely lead to RLO within the MS lifetime. Specifically, RLO on the MS will happen only if the binary is highly eccentric in the post-SN config-

uration. This can be seen from the decaying PDFs at large values for the pre-SN orbital separation in Fig. 3.13. We tested this assumption checking how many systems with initial orbital separation $a_{\rm pre} > 50\ R_\odot$ evolve into successful ones. For all sources except XTE J1118+480, no simulated binary with $a_{\rm pre} > 50\ R_\odot$ evolves into a successful one. For XTE J1118+480 the fraction of systems which evolve into successful ones is 9%.

Concerning the NK and the $M_{\rm ej}$, those ranges are rather arbitrary, due to the great uncertainty on the BH formation process. Nevertheless, larger values for the NK and for the $M_{\rm ej}$ than the extreme ones we chose, would lead to an unbinding of the system, hence they are of no interest to our work.

Using the formalism we showed in Section 3.4.3, we compute $a_{\rm post}$ and $e_{\rm post}$. We assume that the SN ejecta do not have any impact on the companion star properties, its spin for instance, hence $\omega_{\star,\rm post} = \omega_{\star,\rm pre} = \omega_{\rm orb,pre}$. To account for the coupling between tides and magnetic braking, we make sure that $a_{\rm post}$ is less than the value of the maximal orbital separation at that eccentricity and at the calculated $a_{\rm RLO}$ (Section 3.4.2.1). An additional criterion which allows to constrain the allowed parameter space of NK and $M_{\rm ej}$ is the kinematical one: we make sure that the peculiar velocity acquired by the binary at BH formation is larger than the minimum peculiar velocity $v_{\perp,\rm min}$ we inferred from the position of the binary (see Section 3.3.3).

3.4.5 Observational biases on our sample

3.4.5.1 Results from the population model

Because we want to derive general conclusions on the NK and ejected mass at BH formation, we want to generalise the results for the individual systems. In order to do so, we want to have some idea of the effect of the different NKs and ejected masses on the observational properties of the systems, and thus of possible observational biases that make that the observed systems are predominantly those with particular NKs and/or ejected masses.

We build a population of BH-LMXBs formed by a BH of mass $8\ M_\odot$ and a companion of mass $1\ M_\odot$. The magnitude of the NK, the mass ejected at BH formation, and the initial orbital separation are drawn from uniform distributions between 0 - 1000 km/s, 0 - 10 $M_\odot$, and 0 - 50 $R_\odot$ respectively, whereas the orientation of the NK is random over a sphere centered on the BH progenitor. For those binaries that stay bound in the SN, we select only those ones which undergo RLO within the MS lifetime. We show the results in Fig. 3.6. The higher density region is for mild kicks around $100 - 200$ km/s, and small $M_{\rm ej}$. Such a combination of these two parameters, allow the orbital separation in the post-SN configuration to fall within $a_{\rm max}$.

We then populate the Galaxy following the stellar density in the thin disc (Binney & Tremaine 2008 and McMillan 2011), and we follow the trajectories of the successful binaries for 10 Gyr. The observed BH low-mass X-ray binaries all lie within 10 kpc from the Sun (see Table 3.2). This is very likely due to the fact that the binary has to be relatively close so that a dynamical measurement of the BH mass via optical spectroscopy is possible. We analyse how many of the simulated binaries satisfy this proximity-criterium as a function of the NK and $M_{\rm ej}$. We show the results of this calculation in Fig. 3.7, where for every bin (NK, $M_{\rm ej}$) of the plot in Fig. 3.6, we compute the fraction of systems that lie within 10 kpc from the Sun with respect to the total number of winning binaries in that bin. From the plot, it is evident that we are biased towards binaries in which the BH received a low NK. So even if BHs received high kicks, we would not observe most of them.

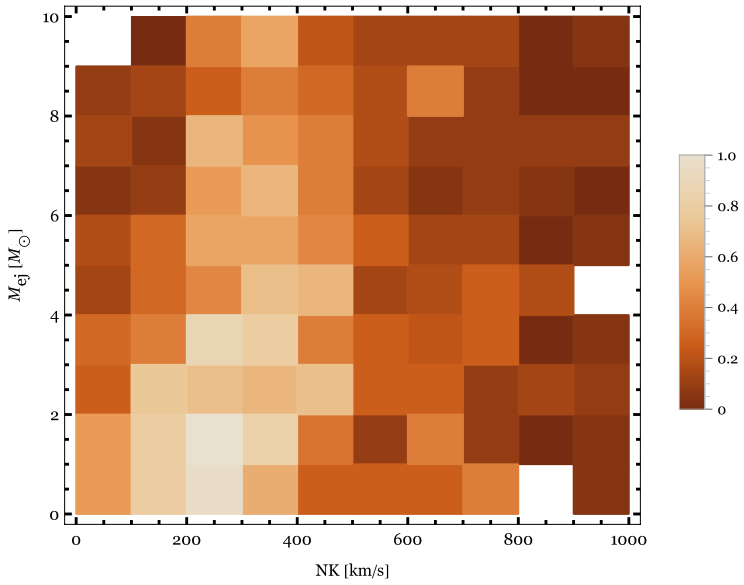

Figure 3.6: Results of a binary population synthesis study of black-hole LMXBs. We select only those binaries which undergo RLO within the MS lifetime, and we show their optimal parameter space for the mass ejected in the SN and the NK.

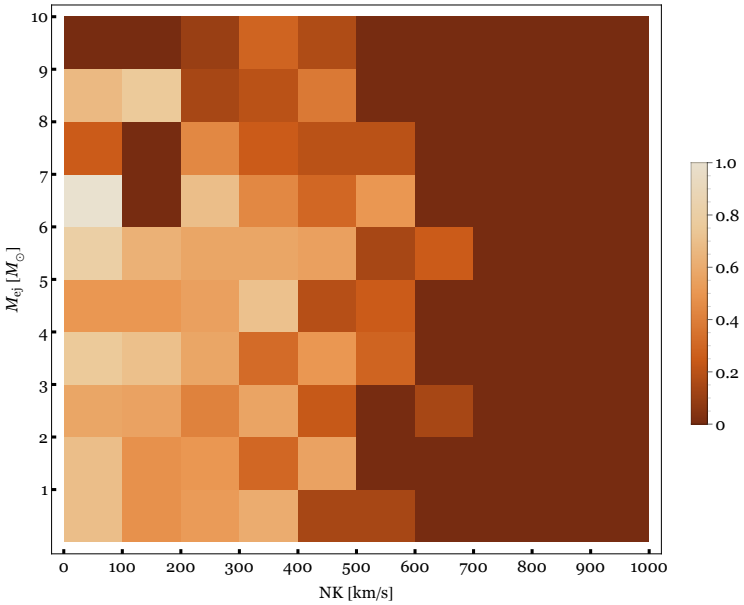

Figure 3.7: For every 2D-bin of the left plot, we show here the fraction of systems which reside within 10 kpc from the Sun after orbiting in the Galactic potential for 10 Gyr.

3.4.5.2 Hyper-velocity systems

Related to the previous discussion, we wonder how likely it is that we are missing systems in the halo of the Galaxy. Taking a Galactic local escape velocity of ~ 500 km/s (Smith et al. 2007), the minimum NK the BH has to acquire for the binary to escape the Galactic potential, is ~ 550 km/s (for every choice of initial orbital separation and ejected mass in the SN). A binary moving with a peculiar velocity of 500 km/s would travel a distance of 500 kpc in 1 Gyr. However, the probability for the binary to stay bound with such a large NK is of ≈ 0.1 only, as we can see in Fig. 3.5. Thus, we expect most of these hyper-velocity binaries to get unbound.

Yet, it is likely that we are missing systems in the halo of our Galaxy. We performed a test integrating the Galactic orbit of BH-LMXBs in which the BH received a NK at birth. Even with a mild NK of 200 km/s, the BH-LMXB would move far away from the Sun reaching the halo in 10 Gyr, out to $R \sim 60$ kpc. So even if the binary stays bound in the BH formation event, it would remain undetectable optically.

3.5 Results

With the numerical method described above we calculate the possible combinations of NK and ejected mass that are compatible with the observed properties of the seven BH-LMXBs in our sample.

3.5.1 Different models

We vary the physics involved in the binary evolution (mass-radius power-law index α, maximum transferred mass ΔM) and we take into account the uncertainty in the distance of the source, to test what is the resulting uncertainty on the lower limits for the NK and the mass ejected in the SN. Furthermore, we test the different MB prescriptions (VZ and IT, see Section 3.4.2.1). The models we test are:

1. (standard model) VZ, $\Delta M = 1 M_{\odot}, \alpha = 0.82$
2. IT, $\Delta M = 1 M_{\odot}, \alpha = 0.82$
3. VZ, $\Delta M = 0.4 M_{\odot}, \alpha = 0.82$
4. IT, $\Delta M = 0.4 M_{\odot}, \alpha = 0.82$
5. VZ, $\Delta M = 1 M_{\odot}, \alpha = 0.69$

For all the models, we simulate 80×10^6 initial binaries.

3.5.2 Lower limits on the natal kick and ejected mass

We show in Fig. 3.8 the density plots of possible combinations of NK-$M_{\rm ej}$ that can lead to the currently observed properties of the seven systems, for Model (i).

There is a typical trend in the higher-density region of the plots, which indicates an increasing ejected mass for an increasing natal kick. This is caused by the constraint on the orbital separation in the post BH-formation configuration: the binary has to be compact enough for mass transfer to start while the companion is still on the MS. In the absence of a large NK, large ejected mass would widen

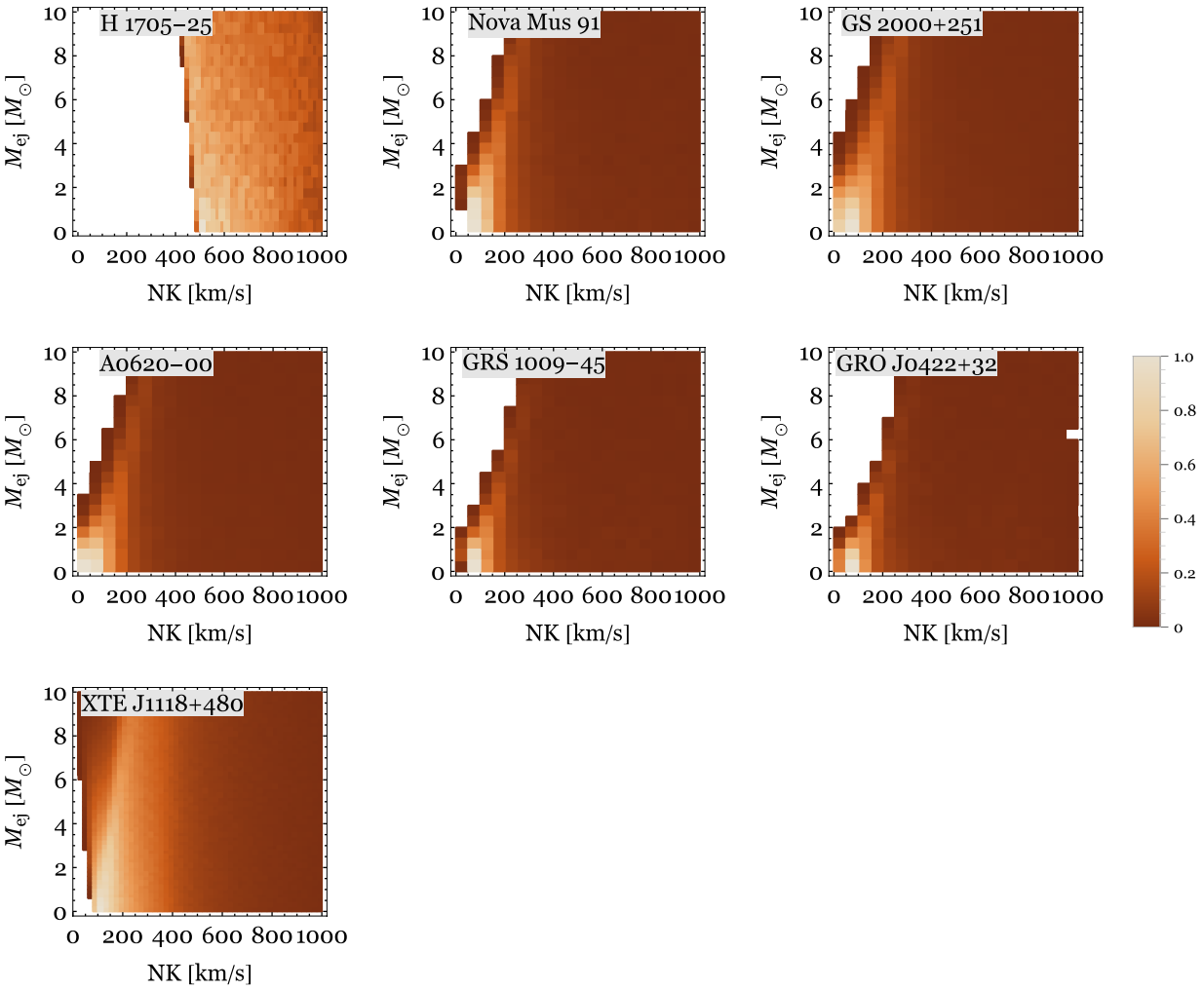

Figure 3.8: Density plots showing the allowed parameter space for the mass ejected M_{ej} and the natal kick NK at BH formation for the seven short-period black-hole low-mass X-ray binaries, in the framework of our standard model (i), see text for details.

the system too much. Only if a NK counters that effect are larger ejected masses permitted; but there is a decreasing fraction of NK-orientations that allow this (see the decreasing density along the trend).

The density plots clearly separate the systems in at least two classes: five systems that have the highest densities at or close to the origin, and two systems (H1705-25 and XTE J1118+480) that have the highest densities at large NK. However, there is still a significant difference between the five low-kick systems: two of them (Nova Mus 91 and GRS 1009-45) actually exclude or have very low density to have no kick. Finally, we note that all systems have significant density at $M_{ej} = 0$.

We need to point out that these distributions do not correspond to probability distributions of the actual values of the parameters for the systems, as the parameter range and parameter distributions that we used in the Monte Carlo (flat) will likely not represent the real ones. However, as we used flat input distributions, the resulting probabilities do show how much fine tuning in the initial binary parameters and NK orientations is needed to survive and match the kinematic and orbital properties of the binaries.

In order to quantify our results, we show in Fig. 3.9 and 3.10 the cumulative distribution for the

NK and for the ejected mass for each of the 7 sources for our Monte Carlo calculations. We define a *minimum* NK and ejected mass as a cut at the 5% probability in these cumulative distributions, i.e. a limit at which the 95% of the cumulative distribution is higher. These lower limits are shown in Table 3.3 and the range of values for each of the sources is a consequence of the uncertainty on the physics involved (i.e. the different models we use) and on the distance. The variation of the parameters involved in the binary evolution, namely the amount of mass transferred to the BH, the mass-radius index and the strength of MB, do not affect greatly the lower limits on the NK and on the $M_{\rm ej}$ (see second and third column in Table 3.3 for the first six binaries). These lower limits are mostly affected by the peculiar velocity of the system, hence by the height of the system from the Galactic plane, and are therefore consistent with the ones by Repetto et al. 2012 that accounted for the kinematics of the sources only. Indeed, in the case of H 1705-250, the large range for the NK is due to the large (25%) uncertainty in the distance to the source. Whereas the large value for the NK is due to the fact that the binary resides right above the Galactic bulge, very close to the Galactic centre where the Galactic potential is strongest.

Typically, these lower limits fall in lower density regions of the plots in Fig. 3.8 and thus still require severe fine tuning of in particular the NK orientation. We also wish to note that assuming all (x, y, z) directions for the NK are equally probable, the lower limits for the NK indicated in the table are to be multiplied by the square root of 3.

We also checked the effect of taking a non-conservative mass transfer rather than a conservative one, using formula 3.3 for tracing backwards the semi-detached phase, and taking $\beta = 0.1$. When comparing the results of this model with the results of Model (i), for example, we find that the lower limits on the NK and on $M_{\rm ej}$ do not change by more than 7%, for all the 7 sources.

The fact that all the highest-density regions in Fig. 3.8 are skewed towards low kicks (except for H 1705-250 and XTE J1118+480), does not mean that high BH kicks are excluded. The reason why we are biased towards small NKs is the proximity of the sources to the Sun. This can be seen in Fig. 3.11, where we plot the whole sample of confirmed BH low-mass X-ray binaries as a function of their distance to the Sun and the lower limit on the NK. Referring back to our BPS study, it is evident that the higher the kick, the lower the probability for the system to be in the proximity of the Sun (see Fig. 3.7).

From our results, it is possible to highlight three different cases:

1. *Standard systems*: systems with a low peculiar velocity at birth, which can be consistent either with a small NK, or with a kick imparted to the binary as a result of the mass ejection in the SN event.

2. *Zero ejected mass systems*: systems consistent with a non-zero NK *but* zero ejected mass at BH formation.

3. *High NK systems*: systems consistent with a high NK, comparable to NS natal kicks.

We will discuss these three scenarios in Sec. 5.5.

3.5.3 Correlation natal kick VS mass of the black hole

In Fig. 3.12 we plot our lower limits for the NK as a function of the BH mass to see if there is any correlation. From our results, we find so far (with our limited sample) no evidence for a correlation

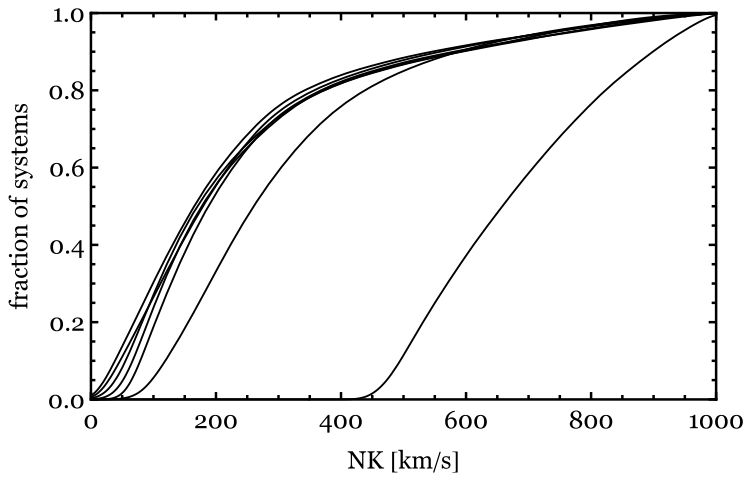

Figure 3.9: Cumulative distribution for the natal kick received by the black hole in short-period BH-LMXBs, in the framework of our standard model (i), see Text for details. From left to right: 1A 0620-00, GS 2000+251, GRO J0422+32, GRS 1009-45, Nova Mus 1991, XTE J1118+480, H 1705-250.

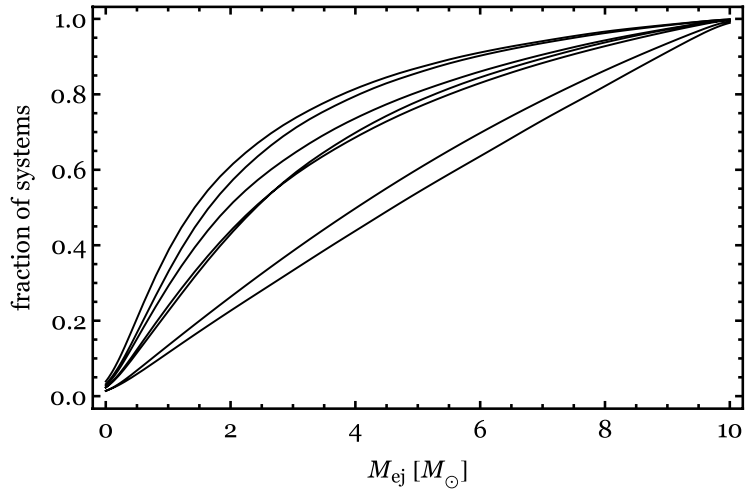

Figure 3.10: Cumulative distribution for the ejected mass at BH formation in short-period BH-LMXBs, in the framework of our standard model (i), see Text for details. From left to right: GRO J0422+32, 1A 0620-00, GRS 1009-45 and Nova Mus 1991 (overlapping curves), GS 2000+251, XTE J1118+480, H 1705-250.

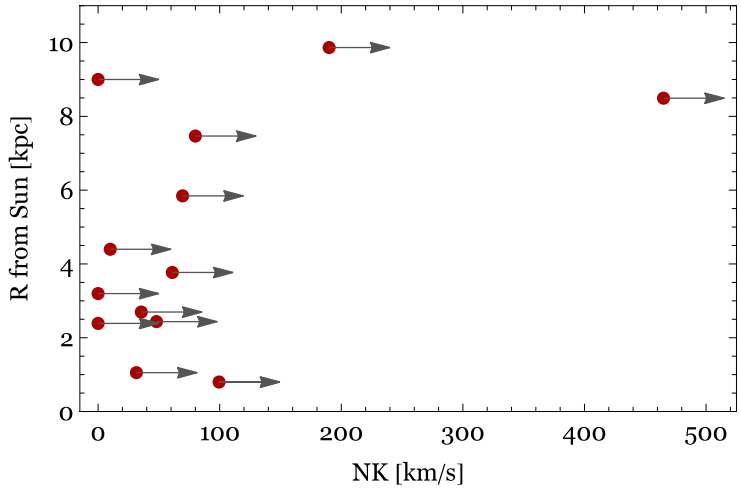

FIGURE 3.11: BH low-mass X-ray binaries as a function of their distance R from the Sun and the lower limit on the NK, as computed in Paper I and in this work.

TABLE 3.3: The second and third column show the minimum natal kick and the minimum mass ejected at BH formation. The third column shows $a_{\rm pre,max}$ such that the binary undergoes mass transfer within the MS lifetime. The range indicates how the values vary when changing the assumption on the parameters involved in the binary evolution of the sources (see Text for a description of the different models we consider). The last column shows $a_{\rm pre,max}$ such that the binary stays bound in the SN.

Source	min NK [km/s]	min $M_{\rm ej}$ $[M_\odot]$	max $a_{\rm pre}$, RLO on MS $[R_\odot]$	max $a_{\rm pre}$, bound in SN $[R_\odot]$
GS 2000+251	24-47	0.13-0.33	9-37	7800
A0620-00	20-43	0.09-0.32	8-37	8400
Nova Mus 91	62-77	0.17-0.34	8	1400
XTE J1118+480	93-106	0.31-0.37	23-38	570
GRS 1009-45	49-73	0.08-0.28	8-38	2400
GRO J0422+32	35-61	0.04-0.26	7-38	3000
H 1705-250	415-515	0.40-0.50	11-19	27

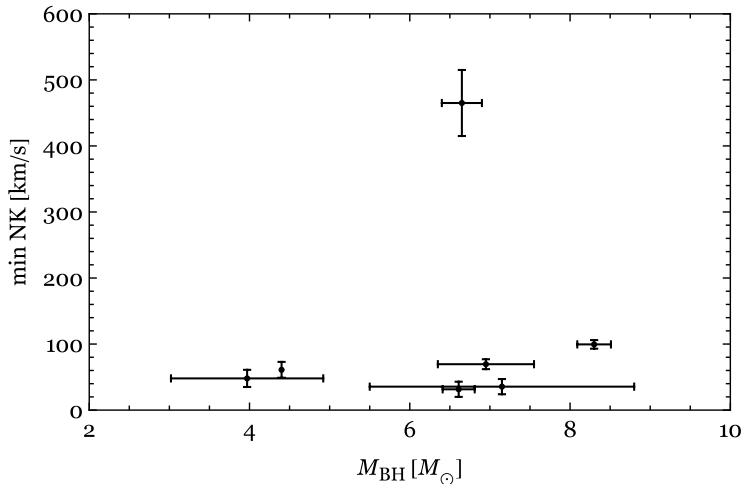

FIGURE 3.12: Short-period BH low-mass X-ray binaries as a function of black hole mass and the minimum natal kick which results from our simulations.

between NK and BH mass. If we found a correlation, such as lighter BHs receiving higher kicks, that could be a hint for a NK happening on a shorter timescale than the fallback timescale.

3.5.4 Initial orbital separation

We show in Fig. 3.13 the probability density function for the orbital separation right before BH formation for the seven sources.

In the third column of Table 3.3, we show the maximal orbital separation right before BH formation such that the binary stays bound in the SN *and* undergoes mass transfer within the MS-lifetime. In the fourth column, we show the maximum value for $a_{\rm pre}$ such that the binary stays bound in the SN. The range of values correspond to varying our models. Comparing the values of the last two columns, we see that the constraint to have RLO within MS lifetime, is much more limiting than having the binary to stay bound in the SN. As a consequence, we expect that there are many detached BH+MS-star binaries which would evolve to longer and longer periods due to the nuclear expansion of the companion, finally evolving into BH+WD binaries.

3.6 Discussion

There are three BH-formation scenarios which are compatible with some of the seven sources we studied.

3.6.1 Zero ejected mass systems

Five systems (H 1705-250, Nova Mus 91, GRS 1009-45, GRO J0422+32, XTE J1118+480) are consistent with a NK, while not requiring the ejection of mass at BH formation. The NK at which the one dimensional NK density function for $M_{\rm ej} = 0$ peaks is correspondingly: 525, 76, 68, 54, 114 km/s. We wish to stress that these value do not correspond to the most likely value of a probability density function, rather they are the values of the NK which require less fine-tuning.

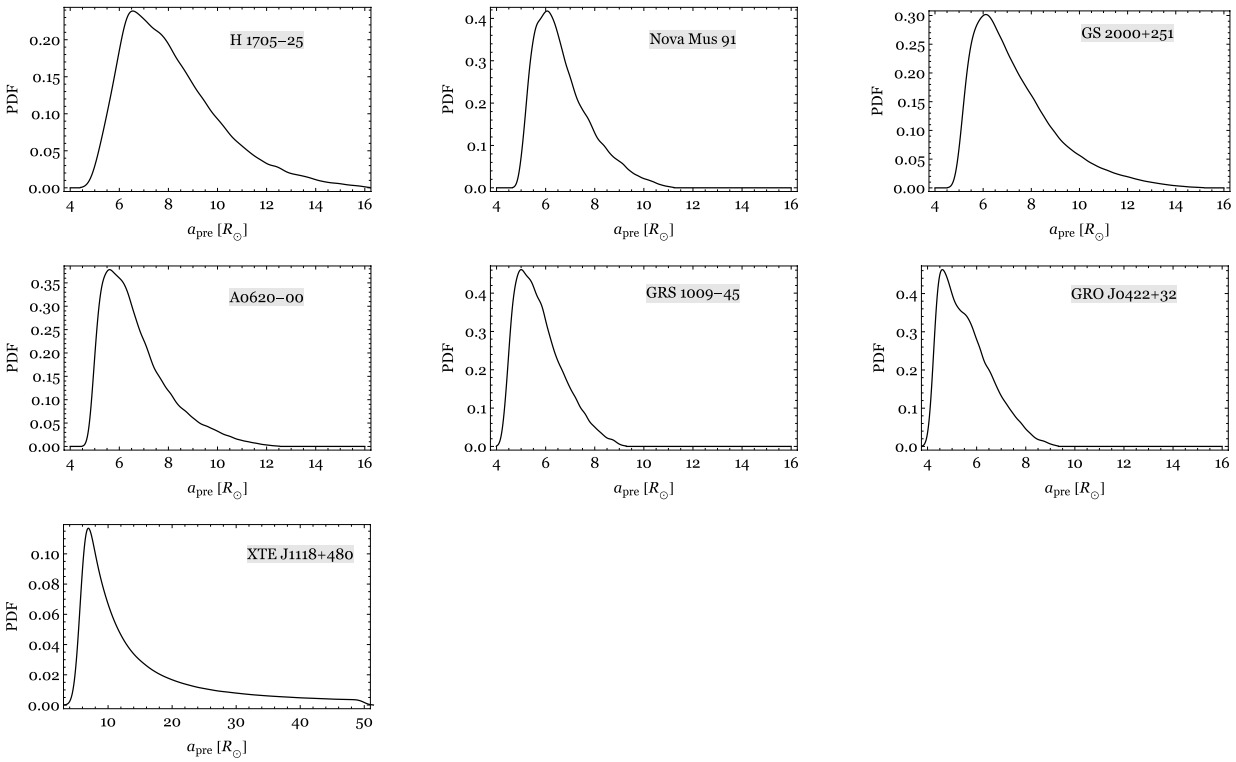

Figure 3.13: Probability density function for the orbital separation right before black hole formation for short-period BH-LMXBs, in the framework of our standard model (i), see Text for details.

Zero ejected mass at BH formation could be consistent with a BH formed in the dark (no SN, i.e. no baryonic mass ejected) and with a NK caused by asymmetric neutrino emission or asymmetric GW emission. When a BH is formed, the gravitational mass defect which is equal to the negative binding energy, is calculated to be $\sim$ 10% of BH mass (Zeldovich & Novikov 1971). If this mass leaves the system in the form of neutrinos, the predicted ejected mass can be consistent with our limits of Table 3.3.

We note, however, that in the case of XTE J1118+480 there is evidence for an explosion having occurred from the chemical enrichment in the spectra of the companion to the BH (González Hernández et al. 2006).

Furthermore, we wish to highlight that our study is the first in suggesting that few of the BHs in LMXBs might have been formed without baryonic mass ejection. This was found for few BHs in high-mass X-ray binaries (see Valsecchi et al. 2010, Mirabel & Rodrigues 2003).

3.6.2 Standard systems

Five sources out of seven (Nova Mus 91, GS 2000+251, 1A 0620-00, GRS 1009-45, GRO J0422+32) require only a small peculiar velocity at birth, of the order of few tens of km/s or less (see Table 3.2). This small peculiar velocity could be imparted to the binary as a result of mass ejection in the SN event. We can compute how much ejected mass is needed to account for the small peculiar velocity (see Fig. 3.14), in a similar manner as done previously by Nelemans et al. 1999. In order to compute the kick received by the binary due to the mass ejection (MLK), we use formula 4.3. We trace the orbital binary properties

backwards assuming a transferred mass of 1 $M_\odot$ and $\alpha = 0.82$. As a test, we assume a semi-major axis in the pre-SN configuration of 1.5 $a_{\rm RLO}$ (solid line) and of 5 $a_{\rm RLO}$ (dashed line). The plots show the amount of mass ejected needed to account for the peculiar velocity of the 5 sources aforementioned. There is an upper limit on $M_{\rm ej}$ such that the binary stays bound in the SN, i.e. the ejected mass has to be less than half of the total initial mass, which translates into $M_{\rm ej} < M_{\rm BH} + M_\star$ (vertical lines in Fig. 3.14). All of the five systems but Nova Mus 91, can be explained by mass-ejection only.

Alternatively, density wave scatterings could impart a velocity to the system of the order of few tens km/s (Brandt et al. 1995), with a maximum value of 40 km/s (Mihalas & Binney 1981).

As previously discussed in Sec. 3.3.1, GRS 1009-45 lacks strong constraints on the masses of its components. In particular, the BH mass quoted in Table 3.1 is a strict lower limit. We then estimate the MLK taking a larger BH mass of 7 $M_\odot$ and a companion mass of 0.98 $M_\odot$. We find that for $a_{\rm pre} = 1.5\ a_{\rm RLO}$, the ejected mass needed to account for the peculiar velocity of the system is $\sim 7\ M_\odot$. Calculations by Fryer & Kalogera 2001 indicate a maximum ejected mass at BH formation of $\sim 4\ M_\odot$. We conclude that it is essential to better constraint the component masses in GRS 1009-45 in order to discriminate between a standard scenario and a non-zero NK scenario.

Concerning GRO J0422+32, we check what is the effect of using BH and companion-star masses from Reynolds et al. 2007 ($M_{\rm BH} = 10.4\ M_\odot$ and $M_\star = 0.4\ M_\odot$). For $a_{\rm pre} = 1.5\ a_{\rm RLO}$, the MLK is always lower than the peculiar velocity of the systems, for every $M_{\rm ej}$. Again, this highlights the importance of correctly estimating the component masses.

3.6.3 High natal kick systems

Two out of seven sources require a high NK at birth (H 1705-250 and XTE J1118+480), comparable to NS natal kicks. This could be a hint for the NK happening on the same timescale of the fallback. A high NK for the BH in XTE J1118+480 was already suggested by Fragos et al. 2009.

As an alternative explanation, these two systems could have been ejected from a GC. None of the BH X-ray binaries currently known are found in a GC. So far, there is evidence for two BHs in a Milky Way GC (Strader et al. 2012), and one BH in an extragalactic GC (Maccarone et al. 2007). However, no optical companion has yet been found for these candidates, hence an accurate estimate of the mass of the compact object does not exist. A GC origin for XTE J1118+480 seems unlikely, due to the super-solar surface metallicity of the companion (Fragos et al. 2009, González Hernández et al. 2006).

H 1705-250 is the source which looks most different from all the other sources in the sample. It is located right above the Galactic bulge, at Galactic coordinates $R \sim 0.5$ kpc, $z \sim 1.35$ kpc. Its systemic radial velocity was measured by Remillard et al. 1996, giving a value of 10 ± 20 km/s. We conclude that either the system is moving perpendicularly to our line of sight, or that a GC origin for the system is more likely.

Looking at Fig. 3.3, there might be at least 5 other systems hinting for a high NK, those ones whose peculiar velocity at birth $v_{\perp,\rm min}$ is similar to the one of XTE J1118+480. Future work is needed to precisely determine the mass of the compact object in such systems.

3.6.4 Effect of the uncertainty on the distance

The most accurate method to determine the distance to a BH X-ray binary, is to estimate the absolute magnitude of the companion star, see Jonker & Nelemans 2004. This method has been used for all the 7

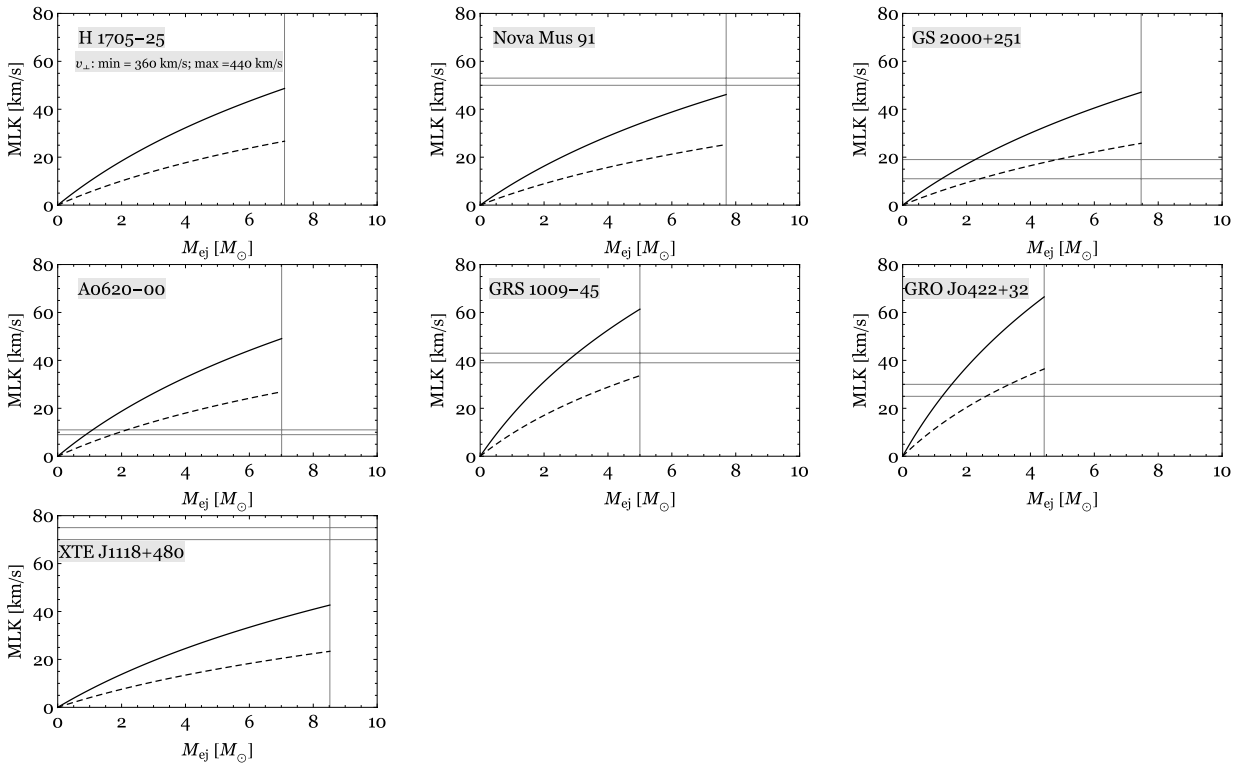

Figure 3.14: Mass-loss kick (MLK) as a function of the mass ejected at BH formation for the short-period BH-LMXBs. The vertical lines show the upper limit on the mass ejected at BH formation for the binary to stay bound. The solid grey lines correspond to the lower and upper limit on the peculiar velocity at birth. The black solid and black dashed line correspond to different assumptions on the pre-SN orbit (see Text). The point of intersection between these lines and the limits on the peculiar velocity depicts when a system can be explained by mass ejection only.

BH-LMXBs in our sample, except for Nova Mus 91, for which the distance was estimated by Hynes 2005 through the interstellar absorption properties of the source, which is a less reliable method. Orosz et al. 1996 found a distance of $d = 5.5 \pm 1$ kpc, estimating the spectral type and luminosity of the companion. Such a distance would give $v_{\perp,\mathrm{min}} = 50 - 56$ km/s, still consistent with our value of $v_{\perp,\mathrm{min}} = 50 - 53$ km/s (see Table 3.2).

The major source of systematic errors when estimating the distance through the absolute magnitude of the companion, comes from a failure in accounting for the right disc-contribution to the light of the star (see Sec. 6 in Paper I for a discussion). Hynes 2005 warn about possible systematics on the measurement by Gelino 2001 of the distance to GRS 1009-45, due to the assumed small veiling from the disc. Taking into account a larger contribution from the disc, Barret et al. 2000 obtained a distance $d = 5 - 6.5$ kpc. This translates into a minimum peculiar velocity $v_{\perp,\mathrm{min}} = 48 - 52$ km/s, larger than the one taken in our work (see Table 3.2). This results in a minimum NK of ~ 62 km/s, when performing a set of simulation in the framework of our standard model (i). This value is still consistent with the range shown in Table 3.3.

3.7 Conclusions

There are five main conclusions which result from this work:

1. The lower limit on the NK is not greatly affected by the binary evolution of the sources. It is mostly affected by the kinematics of the system, and therefore by the uncertainty on the distance. In this respect, our results are consistent with the ones in Repetto et al. 2012, who calculated lower limits on BH natal kicks basing their study on kinematical arguments. Variations of the assumptions on MB and mass transfer give very similar results.

2. Even if the lower limit on the NK is not affected by the binary evolution of the system, in order to unravel what are the optimal combinations of NK and mass ejected in the SN, it is necessary to follow the details of the whole evolutionary paths of BH-LMXBs. In particular, this method allowed us to find binaries consistent with a neutrino-driven NK.

3. Our work enables us to highlight three possible scenarios for the birth of the BH. Two of these scenarios have been discussed previously in the literature: either the BH does not receive any NK, or it receives a NS-like NK. The third scenario that we suggest, is a BH having formed with a NK and zero baryonic mass ejection. It is the first time that this scenario has been applied to the evolution of BH-LMXBs, whereas it was first found to be consistent with the formation of few BHs in high mass X-ray binaries (see Valsecchi et al. 2010, Mirabel & Rodrigues 2003).

4. We find evidence for a high NK (i.e. a NS-like NK) in two of the sources, and potentially 5 BH X-ray binary candidates whose minimum peculiar velocity at birth suggests a high NK.

5. Our population study highlights that, due to the limits of optical spectroscopy, there exists a bias towards BH-LMXBs being close (within 10 kpc) to the Sun. For the same reason, NK estimates are biased towards low/mild NKs (less than $100 - 200$ km/s).

3.8 Acknowledgments

We are grateful to the anonymous referee for very pertinent insights, especially on the observational properties of the binaries, and on the implications of the uncertainty on these properties on our study. SR thanks Bailey Tetarenko for having provided the catalogue of BH candidates, and for her thorough and critical reading of the manuscript. The work of SR is supported by the Netherlands Research School for Astronomy (NOVA).

3.9 Appendix

Analytical treatment of the mass transfer phase

The orbital angular momentum of a binary is written as

$$J_{\rm orb} = \mu\sqrt{GMa},$$

in terms of the reduced mass μ, the total mass of the binary M, and the semi-major axis a. Using Paczyński 1971 relation for the Roche radius, $R_L \approx 0.46\ a\ \left(\frac{M_\star}{M}\right)^{1/3}$, and the fact that the star is filling its Roche lobe during mass-transfer, $R_L = R_\star = fM_\star^\alpha$, we can express $J_{\rm orb}$ in terms of the component masses only:

$$J_{\rm orb} = \sqrt{Gf}M_{\rm BH}M^{-1/3}M_\star^{\frac{5}{6}+\frac{\alpha}{2}}$$

This expression can then be derived with respect to $M_\star$:

$$\frac{dJ_{\rm orb}}{dM_\star} = M_{\rm BH}M^{-\frac{1}{3}}(\frac{5}{6}+\frac{\alpha}{2})M_\star^{-\frac{1}{6}+\frac{\alpha}{2}}\sqrt{Gf} - M^{-\frac{1}{3}}M_\star^{\frac{5}{6}+\frac{\alpha}{2}}\sqrt{Gf}$$

The balance equation 3.1 then becomes:

$$\frac{\dot{a}}{a} = \frac{2}{J_{\rm orb}}\frac{dJ_{\rm orb}}{dM_\star}\dot{M}_\star + 2\beta\frac{\dot{M}_\star}{M_{\rm BH}} - 2\frac{\dot{M}_\star}{M_\star} + (1-\beta)\frac{\dot{M}_\star}{M}$$

The last equation can be integrated analytically obtaining 3.2 and 3.3.

3.9.1 Fitting formulae for the maximal orbital separation

We show in Table 3.4 the parameters for the fitting of the maximal orbital separation as a function of the eccentricity (see expression 3.5).

Table 3.4: Fitting parameters for $a_{\max}$.

Source	α	β	γ	δ	ϵ
H 1705-250					
model1	8.94	-2.84	-2.43	-3.16	1.00
model 2	8.93	-2.81	-2.45	-3.16	1.00
model 3	11.00	-3.38	-2.40	-6.28	1.00
model 4	8.60	-4.70	-0.90	-4.63	1.00
model 5	7.84	-1.68	-3.94	-3.16	1.00
Nova Mus 91					
model 1	6.69	-0.79	-7.90	-3.23	1.00
model 2	6.68	-0.82	-7.24	-3.20	1.00
model 3	11.34	-7.45	-0.79	-6.32	1.00
model 4	8.20	-5.51	-0.61	-4.25	1.00
model 5	6.46	-0.68	-9.17	-3.23	1.00
GS 2000+251					
model1	8.22	-1.96	-3.49	-3.20	1.00
model 2	8.21	-1.94	-3.47	-3.18	1.00
model 3	11.01	-2.70	-3.38	-6.23	1.00
model 4	7.86	-3.69	-1.11	-4.25	1.00
model 5	7.02	-1.01	-6.26	-3.20	1.00
1A 0620-00					
model 1	7.01	-1.07	-5.86	-3.14	1.00
model 2	7.00	-1.07	-5.68	-3.12	1.00
model 3	10.80	-3.05	-2.73	-6.16	1.00
model 4	7.35	-4.22	-0.84	-3.96	1.00
model 5	6.37	-0.69	-8.77	-3.15	1.00
GRS 1009-45					
model 1	5.52	-0.53	-10.64	-2.86	1.00
model 2	5.50	-0.54	-9.99	-2.83	1.00
model 3	10.15	-3.95	-1.68	-5.79	1.00
model 4	6.69	-5.39	-0.54	-3.57	1.00
model 5	11.66	-11.20	-0.47	-6.36	1.00
GRO J0422+32					
model 1	11.73	-11.29	-0.47	-6.39	1.00
model 2	5.49	-0.54	-10.00	-2.83	1.00
model 3	9.91	-2.92	-2.55	-5.66	1.00
model 4	6.31	-3.93	-0.76	-3.41	1.00
model 5	5.20	-0.50	-10.74	-2.75	1.00
XTE J1118+480					
model 1	11.73	-11.29	-0.47	-6.39	1.00
model 2	8.68	-4.09	-0.90	-4.43	1.00
model 3	10.98	-2.25	-4.41	-6.11	1.00
model 4	6.67	-3.09	-1.14	-3.62	1.00
model 5	11.66	-11.20	-0.47	-6.36	1.00

Chapter 4

The Galactic distribution of X-ray binaries and its implications for compact object formation and natal kicks

S. Repetto, A. Igoshev, G. Nelemans

in press (MNRAS)

Abstract

The aim of this work is to study the imprints that different models for black hole (BH) and neutron star (NS) formation have on the Galactic distribution of X-ray binaries (XRBs) which contain these objects. We find that the root mean square of the height above the Galactic plane of BH- and NS-XRBs is a powerful proxy to discriminate among different formation scenarios, and that binary evolution following the BH/NS formation does not significantly affect the Galactic distributions of the binaries. We find that a population model in which at least some BHs receive a (relatively) high natal kick fits the observed BH-XRBs best. For the NS case, we find that a high NK distribution, consistent with the one derived from the measurement of pulsar proper motion, best fits the observed data. We also analyse the simple method we previously used to estimate the minimal peculiar velocity of an individual BH-XRB at birth. We find that this method may be less reliable in the bulge of the Galaxy for certain models of the Galactic potential, but that our estimate is excellent for most of the BH-XRBs.

4.1 Introduction

The formation mechanism of compact objects, neutron stars (NSs) and black holes (BHs), is an unsolved problem in high-energy astrophysics. A model for the formation of such objects requires to perform physically-motivated simulations of the core-collapse supernova, which is computationally challenging

(see e.g. Fryer & Warren 2002; Janka 2012). Another possible way to investigate the formation of NSs and BHs is to study the birth and evolution of X-ray binaries (XRBs) hosting a BH or a NS accreting from a stellar companion. The orbital parameters, peculiar velocities and Galactic position of these binaries directly follow from their evolutionary history, and are affected in particular by the conditions at the moment of compact object formation (see e.g. Brandt & Podsiadlowski 1995; Kalogera et al. 1998; Nelemans et al. 1999; Pfahl et al. 2002b; Nelemans 2007).

The measurement of pulsar proper motions (see e.g. Lyne & Lorimer 1994; Hansen & Phinney 1997; Hartman 1997; Hobbs et al. 2005), combined with the study of NS-XRBs (e.g. Johnston et al. 1992; Kaspi et al. 1994; Fryer & Kalogera 1997), has exposed evidence that some NSs receive a low velocity, whereas others a high velocity at formation (so called *natal kicks*, NKs). The prevailing idea is that NSs are formed either in a standard core-collapse supernova (SN), or in a less energetic type of SN where the core has a smaller mass. The latter can take place either as an electron-capture SN (Podsiadlowski et al. 2004; Takahashi et al. 2013; Beniamini & Piran 2016), or as an iron core-collapse SN with a small iron-core mass (see e.g. Tauris et al. 2015). For the case of BHs, observations are rather scarce and patchy, thus it is not yet possible to discriminate between different models of BH formation (Mirabel & Rodrigues 2003; Jonker & Nelemans 2004; Willems et al. 2005; Dhawan et al. 2007; Fragos et al. 2009; Miller-Jones et al. 2009b; Wong et al. 2012; Wong et al. 2014; Repetto & Nelemans 2015). In this paper, one of our goals is to investigate whether the observed Galactic distribution of X-ray binaries hosting a BH can reveal something about how BHs are formed. The main underlying idea is that any offset of a BH-XRB from the Galactic plane (assumed as birth place) is a signature of some peculiar velocity of the system with respect to the circular Galactic motion. The magnitude of such velocity gives clues on the SN mechanism, in particular on the magnitude of the NK at birth. The idea of using the Galactic position and/or gamma-velocities of a population of XRBs to investigate the formation of compact objects was employed previously for the NS case (see e.g. Brandt & Podsiadlowski 1995; Johnston 1996).

We covered the topic of BH formation in two previous works. In Repetto et al. 2012, we followed the Galactic trajectories of a simulated population of BH-XRBs, and investigated which NK distribution gives rise to the observed z-distribution of BH-XRBs (where z is the height above the Galactic plane). The aim was to discriminate between *high* and *reduced* NKs for BHs. High NKs are larger than the NK expected in a standard formation scenario for BHs, in which the BH forms via fallback of material on to the proto-NS and the NK is caused by asymmetries in the SN ejecta. In the standard scenario, the NK would conserve the linear-momentum and roughly scale as the NK received by the NS multiplied by the ratio between the mass of the BH and the mass of the NS. We call these kicks as *reduced* or *momentum-conserving* NKs. If the NS receives a NK of the order of 300 km/s, a 10 $M_{\odot}$ BH would get a NK of $\approx$ 40 km/s. We define *high* NKs as $\gtrsim$ 100 km/s. In Repetto et al. 2012, we found that high NKs, comparable to NS NKs, were required. In Repetto & Nelemans 2015, we combined the information from the kinematics and binary evolution of a subset of BH-XRBs to find evidence both for low and high NKs. In this Paper, we aim at complementing and extending those previous studies. Following up on the work by van Paradijs & White 1995 and White & van Paradijs 1996, Jonker & Nelemans 2004 found that the root-mean-square (rms) value of the height above the Galactic plane of BH-XRBs is similar to that of NS-XRBs, suggesting that BHs could also receive a *high* kick at formation, or even one as high as NSs. In this work, we develop this idea further. We build synthetic populations of BH-

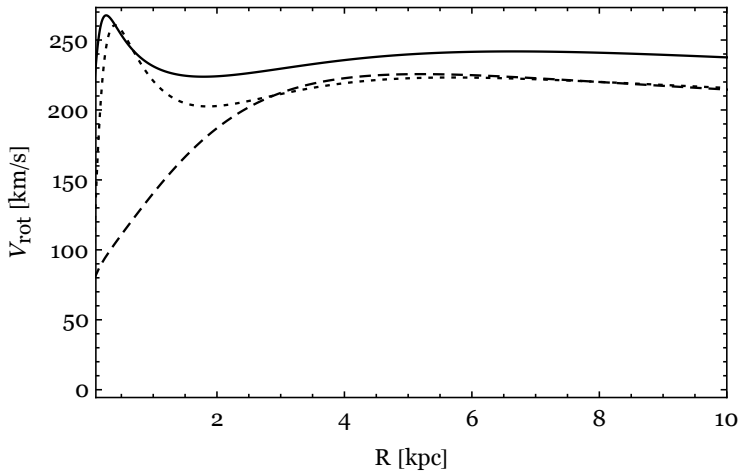

Figure 4.1: Rotation curve for the Galactic potentials used in this work: Bovy 2015 (dashed line), Paczynski 1990 (dotted line), Irrgang et al. 2013 (solid line).

and NS-XRBs and we model their binary evolution and their kinematics in the Galaxy, to investigate whether different assumptions on compact object formation (such as a different distribution for the NK and/or a different amount of mass ejected in the SN) have an imprint on the observed Galactic distribution of BH- and NS-XRBs, and we quantify these effects.

Furthermore, we will dedicate part of this work to discuss a method we previously employed to calculate the minimum peculiar velocity at birth of individual BH-XRBs (Repetto et al. 2012; Repetto & Nelemans 2015). The difference of the Galactic potential value between the observed position (R, z) and its projection on to the Galactic plane was used to analytically derive a lower limit for the peculiar velocity at birth. This method has been recently challenged by Mandel 2016. We investigate how robust our estimate is, i.e. how close this estimate is to the true value of the minimal peculiar velocity at birth, how this estimate scales with the distance from the Galactic centre, and how it varies for different choices of the Galactic potential.

The paper is structured as follows. In Section 4.2 we study our estimate for the peculiar velocity at birth of individual BH-XRBs. In Section 4.3 we build synthetic populations of BH- and NS-XRBs for different assumptions on the compact object formation. In Section 4.4 we look at the Galactic distributions of these synthetic binaries while investigating how they differ, and inferring which NK distribution fits best the observed Galactic position of NS- and BH-XRBs. In Section 4.5 we discuss our findings and in Section 4.6 we draw our conclusions.

4.2 Intermezzo

4.2.1 On the estimate of the peculiar velocity at birth

XRBs are thought to originate from binary progenitors born in the Galactic plane, the birth-place of most massive stars (Brandt & Podsiadlowski 1995). When the compact object forms, the binary typically acquires a peculiar velocity. The mass ejection in the SN imparts a recoil velocity to the binary; the NK adds up vectorially to this velocity, giving the total peculiar velocity of the binary, $\vec{V}_{\rm pec}$. Such a systemic

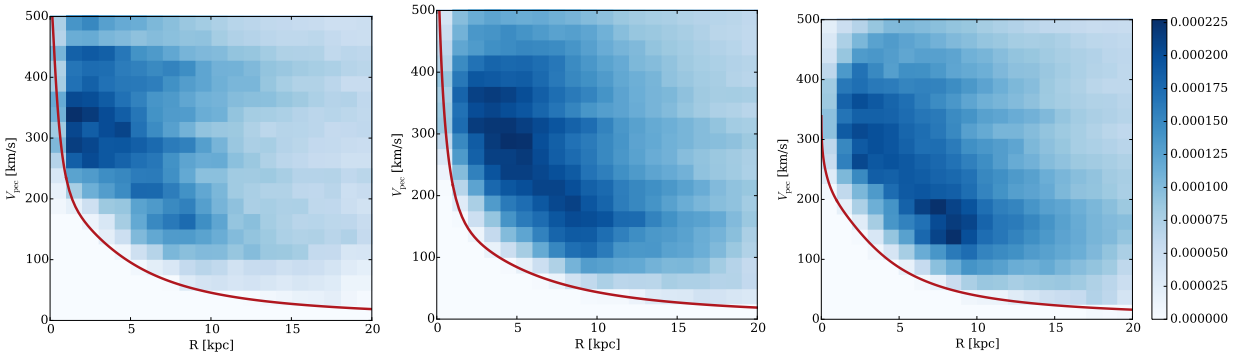

FIGURE 4.2: Density plots showing the fraction of systems in every bin of initial peculiar velocity $V_{\rm pec}$ and distance from the Galactic centre R (projected on to the Galactic plane) of points which reach a height above the Galactic plane greater than 1 kpc. The red line shows our analytical estimate $V_{\rm pec,min}$. We use three different potentials; from left to right: Paczynski 1990, Irrgang et al. 2013, Bovy 2015.

velocity adds up vectorially to the local Galactic rotation and probably has no preferential orientation. The full 3D velocity is measured only for a handful of BH-XRBs (see Miller-Jones 2014). For these, the integration of the orbit backwards in time can in principle provide an estimate for $\vec{V}_{\rm pec}$ at birth. However, uncertainty in the distance and differences in the Galactic potential can prevent a unique determination of the initial position (see e.g. Fragos et al. 2009; Miller-Jones et al. 2009b). When the full 3D peculiar velocity is not known, one can estimate $\vec{V}_{\rm pec}$ at birth using a simple model. For an object located at Galactic height z[1], we expect a trajectory purely perpendicular to the plane to be the one which minimises the initial $\vec{V}_{\rm pec}$. In our previous works Repetto et al. 2012 and Repetto & Nelemans 2015, we estimated the minimum peculiar velocity at birth of a BH-XRB employing energy conservation along such trajectory, and assuming that the maximum height z from the plane is the observed one. We get:

$$V_{\rm pec,min} = \sqrt{2[\Phi\left(R_0, z\right) - \Phi\left(R_0, 0\right)]}, \tag{4.1}$$

where $\Phi\left(R, z\right)$ is a model for the Galactic potential, R_0 is the measured distance of the binary from the Galactic centre projected on to the Galactic plane, and z is the current height above the plane.

Recently Mandel 2016 argued that the difference in the gravitational potential between the observed location and its projection on to the Galactic plane is not an accurate estimate of the required minimum peculiar velocity at birth. He suggests that there are always possible trajectories different from a purely perpendicular one which require a lower $V_{\rm pec}$ at birth than the one estimated through equation 4.1 to reach the same offset from the Galactic plane.

We check the validity of our estimate for the peculiar velocity at birth, $V_{\rm pec,min}$, for high-z sources, performing a Monte Carlo simulation using the Python package for galactic dynamics `galpy`[2] (Bovy 2015). We simulate 1.1×10^7 points, whose initial conditions are set as follows: 1) the initial position is at $(R, z) = (R_i, 0)$, where R_i is uniformly distributed between 0 and 18 kpc; 2) the initial peculiar velocity $V_{\rm pec}$ is uniform between 0 and 500 km/s; 3) the orientation of this velocity is uniformly distributed over

[1]Throughout this work, we use a reference frame centered at the Galactic centre and cylindrical coordinates with R: the distance from the Galactic centre, and z: the height above the Galactic plane.

[2]Available at `https://github.com/jobovy/galpy`

a sphere. We note that since we are only interested in the minimum value of $V_{\rm pec}$, the shape of the assumed velocity distribution is not important. We add the circular motion in the Galactic disc to the 3D peculiar velocity $\vec{V}_{\rm pec}$. We integrate the orbits in the Galaxy for 5 Gyr, using a 4th-order Runge-Kutta integrator, and we check for conservation of energy over the trajectory making sure that the relative error on the energy is less than 10^{-5} at the final step. We record the positions (R, z) 500 times over the orbit sampling from constant time steps, along with the initial peculiar velocity $V_{\rm pec}$. From the simulated points, we select only those ones located at $z^2 > 1$ at the sampled times over the trajectory, to represent high-z sources. We perform the simulation for three different choices of the Galactic potential: model 2 of Irrgang et al. 2013[3] , Paczynski 1990, and the `MWPotential2014` potential from Bovy 2015, which are all multi-component potentials consisting of disc, bulge, and halo. The Paczynski 1990 potential is made up of two Miyamoto-Nagai potentials for disc and bulge, and one pseudo-isothermal potential for the halo. The Bovy 2015 potential is made up of a power-law density profile with an exponential cut-off for the bulge, a Miyamoto-Nagai Potential for the disc, and a Navarro-Frenk-White profile for the halo. The Irrgang et al. 2013 potential is composed of two Miyamoto-Nagai potentials and a Wilkinson-Evans potential for the halo. We show the rotation curve of each of the three potentials in Figure 4.1. Irrgang et al. 2013 is the potential used by Mandel 2016; Paczynski 1990 is the one we adopted in Repetto et al. 2012; the `MWPotential2014` is a realistic model for the Milky Way potential favoured by Bovy 2015. We present the results of this simulation in Figure 4.2. The red line is our estimate for the peculiar velocity taking $z = 1$ kpc in equation 4.1 and it follows the lower edge of the simulated points.

Figure 4.2 shows that our analytical estimate (eq. 4.1) successfully describes the value and trend of the minimal peculiar velocity as a function of the Galactocentric distance.

In order to better quantify the goodness of our estimator $V_{\rm pec,min}$, we compute the ratio $\gamma = V_{\rm pec}/V_{\rm pec,min}$ using 1 kpc-wide bins in R, for those points which reach a height above the Galactic plane along their orbit in the range $|z| = (1, 1.1)$ kpc. The velocity $V_{\rm pec}$ is the actual initial peculiar velocity which we showed in Figure 4.2. We plot γ in Figures 4.3, 4.4, 4.5, for the three different potentials. $V_{\rm pec,min}$ is an excellent estimator for $R > 1$ kpc, since at these radii γ is equal or greater than 1. It is less robust in the inner part of the bulge for the Paczynski 1990 and Irrgang et al. 2013 potentials, but not in the `MWPotential2014` potential, that is fit to the most recent dynamical constraints on the Milky Way and has a more realistic bulge model (Jo Bovy, private communication). In the bulge region, our estimate is steeper than the real minimal peculiar velocity for the first two potentials, i.e., it varies strongly for small variation in R. This can be seen in Figure 4.6, where for every position (R, z) we show as a density map the real minimal peculiar velocity at birth necessary to reach that position. We integrated 10^4 orbits for 5 Gr and using as potential the one in Irrgang et al. 2013. The contour lines show our analytical estimate $V_{\rm pec,min}$; the discrepancy between the two velocities is evident in the inner region of the Galaxy.

Figures 4.3, 4.4, 4.5 also show an increase of the average value of γ with larger distances R. This is an artefact caused by our choice of the $V_{\rm pec}$ initial distribution (uniform between $0 - 500$ km/s).

From our extensive analysis, we find that the estimate $V_{\rm pec,min}$ accurately represents the real minimal value for the peculiar velocity at distances from the Galactic centre $\gtrsim 1$ kpc, and can be safely applied to estimate the peculiar velocity at birth of XRBs born in the Galactic plane.

[3]When referring to the Irrgang et al. 2013 Galactic potential, we will hereafter refer to their model 2.

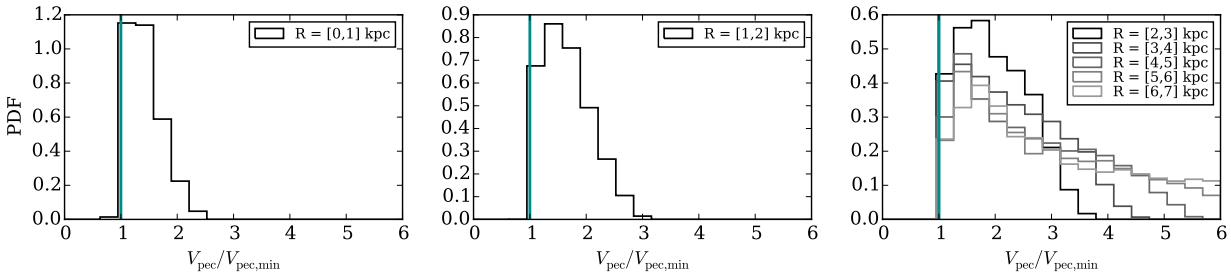

Figure 4.3: Ratio $V_{\rm pec}/V_{\rm pec,min}$ for points such that the observed position is at $1 < z < 1.1$ kpc. Each panel shows a different R-bin. The Galactic potential is from Bovy 2015.

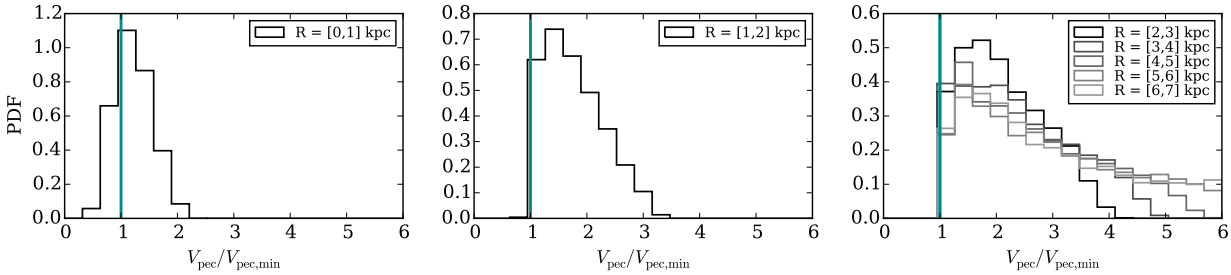

Figure 4.4: Ratio $V_{\rm pec}/V_{\rm pec,min}$ for points such that the observed position is at $1 < z < 1.1$ kpc. Each panel shows a different R-bin. The Galactic potential is from Irrgang et al. 2013.

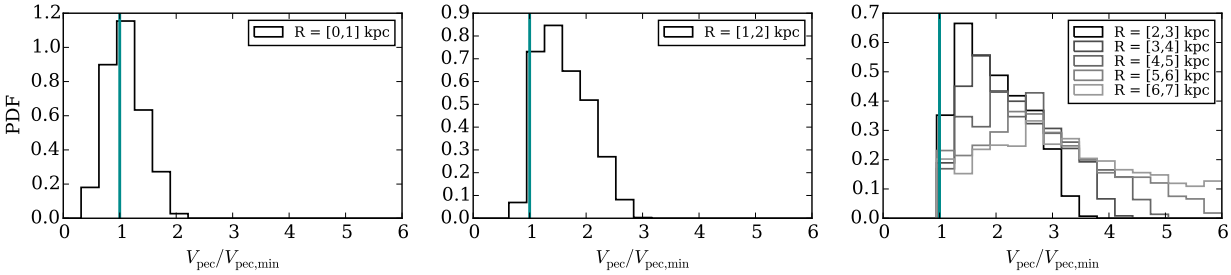

Figure 4.5: Ratio $V_{\rm pec}/V_{\rm pec,min}$ for points such that the observed position is at $1 < z < 1.1$ kpc. Each panel shows a different R-bin. The Galactic potential is from Paczynski 1990.

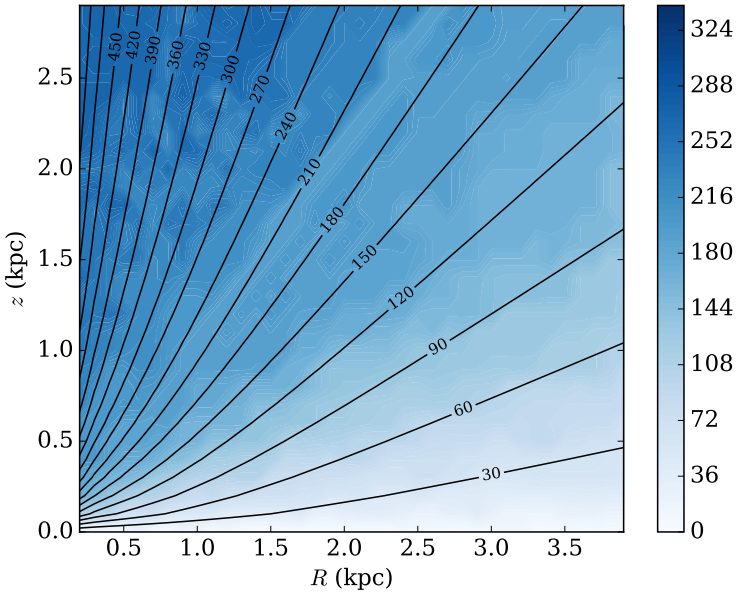

FIGURE 4.6: Density map showing with colour coding the minimal value for the peculiar velocity at birth $V_{\rm pec}$ of simulated points which reach that position (R, z). The contour lines show our analytical estimate $V_{\rm pec,min}$ at that position. The estimate differs strongly from the real value in the bulge region (each solid line differs by ± 30 km/s from the closest-neighbouring one). The potential used is from Irrgang et al. 2013.

4.2.2 Effect of a different choice of the Galactic potential with an application to the observed black hole X-ray binaries

The estimate $V_{\rm pec,min}$ is a function of the potential used, in particular in the bulge, as can be seen in Figure 4.7, where we show $V_{\rm pec,min}$ for the Paczynski 1990, Irrgang et al. 2013 and Bovy 2015 potentials, and assuming $z = 1$ kpc in eq. 4.1. Additionally, from Figures 4.3, 4.4, 4.5, we note that the fraction of systems with $\gamma < 1$ in the region $R = [0, 1]$ kpc also strongly depends on the potential. The minimum values $\gamma_{\rm min}$ are: $1.01, 0.72, 0.61$ for Bovy 2015, Irrgang et al. 2013, Paczynski 1990 potential respectively, where these lower limits are defined such that 95% of the points in the same bin have a value larger than the lower limit.

Figure 4.2 also shows that the Galactic bulge ($R \lesssim 1$ kpc) is much less populated (an order of magnitude fewer systems than in regions at larger distance from the Galactic center). There are two reasons for this: i) the bulge volume is small; ii) it is unlikely for a binary born in the Galactic disc to overcome the strong potential well in its motion towards the Galactic bulge. The inaccuracy of our analytical estimate in the bulge region affects only the source H1705-250, which is the only BH-XRB located close enough to the Galactic centre (see Table 4.2), at $(R, z) \approx (0.5, 1.3)$ kpc (Remillard et al. 1996). Without a measurement of its 3D peculiar velocity, it is impossible to discriminate between a birth in the disc or a birth in the bulge (hence close to its observed position). More in general, bulge sources are not suitable for estimating the peculiar velocities at birth, since the current view on bulge formation is that it was not formed in situ. The bulge population is thought to come from the disc through dynamical instabilities (Gerhard 2015), with most of its mass coming from major and minor merger events with satellite galaxies (De Lucia et al. 2011).

TABLE 4.1: Minimum peculiar velocity at birth for short-period BH-XRBs. The velocities are estimated using three different Galactic potentials and are given in km/s. The numbers in parenthesis for H 1705-250 correspond to correcting the estimates for the inaccuracy of our analytical estimate in the bulge of the Galaxy (see Text).

	$V_{\rm pec,min}$ [km/s]			
Source	Bovy	Pac.	Irrgang	Repetto et al. 2015
XTE J1118+480	62	70	68	72
GRO J0422+32	20	25	22	25
GRS 1009-45	34	40	37	41
1A 0620-00	8	10	8	10
GS 2000+251	12	15	12	15
Nova Mus 91	44	51	46	52
H 1705-250	259 (262)	363 (158)	350 (186)	402
XTE J1650-500	17	21	16	-
XTE J1859+226	61	68	68	-

We compute the minimum peculiar velocity at birth for the seven short-period BH-XRBs studied by Repetto & Nelemans 2015, using the three Galactic potentials (see Table 4.1). We add to this sample two other short-period BH-XRBs which we did not consider in Repetto & Nelemans 2015 (XTE J1650-500 and XTE J1859+226), due to the lack of a strong constraint on the BH mass (Casares & Jonker 2014). For H 1705-250, we put in parenthesis the velocity $V_{\rm pec,min}$ multiplied by the factor γ found above.

We have found an error in the halo component of the Paczynski 1990 potential that we used for the computation of $V_{\rm pec,min}$ in Repetto & Nelemans 2015. This mostly affects the bulge source H 1705-250, whereas the other six sources are not greatly affected (compare third and last column in Table 4.1).

Accounting for the thickness of the Galactic disc instead of assuming a birth place at $z = 0$ does not significantly affect the minimal peculiar velocity (see Belczynski et al. 2016b).

Mandel 2016 used the source H 1705-250 to conclude that the difference in the Galactic potential between the observed position and the projection of this position on to the Galactic plane is not a conservative estimate of the minimal initial velocity of the binary. They show an example of a trajectory for H 1705-250 which starts from the Galactic plane and ends at the observed position for an initial velocity of ≈ 230 km/s, lower than the value provided by eq. 4.1 (see Table 4.1). We agree with his conclusion, but only as far as sources close (or in) the bulge are concerned. On the contrary, for sources located at $R \gtrsim 1$ kpc, our analytical estimate perfectly matches the real minimal velocity. In Repetto & Nelemans 2015 we used the high minimal velocity at birth for XTE J1118+480 and H 1705-250 to claim that at least two out of the seven BH-XRBs we considered were consistent with a high (or relatively high) NK. This holds true with our current revision of the minimal velocities at birth, and we find another BH-XRB that is potentially consistent with a relatively high NK: XTE J1859+226.

The velocities we have been dealing so far with are *minimal* velocities, and do not necessarily correspond to *expected* (*realistic*) velocities. In what follows, we study the latter.

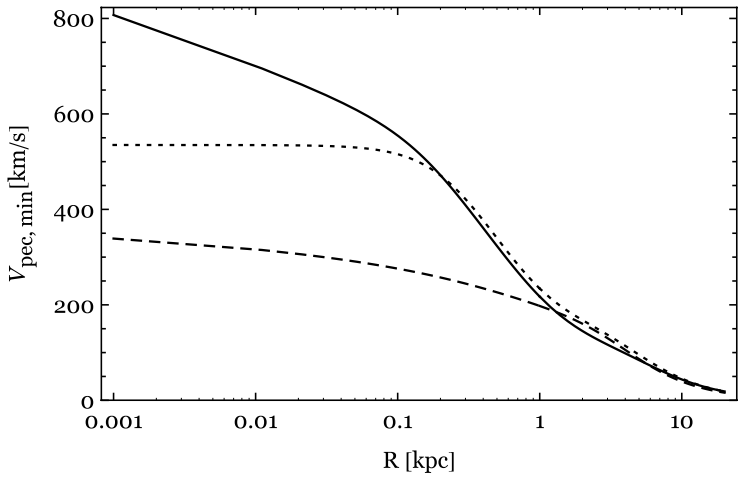

FIGURE 4.7: Analytical estimate $V_{\rm pec,min}$ for the peculiar velocity at birth as a function of the distance from the Galactic centre R (projected on to the Galactic plane) for the three different Galactic potentials used in this work: Bovy 2015 (dashed line), Paczynski 1990 (dotted line), Irrgang et al. 2013 (solid line). We assumed $z = 1$ kpc.

4.3 A Binary Population Synthesis of black hole and neutron star X-ray binaries

In this part of the work, instead of dealing with the minimal peculiar velocities, we deal with the expected peculiar velocities. We perform a binary population synthesis study of short-period ($P_{\rm orb} < 1$ day) BH- and NS-XRBs, starting just before the BH/NS formation, varying the conditions at the formation of the compact object. The goal is to investigate the impact that different BH and NS formation assumptions have on the Galactic distribution of X-ray binaries containing a NS or a BH. We assume that the binaries are formed in the Galactic thin disc, where most of the massive stars reside. In this study, we do not account for the possibility that a few systems could have been formed in the halo (i.e. in star clusters that have now been dissolved), and neither of the possibility that a few systems could have been ejected from globular clusters (GCs) via N-body interactions. GCs seem to be very efficient in producing NS-LMXBs, as 10% of all NS-LMXBs are found in globular clusters, which contain only $\sim 0.1\%$ of all the stars in the Galaxy (Irwin 2005). Such an investigation is, however, outside the scope of this paper.

We take different models for the formation of the compact object. The NK is drawn either from a Maxwellian distribution with $\sigma = 40$ km/s (representing a low-NK case) or from a Maxwellian distribution with $\sigma = 100$ km/s (representing a high-NK case). We assume a certain amount of mass ejection in the SN, $M_{\rm ej}$. BHs are thought to form either via prompt collapse of the progenitor star or via partial fallback of the SN ejecta onto the proto-NS (see Fryer & Kalogera 2001). In our models, the progenitors of BHs either do not eject any mass at collapse, or they eject $4\ M_\odot$. Stars with a ZAMS-mass larger than $\approx 25 M_\odot$ are thought to leave a BH behind (see e.g. Fryer & Kalogera 2001; Tauris & van den Heuvel 2006). For a progenitor of mass $25 - 60\ M_\odot$, the helium core mass (which collapses into a BH) is between $\approx 8 - 11\ M_\odot$ (Belczynski et al. 2008), which motivates our (conservative) choice for $M_{\rm ej}$. For the previous models, we assume a BH mass of $8\ M_\odot$ (which is the typical mass for BHs in our Galaxy; Özel et al. 2010). We also picture a higher-mass helium star ($M_{\rm He} = 15\ M_\odot$) which directly collapses into a

BH with no mass ejection. For NSs, the ejected mass is calculated as: $M_{\rm ej} = M_{\rm He} - M_{\rm NS}$, where $M_{\rm He}$ is the helium core mass ($M_{\rm He} = [2.8-8]\ M_\odot$, see Tauris & van den Heuvel 2006), and $M_{\rm NS} = 1.4\ M_\odot$. For the BH case the models are:

- Model 1: high NK, $M_{\rm He} = 8\ M_\odot$, $M_{\rm ej} = 0$;
- Model 2: low NK, $M_{\rm He} = 8\ M_\odot$, $M_{\rm ej} = 0$;
- Model 3: high NK, $M_{\rm He} = 8\ M_\odot$, $M_{\rm ej} = 4$;
- Model 4: low NK, $M_{\rm He} = 15\ M_\odot$, $M_{\rm ej} = 0$.

For the NS case the models are:

- Model 5: high NK, $M_{\rm ej}$ uniform between $[1.4, 6.6]\ M_\odot$;
- Model 6: low NK, $M_{\rm ej}$ uniform between $[1.4, 6.6]\ M_\odot$.

For all the models, we simulate 3×10^7 binaries composed of the helium star (which core-collapses) and a companion star of $1\ M_\odot$. The pre-SN orbital separation is uniformly drawn in the range $0-50\ R_\odot$ with zero initial eccentricity. We calculate the effect of the compact object formation on the orbital properties and on the kinematics of the binary (for more details on the method, see Repetto & Nelemans 2015). In particular, the effect of the mass ejection together with the NK impart a peculiar velocity to the binary:

$$V_{\rm pec} = \sqrt{\left(\frac{M_{\rm BH}}{M'}\right)^2 V_{\rm NK}^2 + V_{\rm MLK}^2 - 2\frac{M_{\rm BH}}{M'} V_{\rm NK,x} V_{\rm MLK}}, \tag{4.2}$$

where M' is the total mass of the binary after the SN, $V_{\rm NK}$ is the magnitude of the NK, $V_{\rm NK,x}$ its component along the orbital speed of the BH progenitor, and $V_{\rm MLK}$ is the *mass-loss kick*:

$$V_{\rm MLK} = \frac{M_{\rm ej}}{M'} \frac{M_\star}{M} \sqrt{\frac{GM}{a}}, \tag{4.3}$$

the recoil the binary gets because of the instantaneous mass ejection $M_{\rm ej}$ (M is the initial mass of the binary; $M_\star$ is the mass of the companion; a is the initial orbital separation). We follow the evolution of the binaries under the coupling between tides and magnetic braking using the method developed in Repetto & Nelemans 2014, and select those systems that start mass transfer (MT), i.e. become X-ray sources, while the donor is on the main sequence.

We choose the radial distribution of the binaries to follow the surface density of stars in the thin disc: $\Sigma(R) \sim \Sigma_0 \exp(-R/R_{\rm d})$, with $R_{\rm d} \sim 2.6$ kpc (McMillan 2011; Bovy et al. 2012), and with a maximum distance from the Galactic Centre of $R_{\rm max} = 10$ kpc. Concerning the height above the plane, we model it as an exponential with scale height h equal to the scale height of the thin disc ($h = 0.167$ kpc; Binney & Tremaine 2008). This is a conservative choice for the scale height, being the scale height of massive stars in the disc typically smaller ($h \sim 30$ pc; see Table 4 in Urquhart et al. 2014). We assume that the stars follow the Galactic rotation, with no additional component. Encounters of the stars in the disk with spiral density waves cause a velocity dispersion on a timescale of $\sim 5 \times 10^9$ Gyr of 40, 25, 21 km/s in the U, V, W components respectively (Mihalas & Binney 1981). We neglect this influence.

We integrate the orbit of the binaries for 5 Gyr using the `MWPotential2014` potential from Bovy 2015, which is a realistic model for the Milky Way potential. We record the position along the orbit every 5 Myr after 1 Gyr.

Table 4.2: Galactic position of the three classes of BH-XRBs; R is the distance from the Galactic centre, $|z|$ is the absolute value of the height above the plane. In parenthesis we put the uncertainty on the measurements. See Corral-Santana et al. 2016 for the references for the distance measurements.

Name	R (kpc)	$\|z\|$ (kpc)
short-period confirmed		
XTE J1118+480	8.74 (0.1)	1.52 (0.2)
GRO J0422+32	10.38 (0.65)	0.51 (1.15)
GRS 1009-45	8.49 (0.25)	0.62 (0.1)
1A 0620-00	8.93 (0.08)	0.12 (0.01)
GS 2000+251	7.21 (0.3)	0.14 (0.08)
Nova Mus 91	7.63 (0.2)	0.72 (0.1)
H 1705-250	0.53 (2.9)	1.35 (0.85)
XTE J1650-500	5.71 (1.35)	0.15 (0.075)
XTE J1859+226	10.03 (3.05)	1.87 (0.65)
long-period confirmed		
SAX J1819.3-2525 (V4641 Sgr)	2.00 (0.6)	0.52 (0.1)
XTE J1550-564 325.8825	4.96 (0.15)	0.14 (0.05)
GRS 1915+105	6.62 (0.99)	0.03 (0.008)
GS 2023+338 (V404 Cyg)	7.65 (0.001)	0.09 (0.005)
short-period candidates		
MAXI J1836-194	2.08 (1.15)	0.65 (0.25)
MAXI J1659-152	0.82 (1.55)	2.45 (1.05)
XTE J1752-223	2.15 (1.55)	0.22 (0.1)
SWIFT J1753.5-0127	3.64 (0.65)	1.27 (0.45)
4U 1755-338	1.56 (1.8)	0.55 (0.25)
GRS 1716-249	5.62 (0.4)	0.29 (0.05)

4.3.1 Observational samples

4.3.1.1 Black Hole X-ray Binaries

Using the catalogue of Corral-Santana et al. 2016, we classify the systems into three main groups:

1. short-period, dynamically confirmed BH-XRBs (9 systems);
2. short-period, dynamically confirmed BH-XRBs + short-period BH candidates (13 systems);
3. short- and long-period, dynamically confirmed BH-XRBs (15 systems),

which we list in Table 4.2, along with their Galactic position (R, z) derived from their sky-position and distance. Dynamically-confirmed BHs are those for which a dynamical measurement of the BH mass is available (see e.g. Casares & Jonker 2014).

The observed BH-XRBs are both long ($P_{\rm orb} > 1$ day) and short orbital period ($P_{\rm orb} \lesssim 1$ day), thereby originating from different evolutionary paths. Hence, in order to compare the observed systems with the simulated binaries, we need to produce two separate synthetic population of binaries, one population with short-period and one population with long-period, to which we compare the observed binaries according to their type. For the short-period binaries, we follow the binary evolution of simulated binaries using the method we explained in Section 4.3. For the long period ones, which are driven by the nuclear evolution of the donor, we model them assuming the post supernova orbital separation to be such that $a_{\rm circ} = a_{\rm postSN}(1 - e^2) \leq 20\ R_{\odot}$, where $a_{\rm circ}$ is the circularised orbital separation and e is the eccentricity in the post-SN configuration. This assumption is based on the fact that long-period binaries evolve to longer and longer period during the MT phase, hence: $a_{\rm circ} \approx a_{\rm MT,0} < a_{\rm MT,obs}$, where $a_{\rm MT,0}$ is the orbital separation at the onset of MT, and $a_{\rm MT,obs}$ is the observed orbital separation. The assumptions on the compact object formation are the same as for the short-period binaries, as well as the masses of the binary components. Since our simulated binaries have a companion mass of 1 $M_{\odot}$, we exclude from the observed sample those binaries with a companion mass: $\gg 1\ M_{\odot}$ (GRO J1655-40 and 4U 1543-475).

We account for a possible observational bias on the dynamically-confirmed BH-XRBs. In order to get a dynamical measurement of the BH mass, high signal-to-noise optical spectra are required; this might be prevented in regions of high extinctions, i.e. in and close to the Galactic plane. We then remove from our simulated populations those binaries which are located at $z \leq 0.1$ kpc. We note that the lowest z in the sample of short-period dynamically confirmed BH binaries is for 1A 0620-00 ($z \approx -0.12$ kpc; see Table 4.2). For the long-period binaries, we exclude from the study the sources GRS 1915+105 (donor spectral type: K1/5 III) and V404 Cyg (donor spectral type: K0 IV), which are located at $z \approx -0.03$ and $z \approx -0.09$ kpc respectively (see Table 4.2). These two systems do have a dynamical measurement of the BH mass (see Casares & Jonker 2014). In Figure 4.8 we plot the absolute value of the height z versus the spectral type and luminosity class of the 15 dynamically-confirmed BH-XRBs (the spectral types are from Corral-Santana et al. 2016). At small z, stars have an earlier spectral type and/or are giants or sub-giants. Whereas MS/dwarf stars, tend to be seen at larger distances above the plane.

The long-period binaries we consider in our study, after removing those sources close to the Galactic plane, are SAX J1819.3-2525 and XTE J1550-564, which have a current orbital separation of 16 $R_{\odot}$ and 12 $R_{\odot}$ respectively, consistent with our assumption on $a_{\rm circ}$.

4.3.1.2 Neutron Star X-ray Binaries

The Galactic population of NS-XRBs consists of more than 30 objects (see Jonker & Nelemans 2004 and references therein). For our study, we select the 10 ones with a short-orbital period ($P_{\rm orb} < 1$ day; see Table 2 in Jonker & Nelemans 2004). The identification of a NS-XRB typically occurs via the detection of X-ray bursts which ignite on the surface of the NS. Therefore, unlike for BHs, there are potentially no biases against the identification of such systems. Instead, in the BH case, a dynamical mass measurement is necessary to fully confirm the nature of the source, hence dynamically-confirmed BHs are biased towards being in regions of low extinction.

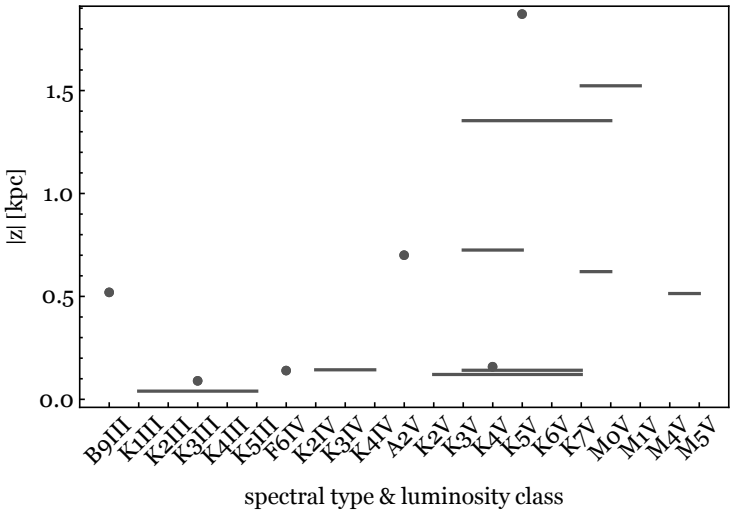

Figure 4.8: The height above the Galactic plane $|z|$ and the spectral type and luminosity class of the 15 dynamically-confirmed BH-XRBs. When the spectral type of the donor star in the system is not univocally identified, we indicate the range of possible types.

4.4 Results of the Binary Population Synthesis

4.4.1 The expected vertical distribution of black hole and neutron star X-ray binaries

The scale height of BH- and NS-XRBs is a proxy to study the effect of different compact object formation mechanisms on to the Galactic distribution of the binaries. We quantity the scale height of the binaries as the rms of their height z as a function of R for all points. To plot the results, we bin the systems into 1 kpc-wide bins in the R-direction. We show the results in Figure 4.9 for the six models. The monotonic rise of $z_{\rm rms}$ is expected, since the Galactic potential becomes weaker further away from the Galactic centre, and the binary moves further up for the same initial velocity. It is interesting to note that if BHs and NSs receive the same NK, they would still show a different scale height, with NSs reaching larger distances from the Galactic plane (compare black solid line with grey solid line, and black dashed line with grey dashed line). This is due to the fact that for the same linear momentum, a binary with a larger mass receives a lower $V_{\rm pec}$ (as is shown in Figure 4.10). If the progenitor of the BH ejects mass at core-collapse as in Model 3 (see black dashed-dotted line in Figure 4.9), it will move further out from the plane than when no mass is ejected, since the mass ejection adds an extra contribution to $V_{\rm pec}$. Furthermore, $V_{\rm pec}$ does not depend on the mass of the BH when no mass is ejected at BH formation (black dashed and black dotted lines in Figure 4.9), since it scales as $V_{\rm pec} = \sqrt{\left(\frac{M_{\rm BH}}{M_{\rm BH}+M_2}\right)^2 V_{\rm NK}^2} \sim V_{\rm NK}$, for low-mass companion stars (see equation 4.2).

In Figure 4.10 we also show as arrows the lower limits on the peculiar velocity at birth of the 9 BH-XRBs we studied in Section 4.2.2. It is clear that a high-NK distribution (darker-grey solid line) more easily accounts for the higher-velocity systems, as 4 systems lie in or beyond the high-velocity tail of the distribution corresponding to the low-NK model.

Jonker & Nelemans 2004 found a similar $z_{\rm rms}$ between NS- and BH-XRBs and deduced that BHs should receive NKs too, unless differences in the binary evolution and observational biases were strong. We confirm that accounting for binary evolution does not strongly change the Galactic distributions of

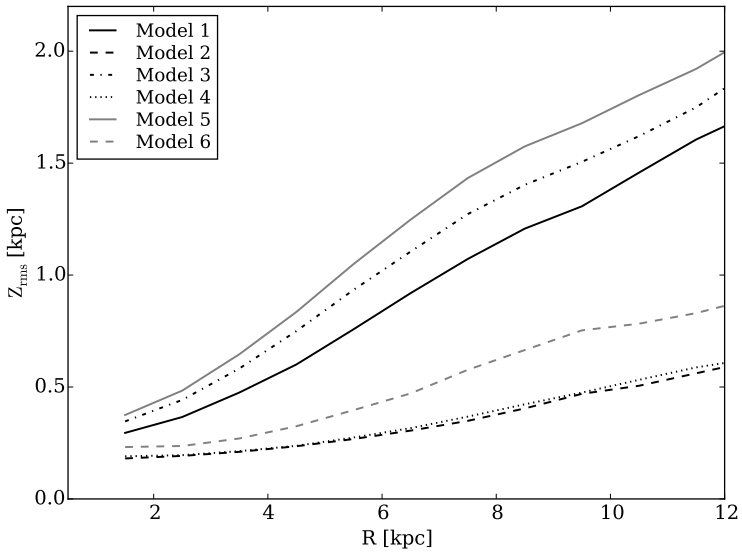

FIGURE 4.9: Root-mean-square of the height z above the Galactic plane of simulated BH- and NS-XRBs for the different models used.

BH- and NS-XRBs. However, the scale height does strongly depend on the position in the disc.

We compute the $z_{\rm rms}$ of the observed BH-XRBs, both of the whole sample and of the dynamically-confirmed systems only. We find a rms of $\approx$ 0.93 kpc and $\approx$ 0.80 kpc respectively. For the NS systems, we calculate a $z_{\rm rms}$ of 1.24 kpc, when excluding the source XTE J2123Đ058 since its velocity is consistent with being a halo source, as Jonker & Nelemans 2004 noted. In Figure 4.11 we show the Galactic distribution of NS and BH systems (the lines account for the uncertainty in the distance to the source). The result that NS systems should have a larger scale height than BH systems is consistent with what the observed populations show.

4.4.2 The influence of the orbital separation distribution of the binary progenitors

In the models we used in Section 4.3, the orbit of the binary progenitors of BH- and NS-XRBs was chosen to be uniformly distributed in the range $[0, 50]$ $R_\odot$. It could be that this choice biases our results towards certain values for $V_{\rm pec}$. To test this, we check how the distribution of the initial orbital separation of the binaries (i.e. prior to the formation of the compact object) varies with the magnitude of the NK and of $V_{\rm pec}$. From Figure 4.12, it is clear that the majority of the initial orbital separations are constrained to lie within a small range ($a_{\rm preSN} \lesssim 10\ R_\odot$) both for NS and BH systems, and both for high and low NKs. Furthermore, there is no clear trend of $V_{\rm pec}$ with respect to $a_{\rm preSN}$. We hence conclude that it is unlikely that the peculiar velocities $V_{\rm pec}$ would be very much influenced if the pre-SN orbits had a distribution different from the uniform one we use in our study, or if they were drawn from a smaller range.

4.4.3 Comparison with observations: black hole X-ray binaries

We now turn to the comparison of the different models with the observed BH-XRBs. In order to compare the simulations with the observed systems, we note that every subgroup of BH binaries of Table 4.2 gives rise to a certain 2D distribution in R and z. One way of proceeding would be to

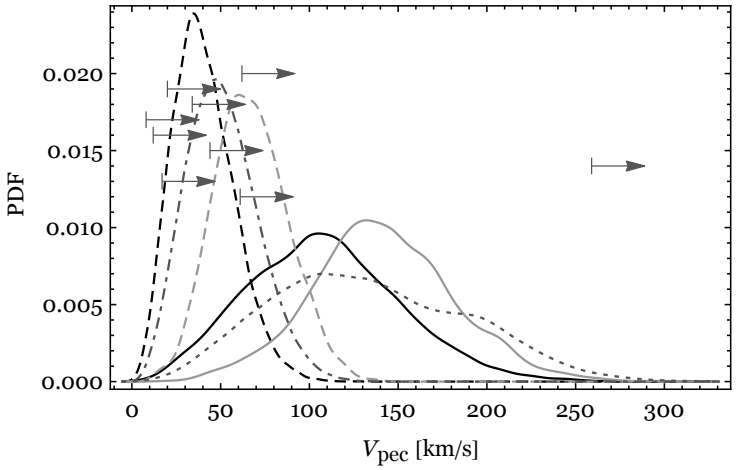

Figure 4.10: Distribution of the peculiar velocity $V_{\rm pec}$ (after the formation of the compact object) of BH-XRBs in Model 1 (black solid line) and Model 2 (black dashed line), and of NS-XRBs in Model 3 (grey solid line) and Model 4 (grey dashed line). The dotted and dotted-dashed dark-grey lines are variations of Model 1 (see Section 4.5 for details). The arrows represent the lower limits on the peculiar velocity at birth for the 9 short-period BH-XRBs using the potential from Bovy 2015.

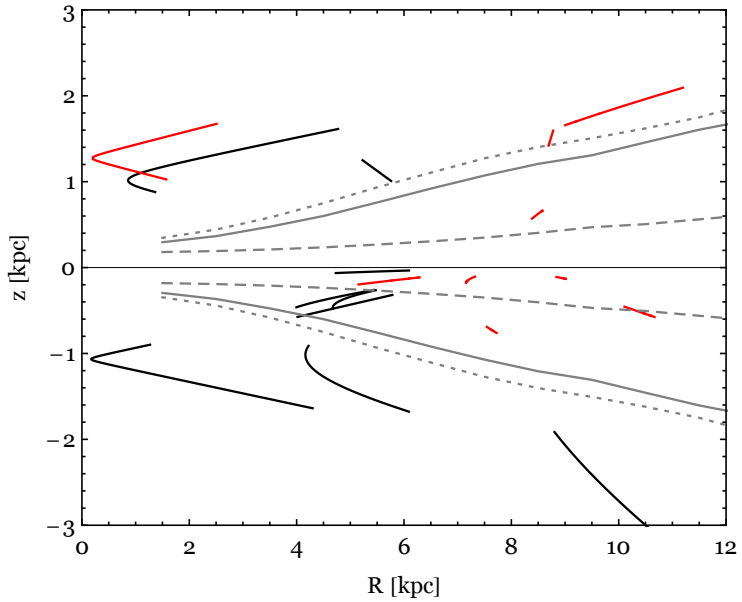

Figure 4.11: Galactic distribution of BH-XRBs (red lines) and NS-XRBs (black lines). R is the distance from the Galactic center projected on to the plane, and z is the height above the plane. One NS-XRB falls off the figure: XTE J2123-058. For each source, the line accounts for the uncertainty on the distance. We also show the results from the population study in terms of $z_{\rm rms}$ as a function of R: model 1 (grey lines), model 2 (grey-dashed lines), model 3 (grey-dotted lines).

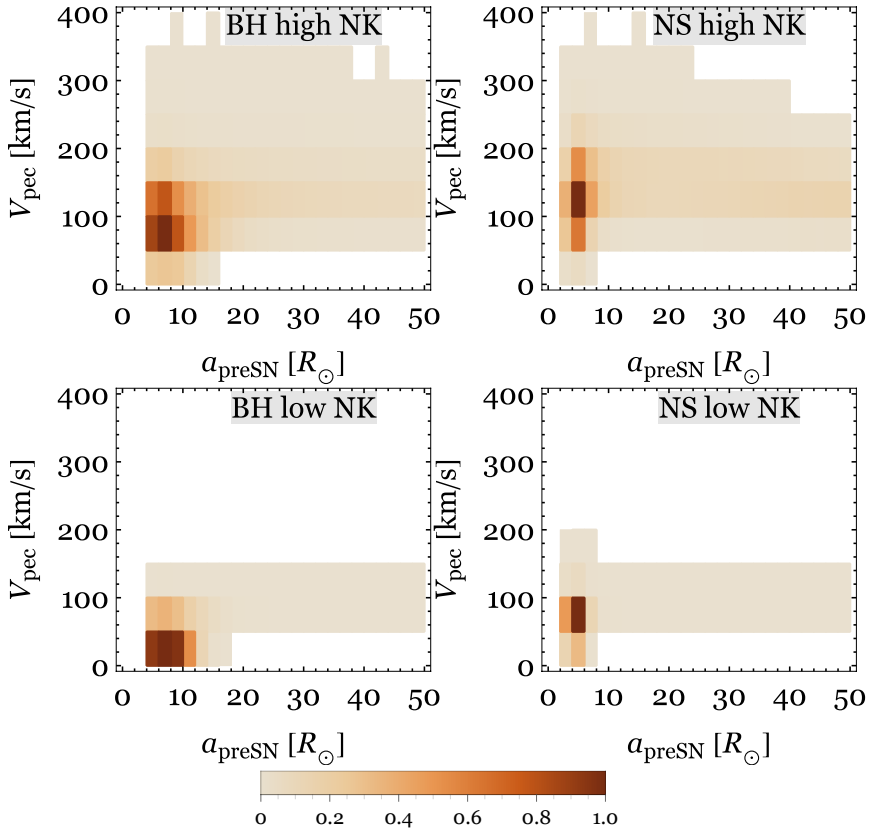

Figure 4.12: Density plots showing the allowed parameter space for the peculiar velocity at birth $V_{\rm pec}$ and the orbital separation $a_{\rm preSN}$ of BH- and NS-XRBs prior to the formation of the compact object. Each panel corresponds to different assumptions on compact object formation. Darker colours correspond to a larger density of systems.

Table 4.3: D-values of the KS-test for different systems and in the different models: high NK, low NK, and a model made of a superposition of the high- and low-NK in equal parts.

Subgroup	High NK D (P)	Low NK D (P)	50-50 D(P)	N	Fig.
BH-XRBs, short P., confirmed	0.26 (0.57)	0.34 (0.24)	0.19 (0.92)	8	4.14
BH-XRBs, short P., confirmed + candidate	0.20 (0.61)	0.39 (0.03)	0.28 (0.22)	13	4.15
BH-XRBs, short and long P.	0.27 (0.39)	0.35 (0.14)	0.21 (0.75)	10	4.16
BH-XRBs, whole sample	0.22 (0.43)	0.40 (0.01)	0.29 (0.12)	15	4.17
NS-XRBs	0.39 (0.06)	0.63 (0.00)	-	10	4.18

compare the 2D simulated distribution with the 2D observed one. However, we do not know what is the real R-distribution of the binaries, whether it follows the density of stars in the disc or not. Hence we compare the data with the simulated populations dividing the Galaxy into 1 kpc-wide bins along the R-direction. This also allows to account for the fact that the Galactic potential is a strong function of the position in the disk, as we showed in Section 4.2.2. For every R-bin, we compute the cumulative distribution function (CDF) of the height z above the Galactic plane based on the population synthesis results within Model 1 and Model 2 (see as an example black and grey lines in Figure 4.13, for the bin: $R = [8, 9]$ kpc). Then we calculate where in the cumulative distribution the observed systems lie (see as an example the intersection between the blue vertical lines and the CDFs in Figure 4.13). In such a way, we obtain a list of percentiles. If the model is correct, we expect these percentiles to be drawn from the uniform distribution. We note that we have removed from our comparison those sources located in the bulge of the Galaxy (i.e. H 1705-250 and MAXI J1659-152), which could have had a different origin rather than having formed in the plane (see Section 4.2.2). We plot the cumulative distribution of these percentiles in Figures 4.14, 4.15, 4.16. Each figure corresponds to one of the subgroups of binaries we previously listed; the solid lines correspond to Model 1 and the dashed lines correspond to Model 2. We also consider a model which consists of a superposition of Model 1 and Model 2 in equal parts (see thin solid in Figure 4.14, in the case of the short-period confirmed BH-XRBs). The model which fits best is the one which comes closer to the diagonal line (that represents the cumulative of a uniform distribution). In all three cases, a high NK distribution is the best-fit one.

We perform a Kolmogorov-Smirnov (KS) test to measure how close is the distribution of percentiles to the diagonal line of Figures 4.14, 4.15, 4.16. We summarise the D-values and their corresponding probabilities in Table 4.3 for every subgroups of BH-XRBs. For each of the sub-groups the high-NK model fits the data best, although in the two groups with confirmed BHs only, the low-NK is also consistent with the data. Only for the combination of confirmed and candidate systems, the low-NK model is inconsistent. Interestingly, the model in which the BHs receive both low and high NKs, fits the data best for the confirmed systems (both short-period and long+short period).

We also make the comparison between observations and simulations for the whole sample of BH-XRBs, when combining the three classes, and we show the results in Figure 4.17 and the KS-test statistics in Table 4.3.

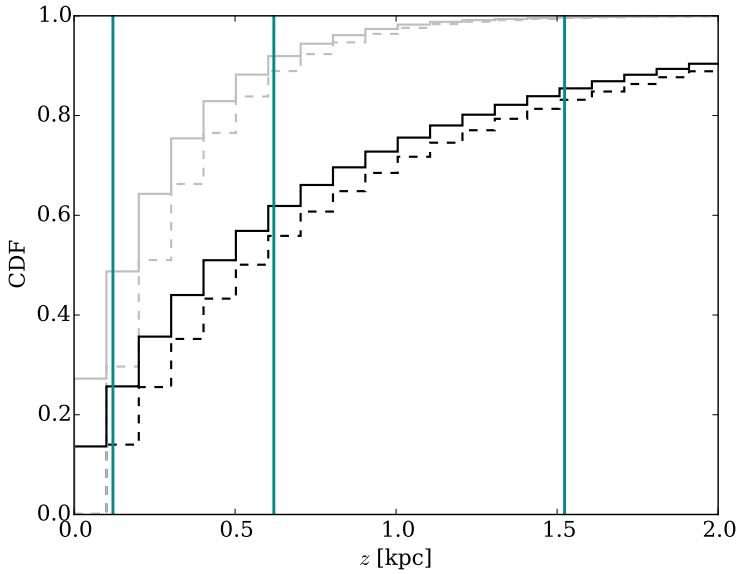

Figure 4.13: The cumulative distribution for $|z|$ for Model 1 (black lines) and Model 2 (grey lines), in the bin $R = [8, 9]$ kpc. Solid lines correspond to the whole sample of simulated binaries; dashed lines correspond to the remaining part of the sample after the exclusion of systems close to the Galactic plane, i.e. $z \leq 0.1$ kpc. The blue vertical lines represent the observed $|z|$ of 3 BH-XRBs (from left to right: 1A 0620-00; GRS 1009-45; XTE J1118+480).

4.4.3.1 Effect of the distance uncertainty

The distance d to a BH-XRB is typically estimated by measuring the apparent magnitude of the companion star in a certain colour band, and computing its absolute magnitude. Once an estimate of the reddening towards the source is known and the spectral type of the donor star is clearly identified, the distance can be calculated. In the best case scenario, one would have the apparent magnitude of the source in different bands, and then would compute the scatter between the derived distances as estimate of the distance uncertainty. We expect such uncertainties to follow a Gaussian distribution. However, in case a range of spectral types is equally probable, we expect the errors on the distance to be distributed more uniformly. To investigate the influence of the uncertainty in the distance, and since for most of the literature there is no easy way of determining the type of error distribution, we randomly generate 100 values for the distance to each BH-XRB, either distributed as a Gaussian (with σ equal to the distance uncertainty δ) or as a uniform distribution in the range $(d - \delta, d + \delta)$. Such errors can cause a binary to move from one R-bin to the adjacent one, affecting the percentile values. However, we find that there is no systematic shift that would make low NKs fit best the observed data, δ being smaller than the discrepancy between the two distributions.

4.4.4 Comparison with observations: neutron star X-ray binaries

. We compare the observed z distribution of NS systems with the distribution of the two simulated population of NS-XRBs in the context of Model 5 and Model 6. We perform the comparison in the same way we did for BH-systems in Section 4.4.3. From Figure 4.18 we see that none of the distributions (solid and dashed lines) fits the data. Our goal is not to calibrate the NS NK distribution from the NS-XRB population, nor from a population model of radio pulsars (cf. Hartman et al. 1997), but we

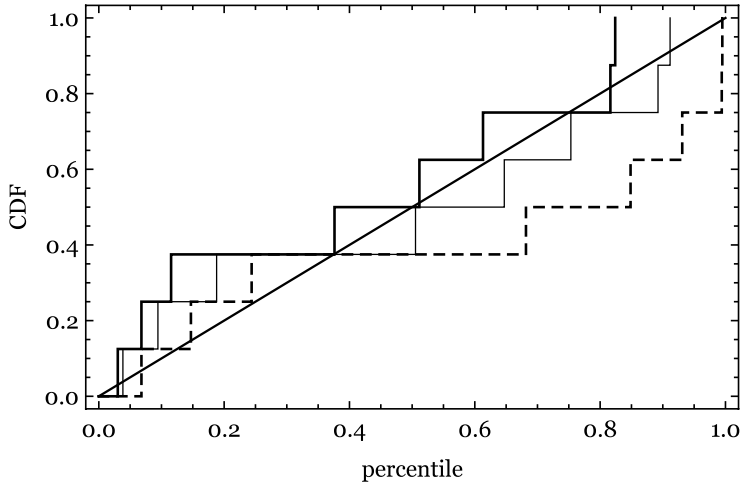

Figure 4.14: Cumulative distribution of the percentiles associated with short- period dynamically-confirmed BH-XRBs in Model 1 (solid line) and Model 2 (dashed line). The thin solid line is a blend of Model 1 and 2 ($50 - 50\%$). The model which fits best the observed data is the one closer to the diagonal line.

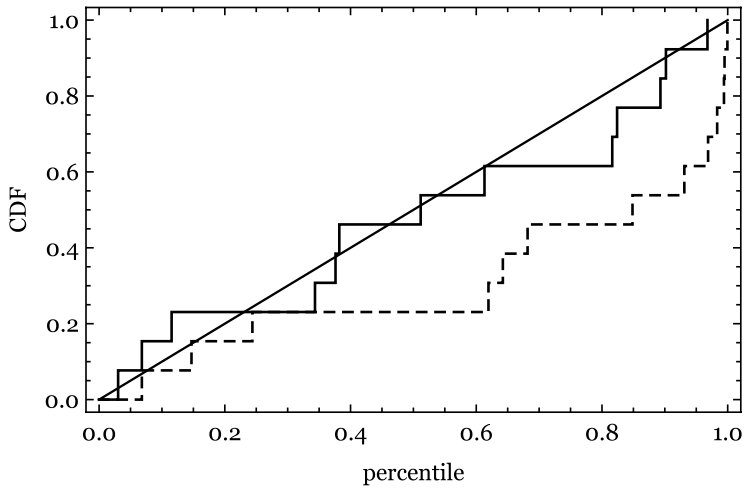

Figure 4.15: Cumulative distribution of the percentiles associated with short- period dynamically-confirmed and candidate BH-XRBs in Model 1 (solid line) and Model 2 (dashed line). The model which fits best the observed data is the one closer to the diagonal line.

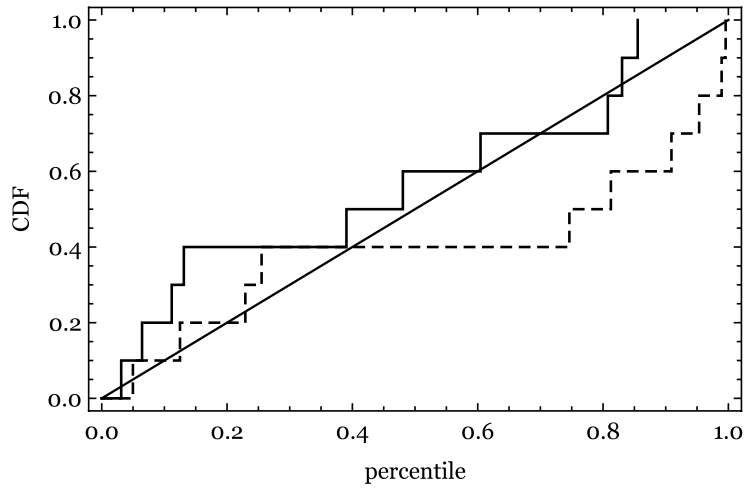

Figure 4.16: Cumulative distribution of the percentiles associated with short and long period dynamically-confirmed BH-XRBs in Model 1 (solid line) and Model 2 (dashed line). The model which fits best the observed data is the one closer to the diagonal line.

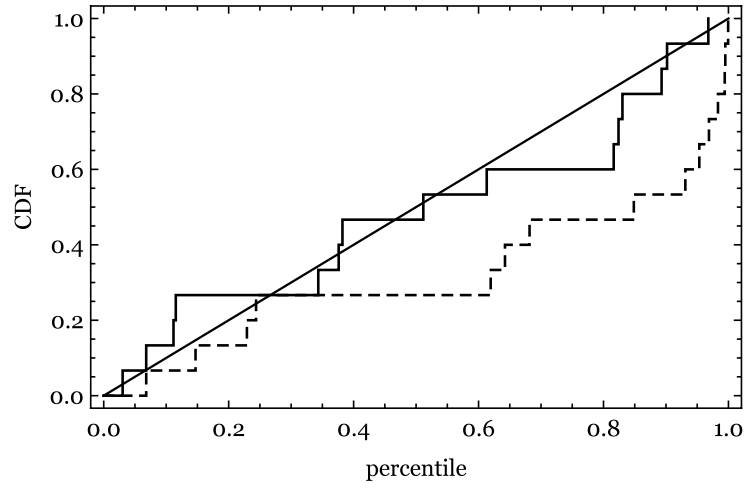

Figure 4.17: Cumulative distribution of the percentiles associated with the whole sample of BH-XRBs in Model 1 (solid line) and Model 2 (dashed line). The model which fits best the observed data is the one closer to the diagonal line.

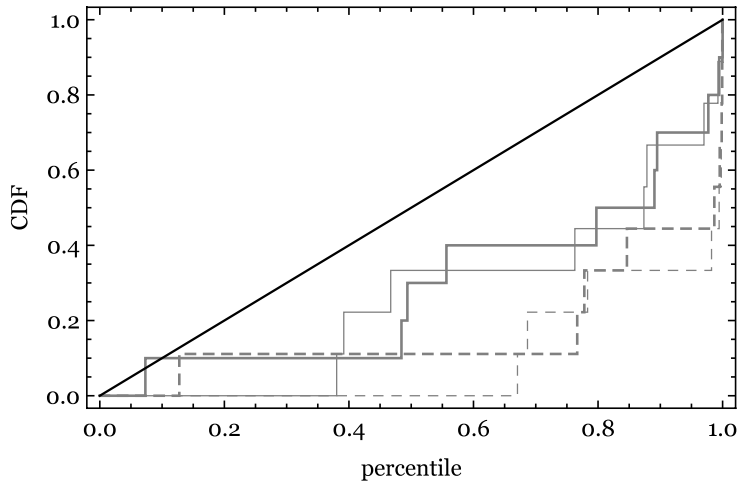

Figure 4.18: Cumulative distribution of the percentiles associated with short- period NS-XRBs in Model 5 (solid line) and Model 6 (dashed line). We also show the effect of removing from the study the only observed source located in the Galactic plane (thin solid and thin dashed lines). The model which fits best the observed data is the one closer to the diagonal line.

anyhow wish to note that the observed population of NS-XRBs seems to be consistent with NKs larger than $\approx$ 100 km/s. This is in line with the catalogue of pulsar proper motions by Hobbs et al. 2005, who inferred a mean pulsar birth velocity of $\approx$ 400 km/s. However, the derivation of pulsar velocities from the measured proper motions has to be taken with caution, because of the possible uncertainties in the proper motion measurements as well as in the distance measurements. More in general, underestimating proper motion measurement errors can lead to an overestimate of pulsar velocities, as noted by Hartman 1997. The distance to a pulsar is typically estimated through parallax. Igoshev et al. 2016 showed that a more proper Bayesian approach to calculate the distance probability function from a single parallax measurement has to be used. Such method has not been applied yet to the whole population of pulsars.

We show the results of the KS-test for NS systems in Table 4.3: both models have large D-values.

We also show the effect of a potential bias for low-z systems by removing all points with $|z| < 0.1$ kpc from the simulation and removing the only source which is located in the Galactic disc at $z < 0.1$ kpc (4U1608-522; solid thin and dashed thin lines in Figure 4.18).

4.5 Discussion

1. In our models of Section 4.3, We have assumed an ejected mass at BH formation of 0 or 4 $M_\odot$. Taking $M_{\rm ej} = 8\ M_\odot$ would not greatly affect the scale height of the binaries in the case of a high NK distribution, since the typical peculiar velocities are comparable to the case when 4 $M_\odot$ are ejected (see dotted line in Figure 4.10). This is due to the fact that a high ejected-mass is compatible only with the lower-velocity tail of the NK distribution in order for the binary to stay bound. In the case of a low NK distribution, the higher ejected-mass has a greater effect on the average peculiar velocity (see dashed-dotted line in Figure 4.10). However, the NS systems velocities are still larger. In order for BH systems to have the same peculiar velocity as NS systems,

we would need that $V_{\rm MLK,BH} = V_{\rm MLK,NS} + (1/2) \times V_{\rm NK}$, which follows from the expression for $V_{\rm pec}$ (equation 4.2), imposing that $V_{\rm pec,BH} = V_{\rm pec,NS}$ and assuming that $V_{\rm NK,x} = V_{\rm NK}$. This would constraint $M_{\rm ej}$ to be much larger than what is allowed for the binary to stay bound.

2. In the modelling of the progenitors of BH- and NS-XRBs, we assumed a flat initial orbital separation between $[0, 50]$ $R_\odot$ (Section 4.3). In Repetto & Nelemans 2015 we verified that larger separations do not contribute to the final separation of the binary (see their Figure 13). This is due to the fact that the coupling between tides and magnetic braking, which is responsible for the shrinking of a binary to short $P_{\rm orb}$, decreases strongly with larger orbital separations. In the long-period BH-XRB case, this choice is also acceptable, as none of the observed binaries in our sample have an orbital separation larger than 50 $R_\odot$. There could be of course cases in which the orbit in the post-SN phase is highly eccentric and very wide, but these cases would contribute only to a minority of the systems. Furthermore, we have proved that the peculiar velocity of the systems would not be affected if the orbital separation was drawn from a smaller range (see Figure 4.12).

3. We have assumed that the companion of BHs and NSs are stars with an initial mass of 1 $M_\odot$. Pfahl et al. 2003 argued that the majority of LMXBs have likely originated from binaries with an intermediate mass companion ($\approx 2 - 3$ $M_\odot$). We have checked how our results would be affected when taking a companion of initial mass: 3 $M_\odot$. The peculiar velocity right after the BH formation (see Figure 4.10) would decrease due to the larger binary mass: by a factor of ≈ 1.5 on average. This implies that the NK would need to be even larger in order for the simulated systems to match the observed ones.

4. The two Maxwellian distributions used in Section 4.3 do not correspond to the real physical distributions, but rather are representative of two complementary distributions, one generating large kicks, the other generating low kicks. The choice of two distributions peaked at two different velocities serves the purpose of analysing how close in magnitude are the velocities received by BHs with respect to the velocities received by NSs. The NK distribution of NSs can be estimated via proper motion studies of pulsars. The pulsar birth speed distribution has been estimated as a Maxwellian distribution with $\sigma = 265$ km/s by Hobbs et al. 2005; however, one should bear in mind the caveats discussed in Sec. 4.4.4. For BHs, the number of sources with measured 3D space velocity (5; see Miller-Jones 2014) is not sufficient to allow for a calibration of their NK distribution.

5. When comparing the observed BH-XRBs with the synthetic BH-XRBs which result from our population synthesis, we found that the population in which BHs receive high NKs best fit the observed data. This conclusion gains strength when including in the comparison between observations and simulated population the sources located in the bulge of the Galaxy (i.e. H 1705-250 and MAXI J1659-152). In this case, the KS-values for the short-period confirmed BH-XRB sample are: $(D, p)_{\rm highNK} = (0.22, 0.74)$, $(D, p)_{\rm lowNK} = (0.40, 0.08)$, and for the short-period confirmed + candidates BH-XRB sample are: $(D, p)_{\rm highNK} = (0.28, 0.15)$, $(D, p)_{\rm lowNK} = (0.46, 0.00)$. When including the simulated binaries in the Galactic plane to our comparison, the high-NK case becomes stronger for the short-period confirmed BH-XRB sample. The KS-test values become: $(D, p)_{\rm highNK} = (0.16, 0.98)$, $(D, p)_{\rm lowNK} = (0.39, 0.13)$.

6. For an illustrative purpose, we also compare the observed population of NS-XRBs to a simulated one in which the NK is drawn from a Maxwellian distribution with $\sigma = 265$ km/s (Hobbs et al. 2005). The results of the KS test favours this distribution with respect to the two we took in our study: $(D, p)_{\rm Hobbs} = (0.21, 0.72)$.

4.5.1 A note on our Kolmogorov-Smirnov test

In assessing the quality of the fit of our simulations, we used the classical application of the KS-test. In order to test its validity and determine the *power* of the test in distinguishing the two hypothesis we draw samples of various sizes from the simulated populations, and we calculate the D-value distribution of each of these samples, according to the rules described in Section 4.4.3. We find that the probabilities follow the classical KS test (as expected) to an accuracy (5%) that is comparable to the Poisson noise in our simulations ($\approx 3\%$). More interesting is the measurement of how often we obtain D-values smaller then the ones we measured for our observed samples when *testing the wrong hypothesis* - i.e. when using a sample drawn from the high (low) NK synthetic population and testing the low (high) NK hypothesis (also known as false negative rate). For the BH case, we find D-values smaller than the ones in Table 4.3 in less than $\beta \approx 10\%$ of the cases, for the high NK hypothesis, and in more than $\beta \approx 30\%$ for the low NK hypothesis. A particularly interesting fact is that $\beta = 0.015$ for short-period confirmed + candidate BH-XRBs. If we accept the $\alpha = 3\%$ confidence level and use the standard 4-to-1 weighting (i.e. $4\alpha = \beta$), the test we developed has enough power to distinguish between the high- and low-NK hypothesis in this case, and that the high-NK hypothesis is clearly preferable. This is a *non*-expected result given the small number of object, and it can potentially dissolve if some of the BH candidates turn out to be NS-XRBs. To calculate what is the optimal number of observed systems to decrease such rate β, we draw samples of various sizes from the population synthesis results of Model 1 and we test the low-NK hypothesis, and vice-versa. To decrease this rate to the level that in 95% of cases we obtain $\beta < 1\%$, we find that it is necessary to increase the size of the observed sample to ≈ 40 systems, both in the BH and NS case.

4.6 Conclusions

In this work we performed a binary population synthesis study of BH and NS X-ray binaries, tracing their binary evolution from the moment of compact object formation until the observed phase of mass transfer, and integrated their orbits in the Galaxy. The main goal was to investigate whether different assumptions on compact object formation manifest themselves in the Galactic distribution of the binaries. We found that these assumptions do affect the scale height of the binaries, which we quantified through their $z_{\rm rms}$. In particular, we found that if BHs and NSs receive the same NK at birth, NSs would still have a larger scale height above the Galactic plane, due to the fact that their systemic velocities acquired when the compact object is formed are typically larger, their total binary mass being smaller. The larger scale eight of NS-XRBs with respect to BH-XRBs is clearly seen also in the observed populations. We also found a clear trend for both populations of increasing scale height for larger Galactocentric radii, which should manifest itself, but which is not clearly observed in the current populations (see Figure 4.11).

The main outcome of this study is that when analysing the z-distribution of the observed BH systems as a function of R, the simulated population in which at least some BHs receive a (relatively) high NK (~ 100 km/s) fits the data best. This is in agreement with previous findings by Repetto et al. 2012, who compared the observed and simulated populations of BH-XRBs only in the z-direction, whereas we compare the 2D distributions, accounting for how the binaries are distributed along the R-direction as well. Furthermore, we increased the sample of sources adding 6 BH candidates, updated their distances according to the recently published BH catalogue of Corral-Santana et al. 2016, and followed the binary evolution of the binaries in a detailed way (accounting in particular for magnetic braking and tides).

In this work we also checked numerically the validity of a simple one-dimensional analytical estimate for the peculiar velocity at birth of BH-XRBs which we used in our previous works Repetto et al. 2012 and Repetto & Nelemans 2015. We found that this estimate is less reliable for some gravitational potentials for sources in the bulge of the Galaxy, i.e at $R \leq 1$ kpc. This was also shown by Mandel 2016, who studied the kinematics of H 1705-250, a BH-XRB close to the Galactic bulge. However, the estimate is very robust for systems at Galactocentric radii larger than 1 kpc. Repetto & Nelemans 2015 followed the binary evolution of seven short-period BH-XRBs and estimated their minimal peculiar velocity at birth, to conclude that two out of the seven sources were consistent with a high (or relatively high) NK at birth. This conclusion remains valid even in view of the current analysis.

Jonker & Nelemans 2004 found that the rms-value of the distance to the Galactic plane for BH-XRBs was consistent with that of NS-XRBs. This was suggestive for BHs receiving a kick-velocity at formation. We revised the distances and updated the sample of BH-XRBs using the catalogue from Corral-Santana et al. 2016 and we found that NS systems have a larger scale height than BH systems, a trait which is also present in the simulated populations.

Finally, we find that the comparison of the data to our simulations is limited by the small number of observed BH- and NS-XRBs, and thus that more systems should be found to determine in more detail the NK that BHs receive. In this respect, the possible future discovery of new BH transients with Gaia (Maccarone 2014), and through dedicated surveys such as the Galactic Bulge Survey (Jonker et al. 2011), is promising.

4.7 Acknowledgments

SR is thankful to Jo Bovy for answering her questions concerning Galpy and for useful comments on the manuscript. SR wishes to warmly thank her office mates (Pim van Oirschot, Martha Irene Saladino, Laura Rossetto, Thomas Wevers) at Radboud University for their great moral support during the hectic times of finishing up her thesis. SR wishes to acknowledge Melvyn B. Davies with whom she started her research on black hole natal kicks. This research has made use of NASA's Astrophysics Data System.

Chapter 5

Follow-up observations of the Galactic Bulge Survey source CX1004: a candidate Black Hole X-ray Binary

S. Repetto, M.A.P. Torres, T. Wevers, M. Heida, G. Nelemans, P.G. Jonker, L. Wyrzykowski, C.T. Britt, C.O. Heinke, R.I. Hynes, C.B. Johnson, T.J. Maccarone

to be submitted

Abstract

We report on optical and near-infrared observations of the X-ray source CXOGBS J174623.5-310550 (hereafter CX1004), that due to the large broadening of the Hα emission line is a candidate black hole X-ray binary. Analysis of three nights of spectroscopy with X-shooter supports an M2 spectral classification for the optical counterpart which shows no sign of radial velocity variations. In addition, the M2 star contributes $\approx$ 90 per cent to the total light and show no sign of rotational broadening. The variations in the I-band OGLE light curve and between the r-band Mosaic-II/DECam light curves also show evidence for a disc contribution to the overall light at the level of several tens of a per cent. These results could imply that the proposed optical counterpart is a chance line of sight interloper or that CX1004 is part of a hierarchical triple hosting a black hole system or a cataclysmic variable (CV), with the M-type star in a wide (0.2 kpc) orbit around the inner binary. Optical imaging does not show a significant positional offset between the I-band and B-band counterparts ($<$ 0.06 arcsec) and between the i'-band and Hα narrow-band counterparts ($<$ 0.04 arcsec). We also identify a $K = 16.6 \pm 0.2$ mag infrared counterpart; from the I $-$ K $= 2.7$ colour, we estimate a reddening of $A_{\rm I} \approx 0.93$, which translates into a distance of 1.2 kpc for an M2V star. We calculate an expected K_2 of $\approx$ 520 km s^{-1} in the BH case and of $\approx$ 377 km s^{-1} in the CV case, from the correlation between the full width at half maximum of the Hα line and K_2 of Casares 2015. Another correlation between the

binary mass ratio q with the ratio of the double peak separation to the full width at half maximum of the Hα line of Casares 2016, delivers $q = 0.05 \pm 0.01$ in the case of a BH and $q = 0.23 \pm 0.04$ in the case of a CV.

5.1 Introduction

Interacting binaries containing compact objects provide a means to study the physics of accretion as well as the evolution of stars (in binaries), and in particular the formation of their compact remnants: white dwarfs (WDs), neutron stars (NSs), or black holes (BHs). BHs can be used as laboratories to study the physics of accretion (see e.g. Remillard & McClintock 2006) and general relativistic effects in the strong-field regime (see e.g., Wex & Kopeikin 1999; Narayan et al. 2002; Remillard & McClintock 2006; Bambi 2012). Furthermore, the measurement of the orbital decay in X-ray binaries containing a BH may be used to set constraints on alternative theories of gravity (see e.g., González Hernández et al. 2014; Johannsen et al. 2009). In order to enlarge the sample of interacting binaries in a systematic way, the Galactic Bulge Survey (GBS, Jonker et al. 2011; Jonker et al. 2014) was performed, covering twelve square degrees towards the bulge with X-ray, optical, infrared and radio studies. Earlier results of the GBS have been reported in Maccarone et al. 2012; Ratti et al. 2013; Britt et al. 2014; Hynes et al. 2014; Johnson et al. 2014; Wevers et al. 2016.

Black-hole low-mass X-ray binaries (BH-LMXBs) in quiescence are the optimal tool to measure BH masses through phase-resolved spectroscopy of the light coming from the donor star. In practice, a lower limit on the mass of the BH can be determined once the orbital period and the radial velocity semi-amplitude of the companion star are known (see e.g. Charles & Coe 2006). The current Galactic population of stellar-mass BHs amounts to 18 objects with a dynamical mass measurement (Casares & Jonker 2014; Corral-Santana et al. 2016). Increasing the sample of BHs is of great importance for three main reasons. Firstly, different supernova models predict a different BH mass distribution (Fryer & Kalogera 2001; Belczynski et al. 2012; Fryer et al. 2012; Ugliano et al. 2012). Secondly, increasing the sample of BHs with measured space velocity would help in the long debate on the type of natal kicks received by BHs at formation (Jonker & Nelemans 2004; Miller-Jones 2014; Repetto & Nelemans 2015; Repetto et al. 2016). Thirdly, the comparison between the observed number of BH-LMXBs and the predicted number from population synthesis models, would help in unraveling the physics involved in the formation and evolution of these sources (Romani 1992; Portegies Zwart et al. 1997; Kalogera & Webbink 1998; Pfahl et al. 2003; Belczynski & Taam 2004; Yungelson et al. 2006; Kiel & Hurley 2006).

In this Paper, we present the optical and infrared study of the X-ray source CXOGBS J174623.5-310550 (hereafter, CX1004), which is a potential quiescent BH-LMXB discovered in the GBS area (Torres et al. 2014). In what follows, we give a description of the system in Section 5.2, and the observations and data reduction steps in Section 5.3. In Section 5.4, we analyse the emission and absorption lines found in the spectra, we identify the spectral type of the optical counterpart, and we present the available photometric data and their implications. In Section 5.5 we contextualise our findings, and in Section 5.6 we draw our conclusions.

5.2 CX1004

CX1004 is a faint X-ray source in the GBS at (α, δ) = (17:46:23.5, -31:05:50) detected with 3 counts (Jonker et al. 2011), implying an X-ray luminosity of $L_x(d, N_H = 10^{21}) = 2.4 \times 10^{31} \times (\frac{d}{1.0 \text{ kpc}})^2$ erg s^{-1}.

Wevers et al. 2016 detected the optical counterpart of CX1004 at $r' = 20.75 \pm 0.02$ and $i' = 19.35 \pm 0.01$ in MOSAIC-II observations taken on 21 and 29 June 21 2006.

No orbital periodicity has yet been found for this system. The Mosaic-II r'-band light curve from Torres et al. 2014 does not show any ellipsoidal variations or significant photometric variability on a time-span of 8 days.

Initial spectra of CX1004 taken with the VIsible Multi-Object Spectrograph (VIMOS) mounted at the 8.2-m ESO Unit 3 Very Large Telescope (VLT; Cerro Paranal, Chile) were analysed by Torres et al. 2014. The optical spectrum was consistent with that of an early M-type star and showed a broad double-peak Hα emission line (FWHM = 2120 ± 20 km s^{-1}), flagging CX1004 as an accreting binary, either a low accretion rate high-inclination CV or a quiescent LMXB hosting a NS or a BH. Subsequent follow-up with the Gemini Multi-Object Spectrograph (GMOS), allowed Wu et al. 2015 to confirm the large broadening of the Hα emission line (FWHM = 2500 ± 100 km s^{-1}).

5.3 Observations and data reduction

5.3.1 Spectroscopic data

Time-resolved spectroscopy of CX1004 was obtained using the medium resolution X-shooter echelle spectrograph (Vernet et al. 2011) mounted at the 8.2-m ESO Unit 2 VLT. The observations were obtained in visitor mode under program 088.D-0096(A) during 1, 2, 3 March 2012. X-shooter provides spectra covering a large wavelength range of $3000 - 24800$ Å, split into three spectroscopic arms: UVB, VIS and NIR. For our analysis we focus on the VIS and UVB data, which cover the range $3000 - 10240$ Å with a dispersion of 0.2 Å pixel^{-1} in both arms. The NIR-arm data were not used due to their lower signal-to-noise ratio and pollution from a nearby field star. The observations were taken with a slit width of 0.9 arcsec in the VIS arm and of 1.0 arcsec in the UVB arm, which deliver a slit-limited resolution of $R = \lambda/\Delta\lambda \simeq 7450$ and $\simeq 4350$, respectively. We executed observing blocks consisting of an ABBA nodding sequence, with integration times for each spectrum of 900 s (VIS) and 877 s (UVB). To reduce systematic effects due to possible excursions of the target position with respect to the slit center, we re-acquired CX1004 at the start of each 1-hour-long observing block. We also observed with the same setup and in nodding mode three early M-type stars that we will use for the analysis presented in Sections 5.4.1 and 5.4.2: BD+05 3409 (M1V); Ross 695 (M2)[1]; Wolf 358 (M5.0V).

Six, eight, and six spectra were collected on 1 March from airmass 1.6 to 1.2, on 2 March from airmass 1.9 to 1.2, and on 3 March 3 airmass 1.6 to 1.2. From the width of the source spatial profile at spectral positions close to λ6300 we measure a mean image quality ranging from 1.7 to 1.4 arcsec, 3.4 to 2.0 arcsec and 3.2 to 1.5 arcsec FWHM for the first, second and third night, respectively. A similar FWHM was found at positions near λ9000. Therefore, the VIS and UVB data were obtained in

[1]We note that Ross 695 was classified as an M2 D star by Koen et al. 2010, where D stands for a star affected by probably spurious variability, due to the presence of a close companion.

slit-limited conditions.

We reduced each 900 s VIS and each 877 s UVB frame separately in order to maximise the time resolution. We processed the data using the 3.10.2 version of `EsoRex`, a software package delivered within the X-shooter pipeline (Modigliani et al. 2010). The spectra were bias and flat field corrected. The echelle orders were merged and rectified, and wavelength calibrated. In this way the pipeline produced 2D spectra. After numerous tests to investigate how to maximise the signal-to-noise on the extracted 1D spectra, we performed the extraction of each spectrum with `IRAF` using an extraction aperture with size equal to the FWHM measured from the spatial profile of the spectrum in question. The resulting 20 spectra were then imported in `MOLLY`[2], rebinned to a uniform pixel scale, and shifted to a heliocentric velocity frame. We checked the zero point of the wavelength calibration of our spectra measuring the velocity shift of the sky emission lines [OI] $\lambda\lambda 6300.304, 8310.719$ (Osterbrock et al. 1996). We use these shifts to correct for the zero-point deviations the spectral regions covering Hα and the Ca II infrared triplet. The median offsets in the two sky lines are: $(3.6, 4.3)$ km s^{-1} for 1 March, $(-3.6, -1.3)$ km s^{-1} for 2 March, and $(-1.6, 1.4)$ km s^{-1} for 3 March. The error on the offset is negligible (less than $\approx 6 \times 10^{-4}$ km s^{-1}). No suitable sky emission lines were available in the spectral range covered by the UVB arm, thereby a zero-point correction was not possible.

5.3.2 Photometric data

5.3.3 MOSAIC-II

CX1004 was observed using the MOSAIC-II imager mounted in the prime focus of the 4-m Victor M. Blanco telescope at CTIO, Chile. The observations were taken during 2 nights in 2006, on 21 and 29 June. The MOSAIC-II instrument consists of a mosaic of 8 CCDs with a total field of view of $36' \times 36'$ and has a pixel-scale of $0.27''$ pixel^{-1}. The field was observed in three filters: r', i', H_α, and the exposure times were 120, 180 and 480 s respectively. The data were reduced using the pipeline developed by the Cambridge Astronomical Survey Unit (CASU), which is described in detail in González-Solares et al. 2008, and which performs bias-subtraction, flat-field correction, and sky-background subtraction. For more details on the observations see Wevers et al. 2016.

5.3.4 OGLE

CX1004 is within the Galactic bulge fields monitored in the I-band by the Optical Gravitational Lensing Experiment (OGLE)-IV survey[3] on 23 April 2010 and 19 March 2011 (OGLE-IV object id: BLG659.29.18319), collecting a total of 60 data points; the pixel scale was 0.26 arcsec. For more details on the survey and the data reduction technique, see Udalski et al. 2015.

5.3.5 VVV

Archival infrared images from the VISTA Variables in the Via Lactea Survey (VVV, Minniti et al. 2010) were inspected to search for the infrared counterpart to CX1004. The 4m VISTA (Visible and Infrared Survey Telescope for Astronomy) located at Paranal Observatory makes use of VIRCAM, a camera with

[2] `MOLLY` is a program for handling 1D spectroscopic data written by Tom Marsh: `http://deneb.astro.warwick.ac.uk/phsaap/software/molly/html/INDEX.html`

[3] ogle.astrouw.edu.pl

a 1.1×1.5 square degrees field of view and 0.34 arcsec pixel^{-1} scale. In our study (Section 5.4.6), we used data acquired in the K-band during August 2012 and March 2013 with total time on-source of 48 s and an image quality better than 0.8 arcsec.

5.3.6 DECam

As part of the GBS variability survey (Britt et al. 2014, Johnson et al. in prep), time-resolved photometry of the field containing CX1004 was observed during 10-11 June 2013 and 30 June - 1 July 2014, using the Dark Energy CAMera (DECam; DePoy et al. 2008) mounted on the 4-m Blanco telescope at Cerro Tololo, Chile, collecting a total of 109 data points. DECam uses a 62 2k $\times$ 4k CCD mosaic to cover a 2.2 square degree field of view with a 0.27 arcsec pixel^{-1}. SDSS r'-band images were taken consisting of 2×90 s followed by 2×1 s exposures to account for faint and bright sources. The seeing was between $0.8-2.5$ arcsec on average over both nights. The images were calibrated using the American Association of Variable Star Observers (AAVSO) Photometric All-Sky Survey DR9 (APASS; Henden et al. 2016) with an average uncertainty of 0.05 magnitudes. The DECam data were reduced with the NOAO DECam pipeline[4]. The fluxes and magnitudes were extracted using the `PHOT` task in `IRAF` along with several other tasks including `TXDUMP`. For more details on the procedure, see Johnson et al. in prep.

5.3.7 FORS2

Single B- and I-band images of the field containing CX1004 were obtained with the FOcal Reducer and low dispersion Spectrograph 2 (FORS2; Appenzeller et al. 1998) mounted on the Cassegrain focus of the 8.2-m ESO Unit 1 VLT. The observations were obtained in visitor mode under program 095.D-0973(A) during June 12, 2015. The instrument was used with the standard resolution collimator and the mosaic of two 2×4 k MIT CCDs. The detector was binned 2×2 providing a 0.25 arcsec pixel^{-1} scale. The integration times were 300 s and 30 s for the images taken with the B- and I-Bessel filters, respectively. The image quality was of 0.9 arcsec (B-band) and of 0.75 arcsec FWHM (I-band). The data were bias subtracted and flat-field corrected using standard tasks in `IRAF`. The high signal to noise achieved in these observation allowed us to measure its position with precision and to perform the astrometric study presented in Section 5.4.5.

[4] http://ast.noao.edu/sites/default/files/NOAO_DHB_v2.2.pdf

Table 5.1: Journal of observations.

Instr.	Date (UT)	No. of spectra/ images	Exp. time (s)	Grism/ filter	Seeing (arcsec)	Slit width (arcsec)	Spec. range (Å)	Resol. (Å)	Disp. (Å pix^{-1})	Pix. scale (arcsec pix^{-1})
Mosaic-II	20-30 June 2006	1	120, 180	r', i'	1.1	-	-	-	-	0.27
OGLE	23 April 2010 19 Mar 2011	60	100	I	1.3	-	-	-	-	0.26
VIMOS	28 June 2011	2	875	MR-2.2	1.2	1.0	4800-10000	10	2.5	-
X-shooter	1, 2, 3 Mar 2012	20	900	ech. VIS	0.8; 1.4; 1.2	0.9	5595-10240	0.6	0.2	-
X-shooter	1, 2, 3 Mar 2012	20	877	ech. UVB	0.8; 1.4; 1.2	1.0	3000-5595	0.6	0.2	-
Gemini	14, 17 May 2012	12	900	G5325	0.8; 0.75	0.75	4800-7600	5	1.36	-
VVV	August 2012 Mar 2013	2	48	K	$\gtrsim 8$	-	-	-	-	0.34
DECam	10-11 June 2013 30 June, 1 July 2014	4	$1, 90$	r'	$0.8 - 2.5$	-	-	-	-	0.27
FORS2	12 June 2015	1	300, 30	b_HIGH I_Bessel	0.9-0.75	-	-	-	-	0.25

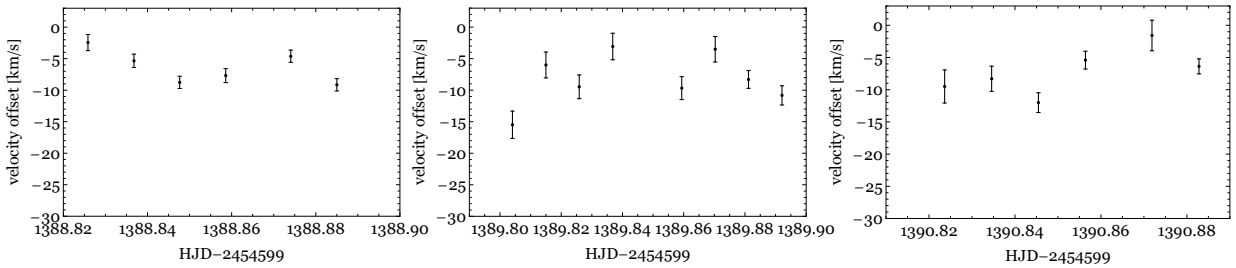

Figure 5.1: Radial velocities derived from the Ca II triplet during the three nights of X-shooter observation. The RVs are obtained cross-correlating the 20 CX1004 spectra with a template of spectral type M2.

5.4 Data Analysis and Results

5.4.1 Radial Velocities from photospheric lines

We measure the radial velocities (RVs) of the optical counterpart from the spectra with the method of cross-correlation with a template star (Tonry & Davis 1979). Prior to the cross-correlation, target and template spectra were resampled into a common logarithmic wavelength scale and normalised in the range $8010 - 8810$ Å by dividing with the result of fitting low-order spline functions to the continuum while masking strong spectral features. This spectral range was chosen because it contains the Ca II infrared triplet; this sharp feature is clearly detected in most of the spectra despite their low signal-to-noise ratio due to the faintness of the source and poor seeing conditions during the observations. We cross-correlate each target spectrum with the spectrum of the template star with spectral class M2, which is the spectral type which best matches the spectrum of CX1004 (see Section 5.4.2). We correct the template star for its intrinsic systemic velocity (51.17 km s^{-1}; Nidever et al. 2002). We cross-correlate the spectra masking all the spectrum but the Ca II triplet lines. In the red part of the spectrum the Na I doublet is also evident, but we choose not to include it while performing the cross-correlation since it is contaminated by telluric absorption lines. We do not see any evidence for a radial velocity (RV) offset among the three nights of observation (see Fig. 5.1). The mean and standard deviation of the measurements night by night are: -11 ± 2 km s^{-1} for 1 March, -13 ± 5 km s^{-1} for 2 March, and -14 ± 6 km s^{-1} for 3 March. We note that the resulting cross-correlation functions show a single well-defined peak.

5.4.2 Spectral classification and rotational broadening

Based on the presence in the 2011 VIMOS spectrum of prominent molecular bands (TiO α, β, γ and γ' band systems) and the non detection of TiO δ and ϵ band systems redward of 8000 Å, Torres et al. 2014 supported an early M-type classification for the optical counterpart to CX1004. Our X-shooter spectra which are free of strong contamination from a field star NE from the counterpart (see finding chart in Torres et al. 2014) confirm these results. In particular, there is no evidence for TiO molecular bands in the range $8200 - 8800$ Å (see Figs. 5.2 and 5.3). Molecular bands start to be evident in this region for spectral types later than M3 (see e.g. Jones et al. 1984; Zhong et al. 2015). To verify our visual classification, that does not account for the possible contribution to the optical continuum from an accretion flow, and to determine the rotational broadening of the M-type star, we made a more

detailed analysis of the X-shooter spectra.

In order to put come constraints on the spectral type, an optimal subtraction method (Marsh et al. 1994) was applied, focusing again on the Ca II infrared triplet. First, we cross-correlate each normalised target spectrum with each normalised template spectrum, to shift each target spectrum to the template's reference frame in order to avoid any smearing of the lines in CX1004. Next, the velocity-shifted spectra were averaged, with different weights in order to maximise the signal-to-noise of the resulting sum. Before proceeding with the optimal subtraction, we compute the rotational broadening with a bootstrap technique, which allows for the the estimation of the real errors (Steeghs & Jonker 2007). We use a uniform grid of values for the rotational broadening $V \sin i$, from 0 km s^{-1} to 100 km s^{-1} in steps of 2 km s^{-1}, we broaden the template by these values, and we subtract the resulting template spectrum from the CX1004 spectrum. The limb darkening was assumed to be 0.5. For each template, we are then able to produce a χ^2 curve as a function of the assumed rotational broadening, whose minimum we find through a cubit fit (see Table 5.2). We note that only in the case of the M5.0V template the χ^2-curve shows a well-defined minimum, whereas for the M1V and M2 template, the curve is monotonic, hence the corresponding values for the rotational broadening in Table 5.2 are upper limits. We broaden each template by the respective rotational broadening value, and we perform the optimal subtraction between the spectrum of CX1004 and the broadened version of the template. In the optimal subtraction process, the underlying assumption is that the target spectrum is a sum of a scaled version of the template and a disc contribution multiplied by its veiling factor: target = $f\times$ template + $(1-f)\times$ disc, where the disc contribution is assumed to be constant and $(1-f)$ is the veiling factor, i.e the disc contribution to the spectrum. Such a procedure is iterative, varying the multiplicative factor f until the χ^2 between the residual of the subtraction and a smoothed version of itself is minimised. The smoothing is obtained convolving the residual with a Gaussian with FWHM which is allowed to vary. The underlying assumption is that a smoother version of the residual is the correct representation of the disc. We vary the smoothing FWHM from 25 to 100 Å. For the f-values we take their average, as well as for the χ^2 values. From the χ^2 values (see Table 5.2), we find that an M2-star provides the best fit to the averaged spectrum, therefore we adopt the M2-star as the appropriate template. We find no evidence for rotational broadening of the lines in the spectrum of CX1004, and that the M2-star contributes $\approx 90\%$ of the flux. This result implies a low rotational broadening for the photospheric lines of the M2 star, $V \sin i \lesssim 35$ km s^{-1}, which is the spectral resolution at the CaII triplet region. We show in Fig. 5.2 the M2-star spectrum together with CX1004; only the spectral range in which most prominent absorption features are located is presented. In Fig. 5.3 we show the Ca II infrared triplet region of CX1004 (top); the M2-template (middle); and the residual after the optimal subtraction (bottom).

5.4.3 Study of the emission lines

Only Balmer lines in emission (up to Hγ) are detected in our spectra. In order to study the Hα and Hβ line profiles, we normalised them by fitting their adjacent continuum using a low-order spline function while masking strong absorption features and emission artefacts. To increase the signal-to-noise, we averaged the resulting Hα profiles taken during the same night. In this process, we neglect a few spectra due to their low signal-to-noise ratio and/or strong contamination from the sky or prominence to twilight (three spectra excluded in the second night; one spectra excluded in the third night). The

Table 5.2: Spectral classification ($d.o.f.$ = degrees of freedom); the χ^2-values correspond to the results of the optimal subtraction.

Star ID	Spectral Type	f	χ^2/d.o.f
	(km s^{-1})		
BD+05 3409	M1V	1.00 ± 0.05	8.4
Ross 695	M2	0.90 ± 0.01	7.8
Wolf 358	M5.0V	1.20 ± 0.08	9.6

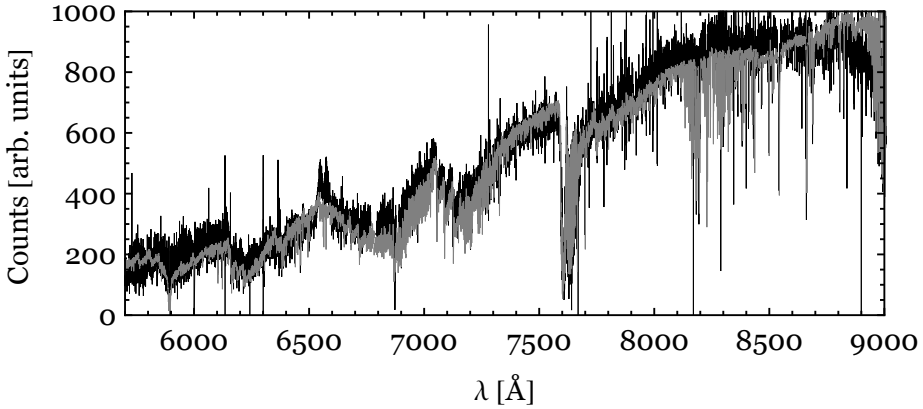

Figure 5.2: X-shooter CX1004 averaged spectrum for the first night of observation (black) together with the M2 template star (grey). The template was rescaled in counts to help the comparison with CX1004 (the multiplicative factor is ≈ 1.8).

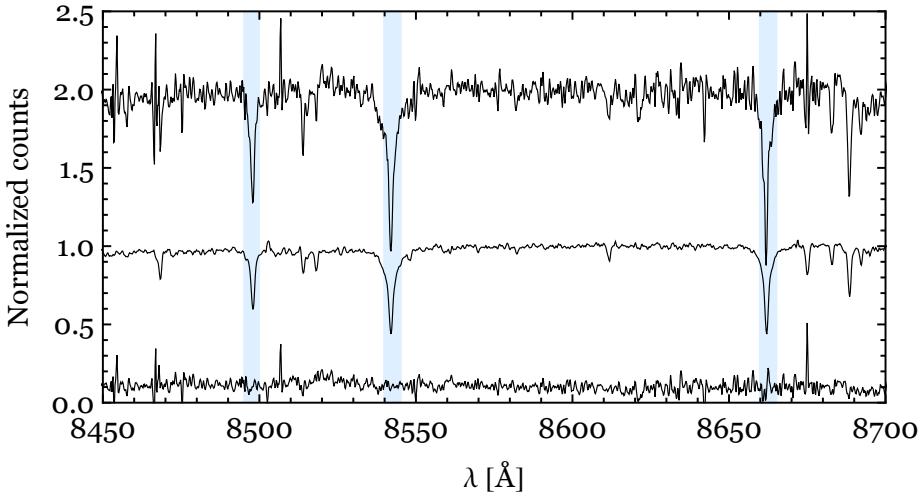

Figure 5.3: From top to bottom: normalised averaged X-shooter spectrum of CX1004 (shifted on the y-axis by $+1$); normalised spectrum of the M2 template; residual after the optimal subtraction. We indicate with the shaded area the Ca II triplet. After optimally subtracting the M2-star light, approximately 10% of the light remains.

TABLE 5.3: Emission line parameters: FWHM (in Å and in km s^{-1}); RV from the centroid of the line; peak to peak separation (ΔV^{pp}). The RV of the line centroid was derived from a two-Gaussian fit to the line profile. The FWHM was derived from a one-Gaussian model. The χ^2/d.o.f values for the two-Gaussian model are provided in column 6.

Spectrum	FWHM (Å)	FWHM (km s^{-1})	RV (km s^{-1})	ΔV^{pp} (km s^{-1})	χ^2/d.o.f
		Hα λ6562.760			
Xsh -1 March 2012	49 ± 0.5	2264 ± 23	-13 ± 6	1316 ± 12	9
Xsh - 2 March 2012	47 ± 0.7	2136 ± 34	-91 ± 6	1342 ± 13	8
Xsh - 3 March 2012	62 ± 1.5	2858 ± 68	11 ± 13	1413 ± 25	8
Gemini - 14 May 2012	48 ± 2	2181 ± 82	-59 ± 50	1262 ± 50	0.6
Gemini - 17 May 2012	50 ± 2	2297 ± 93	-66 ± 34	1330 ± 34	0.8
		Hβ λ4861.327			
Xsh - 1, 2, 3 March 2012	37 ± 0.6	2310 ± 34	-78 ± 12	1356 ± 14	11

averaged Hα profile shows a broad and double-peak Hα emission line (see Fig. 5.4), as well as two prominent absorption features superimposed, one located at the core of the Hα line as well as the Ca I line at λ6573. In Fig. 5.4, we also show our M2-template normalised spectrum in green, after multiplication by 0.9 (which is the factor f we derived in Section 5.4.2 through the optimal subtraction). The two absorption lines are evidently seen in the M2 spectrum and align with the ones of CX1004. Hence, we attribute the two lines in CX1004 as being photospheric in origin. Since the Hα emission is affected by such photospheric absorption, we fit the emission profile masking the absorption core present between the two emission line peaks. To calculate the FWHM of the Hα line, we fit a Gaussian function to the profile, using `mgfit` in `MOLLY`. In addition, a two-Gaussian model allows us to measure the velocity shift of the blue (V_b) and red (V_r) peaks with respect to the rest wavelength. Their mean $(V_r + V_b)/2$ gives the velocity shift of the centroid with respect to the line rest wavelength. The results are shown in Table 5.3. Due to the presence of the absorption core, we cannot currently establish whether the formally significant offset between the X-shooter RVs is real. We also provide the peak to peak separation ΔV^{pp} of the Hα profile, calculated as: $|V_r - V_b|$. When fitting the Hα profile without masking the core, the FWHM values are not affected by more than 10%. The RV changes are within the uncertainties shown in Table 5.3; the ΔV^{pp} values do not change by more than 2%.

The UVB part of the X-shooter spectra shows a broad double-peak Hβ emission line. To increase the signal-to-noise ratio, we average the 17 best spectra, normalise the resulting spectrum, and fit the Hβ line both with a single and double Gaussian. We show the results of the fit in Table 5.3 and the averaged spectrum in Fig. 5.5. The FWHM is consistent with that of the Hα profile.

5.4.4 Reanalysis of the VIMOS and GMOS data

We reanalyse the previously published spectroscopy of CX1004. The data consist of 2 900 s spectra obtained in 2011 with VIMOS and 12 900 s spectra obtained in 2012 with GMOS (see Table 1 for

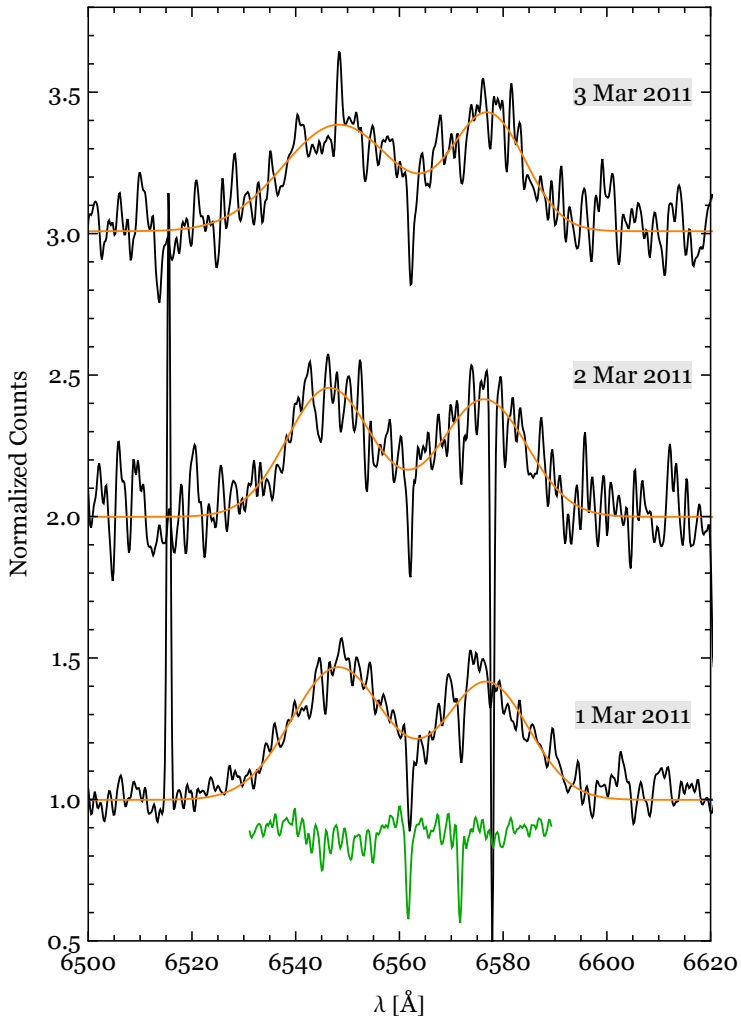

Figure 5.4: Double-peak Hα profile for the night-by-night average X-shooter spectra of the three observing nights. The spectra were Gaussian-smoothed using a smoothing box of 4 pixels. In orange we show the double-Gaussian fit. In green we show the normalised spectrum of our M2 template, after the multiplication by 0.9, the f factor which we calculated through optimal subtraction in Section 5.4.2.

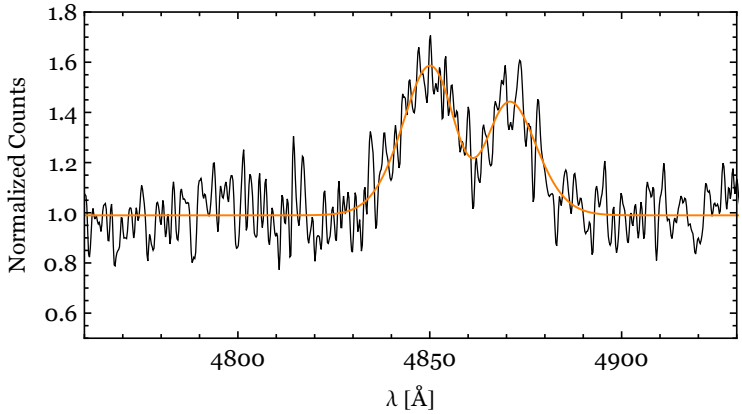

Figure 5.5: Double-peak Hβ profile of the averaged X-shooter spectrum. The spectra were Gaussian-smoothed using a smoothing box of 3 pixels. The orange line is the double-Gaussian fit.

further details). For the GMOS data, Wu et al. 2015 measured a FWHM of 2500 ± 100 km s^{-1} for the Hα profile, and a radial velocity of RV $= -15 \pm 20$ km s^{-1} using a double-Gaussian fit. We reanalyse the Gemini data, correcting them for the zero-point offsets using the sky emission line [OI] λ6300.304, and recalculate the line parameters (shown in Table 5.3). We also calculate the RV of the Hα centroid on the 8 best spectra (3 spectra for the first night, and 5 for the second night), to trace the motion of the putative compact object. We obtain: RV$= -80\pm90, -54\pm161, -49\pm59, -221\pm126, 3\pm106, 78\pm103, -26 \pm 81, -105 \pm 52$ km s^{-1} , respectively. The errors on the RVs are too large for allowing any identification of a clear trend.

For the VIMOS data, Torres et al. 2014 fitted the Hα profile in the combined VIMOS spectra, obtaining a FWHM of 2120 ± 20 km s^{-1}, and a significant RV of -170 ± 20 km s^{-1} for the centroid of the line. A comparable velocity was obtained from photospheric absorption lines. We reanalyse the spectra recomputing the emission line parameters, finding a RV offset for the centroid of the Hα line consistent with the value in Torres et al. 2014. The multi-slit mask of the VIMOS observations of CX1004 was designed to have the counterpart centered on a 1.0 arcsec width slit. However, examination of the acquisition images and the spatial profile for the spectrum of CX1004 shows that the source was not well-centered. The slit was offset in the NE direction such that included significant contaminating light from the field star NE from CX1004. This positional departure from the slit center could have introduced large RV offsets given the 2.5 Å pixel^{-1} dispersion (equivalent to 114 km s^{-1} per pixel at Hα). Since we cannot quantify the effect with the available data, we deem the RVs in Torres et al. 2014 to be unreliable.

5.4.5 Testing the interloper hypothesis: positional offsets of CX1004

The lack of any RV variations in the optical spectra deems it likely that the M-star is not associated with the Hα-emitting source, i.e that the M-star is an interloper which happens to be along the same line of sight of the accreting binary. To investigate this, we probe whether we can find any departure between B-band/Hα images (where the interacting binary might dominate), and I-band/i'-band images (where the M-type star dominates). For that goal, B and I-band images of the field were taken with FORS2 (see Section 5.3.2 for details on the observations). We additionally used the optical data overlapping with the GBS X-ray fields taken with MOSAIC-II (Wevers et al. 2016), focusing on the Hα and i' band images. We cross-match sources between the two images and use the GBS coordinates from Wevers et al. 2016 to calculate the positional offset between the two images.

We compute the astrometry of the B- and I-band images using the openly available tool `astrometry.net`[5]. Then we use the routines *imexamine*, *imcentroid*, *imalign*, *wregister* in `IRAF`, to shift the red and blue image to the same reference frame. In this alignment, we exclude the candidate counterpart of CX1004. We use the `Aperture Photometry Tool (APT)`[6] to perform PSF photometry on the images, computing the emission centroid of 103 point sources in each image. The stars are within a radius of $\approx$ 500 arcsec from our target. The centroid is delivered in pixel coordinates, which we convert into sky coordinates. Then we calculate the offset between the I- and B-band image in terms of Δ_x, Δ_y, in arcsec. We show the results in Fig. 5.6 (solid line), where the 2-dimensional offsets $\sqrt{\Delta_x^2 + \Delta_y^2}$ are presented as a cumulative distribution. We see that the offset for CX1004 (indicated with a solid

[5]See http://nova.astrometry.net/

[6]See http://www.aperturephotometry.org/aptool/

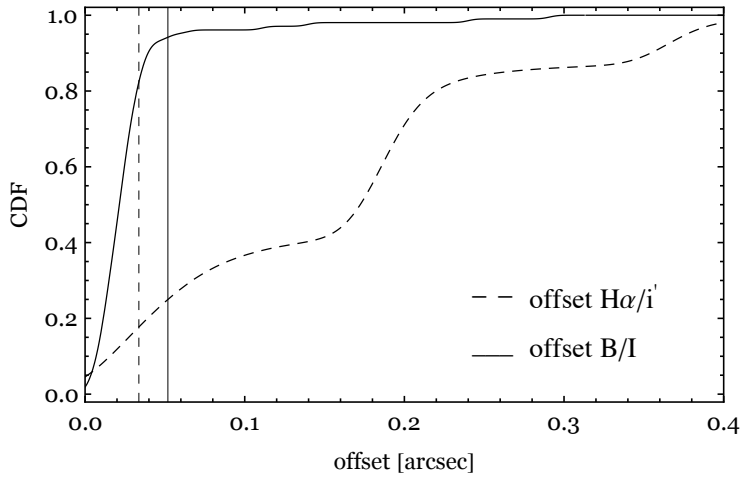

Figure 5.6: Cumulative distribution function (CDF) of the offset in arcseconds between the B- and I-band counterparts of stars in the field of CX1004 (solid line), and between their Hα and i' counterparts (dashed line). The offsets for CX1004 are indicated with the two vertical lines.

vertical line) is not significantly different from the offset found for the others stars in the field. Its offset is computed as $\sqrt{\Delta x^2 + \Delta y^2} \approx 0.05$ arcsec. The fraction of systems with an offset larger than the one found for CX1004 is 6%.

To compute the offset between the Hα and i' Mosaic-II images, we use the available coordinates of the sources in the CX1004 field from the GBS catalogue, after having cross-matched 8197 the sources in the two images. The stars are within a radius of ≈ 1000 arcsec from our target. In this way, the offset is computed in terms of physical coordinates RA and Dec. We show the results in Fig. 5.6 (dashed line), where the 2-dimensional offsets are computed combining in quadrature the offset in the RA and Dec coordinates. The offset for CX1004 is ≈ 0.03 arcsec and is shown as a dashed vertical line. The fraction of systems with an offset larger than the one found for CX1004 is 80%.

We find that there is no strong evidence for an offset between B/I-band images and r/Hα images, and thus for the M-type star to be an interloper, unless the interloper is perfectly aligned with CX1004 or the offset is below our detection thresholds.

5.4.5.1 PSF photometry

We also perform point-spread-function (PSF) photometry on both the B- and I-band FORS2 images using dedicated tools in IRAF. We find no evidence for underlying sources nor residuals in any of the images.

5.4.6 I-band and K-band counterparts

We use the FORS2 I-band image to calculate the apparent magnitude of the CX1004 optical counterpart, $I_{\rm FORS2}$. We compute the instrumental magnitudes of 31 stars in the field of CX1004 using APT. In order to calculate the photometric zeropoints, we cross-match these sources with the ones in the GBS catalogue, whose apparent magnitudes are known. Of these matched sources, we only select those ones which have been flagged as stellar. The photometric zeropoint zp is calculated minimising the

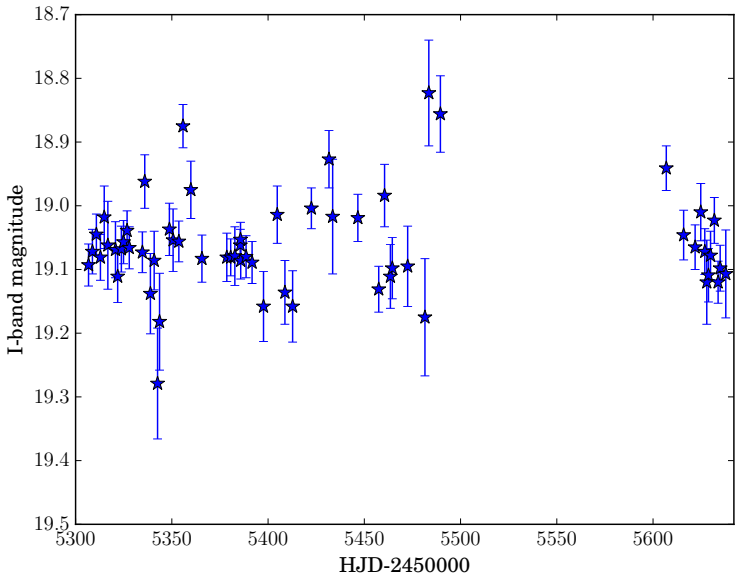

Figure 5.7: OGLE I-band light curve of CX1004.

sum of squares:

$$\sum_i \left[\mathrm{mag_{i,cat}} - (\mathrm{mag_{i,instr}} + zp)\right]^2 \tag{5.1}$$

We calculate the error as the root-mean-square (rms) of the residuals. We obtain a magnitude of $\mathrm{I_{FORS2}} = 19.32 \pm 0.08$ for CX1004.

We clearly detect in the infrared VVV images a point-like source matching the astrometric position of the optical counterpart. We apply PSF fitting using `DAOPHOT` in `IRAF` to compute the instrumental magnitudes of the detected stars in the field. Differential photometry with respect to a nearby and non-variable field star calibrated in VVV was performed to derive $K_\mathrm{s} = 16.6 \pm 0.2$ for CX1004.

5.4.7 OGLE light curve

In Fig. 5.7, we present the I-band OGLE light curve; the average magnitude of CX1004 is $\mathrm{I_{OGLE}} = 19.06 \pm 0.08$, where the error is calculated as the rms, and a maximum variability of $\Delta I = 0.46$. The FORS2 I-band magnitude of $\mathrm{I_{FORS2}} = 19.32 \pm 0.08$ falls among the lower points of the curve. We use the transformation equations between Johnson-Cousins and SDSS magnitude derived by Jester et al. 2005 to convert the i'-band magnitude from Wevers et al. 2016 into I-band magnitude, using r' from Torres et al. 2014, obtaining $\mathrm{I_{GBS}} \approx 18.91$, consistent with the high-end of the OGLE light curve. From the difference between the lowest point of the light curve ($\approx 19.3 \pm 0.1$) and the average (≈ 19.1), we derive a minimum contribution of the disc to the average of several tens of a percent, which is similar to what we found from optimally subtracting the contribution of the M2 star (see Section 5.4.2).

5.4.8 DECam light curve

We show the r'-band DECam light curve of CX1004 in Fig. 5.8, from which we calculate an average of $r'_\mathrm{DECam} = 20.42 \pm 0.03$, where the error is calculated as the rms, and a maximum variability of $\Delta r' = 0.18$. For comparison, from the Mosaic-II observations in 2006, Wevers et al. 2016 calculated

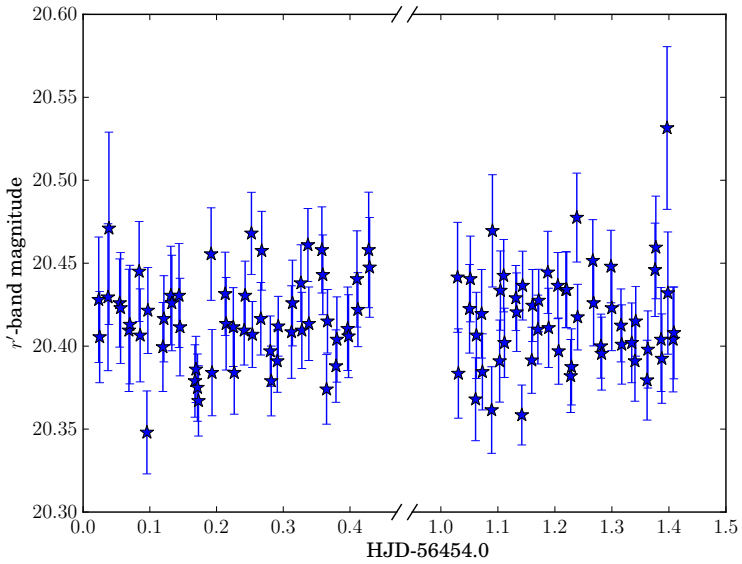

Figure 5.8: DECam r'-band light curve of CX1004.

$r' = 20.75 \pm 0.02$; from the Mosaic-II observations in 2010, Torres et al. 2014 calculated 20.76 ± 0.04 mag and $\Delta r' = 0.2$.

5.4.9 Reddening and distance to the interloper star and to the X-ray source

We estimate the reddening from the observed (I-K) colour of the source. The apparent K-band magnitude of CX1004 is $K = 16.6 \pm 0.2$ (Section 5.4.6). Assuming that the lowest point in the OGLE light curve (I $\approx$ 19.3) is due to light from the M-star only and that the M-star dominates the K-band magnitude, we find an observed colour (I-K) $\approx$ 2.7, which is somewhat redder than the intrinsic colour $(\mathrm{I-K})_0$ of M-dwarfs ($\approx$ 1.98 for M2V; Bessell 1991). Neglecting for the moment the fact that the different bands were not observed simultaneously, we can use the observed colour to estimate the extinction towards the source. Using the relation between the extinction in the I-band and in the K-band ($\mathrm{A_K} \approx 0.225\ \mathrm{A_I}$; Cox 2000), and the intrinsic and observed colours, we estimate an extinction of the order of $A_\mathrm{I} \approx 0.93$. Taking the absolute magnitude for an M2V star ($\mathrm{M_I} \approx 8$; Bessell 1991), we find a distance of $\approx$ 1.2 kpc. The small distance is consistent with the fact that no strong diffuse interstellar bands (DIBs) are found in the spectra (see also Torres et al. 2014). We possibly detect the DIB at λ8620, but it is too weak to allow for a measurement of its equivalent width.

In order to estimate the distance to the X-ray source, we can use the faintest point of the OGLE light curve to estimate a lower limit for the absolute magnitude of the putative donor star in the system. Taking a fairly arbitrary choice of the real companion contributing 10% of the flux of the M2-star (see Section 5.4.2), and assuming that such contribution is constant over the whole spectral range, we find an apparent magnitude of the companion star of I $\approx$ 21.8. We use the 3D dust map from Schultheis et al. 2014 to derive the reddening E(J-K) as a function of the distance along the direction towards the optical counterpart of CX1004. Using the extinction law from Nishiyama et al. 2009, we convert the reddening into a K-band extinction A_K, which we then convert to an extinction in the I-band using $A_\mathrm{K} \approx 0.225\ A_\mathrm{I}$ from Cox 2000. In Fig. 5.9 we show the lower limit for the magnitude of the companion star in the accreting binary as a function of the distance (solid line). We note that the distances shown

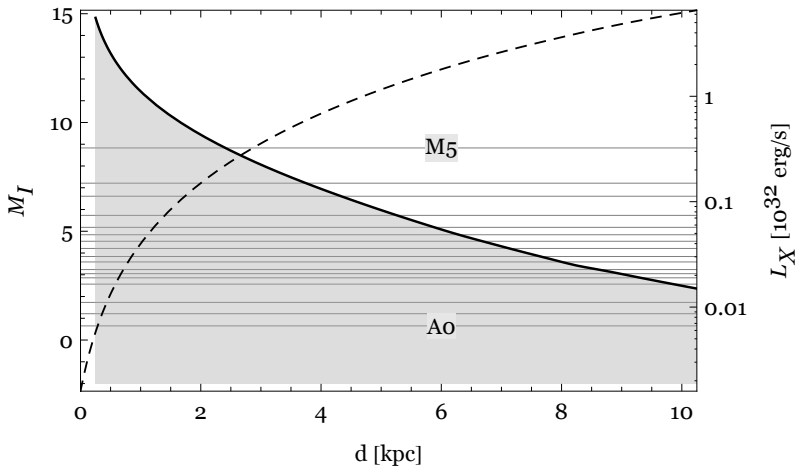

Figure 5.9: Lower-limit for the absolute magnitude of the putative companion star in CX1004 (solid line) and expected X-ray luminosity as a function of the distance (dashed line). The area below the solid line is excluded because otherwise the object would be brighter in the I-band than observed. The horizontal lines show the absolute magnitudes of main sequence stars from A0- to M5-type and subclasses 0, 2 and 5.

in this plot are *lower* limits, as they do not account for a possible contribution from the field star NE of CX1004 or for the additional contribution from the accretion disc. The horizontal lines mark the absolute magnitude of main sequence stars of spectral class from A0V to M5V (with three subclasses: 0, 2, 5, for each spectral type).

We use the previously calculated $A_{\rm I}$-values and the empirical law $N_{\rm H} \approx 2.21 \times 10^{21} A_{\rm V}$ from Güver & Özel 2009, to convert $A_{\rm V} \approx A_{\rm I}/0.479$ (Drilling & Landolt 2000) into a hydrogen column density $N_{\rm H}$. We use PIMMS[7] to convert the 3 counts observed by *Chandra* from CX1004 in the ACIS range $0.5-10$ keV to calculate the unabsorbed flux and hence the X-ray luminosity, which we show in Fig. 5.9 as a function of the distance (dotted line). In this calculation we have assumed a power-law spectrum with index 2.1, which is typical for BH-LMXBs in quiescence (Plotkin et al. 2013). From this plot, we thus can conclude that the X-ray binary should be fairly far away, at $\gtrsim 2$ kpc (or have a companion even later than M5), and thus have a relatively high L_X. The X-ray luminosity is $L_X \approx 1.5 \times 10^{31}$ erg s^{-1} for $d = 2$ kpc, and $L_X = 4.6 \times 10^{32}$ erg s^{-1} for $d = 8$ kpc. It has been shown that there is a clear correlation between the quiescent luminosity of black-hole transients (BHTs) and their orbital period $P_{\rm orb}$ (see Garcia et al. 2001, and Homan et al. 2013 and reference therein). At $P_{\rm orb} \approx 0.5$ days (an orbital-period value which we estimate from the findings of Casares 2015, see Section 5.5), the observed BHTs have a luminosity of $L_X \approx 10^{32}$erg s^{-1} (see Fig. 1 in Homan et al. 2013), a value consistent with the X-ray luminosity of CX1004 at a distance of 8 kpc. Menou et al. 1999 computed the expected X-ray luminosity of BHTs in quiescence combining a model for the loss of binary angular momentum which drives the mass transfer, with a model for the advection dominated accretion flow, which is thought to be the primary component to the emission of quiescent BHTs. For an orbital period of 0.5 days, they calculate an expected L_X of $10^{31} - 3 \times 10^{31}$erg s^{-1} and $3 \times 10^{32} - 10^{33}$erg s^{-1}, depending on which fraction of the transferred mass is advected into the BH (1/3 or 1). These values are consistent with a distance larger than 2 kpc. The X-ray luminosity of Cataclysmic Variables (CVs) in quiescence

[7] https://heasarc.gsfc.nasa.gov/docs/software/tools/pimms.html

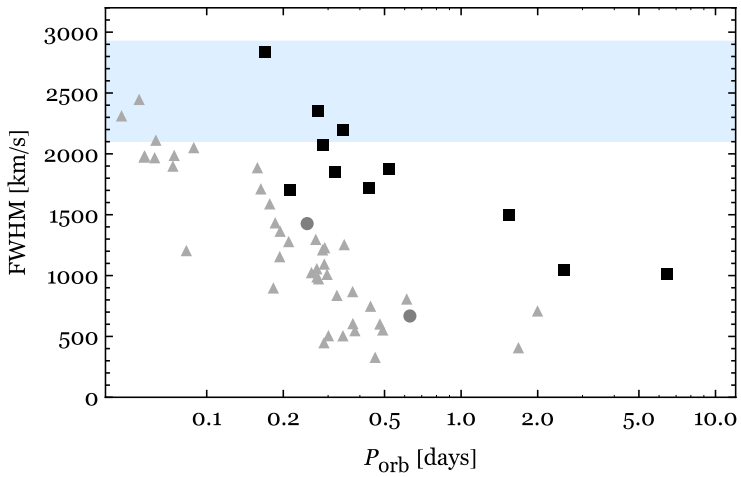

FIGURE 5.10: Accreting binaries as a function of the FWHM of their Hα line and orbital period P_{orb}. Triangles correspond to CVs, circles to XRBs containing a NS, squares to XRBs containing a BH. Data are from Casares 2015. The shaded area indicates the Hα-FWHM of CX1004 (see values in Table 5.3).

is between $\approx 5 \times 10^{28} - 8 \times 10^{31}$ erg s^{-1} (Britt et al. 2015), on the low side of the L_X we found for CX1004. The quiescent luminosity of soft X-ray transients (SXTs) hosting a NS is typically higher, due to the contribution from the NS surface: $\approx 10^{32} - 10^{33}$ erg s^{-1} (Tomsick et al. 2004), on average higher than the one of CX1004.

5.5 Discussion

5.5.1 CX1004 in the context of the known black hole transients

CX1004 displays one of the widest double-peak Hα emission lines, similar to the value found for the widest-Hα BHTs: GS 2000+25 (2207 km s^{-1}, $P_{orb} = 0.34$ days); N Vel 93 (2082 km s^{-1}, $P_{orb} = 0.28$ days); XTE J1859+226 (2361 km s^{-1}, $P_{orb} = 0.27$ days) and XTE J1118+480 (2850 km s^{-1}, $P_{orb} = 0.17$ days); see Casares 2015. The FWHM of the Hα line is a proxy to discriminate between an accreting binary hosting a compact object and other systems showing Hα in emission, such as T-Tauri stars and other classes of young stellar objects.

As shown by Casares 2015, such a large FWHM can be consistent either with a CV with a very short orbital period and seen at high inclination, or with a short-period binary hosting a BH as the accretor. We use the list of CVs, NS-XRBs and BHTs with constrained orbital periods and Hα-FWHM measurements from Casares 2015, and we plot them on a FWHM $- P_{orb}$ plane in Fig. 5.10. BHs are clearly separated from binaries hosting a WD or a NS. Based on its Hα-FWHM, CX1004 would either be *i)* a very short orbital period CV (less than 0.1 day), *ii)* a BH binary with a period around 0.5 day (see shaded area in Fig. 5.10), *iii)* a BH binary with a longer period if the inclination of the system is larger than those shown in the Fig. 5.10. We note that all the BHTs in Fig. 5.10 have an inclination smaller than 80°.

If CX1004 were to follow the recently established FWHM-K_2 correlation found by Casares 2015 for quiescent BHTs and CVs, the expected K_2 would be $\simeq$ 520 km s^{-1} in the BH case, and $\simeq$ 377

km s^{-1} in the CV case (where we have taken a FWHM of 2231 km s^{-1}, which is the average between the maximum and minimum value of the FWHM of CX1004, see Table 5.3). This correlation follows directly from the assumption of an axisymmetric disc in Keplerian motion around the central compact object. Casares 2016 recently found a tight correlation between the binary mass ratio $q = M_2/M_{\rm BH}$ with the ratio of the Hα double peak separation to the Hα-FWHM for quiescent BHTs and CVs. We average all the X-shooter spectra, and we fit the Hα profile with a single Gaussian model, obtaining a FWHM of 2230 ± 16 km s^{-1}. Following the method used by Casares 2016, we fit the Hα profile with two Gaussians with identical width and height (stemming from the assumption that the line profile is symmetric), obtaining a double peak separation DP km s^{-1}. A BHT has a typical mass ratio $q < 0.1$, whereas a CV has a typical mass ratio of $q > 0.1$. From the correlation, we calculate a mass ratio of 0.05 ± 0.01 in the case of a BH system, and of $q = 0.23 \pm 0.04$ in the case of a CV. We average the Gemini spectra and we apply the same method to the resulting spectrum, finding a mass ratio of $q = 0.03 \pm 0.03$ for the BH case, and of $q = 0.15 \pm 0.11$ for the CV case. These results are consistent with the mass-ratio values found from the X-shooter data.

In Section 5.4.3 we found a possible offset of the RVs of the Hα emission. If we interpret this as the movement of the accretor, we can estimate the lower limit on K_1 to be at least half of the offset, i.e. $K_1 \approx 27$ km s^{-1}. This implies a radial velocity semi-amplitude of the companion star of $K_2 = K_1/q \approx 540$ km s^{-1} in the BH case, a value which is consistent with the expected K_2 value from Casares 2015 FWHM-K_2 correlation (≈ 520 km s^{-1}). In the CV case, we get $K_2 = K_1/q \approx 117$ km s^{-1}, a value which is lower than the expected K_2 from the correlation (≈ 377 km s^{-1}), hence the real K_1 should be quite a bit higher (≈ 87 km s^{-1}).

5.5.2 A triple system

The results of the X-shooter spectra provide a puzzle in terms of the interpretation of CX1004 being a low-mass X-ray binary. We do not observe any RV variations expected from a short-period system over our observing run, which spans three consecutive nights, with two hours of observations per night. Furthermore, from our analysis in Sec. 5.4.5, we don't find strong evidence for a positional offset between the X-ray source and the optical counterpart. There is the possibility that the X-ray binary is the inner binary in a hierarchical triple system, with the M-star in the outer orbit. BHTs are the descendant of binaries hosting a massive O-type star with a low-mass companion; such O-type stars have a large binary fraction of wide companions, of around ≈ 0.5 for orbital period less than 20 days, with a mass ratio consistent with a random pairing from the IMF. Furthermore, such massive stars are shown to have an average number of companions of ≈ 2.16 (Duchêne & Kraus 2013; Moe & Di Stefano 2016, in preparation). Further theoretical calculations, like the ones in Naoz et al. 2015 and Michaely & Perets 2016, together with consequent optical follow-up of the putative outer companion, are required to fully confirm the plausibility of this scenario.

5.6 Conclusions

Optical spectra of the counterpart to the GBS source CX1004 were analysed in this work. The results of our spectral analysis provide a puzzle in terms of the interpretation of the system, since the wide double-peak Hα line points towards a short-orbital period accreting binary hosting a WD or a BH,

while on the other hand no RV-variations are detected in our X-shooter spectra. The available data, due to the temporal coverage they have, do not allow us to discriminate between the two most likely interpretations for this system: i) the M-star being an interloper along the same line of sight of CX1004; ii) the M-star being the outer companion in a triple system. In order to discriminate between these two hypothesis, we suggest to perform high-resolution imaging of CX1004 in the UV band (as the angular resolution increases with wavelength), for instance with the Wide Field Camera of the Advanced Camera for Surveys (ACS; Ford et al. 1998) mounted on the Hubble Space Telescope and which delivers a pixel scale of 0.049 arcsec.

5.7 Acknowledgments

The work of SR was supported by the Netherlands Research School for Astronomy (NOVA). Tom Marsh is thanked for developing and sharing his package `MOLLY`. SR is thankful to Jorge Casares VelĞzquez for useful discussions. The OGLE project has received funding from the National Science Centre, Poland, grant MAESTRO 2014/14/A/ST9/00121 to Andrzej Udalski. This work has been partially supported by the Polish National Science Centre grant no. DEC-2011/03/B/ST9/02573. This research has made use of the SIMBAD database, operated at CDS, Strasbourg, France, and of the NASA's Astrophysics Data System.

Bibliography

B. P. Abbott, R. Abbott, T. D. Abbott, et al., 2016. *Physical Review Letters*, 116(6):061102.

M. E. Alexander, 1973. *Ap&SS*, 23:459–510.

I. Appenzeller, K. Fricke, & W. et al Fürtig, 1998. *The Messenger*, 94:1–6.

P. Arras & D. Lai, 1999. *ApJ*, 519:745–749.

Z. Arzoumanian, D. F. Chernoff, & J. M. Cordes, 2002. *ApJ*, 568:289–301.

C. Bambi, 2012. *Phys. Rev. D*, 86(12):123013.

A. J. Barker & G. I. Ogilvie, 2009. *MNRAS*, 395:2268–2287.

M. V. Barkov & S. S. Komissarov, 2010. *MNRAS*, 401:1644–1656.

D. Barret, J. E. McClintock, & J. E. Grindlay, 1996. *ApJ*, 473:963.

D. Barret, J. F. Olive, L. Boirin, et al., 2000. *ApJ*, 533:329–351.

E. M. Basinska, W. H. G. Lewin, M. Sztajno, et al., 1984. *ApJ*, 281:337–353.

K. Belczynski, D. E. Holz, T. Bulik, et al., 2016a. *ArXiv e-prints*.

K. Belczynski, V. Kalogera, F. A. Rasio, et al., 2008. *ApJS*, 174:223–260.

K. Belczynski, S. Repetto, D. E. Holz, et al., 2016b. *ApJ*, 819:108.

K. Belczynski & R. E. Taam, 2004. *ApJ*, 603:690–696.

K. Belczynski, G. Wiktorowicz, C. L. Fryer, et al., 2012. *ApJ*, 757:91.

P. Beniamini & T. Piran, 2016. *MNRAS*, 456:4089–4099.

M. S. Bessell, 1991. *AJ*, 101:662–676.

J. Binney & S. Tremaine, 2008. *Galactic Dynamics: Second Edition*. Princeton University Press.

A. Blaauw, 1961. *Bull. Astron. Inst. Netherlands*, 15:265.

J. M. Blondin, A. Mezzacappa, & C. DeMarino, 2003. *ApJ*, 584:971–980.

J. Boersma, 1961. *Bull. Astron. Inst. Netherlands*, 15:291–301.

C. T. Bolton, 1972. *Nature*, 235:271–273.

I. A. Bonnell & J. E. Pringle, 1995. *MNRAS*, 273:L12–L14.

J. Bovy, 2015. *ApJS*, 216:29.

J. Bovy, H.-W. Rix, C. Liu, et al., 2012. *ApJ*, 753:148.

S. Bowyer, E. T. Byram, T. A. Chubb, et al., 1965. *Science*, 147:394–398.

C. F. Bradshaw, E. B. Fomalont, & B. J. Geldzahler, 1999. *ApJ*, 512:L121–L124.

N. Brandt & P. Podsiadlowski, 1995. *MNRAS*, 274:461–484.

W. N. Brandt, P. Podsiadlowski, & S. Sigurdsson, 1995. *MNRAS*, 277:L35–L40.
C. T. Britt, R. I. Hynes, C. B. Johnson, et al., 2014. *ApJS*, 214:10.
C. T. Britt, T. Maccarone, M. L. Pretorius, et al., 2015. *MNRAS*, 448:3455–3462.
A. Burrows, J. Hayes, & B. A. Fryxell, 1995. *ApJ*, 450:830.
A. G. Cantrell, C. D. Bailyn, J. A. Orosz, et al., 2010. *ApJ*, 710:1127–1141.
J. Casares, 2015. *ApJ*, 808:80.
J. Casares, 2016. *ArXiv e-prints*.
J. Casares, P. A. Charles, & T. Naylor, 1992. *Nature*, 355:614–617.
J. Casares & P. G. Jonker, 2014. *Space Sci. Rev.*, 183:223–252.
J. Casares, I. Negueruela, M. Ribó, et al., 2014. *Nature*, 505:378–381.
P. A. Charles & M. J. Coe, 2006. *Optical, ultraviolet and infrared observations of X-ray binaries*, pages 215–265.
C. Chevalier & S. A. Ilovaisky, 1990. *A&A*, 228:115–124.
R. P. Church, C. Kim, A. J. Levan, et al., 2012. *MNRAS*, 425:470–476.
W. I. Clarkson, P. A. Charles, & N. Onyett, 2004. *MNRAS*, 348:458–468.
D. Clausen, A. L. Piro, & C. D. Ott, 2015. *ApJ*, 799:190.
M. Cocchi, A. Bazzano, L. Natalucci, et al., 2000. *A&A*, 357:527–532.
M. Cocchi, A. Bazzano, L. Natalucci, et al., 2001a. *Mem. Soc. Astron. Italiana*, 72:757–760.
M. Cocchi, A. Bazzano, L. Natalucci, et al., 2001b. *A&A*, 378:L37–L40.
M. Colpi & I. Wasserman, 2002. *ApJ*, 581:1271–1279.
J. M. Cordes, R. W. Romani, & S. C. Lundgren, 1993. *Nature*, 362:133–135.
J. M. Corral-Santana, J. Casares, T. Muñoz-Darias, et al., 2013. *Science*, 339:1048–1051.
J. M. Corral-Santana, J. Casares, T. Muñoz-Darias, et al., 2016. *A&A*, 587:A61.
J. M. Corral-Santana, J. Casares, T. Shahbaz, et al., 2011. *MNRAS*, 413:L15–L19.
A. N. Cox, 2000. *Allen's astrophysical quantities*.
G. H. Darwin, 1879. *The Observatory*, 3:79–84.
M. B. Davies, W. Benz, & J. G. Hills, 1992. *ApJ*, 401:246–259.
M. B. Davies, A. King, S. Rosswog, et al., 2002. *ApJ*, 579:L63–L66.
M. de Kool, E. P. J. van den Heuvel, & E. Pylyser, 1987. *A&A*, 183:47–52.
G. De Lucia, F. Fontanot, D. Wilman, et al., 2011. *MNRAS*, 414:1439–1454.
S. E. de Mink, N. Langer, R. G. Izzard, et al., 2013. *ApJ*, 764:166.
W. Dehnen & J. Binney, 1998. *MNRAS*, 294:429.
M. della Valle, I. F. Mirabel, & L. F. Rodriguez, 1994. *A&A*, 290:803–806.
D. L. DePoy, T. Abbott, & et al. Annis, 2008. In *Ground-based and Airborne Instrumentation for Astronomy II*, volume 7014 of *Proc. SPIE*.
L. Dessart, E. Livne, & R. Waldman, 2010. *MNRAS*, 405:2113–2131.
V. Dhawan, I. F. Mirabel, M. Ribó, et al., 2007. *ApJ*, 668:430–434.
I. Dobbs-Dixon, D. N. C. Lin, & R. A. Mardling, 2004. *ApJ*, 610:464–476.
M. Dominik, K. Belczynski, C. Fryer, et al., 2012. *ApJ*, 759:52.
M. Dominik, E. Berti, R. O'Shaughnessy, et al., 2015. *ApJ*, 806:263.
J.-F. Donati & J. D. Landstreet, 2009. *ARA&A*, 47:333–370.
J. S. Drilling & A. U. Landolt, 2000. *Normal Stars*, page 381.

G. Duchêne & A. Kraus, 2013. *ARA&A*, 51:269–310.

P. P. Eggleton, 1983. *ApJ*, 268:368.

P. P. Eggleton, L. G. Kiseleva, & P. Hut, 1998. *ApJ*, 499:853–870.

E. Ergma & A. Fedorova, 1998. *A&A*, 338:69–74.

H. Falcke, F. Melia, & E. Agol, 2000. *ApJ*, 528:L13–L16.

R. P. Fender, E. Gallo, & D. Russell, 2010. *MNRAS*, 406:1425–1434.

R. P. Fender, S. T. Garrington, D. J. McKay, et al., 1999. *MNRAS*, 304:865–876.

R. P. Fender, T. J. Maccarone, & I. Heywood, 2013. *MNRAS*, 430:1538–1547.

A. V. Filippenko, D. C. Leonard, T. Matheson, et al., 1999. *PASP*, 111:969–979.

A. V. Filippenko, T. Matheson, & A. J. Barth, 1995a. *ApJ*, 455:L139.

A. V. Filippenko, T. Matheson, & L. C. Ho, 1995b. *ApJ*, 455:614.

A. V. Filippenko, T. Matheson, D. C. Leonard, et al., 1997. *PASP*, 109:461–467.

H. C. Ford, F. Bartko, & et al. Bely, 1998. In *Space Telescopes and Instruments V*, editors P. Y. Bely & J. B. Breckinridge, volume 3356 of *Proc. SPIE*, pages 234–248.

T. Fragos, B. Willems, V. Kalogera, et al., 2009. *ApJ*, 697:1057–1070.

C. Fryer & V. Kalogera, 1997. *ApJ*, 489:244–253.

C. L. Fryer, 1999. *ApJ*, 522:413–418.

C. L. Fryer, K. Belczynski, G. Wiktorowicz, et al., 2012. *ApJ*, 749:91.

C. L. Fryer & V. Kalogera, 2001. *ApJ*, 554:548–560.

C. L. Fryer & A. Kusenko, 2006. *ApJS*, 163:335–343.

C. L. Fryer & M. S. Warren, 2002. *ApJ*, 574:L65–L68.

M. Y. Fujimoto, M. Sztajno, W. H. G. Lewin, et al., 1988. *A&A*, 199:L9–L12.

D. K. Galloway, D. Chakrabarty, M. P. Muno, et al., 2001. *ApJ*, 549:L85–L88.

M. R. Garcia, J. E. McClintock, R. Narayan, et al., 2001. *ApJ*, 553:L47–L50.

D. M. Gelino, 2001. *Modeling infrared ellipsoidal variations: Determining the masses of black holes in soft x-ray transients*. Ph.D. thesis, Center for Astrophysics and Space Sciences, University of California, San Diego.

D. M. Gelino, Ş. Balman, Ü. Kızıloğlu, et al., 2006. *ApJ*, 642:438–442.

D. M. Gelino & T. E. Harrison, 2003. *ApJ*, 599:1254–1259.

D. M. Gelino, T. E. Harrison, & B. J. McNamara, 2001. *AJ*, 122:971–978.

O. Gerhard, 2015. In *Fifty Years of Wide Field Studies in the Southern Hemisphere: Resolved Stellar Populations of the Galactic Bulge and Magellanic Clouds*, editors S. Points & A. Kunder, volume 491 of *Astronomical Society of the Pacific Conference Series*, page 169.

A. M. Ghez, S. Salim, N. N. Weinberg, et al., 2008. *ApJ*, 689:1044-1062.

R. Giacconi, H. Gursky, F. R. Paolini, et al., 1962. *Physical Review Letters*, 9:439–443.

S. Gillessen, F. Eisenhauer, S. Trippe, et al., 2009. *ApJ*, 692:1075–1109.

P. Goldreich, D. Lai, & M. Sahrling, 1997. In *Unsolved Problems in Astrophysics*, editors J. N. Bahcall & J. P. Ostriker, pages 269–280.

P. Goldreich & P. D. Nicholson, 1977. *Icarus*, 30:301–304.

J. I. González Hernández, J. Casares, R. Rebolo, et al., 2011. *ApJ*, 738:95.

J. I. González Hernández, R. Rebolo, & J. Casares, 2012. *ApJ*, 744:L25.

J. I. González Hernández, R. Rebolo, & J. Casares, 2014. *MNRAS*, 438:L21–L25.

J. I. González Hernández, R. Rebolo, G. Israelian, et al., 2004. *ApJ*, 609:988–998.
J. I. González Hernández, R. Rebolo, G. Israelian, et al., 2006. *ApJ*, 644:L49–L52.
J. I. González Hernández, R. Rebolo, G. Israelian, et al., 2008. *ApJ*, 679:732-745.
E. A. González-Solares, N. A. Walton, R. Greimel, et al., 2008. *MNRAS*, 388:89–104.
S. Goswami, P. Kiel, & F. A. Rasio, 2014. *ApJ*, 781:81.
M. Gottwald, F. Haberl, A. N. Parmar, et al., 1986. *ApJ*, 308:213–224.
E. Gourgoulhon & P. Haensel, 1993. *A&A*, 271:187.
A. Gualandris, M. Colpi, S. Portegies Zwart, et al., 2005. *ApJ*, 618:845–851.
T. Güver & F. Özel, 2009. *MNRAS*, 400:2050–2053.
B. M. S. Hansen & E. S. Phinney, 1997. *MNRAS*, 291:569.
A. Harpaz & S. Rappaport, 1991. *ApJ*, 383:739–744.
E. R. Harrison & E. Tademaru, 1975. *ApJ*, 201:447–461.
J. W. Hartman, 1997. *A&A*, 322:127–130.
J. W. Hartman, D. Bhattacharya, R. Wijers, et al., 1997. *A&A*, 322:477–488.
A. Heger, C. L. Fryer, S. E. Woosley, et al., 2003. *ApJ*, 591:288–300.
S. Heinz, P. Sell, R. P. Fender, et al., 2013. *ApJ*, 779:171.
A. A. Henden, M. Templeton, D. Terrell, et al., 2016. *VizieR Online Data Catalog*, 2336.
M. Herant, W. Benz, W. R. Hix, et al., 1994. *ApJ*, 435:339–361.
F. Herrmann, I. Hinder, D. Shoemaker, et al., 2007. *ApJ*, 661:430–436.
J. G. Hills, 1983. *ApJ*, 267:322–333.
R. M. Hjellming & M. P. Rupen, 1995. *Nature*, 375:464–468.
G. Hobbs, D. R. Lorimer, A. G. Lyne, et al., 2005. *MNRAS*, 360:974–992.
J. Homan, J. K. Fridriksson, P. G. Jonker, et al., 2013. *ApJ*, 775:9.
J. Homan, M. Méndez, R. Wijnands, et al., 1999. *ApJ*, 513:L119–L122.
J. Homan, R. Wijnands, A. Kong, et al., 2006. *MNRAS*, 366:235–237.
J. R. Hurley, O. R. Pols, & C. A. Tout, 2000. *MNRAS*, 315:543–569.
J. R. Hurley, C. A. Tout, & O. R. Pols, 2002. *MNRAS*, 329:897–928.
P. Hut, 1980. *A&A*, 92:167–170.
P. Hut, 1981. *A&A*, 99:126–140.
R. I. Hynes, 2005. *ApJ*, 623:1026–1043.
R. I. Hynes, M. A. P. Torres, C. O. Heinke, et al., 2014. *ApJ*, 780:11.
A. Igoshev, F. Verbunt, & E. Cator, 2016. *A&A*, 591:A123.
J. J. M. in't Zand, R. Cornelisse, E. Kuulkers, et al., 2001. *A&A*, 372:916–921.
Z. Ioannou, E. L. Robinson, W. F. Welsh, et al., 2004. *AJ*, 127:481–488.
A. Irrgang, B. Wilcox, E. Tucker, et al., 2013. *A&A*, 549:A137.
J. A. Irwin, 2005. *ApJ*, 631:511–517.
G. Israelian, R. Rebolo, G. Basri, et al., 1999. *Nature*, 401:142–144.
P. B. Ivanov & J. C. B. Papaloizou, 2004. *MNRAS*, 353:1161–1175.
N. Ivanova & V. Kalogera, 2006. *ApJ*, 636:985–994.
N. Ivanova & R. E. Taam, 2003. *ApJ*, 599:516–521.
B. Jackson, R. Greenberg, & R. Barnes, 2008. *ApJ*, 678:1396–1406.
H.-T. Janka, 2012. *Annual Review of Nuclear and Particle Science*, 62:407–451.

H.-T. Janka, 2013. *MNRAS*, 434:1355–1361.

H.-T. Janka & E. Mueller, 1996. *A&A*, 306:167.

T. Janssen & M. H. van Kerkwijk, 2005. *A&A*, 439:433–441.

S. Jester, D. P. Schneider, G. T. Richards, et al., 2005. *AJ*, 130:873–895.

T. Johannsen, D. Psaltis, & J. E. McClintock, 2009. *ApJ*, 691:997–1004.

C. B. Johnson, R. I. Hynes, T. Maccarone, et al., 2014. *MNRAS*, 444:1584–1590.

H. M. Johnston, 1996. In *NATO Advanced Science Institutes (ASI) Series C*, editors R. A. M. J. Wijers, M. B. Davies, & C. A. Tout, volume 477 of *NATO Advanced Science Institutes (ASI) Series C*, page 385.

S. Johnston, R. N. Manchester, A. G. Lyne, et al., 1992. *ApJ*, 387:L37–L41.

J. E. Jones, D. M. Alloin, & B. J. T. Jones, 1984. *ApJ*, 283:457–465.

P. G. Jonker, J. C. A. Miller-Jones, J. Homan, et al., 2012. *MNRAS*, 423:3308–3315.

P. G. Jonker & G. Nelemans, 2004. *MNRAS*, 354:355–366.

P. G. Jonker, G. Nelemans, & C. G. Bassa, 2007. *MNRAS*, 374:999–1005.

P. G. Jonker, M. A. P. Torres, R. I. Hynes, et al., 2014. *ApJS*, 210:18.

P. G. Jonker, M. van der Klis, J. Homan, et al., 2001. *ApJ*, 553:335–340.

P. G. et al. Jonker et al., 2011. *ApJS*, 194:18.

S. Justham, S. Rappaport, & P. Podsiadlowski, 2006. *MNRAS*, 366:1415–1423.

P. Kaaret, J. J. M. in 't Zand, J. Heise, et al., 2002. *ApJ*, 575:1018–1024.

V. Kalogera, 1996. *ApJ*, 471:352.

V. Kalogera, 1999. *ApJ*, 521:723–734.

V. Kalogera, C. Kim, D. R. Lorimer, et al., 2004. *ApJ*, 601:L179–L182.

V. Kalogera, U. Kolb, & A. R. King, 1998. *ApJ*, 504:967–977.

V. Kalogera & R. F. Webbink, 1998. *ApJ*, 493:351–367.

R. G. Kaptein, J. J. M. in't Zand, E. Kuulkers, et al., 2000. *A&A*, 358:L71–L74.

V. M. Kaspi, S. Johnston, J. F. Bell, et al., 1994. *ApJ*, 423:L43–L45.

S. D. Kawaler, 1988. *ApJ*, 333:236–247.

P. D. Kiel & J. R. Hurley, 2006. *MNRAS*, 369:1152–1166.

C. Knigge, I. Baraffe, & J. Patterson, 2011. *ApJS*, 194:28.

C. S. Kochanek, 2015. *MNRAS*, 446:1213–1222.

C. Koen, D. Kilkenny, F. van Wyk, et al., 2010. *MNRAS*, 403:1949–1968.

L. Kreidberg, C. D. Bailyn, W. M. Farr, et al., 2012. *ApJ*, 757:36.

S. R. Kulkarni, P. Hut, & S. McMillan, 1993. *Nature*, 364:421–423.

P. Kumar & J. Goodman, 1996. *ApJ*, 466:946.

E. Kuulkers, J. Homan, M. van der Klis, et al., 2002. *A&A*, 382:947–973.

E. Kuulkers, C. Kouveliotou, T. Belloni, et al., 2013. *A&A*, 552:A32.

D. Lai, 2003. In *Radio Pulsars*, editors M. Bailes, D. J. Nice, & S. E. Thorsett, volume 302 of *Astronomical Society of the Pacific Conference Series*, page 307.

D. Lai, D. F. Chernoff, & J. M. Cordes, 2001. *ApJ*, 549:1111–1118.

D. Lai & Y.-Z. Qian, 1998. *ApJ*, 505:844–853.

A. Laor, 1991. *ApJ*, 376:90–94.

M. Lecar, J. C. Wheeler, & C. F. McKee, 1976. *ApJ*, 205:556–562.

V. M. Lipunov, K. A. Postnov, & M. E. Prokhorov, 1997. *MNRAS*, 288:245–259.
A. G. Lyne & D. R. Lorimer, 1994. *Nature*, 369:127–129.
B. Ma & X.-D. Li, 2009. *ApJ*, 691:1611–1617.
T. Maccarone & C. Knigge, 2007. *Astronomy and Geophysics*, 48(5):5.12–5.20.
T. J. Maccarone, 2014. *Space Sci. Rev.*, 183:477–489.
T. J. Maccarone, A. Kundu, S. E. Zepf, et al., 2007. *Nature*, 445:183–185.
T. J. Maccarone, M. A. P. Torres, C. T. Britt, et al., 2012. *MNRAS*, 426:3057–3069.
A. I. MacFadyen, S. E. Woosley, & A. Heger, 2001. *ApJ*, 550:410–425.
I. Mandel, 2016. *MNRAS*, 456:578–581.
T. R. Marsh, E. L. Robinson, & J. H. Wood, 1994. *MNRAS*, 266:137.
R. G. Martin, C. A. Tout, & J. E. Pringle, 2010. *MNRAS*, 401:1514–1520.
K. O. Mason, A. N. Parmar, & N. E. White, 1985. *MNRAS*, 216:1033–1041.
S. Matsumura, S. J. Peale, & F. A. Rasio, 2010. *ApJ*, 725:1995–2016.
J. E. McClintock & R. A. Remillard, 2006. In *Compact stellar X-ray sources*, editors W. H. G. Lewin & M. van der Klis, Cambridge Astrophysics Series, No. 39, page 157. Cambridge Univ. Press, Cambridge.
J. E. McClintock, R. Shafee, R. Narayan, et al., 2006. *ApJ*, 652:518–539.
P. J. McMillan, 2011. *MNRAS*, 414:2446–2457.
S. L. W. McMillan, R. E. Taam, & P. N. McDermott, 1990. *ApJ*, 354:190–200.
K. Menou, A. A. Esin, R. Narayan, et al., 1999. *ApJ*, 520:276–291.
D. Merritt, M. Milosavljević, M. Favata, et al., 2004. *ApJ*, 607:L9–L12.
E. Michaely & H. B. Perets, 2016. *MNRAS*.
D. Mihalas & J. Binney, 1981. *Galactic astronomy: Structure and kinematics /2nd edition/*, page 608. Freeman, W. H. and Co., San Francisco, CA.
M. C. Miller & D. P. Hamilton, 2002. *MNRAS*, 330:232–240.
J. C. A. Miller-Jones, 2014. *PASA*, 31:e016.
J. C. A. Miller-Jones, P. G. Jonker, V. Dhawan, et al., 2009a. *ApJ*, 706:L230–L234.
J. C. A. Miller-Jones, P. G. Jonker, G. Nelemans, et al., 2009b. *MNRAS*, 394:1440–1448.
D. Minniti, P. W. Lucas, J. P. Emerson, et al., 2010. *New A*, 15:433–443.
I. F. Mirabel, V. Dhawan, R. P. Mignani, et al., 2001. *Nature*, 413:139–141.
I. F. Mirabel & I. Rodrigues, 2003. *Science*, 300:1119–1121.
A. Modigliani, P. Goldoni, & et al. Royer, F., 2010. In *SPIE Conference Series*, volume 7737, page 28.
M. Morscher, B. Pattabiraman, C. Rodriguez, et al., 2015. *ApJ*, 800:9.
M. P. Muno, D. W. Fox, E. H. Morgan, et al., 2000. *ApJ*, 542:1016–1033.
T. Murakami, H. Inoue, K. Makishima, et al., 1987. *PASJ*, 39:879–886.
S. Naoz, T. Fragos, A. Geller, et al., 2015. *ArXiv e-prints*.
R. Narayan, M. R. Garcia, & J. E. McClintock, 2002. In *The Ninth Marcel Grossmann Meeting*, editors V. G. Gurzadyan, R. T. Jantzen, & R. Ruffini, pages 405–425.
R. Narayan & J. E. McClintock, 2005. *ApJ*, 623:1017–1025.
L. Natalucci, A. Bazzano, M. Cocchi, et al., 2000. *ApJ*, 536:891–895.
G. Nelemans, 2007. In *Massive Stars in Interactive Binaries*, editors N. St.-Louis & A. F. J. Moffat, volume 367 of *Astronomical Society of the Pacific Conference Series*, page 533.
G. Nelemans, T. M. Tauris, & E. P. J. van den Heuvel, 1999. *A&A*, 352:L87–L90.

D. L. Nidever, G. W. Marcy, R. P. Butler, et al., 2002. *ApJS*, 141:503–522.
H. Nieuwenhuijzen & C. de Jager, 1990. *A&A*, 231:134–136.
S. Nishiyama, M. Tamura, H. Hatano, et al., 2009. *ApJ*, 696:1407–1417.
J. Nordhaus, T. D. Brandt, A. Burrows, et al., 2012. *MNRAS*, 423:1805–1812.
G. I. Ogilvie & G. Lesur, 2012. *MNRAS*, 422:1975–1987.
G. I. Ogilvie & D. N. C. Lin, 2007. *ApJ*, 661:1180–1191.
J. A. Orosz, C. D. Bailyn, J. E. McClintock, et al., 1996. *ApJ*, 468:380.
J. A. Orosz, E. Kuulkers, M. van der Klis, et al., 2001. *ApJ*, 555:489–503.
J. A. Orosz, J. E. McClintock, J. P. Aufdenberg, et al., 2011a. *ApJ*, 742:84.
J. A. Orosz, J. E. McClintock, R. A. Remillard, et al., 2004. *ApJ*, 616:376–382.
J. A. Orosz, E. J. Polisensky, C. D. Bailyn, et al., 2002. In *American Astronomical Society Meeting Abstracts*, volume 34 of *Bulletin of the American Astronomical Society*, page 1124.
J. A. Orosz, J. F. Steiner, J. E. McClintock, et al., 2011b. *ApJ*, 730:75.
D. E. Osterbrock, J. P. Fulbright, & et al. Martel, 1996. *PASP*, 108:277.
F. Özel, D. Psaltis, R. Narayan, et al., 2010. *ApJ*, 725:1918–1927.
B. Paczyński, 1971. *ARA&A*, 9:183.
B. Paczynski, 1976. In *Structure and Evolution of Close Binary Systems*, editors P. Eggleton, S. Mitton, & J. Whelan, volume 73 of *IAU Symposium*, page 75.
B. Paczynski, 1990. *ApJ*, 348:485–494.
E. N. Parker, 1958. *ApJ*, 128:677.
P. M. S. Parkinson, D. M. Tournear, E. D. Bloom, et al., 2003. *ApJ*, 595:333–341.
K. Penev, D. Sasselov, F. Robinson, et al., 2007. *ApJ*, 655:1166–1171.
E. Pfahl, S. Rappaport, & P. Podsiadlowski, 2002a. *ApJ*, 573:283–305.
E. Pfahl, S. Rappaport, & P. Podsiadlowski, 2003. *ApJ*, 597:1036–1048.
E. Pfahl, S. Rappaport, P. Podsiadlowski, et al., 2002b. *ApJ*, 574:364–376.
R. M. Plotkin, E. Gallo, & P. G. Jonker, 2013. *ApJ*, 773:59.
P. Podsiadlowski, 1991. *Nature*, 350:136–138.
P. Podsiadlowski, N. Langer, A. J. T. Poelarends, et al., 2004. *ApJ*, 612:1044–1051.
P. Podsiadlowski, S. Rappaport, & Z. Han, 2003. *MNRAS*, 341:385–404.
O. R. Pols, K.-P. Schröder, J. R. Hurley, et al., 1998. *MNRAS*, 298:525–536.
S. Portegies Zwart, S. McMillan, & Harfst et al., 2009. *New A*, 14:369–378.
S. F. Portegies Zwart & S. L. W. McMillan, 2000. *ApJ*, 528:L17–L20.
S. F. Portegies Zwart & F. Verbunt, 1996. *A&A*, 309:179–196.
S. F. Portegies Zwart, F. Verbunt, & E. Ergma, 1997. *A&A*, 321:207–212.
E. Pylyser & G. J. Savonije, 1988. *A&A*, 191:57–70.
E. H. P. Pylyser & G. J. Savonije, 1989. *A&A*, 208:52–62.
F. A. Rasio & S. L. Shapiro, 1991. *ApJ*, 377:559–580.
F. A. Rasio, C. A. Tout, S. H. Lubow, et al., 1996. *ApJ*, 470:1187.
E. M. Ratti, T. F. J. van Grunsven, P. G. Jonker, et al., 2013. *MNRAS*, 428:3543–3550.
R. Remillard, E. Morgan, D. Smith, et al., 2000. *IAU Circ.*, 7389.
R. A. Remillard & J. E. McClintock, 2006. *ARA&A*, 44:49–92.
R. A. Remillard, J. A. Orosz, J. E. McClintock, et al., 1996. *ApJ*, 459:226.

S. Repetto, M. B. Davies, & S. Sigurdsson, 2012. *MNRAS*, 425:2799–2809.
S. Repetto, A. Igoshev, & G. Nelemans, 2016. *MNRAS*.
S. Repetto & G. Nelemans, 2014. *MNRAS*, 444:542–557.
S. Repetto & G. Nelemans, 2015. *MNRAS*, 453:3341–3355.
M. T. Reynolds, P. J. Callanan, & A. V. Filippenko, 2007. *MNRAS*, 374:657–663.
H. Ritter & U. Kolb, 2003. *A&A*, 404:301–303.
R. W. Romani, 1992. *ApJ*, 399:621–626.
R. W. Romani, 1996. In *Compact Stars in Binaries*, editors J. van Paradijs, E. P. J. van den Heuvel, & E. Kuulkers, volume 165 of *IAU Symposium*, page 93.
R. W. Romani, 1998. *A&A*, 333:583–590.
M. Ruffert & H.-T. Janka, 2001. *A&A*, 380:544–577.
T. D. Russell, R. Soria, J. C. A. Miller-Jones, et al., 2014. *MNRAS*, 439:1390–1402.
M. Schultheis, B. Q. Chen, B. W. Jiang, et al., 2014. *A&A*, 566:A120.
T. Shahbaz, D. M. Russell, C. Zurita, et al., 2013. *MNRAS*, 434:2696–2706.
N. I. Shakura & R. A. Sunyaev, 1973. *A&A*, 24:337–355.
S. Sigurdsson & L. Hernquist, 1993. *Nature*, 364:423–425.
A. C. Sippel & J. R. Hurley, 2013. *MNRAS*, 430:L30–L34.
A. Skumanich, 1972. *ApJ*, 171:565.
A. P. Smale, 1998. *ApJ*, 498:L141–L145.
M. C. Smith, G. R. Ruchti, & Helmi et al, 2007. *MNRAS*, 379:755–772.
D. Steeghs & P. G. Jonker, 2007. *ApJ*, 669:L85–L88.
J. Strader, L. Chomiuk, T. J. Maccarone, et al., 2012. *Nature*, 490:71–73.
T. E. Strohmayer, C. B. Markwardt, J. H. Swank, et al., 2003. *ApJ*, 596:L67–L70.
K. Takahashi, T. Yoshida, & H. Umeda, 2013. *ApJ*, 771:28.
T. M. Tauris, N. Langer, & P. Podsiadlowski, 2015. *MNRAS*, 451:2123–2144.
T. M. Tauris & E. P. J. van den Heuvel, 2006. *Formation and evolution of compact stellar X-ray sources*, pages 623–665.
Y. Tawara, T. Kii, S. Hayakawa, et al., 1984. *ApJ*, 276:L41–L44.
J. H. Taylor & J. M. Cordes, 1993. *ApJ*, 411:674–684.
A. F. Tennant, A. C. Fabian, & R. A. Shafer, 1986. *MNRAS*, 221:27P–31P.
B. E. Tetarenko, A. Bahramian, R. M. Arnason, et al., 2016a. *ApJ*, 825:10.
B. E. Tetarenko, G. R. Sivakoff, C. O. Heinke, et al., 2016b. *ApJS*, 222:15.
S. A. Teukolsky, W. T. Vetterling, B. P. Flannery, et al., 1993. *The Observatory*, 113:214.
The LIGO Scientific Collaboration, the Virgo Collaboration, B. P. Abbott, et al., 2016. *ArXiv e-prints*.
J. A. Tomsick, D. M. Gelino, J. P. Halpern, et al., 2004. *ApJ*, 610:933–940.
J. Tonry & M. Davis, 1979. *AJ*, 84:1511–1525.
M. A. P. Torres, P. G. Jonker, C. T. Britt, et al., 2014. *MNRAS*, 440:365–386.
C. A. Tout, O. R. Pols, P. P. Eggleton, et al., 1996. *MNRAS*, 281:257–262.
A. V. Tutukov, A. V. Fedorova, E. V. Ergma, et al., 1985. *Soviet Astronomy Letters*, 11:52–56.
A. Udalski, M. K. Szymański, & G. Szymański, 2015. *Acta Astron.*, 65:1–38.
M. Ugliano, H.-T. Janka, A. Marek, et al., 2012. *ApJ*, 757:69.
J. S. Urquhart, C. C. Figura, T. J. T. Moore, et al., 2014. *MNRAS*, 437:1791–1807.

A. K. F. Val Baker, A. J. Norton, & H. Quaintrell, 2005. *A&A*, 441:685–688.
F. Valsecchi, E. Glebbeek, W. M. Farr, et al., 2010. *Nature*, 468:77–79.
F. Valsecchi & F. A. Rasio, 2014. *ApJ*, 786:102.
E. P. J. van den Heuvel, 1983. In *Accretion-Driven Stellar X-ray Sources*, editors W. H. G. Lewin & E. P. J. van den Heuvel, page 308.
E. P. J. van den Heuvel & C. de Loore, 1973. *Nature Physical Science*, 245:117–118.
E. P. J. van den Heuvel & G. M. H. J. Habets, 1984. *Nature*, 309:598–600.
A. van der Meer, L. Kaper, M. H. van Kerkwijk, et al., 2005. In *Interacting Binaries: Accretion, Evolution, and Outcomes*, editors L. Burderi, L. A. Antonelli, F. D'Antona, et al., volume 797 of *American Institute of Physics Conference Series*, pages 623–626.
M. H. van Kerkwijk, J. van Paradijs, & E. J. Zuiderwijk, 1995. *A&A*, 303:497.
J. van Paradijs & N. White, 1995. *ApJ*, 447:L33.
F. Verbunt & W. H. G. Lewin, 2006. *Globular cluster X-ray sources*, pages 341–379.
F. Verbunt & E. S. Phinney, 1995. *A&A*, 296:709.
F. Verbunt & C. Zwaan, 1981. *A&A*, 100:L7–L9.
Vernet et al., 2011. *A&A*, 536:A105.
R. A. Wade & K. Horne, 1988. *ApJ*, 324:411–430.
N. A. Webb, T. Naylor, Z. Ioannou, et al., 2000. *MNRAS*, 317:528–534.
E. J. Weber & L. Davis, Jr., 1967. *ApJ*, 148:217–227.
B. L. Webster & P. Murdin, 1972. *Nature*, 235:37–38.
T. Wevers, S. T. Hodgkin, P. G. Jonker, et al., 2016. *MNRAS*.
N. Wex & S. M. Kopeikin, 1999. *ApJ*, 514:388–401.
N. E. White & J. van Paradijs, 1996. *ApJ*, 473:L25.
R. Wijnands, M. P. Muno, J. M. Miller, et al., 2002. *ApJ*, 566:1060–1068.
B. Willems, M. Henninger, T. Levin, et al., 2005. *ApJ*, 625:324–346.
T.-W. Wong, F. Valsecchi, A. Ansari, et al., 2014. *ApJ*, 790:119.
T.-W. Wong, F. Valsecchi, T. Fragos, et al., 2012. *ApJ*, 747:111.
T.-W. Wong, B. Willems, & V. Kalogera, 2010. *ApJ*, 721:1689–1701.
J. Wu, P. G. Jonker, & et al. Torres, M. A. P., 2015. *MNRAS*, 448:1900–1915.
Ł. Wyrzykowski, Z. Kostrzewa-Rutkowska, & J. et al. Skowron, 2016. *MNRAS*, 458:3012–3026.
Z. Xing, J. M. Centrella, & S. L. W. McMillan, 1994. *Phys. Rev. D*, 50:6247–6261.
L. R. Yungelson, J.-P. Lasota, G. Nelemans, et al., 2006. *A&A*, 454:559–569.
J. P. Zahn, 1966. *Annales d'Astrophysique*, 29:489.
J.-P. Zahn, 1975. *A&A*, 41:329–344.
J.-P. Zahn, 1977. *A&A*, 57:383–394.
J.-P. Zahn, 1989. *A&A*, 220:112–116.
J.-P. Zahn, 2008. In *EAS Publications Series*, editors M.-J. Goupil & J.-P. Zahn, volume 29 of *EAS Publications Series*, pages 67–90.
S. N. Zhang, W. Cui, & W. Chen, 1997. *ApJ*, 482:L155–L158.
W. Zhang, S. E. Woosley, & A. Heger, 2008. *ApJ*, 679:639–654.
J. Zhong, S. Lépine, J. Hou, et al., 2015. *AJ*, 150:42.
Z.-Y. Zuo, X.-D. Li, & X.-W. Liu, 2008. *MNRAS*, 387:121–127.

Summary

This Thesis revolves around the topic of black holes (BHs) in X-ray binaries (XRBs). The trigger of this work was to understand how stellar-mass BHs form, a question which we tackled both with theoretical as well as observational studies. The formation mechanism of BHs is an unsolved problem in high-energy astrophysics, in particular when it comes to the amount of mass ejected at formation and to how large is the velocity BHs acquire at birth (the so-called *natal kick*), if they acquire a velocity at all. One way of tackling these uncertainties is to perform physically-motivated simulations of the core-collapse supernova, which is computationally challenging (see e.g. Fryer & Warren 2002; Janka 2012). Another way is to study the birth and evolution of XRBs hosting a BH accreting from a stellar companion, which is the method we use in this Thesis. On the theoretical side, we combine an approach typical of binary population synthesis calculations with a more detailed approach which solves for the binary evolution of each source. When possible, we describe the different evolutionary paths of the binary via analytical calculations and timescale arguments. On the observational side, we combine the techniques of optical spectroscopy and photometry, with the goal of increasing the sample of Galactic BHs.

Chapter I: A preliminary study of black hole natal kicks

The investigation of BH natal kicks was motivated by the study of Jonker & Nelemans 2004, who compared the Galactic distribution of BH and neutron star (NS) XRBs and found that they had a similar scale height above the Galactic plane. It was well-known that NS systems acquired their offset above the Galactic plane as a consequence of the NS natal kick. If was not known at all, on the other hand, whether BHs would also receive suck kicks, and how large would they be. At most, BHs were expected to receive a scaled-down version of such natal kicks, simply because they are larger in mass, and the asymmetric ejection of mass in the supernova would conserve the linear momentum. We build a population of BH-XRBs, follow their trajectories in the Galactic potential, and compare the resulting spatial distribution with the observed one, finding that a population in which BHs receive natal kicks as large as those of NSs fits the height above the plane of the observed population best. This is an unexpected result, which triggers our follow-up study (Chapter IV), in which we use a more realistic model for the binary evolution of the sources.

Chapter II: Tides coupled with magnetic braking

A binary system is not a static system and it undergoes changes of its orbital parameters in time, as a consequence of the loss of orbital energy and orbital angular momentum. In particular, such losses might initiate the mass transfer between the two binary components. One possible way of shrinking the binary separation is when tides are acting together with a stellar wind. In a subset of BH-XRBs, the ones formed by a BH with a companion of mass of the order of one solar mass or less, such winds take the form of a magnetic wind. Magnetic braking is the loss of angular momentum in a stellar wind anchored to the star's magnetic field. Even if the mass loss is negligible (10^{-14} solar masses per year for a Sun-like star), the wind, being forced to corotate with the star out to large stellar radii, removes a great fraction of the star's rotational angular momentum. If the star is in a binary, the tidal torque tends to replenish the star's rotational angular momentum reservoir, transferring angular momentum from the orbit to the star, which causes a secular shrinking of the binary semi-major axis, and can lead to Roche lobe overflow. In most previous studies of the binary evolution of BH-XRBs, this coupling has been simplified and the evolution has been described through timescale considerations only. We check how accurate these timescales are, focusing on the circularisation timescales. We couple the tidal equations within the equilibrium-tide model of Hut 1981 (which we extend to arbitrary inclinations of the stellar spin with respect to the orbital spin) with the equation governing the spin-down of the star due to the magnetic braking. We follow the evolution of different types of binaries formed by a compact object with a Sun-like star: BH low-mass XRBs (BH-LMXBs) and planetary systems formed by a star and a hot Jupiter. We find that an accurate description of the evolution of the binaries requires following the coupled evolution of the rotational and orbital elements under the influence of tides and magnetic braking. In particular, the eccentricity evolution can strongly vary from the exponential decay dictated by a simple timescale calculation. This result was already pointed out by Barker & Ogilvie 2009 for short-period planetary systems, but our study is the first in highlighting the same conclusion for binaries containing a BH, and more in general a compact object. An interesting outcome of the coupling between tides and magnetic braking is the existence, in some cases, of a *pseudo-equilibrium state*, and we find conditions for its attainability. We also couple the tidal equations with a different type of stellar wind, one in which the mass loss in non-negligible, as it happens for high-mass stars. In this case, we find a magnetic-braking-type of solution: the *wind braking*, which drives the binary to Roche lobe overflow, and which we describe analytically.

Chapter III: Backtracing the evolution of black hole X-ray binaries

The goal of this paper is to retrieve the conditions at BH formation from the observed properties of a subset of the Galactic BH-XRB population, those ones with a short orbital period. The orbital parameters, peculiar velocities and Galactic position of these binaries directly follow from their evolutionary history, and are affected in particular by the conditions at the moment of compact object formation. We follow the evolution of the binaries backwards in time, from the current X-ray phase of mass-transfer to the moment the BH formed. The method of retrieving the properties at BH formation from backtracing the evolution of binaries was already employed in previous works such as Willems et al. 2005 and Fragos et al. 2009. In our case, instead of using a detailed binary evolution approach, we build a semi-analytical computational scheme, which is much faster, and which gives consistent results with

the detailed binary evolution calculations. In this way, we find those combinations of natal kick and ejected mass at BH formation which are consistent with the observed properties of the binaries. Such parameter space is further restricted when using the kinematic information of the binary: from the offset of the source above the Galactic plane, we derive a lower limit on its peculiar velocity right after the BH was formed. We find three BH-formation scenarios which are compatible with some of the sources we studied: i) two BHs (and possibly more if accounting for BH candidates as well) are consistent with a NS-like natal kick; ii) five systems are consistent with a standard scenario, in which the BH does not receive any natal kick and the peculiar velocity of the binary is attributable to the mass ejection in the supernova only; iii) five systems are consistent with a natal kick, while requiring no baryonic mass ejection at BH formation. In the third scenario, the BH would then have formed in the dark, i.e. with no supernova, and the natal kick could be driven by asymmetric neutrino emission. It is the first time that this scenario has been applied to the evolution of BH-LMXBs, whereas it was first found to be consistent with the formation of a few (more massive) BHs in high-mass XRBs (Mirabel & Rodrigues 2003; Valsecchi et al. 2010). Another important outcome of this study is that the minimum natal kick is not greatly affected by the binary evolution of the sources; it is mostly affected by the kinematics, and therefore by the uncertainty on the distance. This has the consequence that it is not needed to perform a full modelling of the binary evolution of an XRB in order to set constraints on the natal kick. We furthermore find no evidence for a correlation between the BH mass and the natal kick (within our limited sample of sources); such a correlation is expected in a model in which the natal kick scales inversely as the amount of mass which falls-back onto the proto NS. We also perform a population-synthesis-type of analysis to investigate the effect of the different natal kicks and ejected masses on the observational properties of the systems. This is to check for possible observational biases that would make that the observed systems are predominantly those with particular natal kicks and/or ejected masses. We find that the current population of BH-LMXBs is biased towards low natal kicks, less than $100 - 200$ km/s.

Chapter IV: Neutron star formation VS black hole formation

This work is divided into three main parts. First, we study the imprints that different compact object formation models have on the Galactic distribution of XRBs containing a BH or a NS, building synthetic populations of such binaries. We find that the formation models directly affect the spatial distribution of the binaries, and that even when BHs and NSs receive the same natal kick at birth, NSs would still show a larger scale height above the Galactic plane, which is in line with what we find for the observed populations. We turn then to the comparison between the Galactic distribution of BH- and NS-XRBs with the simulated ones, following and complementing the work in Chapter I, this time solving for the binary evolution of the sources, using the most-updated catalogue of BHs in the Galaxy, and accounting for the uncertainty on the distance to the sources. We find that a population model in which at least some BHs receive a (relatively) high natal kick fits the observed BH-XRBs best. For the NS case, we find that a high natal-kick distribution, consistent with the one derived from the measurement of pulsar proper motion, best fits the observed data. The third part is dedicated to the extensive analysis of the method we previously used (in Chapter I and III) to estimate the minimal peculiar velocity of an individual BH-XRB at birth. We find that this method may be less reliable in the bulge of the Galaxy for certain models of the Galactic potential, but that our estimate is excellent for most of the BH-XRBs.

Chapter V: A new candidate black hole X-ray binary

The last Chapter of this Thesis is dedicated to the optical follow-up of a candidate XRB discovered in the Galactic Bulge Survey of Jonker et al. This survey, which looks for faint X-ray sources in the bulge of the Galaxy, aims at increasing the number of Galactic accreting binaries, and in particular the number of those ones hosting a BH and detected in quiescence. One of the most promising sources discovered by the survey is CX1004, a candidate BH-XRB. We took X-shooter spectra of the optical counterpart to CX1004, which we use to measure the radial velocity of the putative companion star as well as its spectral type. The spectra show a large double-peaked Hα line which would suggest a BH-XRB with a very short orbital period (of the order of 0.5 day) and a semi-amplitude radial velocity of the companion star of 500 km/s. Surprisingly, we find no evidence for any orbital modulation of the radial velocity curve. We identify the star whose photospheric absorption lines we see in the spectra as an M2V star. These results could imply that the M-star is a chance line of sight interloper or that CX1004 is part of a hierarchical triple hosting a BH, with the M-type star in a wide orbit around the inner XRB. Future follow-up observations are required to fully determine the nature of CX1004.

Conclusion & future prospects

This Thesis has fully investigated the possible methods to retrieve information about how BHs form in the core-collapse supernova from the observed properties of BH-XRBs. In Chapter IV, when comparing the Galactic distribution of a synthetic population of BH-XRBs with the observed distribution, we find that a model in which some BHs receive a (relatively) high natal kick best fits the observed data, whereas the low natal kick model gives an unsatisfactory fit. However, due to the limited size of the observed sample of binaries with a solid measurement of the distance (less than 20 objects), the *false negative rate* (FNR), i.e. how many times we get a statistically significant result when using the wrong hypothesis, is still too high (a FNR lager than $\approx 30\%$ for the low natal kick hypothesis). To decrease this rate to the level that in 95% of the cases we obtain a FNR less than 1%, we find that it is necessary to increase the size of the observed sample to ≈ 40 systems. In this respect, future surveys scanning the transient sky, like *Gaia* and *eROSITA*, can detect outbursts of BH-XRBs, potentially increasing the size of the sample.

Very promising is also the detection of gravitational-wave emission from merging BH-BH binaries. Dominik et al. 2012 found that varying BH kicks from zero to velocities as high as the NS birth kicks, the BH-BH binary merger rate goes down by two orders of magnitude, since most of the binaries would get disrupted when the BH forms. Hence, by comparing the observed rate of such mergers with the one predicted from binary population synthesis calculations, it is possible to constrain the BH natal kick distribution (see for example Belczynski et al. 2016a).

In our work, we have assumed that BH-XRBs are the descendant of primordial massive binaries formed in the stellar disk. We did not account for the possibility that some of the observed BH-XRBs, and especially those ones at a large offset from the Galactic plane, could have been ejected from globular clusters via N-body interactions. This topic will be one of the main focuses of my future research.

Samenvatting

Introductie

In de jaren 1960 veranderde zwarte gaten, hierna afgekort als BHs (black holes), van intrigerende theoretische voorspellingen van Einstein's algemene relativiteitstheorie naar detecteerbare astrofysische bronnen. Het was het rijzende tijdperk van de röntgenastronomie en meer en meer röntgenbronnen werden ontdekt buiten ons zonnenstelsel, met behulp van raketgedragen instrumentaria. De eerste geïdentificeerde *kosmische röntgenbron* was Scorpius X-1 (Giacconi et al. 1962), die later een dubblester bleek te zijn bestaande uit een sterk compacte en dode ster, een neutronenster (NS), en een ster met massa en straal vergelijkbaar met die van onze Zon. Bowyer et al. 1965 ontdekten een sterke röntgenbron door middel van geiger detectoren gemonteerd op de Aerobee raket. Zij gaven haar de naam *Cygnus X-1*, naar de constellatie Zwaan, die haar geprojecteerde positie in de ruimte huisvestte. Van deze röntgenstraling werd later begrepen dat deze het teken was van materie aangroeiende op een compact voorwerp. In de optische band viel de röntgenstraallocatie samen met de emissie van een massieve ster, waarmee op basis van haar Doppler verschoven spectraallijnen, het gewicht van het voorwerp dat de röntgenstraling uitzond, kon worden bepaald. Het compacte object bleek een massa te hebben van een paar keer de massa van de zon (Webster & Murdin 1972; Bolton 1972), wat de bovengrens is voor een stabiele NS, en bleek begrensd te zijn binnen een erg compact ruimtegebied: inderdaad een zwart gat.

Zwarte gaten gaten bestaan er in verschillende soorten, afhankelijk van hun massa. Het onderwerp van dit proefschrift zijn de *stellaire-massa BHs*, met een massa die veel kleiner is dan die van hun verwante, superzware zwarte gaten: ongeveer tien zonsmassa's versus honderdduizend tot een miljard zonsmassa's. Astronomen identificeren kandidaat BHs met behulp van röntgentelescopen. De röntgenemissie is afkomstig van een compact object (BH of NS), dat massa accreteert van zijn dubbelster metgezel: dit type dubbelstersysteem heet *X-ray binary* (XRB). Een BH-XRB komt voort uit een oorsprokelijke dubbelster bestaande uit een massieve ster (met een massa groter dan ongeveer 20 maal de massa van onze Zon) en een zonachtige metgezel. Op een bepaald moment tijdens haar evolutie zal de massieve ster door haar nucleaire brandstof heen zijn, ineenstorten en daarbij een BH vormen. Als de dubbelster dit proces overleeft, zal het veranderingen ondergaan in zijn half-lange as als gevolg van het verlies van energie en baanimpulsmoment. Het krimpen van de baan maakt dat de twee compo-

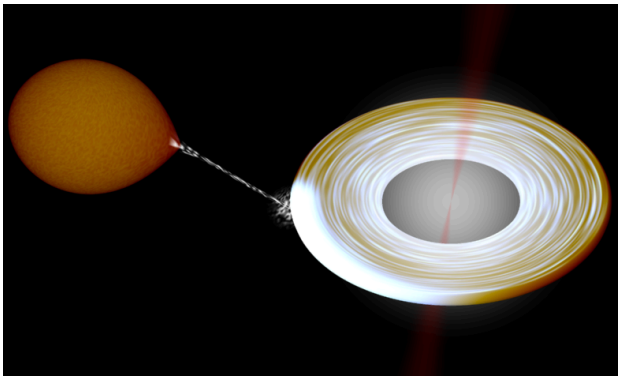

FIGUUR 1: Artist impression van een zwart gat dat massa accreteert van zijn dubbelster metgezel.

nenten steeds dichter bij elkaar komen tot een punt waarbij het stellaire materiaal de invloed van de zwaartekracht van het BH begint te voelen. Dit leidt tot een gasstroom vanuit de ster in de richting van het BH. Het instromende materiaal heeft netto impulsmoment en kan dus niet direct accreteren op het BH. Het vormt in plaats daarvan een accretieschijf waarin materie wordt gecomprimeerd en verhit tot temperaturen van ongeveer 10^7 Kelvin (Shakura & Sunyaev 1973): de dubbelster wordt zichtbaar in de röntgenbandbreedte en wordt - zoals wij dat noemen - een BH-XRB. Terwijl impulsmoment naar buiten beweegt, valt er materie naar binnen en accreteert het op het BH. In figuur 1, ziet u een artistieke impressie van een BH die materie accreteert van een lage-massa ster.

Om de aard van een BH te bevestigen, moet men haar massa bepalen, om zo het verschil te kunnen maken tussen een NS en een BH. Astronomen bepalen de massa van BHs door de baanbeweging van de ster rond het BH te volgen in een BH-XRB. De optische spectraallijnen van de begeleidende ster worden periodiek Dopler-verschoven van het rood naar het blauw. De amplitude en de periode van deze verschuiving hangen direct samen met een ondergrens van de massa van het BH.

De manier waarop BHs worden gevormd is nog steeds onderwerp van discussie, met name als het gaat om de hoeveelheid massa die tijdens de ineenstorting van de kern wordt uitgestoten als ook voor wat betreft de snelheid die het BH bij haar vorming kan krijgen, de zogenaamde *natal kick*. De studie van XRBs die een BH hosten, kan licht werpen op deze twee parameters. In feite volgen de eigenschappen van de baan van deze dubbelsterren en hun Galactische dynamica rechtstreeks uit de fysische omstandigheden op het moment dat het BH werd gevormd. Een opvallend aspect van de Galactische kinematica van BH-XRBs is hun positie ten opzichte van het Galactische vlak. XRBs stammen af van voorloper-dubbelsterren gelegen in de schijf van ons Melkwegstelsel, aangezien we een massieve ster nodig hebben om een BH te vormen, en dergelijke massieve sterren zich in de Galactische schijf bevinden, waar er sprake is van continue stervorming. We zouden daarom verwachten dat XRBs de stellaire dichtheid van de schijf van de Melkweg zouden volgen. Echter, dat doen ze niet. Sommigen zijn tot $1-2$ kpc verschoven ten opzichte van het Galactische vlak, zoals te zien is in figuur 2. Reeds in 2004 ontdekten Jonker & Nelemans dat de schaalhoogte van XRBs die een NS huisvesten vergelijkbaar is met die van XRBs die BH huisvesten. Van NSs was zeer goed bekend dat zij natal kicks krijgen bij hun geboorte in de orde grootte van $300-400$ km/s. Een dergelijke hoge snelheid kan een dubbelster uit zijn geboorteplaats "kicken" in de richting van de halo. Kan het zijn dat BHs een dergelijke kick ook ontvangen? Dit is de fundamentele vraag die ons vanaf het allereerste begin heeft getriggerd.

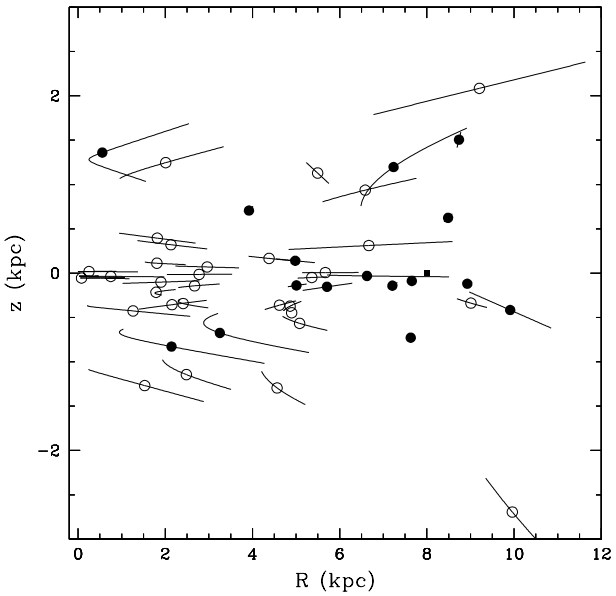

FIGUUR 2: Galactic verdeling van de NS-XRBs (open cirkels) en BH-XRBs (gevulde cirkels). R is de radiale afstand van het Galactic centrum, z is de hoogte boven het Galactische vlak. The Sun wordt aangeduid als een vierkant.

Dit proefschrift

Dit proefschrift draait om het thema BHs in XRBs. De aanleiding van dit werk was om te begrijpen hoe stellaire-massa BHs vormen, een vraag die we aangepakt hebben met zowel theoretische en observationele onderzoeken. Het vormingsmechanisme van BHs is een onopgelost probleem in de hoge-energie astrofysica, met name voor wat betreft de hoeveelheid massa die uitgestoten wordt op het moment van de vorming van het BH, en hoe groot de natal kick is die BHs krijgen bij hun geboorte, als ze al een snelheid krijgen. We bestuderen de geboorte, de evolutie en observationele kenmerken van XRBs die BHs huisvesten die massa accreteren van een zonachtige metgezel. Aan de theoretische kant, combineren we een aanpak die kenmerkend is voor dubbelster-populatiesynthese berekeningen met een meer gedetailleerde benadering, die de dubbelsterevolutie van elke individuele bron beschrijft. Waar mogelijk, beschrijven we de verschillende evolutionaire paden van de dubbelster via analytische berekeningen en tijdschaal-argumenten. Aan de observationle kant combineren we de technieken van optische spectroscopie en fotometrie, met het doel om het aantal waargenomen Galactische BHs te vergroten.

Hoofdstuk I: Een voorstudie over de natal kicks van zwarte gaten

Het onderzoek naar de BH natal kicks werd gemotiveerd door de studie van Jonker & Nelemans 2004, die de Galactische verdeling van BH en NS-XRBs onderzochten en vonden dat deze een soortgelijke schaalhoogte boven het Galactische vlak hebben. Het was bekend dat NS systemen hun oorsprong hebben boven het Galactische vlak ten gevolge van de NS natal kick. Nog geheel onbekend was echter of BHs ook dergelijke kicks zouden krijgen en hoe groot deze zouden zijn. Van BHs werd verwacht dat zij hooguit een kleinere versie van een dergelijke natal kick zouden krijgen, simpelweg omdat ze zwaarder

zijn, en omdat de lineaire impuls behouden zou blijven door de asymmetrische uitstoot van massa in de supernova. We hebben een populatie BH-XRBs gesimuleerd en hun trajecten in de Galactische potential gevolgd. Vervolgens hebben we de ruimtelijke verdeling hiervan vergeleken met de waargenomen verdeling, en concludeerden we dat de populatie waarin de BHs een natal kick krijgen in dezelfde mate als de NSs het beste overeenkomt met de waargenomen verdeling. Dit is een onverwacht resultaat, dat aanleiding gaf tot onze follow-up studie (Hoofdstuk IV), waarin we een meer realistisch model gebruikten voor de dubbelsterevolutie van de bronnen.

Hoofdstuk II: Het gekoppelde effect van getijden en stellaire winden

Een dubbelster systeem is geen statisch system en ondergaat veranderingen in de parameters van haar baan in de tijd ten gevolge van het verlies van omloopenergie en baanimpulsmoment. In het bijzonder kunnen dergelijke verliezen de massa-overdracht tussen de twee componenten van de dubbelster inleiden. Een mogelijke manier van het krimpen van de baan van de dubbelster is wanneer de getijden optreden samen met een stellaire wind. In een deel van BH-XRBs, degene die gevormd worden door een BH met een begeleider massa in de orde van een zonsmassa of minder, krijgt een dergelijke wind de vorm van een magnetisch wind. *Magnetic braking* is het verlies van impulsmoment in een stellaire wind verankerd aan het magnetisch veld van de ster. Zelfs als het massaverlies verwaarloosbaar is (10^{-14} zonsmassa's per jaar in een Zon-gelijkende ster), verwijdert de wind, die gedwongen wordt om mee te draaien tot afstanden van enkele sterstralen, een groot deel van het impulsmoment van de ster. Als de ster een dubbelster is, heeft het getijdenkrachtmoment de neiging om het draaiimpulsmoment-reservoir van de ster weer bij te vullen, door de overdracht van impulsmoment van de baan naar de ster, wat een seculiere inkrimping van de dubbelster's half-lange as veroorzaakt en kan leiden tot *roche-lobe overflow*. In de meeste voorgaande studies van de dubbelsterevolutie van BH-XRBs is dit koppelen vereenvoudigd en is de evolutie slechts op basis van tijdschaal overwegingen beschreven. Wij controleren hoe nauwkeurig deze tijdschalen zijn, met nadruk kijkend naar de tijdschalen van circularisatie van de baan. We koppelen de getijdenvergelijkingen in het "equilibrium-tide" model van Hut 1981, die we uitbreiden tot willekeurige inclinaties, met de vergelijking die het afremmen van de draaiing van de ster om haar eigen as door magnetic braking beschrijft. We volgen de evolutie van verschillende soorten dubbelsterren die gevormd worden door een compact object met een zonachtige ster: black-hole low-mass X-ray binaries (BH-LMXBs) en planetenstelsels bestaande uit een ster en een hete Jupiter. We vinden dat een accurate beschrijving van de evolutie van de dubbelstersystemen vereist dat de gekoppelde evolutie van de rotationele en orbitale elementen onder invloed van magnetic braking gedetailleerd wordt gevolgd. Met name de evolutie van de excentriciteit kan sterk afwijken van het exponentiële verval dat volgt uit een eenvoudige tijdschaal berekening. Dit resultaat werd al verkregen door Barker & Ogilvie 2009 voor planetaire systemen met een korte baanperiode, maar onze studie is de eerste in het benadrukken van de dezelfde conclusie voor dubbelsterren die een BH bavatten, en meer in het algemeen een compact object. Een interessant resultaat van de koppeling tussen getijden en magnetic braking het bestaan, in sommige gevallen, van een emph pseudo-evenwichtstoestand, en we vonden voorwaarden voor het in stand houden daarvan. Ook koppelden we de getijdenvergelijkingen met een ander type sterrewind, een waarin het massaverlies niet verwaarloosbaar is, zoals het geval is voor hoge-massa sterren. In dit geval vinden we een "magnetic braking"-type oplossing: het *wind*

braking mechanisme, dat de dubbelster tot roche-lobe overflow drijft, die wij analytisch beschreven.

Hoofdstuk III : Het terug in de tijd volgen van de evolutie van black hole X-ray binaries

Het doel van dit hoofdstuk is om de omstandigheden tijdens BH formative te achterhalen aan de hand van de waargenomen eigenschappen van een deel van de Galactic BH-XRB populatie: degenen met een korte baanperiode. De parameters die hun baan beschrijven, hun snelheden en de Galactische positie van deze dubbelsterren volgen rechtstreeks uit hun evolutionaire geschiedenis, en worden in het bijzonder beïnvloed door de omstandigheden tijdens BH formatie. We volgen de evolutie van de dubbelsterren terug in de tijd, van de huidige röntgen fase van massa-overdracht tot het moment waarop het BH werd gevormd. We ontwikkelen een semi-analytische computationele tool, die snel is, en die resultaten geeft die consistente zijn met gedetailleerde dubbelsterevolutie berekeningen. Op deze manier vinden we die combinaties van natal kick snelheden en hoeveelheden uitgezonden massa bij BH formatie die in overeenstemming zijn met de waargenomen eigenschappen van de dubbelsterren. Een dergelijke parameterruimte wordt verder verkleind door het gebruik van de kinematische gegevens van zo'n dubbelster: met behulp van de offset van de bron boven het Galactische vlak, leiden we een ondergrens af van zijn snelheid direct na dat het BH is gevormd. We vinden drie scenario's voor de vorming van het BH die compatible zijn met een paar van de waargenomen bronnen. i) Twee BHs (en mogelijk meer als BH kandidaten ook in acht genomen worden) zijn consistent met een NS-achtige natal kick; ii) vijf systemen in zijn in overeenstemming met een standaard scenario waarbij het BH geen natal kick ontvangt en de snelheid van het dubbelstersysteem volledig kan worden toegekend aan de massa die uitgezonden wordt tijdens de supernova; iii) vijf systemen zijn consistent met een natal kick, terwijl voor deze systemen geen baryonische massa uitgezonden hoeft te worden bij de vorming van het BH. In het derde scenario zou het BH dan zijn gevormd in het donker, dat wil zeggen zonder supernova, en de natal kick zou kunnen worden aangedreven door asymmetrische neutrino emissie. Het is de eerste keer dat dit laatste scenario is toegepast op de evolutie van BH-LMXBs. Een ander belangrijk resultaat van dit onderzoek is dat de minimale natal kick snelheid niet sterk wordt beïnvloed door de dubbelsterevolutie van de bronnen; Het wordt voornamelijk beinvloed door de kinematica en derhalve door de onzekerheid op de afstand. Dit heeft tot gevolg dat het niet nodig is om een volledige modellering van de evolutie van een dubbelster XRB uit te voeren om berekeningen te doen aan de natal kick. We bovendien vind geen bewijs voor een verband tussen de BH massa en de natal kick (binnen onze beperkte steekproef van bronnen); een dergelijke correlatie wordt verwacht in een model waarin de natal kick omgekeerd evenredig schaalt met de hoeveelheid massa die terugvalt op de proto-NS. We voeren ook een populatie-synthese-achtige analyse uit om het effect van de verschillende natal kicks en uitgezonden massa's op de waargenomen eigenschappen van de systemen te onderzoeken, om te controleren voor mogelijke observationele onzuiverheden, die zouden inhouden dat voornamelijk systemen met specifieke natal kicks en / of uitgezonden massa's waargenomen worden. We vinden dat de huidige populatie van BH-LMXBs onzuiver is richting systemen met lage natal kick snelheden, van minder dan $100 - 200$ km/s.

Hoofdstuk IV: De Galactische verdeling van de X-ray binaries en de gevolgen daarvan voor de vorming van compacte objecten

Dit werk is verdeeld in drie grote delen. Ten eerste bestuderen we de invloed van verschillende formatiemodellen voor compacte objecten op de Galactische verdeling van XRBs met een BH of een NS, door het maken van synthetische populaties van dergelijke dubbelsterren. We vinden dat de formatiemodellen direct van invloed zijn op de ruimtelijke verdeling van de dubbelsterren, en dat zelfs wanneer BHs en NSs dezelfde natal kicks bij hun geboorte krijgen, NSs nog steeds een grotere schaalhoogte boven het Galactische vlak hebben, wat in overeenstemming is met wat we vinden voor de waargenomen populatie. We richten ons vervolgens op de vergelijking van de Galactische verdeling van BH en NS-XRBs met de gesimuleerde verdelingen, in aanvulling op het onderzoek beschreven in Hoofdstuk III, dit keer rekening houdend met de dubbelsterevolutie van de bronnen, met behulp van de meest recente catalogus van BHs in de Melkweg, en rekening houdend met de onzekerheid in de bepaling van de afstand tot de bronnen. We vinden dat een populatiemodel waarin ten minste sommige BHs een (relatief) hoge natal kick snelheid ontvangen het beste overeenkomt met de waargenomen BH-XRBs. Wat de NSs betreft, vinden we dat een hoge natal kick snelheidsverdeling, in overeenstemming met wat is afgeleid van de meting van de eigenbewegingen van pulsars, het beste overeenkomt met de waargenomen data. Het derde deel van dit hoofdstuk is gewijd aan de uitgebreide analyse van de methode die we in Hoofdstuk III begruikten om de minimale snelheid van een BH-XRB bij geboorte te schatten. We vinden dat deze methode minder betrouwbaar kan in de bulge van de Melkweg voor bepaalde modellen van de Galactische potentiaal, maar onze schatting is uitstekend voor de meeste BH-XRBs.

Hoofdstuk V: Een nieuwe kandidaat zwart gat in de Melkweg

Het laatste hoofdstuk van dit proefschrift is gewijd aan de optische follow-up van een kandidaat XRB, ontdekt in de Galactic Bulge Survey van Jonker et al. Deze survey, waarin gezocht wordt naar zwakke röntgenbronnen in de Bulge van de Melkweg, is gericht op het verhogen van het aantal bekende Galactische accreterende dubbelstersystemen, in het bijzonder op het aantal systemen dat een BH huisvest en die gedetecteerd zijn in rust. Een van de meest veelbelovende bronnen die in deze survey ontdekt is, is CX1004, een kandidaat BH-XRB. We namen X-shooter spectra van de optische tegenhanger van CX1004, waarmee we zowel de radiale snelheid van de vermeende begeleider als zijn spectraaltype meten. De spectra tonen een grote dubbele-piek Hα lijn, wat een BH-XRB met een zeer korte omlooptijd (in de orde van 0.5 dag) zou inhouden en een semi-amplitude radiale snelheid van de begeleidende ster van 500 km/s. Verrassenderwijs vinden we geen bewijs voor enige orbitale modulatie van de radiale snelheidscurve. We identificeren de ster waarvan we fotosferische absorptielijnen zien in de spectra als een M2V ster. Deze resultaten zouden kunnen betekenen dat de M-ster zich toevallig in de zichtlijn bevindt, of dat CX1004 deel uitmaakt van een hierarchische drievoudige ster dat een BH huisvest, met de M-type ster in een wijde baan rond de binnenste XRB. Toekomstige follow-up waarnemingen zijn nodig om de aard van CX1004 volledig te kunnen vaststellen.

Riepilogo

Introduzione

Negli anni Sessanta, i buchi neri sono passati dall'essere pure previsioni teoriche e intriganti della teoria della Relativitá Generale di Einstein, all'essere sorgenti astrofisiche osservabili. Erano gli anni boom dell'astronomia a raggi X, e sempre piú sorgenti al di fuori del nostro Sistema Solare venivano scoperte, utilizzando strumenti a bordo di razzi. La prima fonte cosmica di raggi X é stata *Scorpius X-1* (Giacconi et al. 1962), che si é poi rivelata essere un sistema a due stelle composto da una stella molto compatta e che ha esaurito il suo carburante, una stella di neutroni, e una stella con massa e raggio simili al nostro Sole. Bowyer et al. 1965 hanno scoperto una fonte di raggi X tramite i rivelatori geiger a bordo del razzo Aerobee. Le diedero il nome di *Cygnus X-1* dal nome della costellazione che ospitava la sua posizione proiettata sulla volta celeste. Successivamente, si é poi capito che questi raggi X erano l'impronta di un oggetto compatto che accresceva materia da una stella compagna. Nella banda ottica, la posizione dei raggi X coincideva con l'emissione prodotta da una stella massiccia, le cui righe spettrali si spostavano per effetto Doppler. Grazie a questo spostamento periodico, gli astronomi sono riusciti a misurare il peso dell'oggetto compatto: pesava un paio di volte in piú della massa del sole (Webster & Murdin 1972; Bolton 1972), che é il peso massimo che puó avere una stella di neutroni stabile. Inoltre, tale peso pareva essere confinato in una regione molto compatta: si trattava appunto di un buco nero.

I buchi neri sono di diversi tipi, a seconda della loro massa. Questa tesi é incentrata sui buchi neri di massa stellare: hanno una massa molto piú piccola rispetto alla massa dei loro cugini buchi neri supermassicci: una decina di masse solari contro centinaia di migliaia a un miliardo di masse solari. Questi buchi neri si formano quando una stella massiccia collassa sotto il peso della sua stessa gravitá. Gli astronomi identificano un candidato buco nero con l'ausilio di telescopi a raggi X. L'emissione a raggi X é prodotta da un oggetto compatto (buco nero o stella di neutroni) che accresce materia dalla sua compagna in un sistema binario: questo tipo di sistema stellare binario viene chiamato *binaria a raggi X*. Le binarie a raggi X contenenti un buco nero discendono da binarie costituite da una stella massiccia (con massa superiore a circa venti volte la massa del nostro Sole) e una compagna simile al nostro Sole. Ad un certo punto durante la sua evoluzione, la stella massiccia esaurisce il suo combustibile nucleare, collassa su se stessa, e forma un buco nero. Se la binaria sopravvive questo processo, la separazione tra le due componenti del sistema binario (il buco nero e la stella piccola) si restringe pian piano, a causa

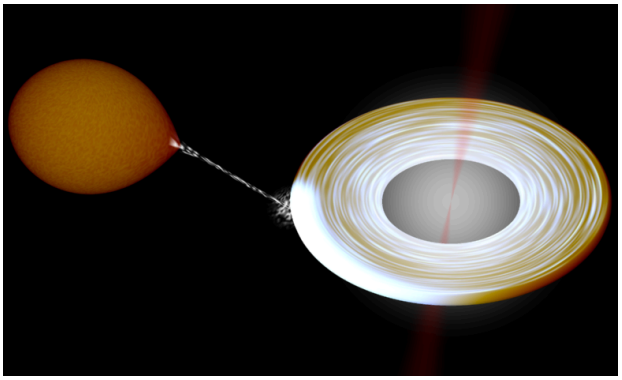

Figuur 1: Impressione artistica di un buco nero che accresce materia dalla sua stella compagna. Il gas fluisce dalla compagna e verso il buco nero formando un disco di accrescimento che si scalda e diventa luminoso nei raggi X. Nell'immagine é anche visibile un jet emesso dalla regione piú vicina al buco nero.

della perdita di energia e momento angolare orbitale. Il restringimento della separazione orbitale fa sí che le due componenti si avvicino sempre di piú l'una all'altra fino ad un momento in cui il materiale stellare incomincia a sentire l'attrazione gravitazionale del buco nero. Ció innesca il flusso di gas dalla stella e verso il buco nero. Tale gas possiede un momento angolare netto e quindi non puó essere accresciuto direttamente sul buco nero. Si forma invece un disco di accrescimento nel quale la materia viene compressa e riscaldata a temperature di circa 10^7 Kelvin (Shakura & Sunyaev 1973): la stella binaria é ora visibile nei raggi X e diventa quella che conosciamo come binaria X. Mentre il momento angolare si muove verso l'esterno del disco, la materia viene accresciuta sul buco nero. Nella Figura 1, presentiamo un'impressione artistica di un buco nero che accresce materia dalla sua stella compagna.

Per confermare la natura di un buco nero, se ne deve determinare la massa, in modo da discriminare tra un buco nero e una stella di neutroni, che é piú leggera. Gli astronomi determinano la massa di un buco nero tracciando il moto orbitale della stella attorno ad esso. Le linee spettrali della stella compagna nella banda ottica si muovono periodicamente verso il blu e verso il rosso per effetto Doppler. L'ampiezza e la frequenza di questo cambiamento sono direttamente collegati al limite inferiore sulla massa del buco nero.

Non si sa ancora bene come si formino i buchi neri, soprattutto quando si tratta della quantitá di massa che viene espulsa durante il collasso della stella massiccia, né tantomeno quale sia la velocitá che i buchi neri acquisiscono alla nascita, il cosiddetto *kick* o calcio. Lo studio delle binarie X che ospitano un buco nero puó far luce su questi due parametri. Infatti, le proprietá attuali delle binarie X discendono direttamente dal loro percorso evolutivo, e sono in particolare influenzate dalla loro dinamica galattica e dalle proprietá della binaria al momento della formazione del buco nero. Un aspetto sorprendente della cinematica dei buchi neri galattici é la loro posizione rispetto al piano galattico. Le binarie X discendono da binarie nate sul disco della Via Lattea, dato che c'é bisogno di una stella massiccia per formare un buco nero, e queste stelle massicce si trovano nel disco galattico, dove c'é formazione stellare continua. Ci aspetteremmo quindi che anche le binarie X si trovassero sul piano galattico. E invece sono un po' piú in alto rispetto ad esso, come si puó vedere nella Figura 2.

Giá nel 2004, Jonker & Nelemans avevano scoperto che l'altezza rispetto al piano galattico delle binarie X che ospitano un buco nero era paragonabile a quella delle binarie X che ospitano una stella

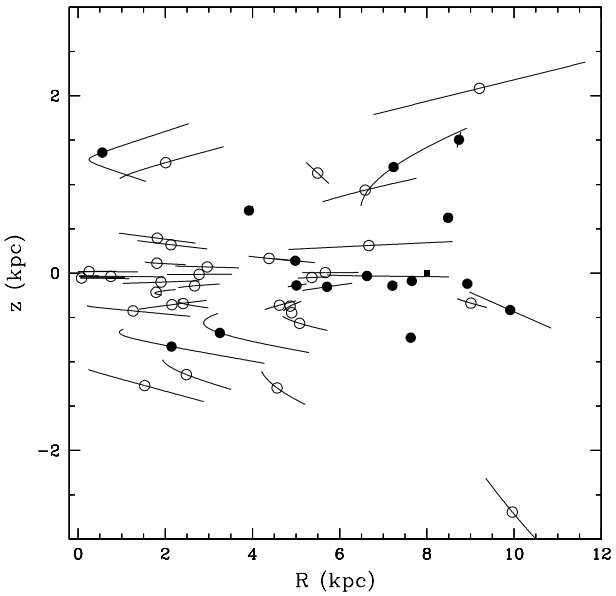

FIGUUR 2: Distribuzione galattica delle binarie X contenenti una stella di neutroni (cerchi aperti), o un buco nero (cerchi pieni). Il parametro R é la distanza della binaria dal centro galattico; il parametro z é l'altezza della binaria rispetto al piano galattico, che si trova a $z = 0$. Il Sole é indicato con un quadrato.

di neutroni. Era ben noto che le stelle di neutroni ottenessero *kicks* alla loro nascita con una veloctá di circa 300/400 chilometri al secondo. Questi *kicks* calciano la binaria verso una posizione distante da quella in cui sono nate. la binaria Poteva essere che anche i buchi neri ricevessero tali calci? Questa é la domanda fondamentale che ha innescato il nostro lavoro fin dall'inizio.

Questa tesi

Questa tesi ruota intorno al tema della binarie X contenenti un buco nero. Desideriamo capire come nascono i buchi neri, e cerchiamo di rispondere a questa domanda con studi teorici e osservativi. Il meccanismo di formazione dei buchi neri é un problema irrisolto in astrofisica, in particolare per quanto riguarda la quantitá di massa che viene espulsa al momento della formazione del buco nero, e quanto é grande il *kick* che i buchi neri acquisiscono alla nascita. Studiamo la nascita, l'evoluzione e le caratteristiche osservative delle binarie X contenenti un buco nero che accresce materia da un compagna simile al nostro Sole. Sul piano teorico, combiniamo un approccio tipico dei calcoli di sintesi delle popolazioni stellari con un approccio piú dettagliato, che descrive l'evoluzione binaria di ogni singola sorgente. Ove possibile, descriviamo i diversi percorsi evolutivi della binaria con calcoli analitici e argomentazioni basate sui tempi scala in gioco. Dal lato osservativo, usiamo le tecniche tipiche della spettroscopia ottica e fotometria, con l'intento di scoprire nuovi buchi neri nella nostra galassia.

Capitolo I: Uno studio preliminare dei kicks ricevuti dai buchi neri alla nascita

Lo studio dei *kicks* dei buchi neri é stato motivato dall'articolo di Jonker & Nelemans del 2004, nel quale hanno studiato la distribuzione galattica dei buchi neri e delle stelle di neutroni e hanno scoperto che avevano un'altezza simile rispetto al piano galattico. Era noto che le stelle di neutroni ricevano una velocitá alla nascita. Questa velocitá le sposta rispetto al piano galattico. Tale *kick* puó essere causato, ad esempio, dall'emissione asimmetrica di materia al momento della esplosione di supernova che forma la stella di neutroni. Ma ancora non si sapeva se anche i buchi neri ottenessero questi calci e quanto grande questo *kick* sarebbe stato. Ci si aspettava che i buchi neri ricevessero una versione ridotta di tale *kick*, semplicemente perché sono piú pesanti. Abbiamo simulato una popolazione di binarie X contenenti un buco nero e seguito il loro moto nella nostra galassia. Abbiamo quindi confrontato la loro distribuzione spaziale con la distribuzione delle binarie osservate, e abbiamo concluso che una popolazione simulata in cui i buchi neri ricevono un *kick* paragonabile ai *kicks* delle stelle di neutroni si avvicina meglio alla popolazione osservata. Questo é un risultato inatteso, che ha dato origine al nostro studio successivo (Capitolo IV), in cui abbiamo utilizzato un modello piú realistico dell'evoluzione delle binarie X.

Capitolo II: L'effetto accoppiato di maree e venti stellari

Un sistema binario non é un sistema statico e col passare del tempo subisce variazioni dei parametri della sua orbita a causa della perdita di energia e momento angolare orbitale. In particolare, il restringimento dell'orbita puó innescare il trasferimento di massa tra le due componenti del sistema binario. Un modo possibile di restringere la separazione tra le due componenti é quando le maree agiscono in contemporanea con un vento stellare. In un insieme di binarie X, quelle formate da un buco nero con una compagna stellare simile al nostro Sole, tale vento assume la forma di un vento magnetico. Il *magnetic braking* é la perdita di momento angolare in un vento stellare ancorato alle linee di campo magnetiche della stella. Anche se la perdita di massa é trascurabile (10^{-14} masse solari all' anno per una stella simile al Sole), il vento, che é costretto a co-ruotare con la stella fino a grandi distanze, rimuove una buona parte del momento angolare della stella. Se la stella é in un sistema binario, il momento di forza delle maree tende ad accelerare nuovamente la rotazione della stella. Il momento angolare viene cosí trasferito dall'orbita alla stella, provocando un declino secolare della separazione orbitale e talvolta innescando il flusso di materia dalla stella all'oggetto compatto. Nella maggior parte degli studi precedenti sulla evoluzione delle binarie X, questo accoppiamento é stato trascurato e l'evoluzione é stata descritta con considerazioni basate su tempi-scala. Controlliamo quanto precise queste considerazioni siano, con una particolare attenzione al tempo che occorre affinché l'orbita della binaria diventi circolare. Usiamo il modello delle maree introdotto da Hut 1981, che estendiamo a inclinazioni arbitrarie. Seguiamo l'evoluzione di diversi tipi di stelle binarie formate da un oggetto compatto e da una stella simile al Sole: buchi neri in binarie X di piccola massa e sistemi planetari composti da una stella e un pianeta simile a Giove. Concludiamo che per descrivere accuratamente l'evoluzione di questi sistemi binari, occorre seguire l'evoluzione accoppiata delle maree e del vento stellare. In particolare, l'evoluzione dell'eccentricitá della binaria puó differire considerevolmente dal decadimento esponenziale dettato da un semplice calcolo basato su tempi-scala. Questo risultato é stato ottenuto in precedenza da Barker & Ogilvie 2009 per i sistemi planetari con breve periodo orbitale, ma il nostro studio é il primo a giun-

gere alla stessa conclusione per stelle doppie composte da un buco nero o stella di neutroni. Inoltre, troviamo alcune conseguenze interessanti dell'accoppiamento tra maree e *magnetic braking*, come la presenza, in alcuni casi, di uno stato di *quasi-equlibrio*. In piú, abbiamo accoppiato le maree con un altro tipo di vento stellare, un vento in cui la perdita di massa non é piú trascurabile, come succede per le stelle massicce. In questo caso, esiste una soluzione simile al *magnetic braking* che puó indurre il trasferimento di materia tra le due stelle, e che descriviamo analiticamente.

Capitolo III: Tracciando indietro nel tempo l'evoluzione delle binarie X contenenti un buco nero

Lo scopo di questo capitolo é determinare le condizioni alla formazione dei buchi neri sulla base delle proprietá osservate di una parte della popolazione di binarie X galattiche: quelle contenenti una stella che ruota attorno ad un buco nero in un tempo breve (minore di un giorno). Tracciamo l'evoluzione di ogni binaria indietro nel tempo, dalla fase corrente di trasferimento di massa al momento in cui il buco nero si é formato. Sviluppiamo un modello di calcolo semi-analitico, che é veloce e che dá risultati coerenti con calcoli piú dettagliati di evoluzione binaria. In questo modo, troviamo le possibili combinazioni di *kick* e quantitá di massa espulsa alla formazione consistenti con le proprietá osservate dei sistemi binari considerati. Tale spazio delle fasi é ulteriormente ridotto con l'uso dei dati cinematici della binaria: dalla distanza della binaria al di sopra del piano galattico, ricaviamo un limite inferiore alla velocitá che aveva la binaria subito dopo la formazione del buco nero. Troviamo tre scenari per la formazione del buco nero e che sono compatibili con le sorgenti del nostro studio: i) due buchi neri (e forse di piú se consideriamo anche i candidati buchi neri) sono consistenti con un *kick* simile a quello ricevuto dalle stelle di neutroni; ii) cinque binarie sono consistenti con uno scenario standard in cui il buco nero nasce senza velocitá; iii) cinque sistemi sono consistenti con un *kick*, ma senza l'emissione di massa barionica al momento della formazione. In questo terzo scenario, i buchi neri si sarebbero quindi formati *al buio*, vale a dire senza un'esplosione di supernova, e il *kick* potrebbe essere impartito dall'emissione asimmetrica di neutrini. É la prima volta che quest'ultimo scenario viene applicato all'evoluzione delle binarie X. Un altro importante risultato di questo studio é che la velocitá minima della binaria alla nascita non é fortemente influenzata dalla evoluzione binaria della stessa. Essa é principalmente influenzata dalla cinematica e quindi dall'incertezza sulla distanza delle sorgenti. Questo implica che non é necessario fare un modello dettagliato dell'evoluzione delle binarie X per misurare i *kicks* alla nascita. Abbiamo anche investigato eventuali *bias osservativi* che farebbero in modo che i sistemi osservati siano solo quelli con una velocitá particolare. Troviamo che l'attuale popolazione delle binarie X é limitata a velocitá natali basse, inferiori a 100-200 chilometri al secondo.

Capitolo IV: La distribuzione galattica delle binarie X e le associate implicazioni per la formazione degli oggetti compatti

Questo lavoro é diviso in tre parti principali. Nella prima parte, studiamo l'effetto che diversi modelli di formazione degli oggetti compatti hanno sulla distribuzione galattica delle binarie X contenenti una stella neutroni o un buco nero. Per fare questo, costruiamo popolazioni sintetiche di binarie X. Troviamo che i vari modelli di formazione influenzano direttamente la distribuzione spaziale delle binarie

X e che, anche se i buchi neri e le stelle di neutroni ricevessero lo stesso tipo di *kick* alla nascita, le stelle di neutroni mostrerebbero sempre un'altezza rispetto al piano galattico piú grande, che é in linea con quanto troviamo per la popolazioni osservate. Nella seconda parte, ci concentriamo sul confronto della distribuzione osservata delle binarie X con buchi neri o con stelle di neutroni con le distribuzioni simulate, seguendo il lavoro fatto nel Capitolo I, ma questa volta prendendo in considerazione l'evoluzione binaria delle sorgenti, utilizzando il piú aggiornato catalogo di buchi neri galattici, e tenendo in conto dell'incertezza nella distanza delle sorgenti. Troviamo che un modello in cui almeno alcuni buchi neri ricevono un *kick* alla nascita relativamente alto, meglio descrive la distribuzione osservata. Per quanto riguarda le stelle di neutroni, un *kick* elevato, in accordo con il *kick* dedotto misurando il moto sul piano del cielo delle pulsars, meglio descrive la posizione delle stelle di neutroni nella nostra galassia. La terza parte di questo capitolo é dedicata all'analisi di un metodo che abbiamo usato nel Capitolo III per stimare la velocitá minima di una binaria X alla nascita. Troviamo che questo metodo puó essere meno affidabile nel *bulge* della Via Lattea per alcuni modelli del potenziale galattico, ma che la nostra stima é eccellente per la maggior parte delle binarie X.

Capitolo V: Un nuovo candidato buco nero nella nostra galassia

Il capitolo finale di questa tesi é dedicato al monitoraggio ottico di una candidata binaria X, scoperta nella *Galactic Bulge Survey* di Jonker et al. Tale *survey*, che cerca sorgenti X nel centro della Via Lattea, ha come conseguenza diretta l'aumento del numero di binarie X note, ed in particolare del numero di sistemi che ospitano un buco nero. Una delle sorgenti piú promettenti scoperte dalla *survey* é CX1004, un candidato buco nero. Abbiamo raccolto spettri ottici di CX1004 con X-shooter, uno strumento situato nel fuoco del telescopio VLT a Paranal. Analizzando tali spettri, abbiamo misurato sia la velocitá lungo la linea di vista della presunta compagna al buco nero, sia il suo tipo spettrale. Gli spettri mostrano un'ampia riga dell'idrogeno in emissione, che potrebbe essere prodotta in un disco molto caldo attorno ad un buco nero. Sorprendentemente, non troviamo tuttavia alcun cambiamento periodico della velocitá lungo la linea di vista. Ci aspetteremmo un tale cambiamento, in quanto la stella compagna dovrebbe spostarsi o verso di noi o via da noi nel suo moto attorno al buco nero. Questi risultati implicano o che la stella ottica sia in realtá una stella che non appartiene al sistema binario, oppure che CX1004 fa parte di una stella tripla (un sistema a tre corpi) che ospita un buco nero. Sono necessarie future osservazioni per determinare appieno la natura di CX1004.

Curriculum vitæ

I was born on a snowy morning on 30th December 1985, in Savigliano, Italy. I spent my childhood in Marene, a tiny town in the countryside of North-West Italy. I attended Liceo Scientifico G. Arimondi in Savigliano, a high school with a preference for scientific disciplines. During high school, I tackled every subject with dedication, with my favorite ones being math, physics, English literature and English language, and politics. Various music classes, such as solfeggio and singing, delighted my spare time. When I was a kid, I had this dream of becoming an ethologist (the scientist who studies the animal behaviour). However, when the time came to make up my mind on the college curriculum, I chose for physics. I found physics more challenging, more complete and absorbing, plus I thought it would create a mind-set I was very much drawn to. I graduated from Liceo G. Arimondi with honors, with a final essay on the fractal structure of the universe (I was scientifically naive at that time!).

With the wish of moving out of the nest and finding my own way, I moved to Pavia, a college town South of Milano, where I enrolled in a bachelor's degree course in physics. My bachelor's thesis project dealt with radio-quiet neutron stars and was carried out at the National Institute for Astrophysics (INAF) in Milano, within the group led by Patrizia Caraveo and Giovanni Bignami. Being very fond of equations and theory, I enrolled in a master's degree course in theoretical physics, with my favorite subjects being quantum mechanics, modern physics, and mathematical methods applied to physics. My interest gravitated towards astronomy as soon as I took a course in astrophysics, taught by Andrea De Luca.

I have always been very much attracted to traveling and experiencing new cultures; such desire triggered my enrollment into the Erasmus programme, for which I was selected on the basis of very good grades. The Erasmus programme allowed me to spend seven months in Lund, a joyful town (yes, joyful, in spite of the long and dark winter days) in Skåne, South of Sweden. Those were some of the busiest (and delightful) months of my life. At Lund Observatory, I wrote my master's thesis under the supervision of Melvyn B. Davies, who introduced me to scientific research. During those months, I went from a book-based knowledge to making my first steps in research within the framework of

academia. I received my master's degree cum laude.

In spring 2011, I was invited for a job interview by Gijs Nelemans and Peter Jonker, who were looking for a new PhD candidate to work on the formation of stellar black holes. Gijs and Peter later hired me as a PhD student at the Department of Astrophysics of the Radboud University Nijmegen, where I started in October 2011.

During my PhD, I had the wonderful opportunity to attend conferences, workshops and schools, both abroad and in the Netherlands, thanks to Gijs's and NOVA's support. I gave invited talks at conferences/symposiums in Bonn (Germany), Lund, Groningen (the Netherlands). In addition, I presented contributed talks/posters at conferences in Bamberg (Germany), Lake Louise (Canada), Boston (US), Aspen (US), Stockholm (Sweden). I attended the SIGRAV graduate school on Astrophysical Black Holes (Como, Italy), the summer school on Binary Stars (Leuven, Belgium), and the NOVA fall school (Groningen). Furthermore, I visited the Netherlands Institute for Space Research (SRON) in Utrecht to carry out research with Peter Jonker and Manuel Torres, learning the methods and tools of observational astronomy. The experience with observational astronomy started in March 2012, when I was lucky enough to visit the Paranal Observatory in Chile to take data from the Very Large Telescope under the guide of Manuel. In January 2015, I could plan and go on a US tour presenting my work at different institutes (American Museum of Natural History and Columbia University in New York, Johns Hopkins University in Baltimore, Northwestern University in Evanston). I was invited to give seminars at Warsaw University (Poland) in October 2014, at Lund Observatory in June 2015, and at the Technion (Israel) in July 2015. Being a teaching assistant for the courses "Radiative Processes" and "Tensors and Applications" was very enjoyable; for the latter, I also gave a couple of full lectures on special relativity and an introduction to manifolds. I was presented with an award from the Study Committee of Physics and Astronomy of RU Nijmegen for outstanding teaching in 2014 for the course on Tensors. During my first year of PhD, I revived the Journal Club of the Astronomy Department which I organized for two years. I was also occasionally involved with the public outreach of the Astronomy Department, such as the one during the Lustrum celebration. I initiated scientific collaborations with the University of Warsaw and the Alberta University (Canada), at my own initiative.

Currently, I am a postdoctoral researcher at the Technion in Haifa, working with Hagai Perets on the dynamics of stars in globular clusters. I keep my mind healthy by doing sports - such as swimming, running, yoga, by studying languages, and with books and music. I have run a marathon (42 km, Amsterdam 2013), a half-marathon (21 km, Nijmegen 2015), and various shorter races in Tilburg and Nijmegen. Traveling is a big passion of mine, and in particular to places where nature overwhelms me with its beauty and boundlessness.

List of publications

Refereed publications

The Galactic distribution of X-ray binaries and its implications for compact object formation and natal kicks.
Repetto S., Igoshev A., Nelemans G.
Monthly Notices of the Royal Astronomical Society, *2016*, in press

The first low-mass black hole X-ray binary identified in quiescence outside of a globular cluster.
Tetarenko B.E., Bahramian A., Arnason R.M., Miller-Jones J.C.A., **Repetto S.**, Heinke C.O, Maccarone T.J., Chomiuk L., Sivakoff G.R., Strader J., Kirsten F., Vlemmings W.
The Astrophysical Journal, Volume 825, Issue 1, 10 pp., *2016*

Compact Binary Merger Rates: Comparison with LIGO/Virgo Upper Limits.
Belczynski K., **Repetto S.**, Holz D., O'Shaughnessy R., Bulik T., Berti E., Fryer C., Dominik M.
The Astrophysical Journal, Volume 819, Issue 2, 27 pp., *2016*

The Formation of Cataclysmic Variables: The Influence of Nova Eruptions.
Nelemans G., Siess L., **Repetto S.**, Toonen S., Phinney E. S.
The Astrophysical Journal, Volume 817, Issue 1, 8 pp., *2016*

Constraining the formation of black-holes in short-period Black-Hole Low-Mass X-ray Binaries.
Repetto S., Nelemans G.
Monthly Notices of the Royal Astronomical Society, Volume 453, pp. 3341-3355, *2015*

Discovery of a red supergiant counterpart to RX J004722.4-252051, a ULX in NGC 253.
Heida M., Torres M. A. P., Jonker P. G., Servillat M., **Repetto S.**, Roberts T. P., Walton D. J., Moon D.-S., Harrison F. A.
Monthly Notices of the Royal Astronomical Society, Volume 453, Issue 4, p.3510-351, *2015*

VLT spectroscopy of the Black Hole Candidate Swift J1357.2-0933 in Quiescence.
Torres M.A.P., Jonker P.G., Miller-Jones J. C. A, Steeghs D., **Repetto** S., Wu J.
Monthly Notices of the Royal Astronomical Society, Volume 450, Issue 4, p.4292-4300, *2015*

The coupled effect of tides and stellar winds on the evolution of compact binaries.
Repetto S., Nelemans G.
Monthly Notices of the Royal Astronomical Society, Volume 444, pp. 542-557, *2014*

Investigating stellar-mass black hole kicks.
Repetto S., Davies M.B., Sigurdsson S.
Monthly Notices of the Royal Astronomical Society, Volume 425, Issue 4, pp. 2799-2809, *2012*

Publications in preparation

Follow-up observations of the Galactic Bulge Survey source CX1004: a candidate Black Hole X-ray Binary.
Repetto S., Torres M.A.P, Wevers T., Heida M., Nelemans G., Jonker P.G., Wyrzykowski L., Britt C.T., Heinke C.O., Hynes R.I., Johnson C.B., Maccarone T.J., Steeghs D.T.H., *2016*, to be submitted

Cygnus X-1: its past and future evolution.
Repetto S., Nelemans G., et al., in preparation

Acknowledgments

You are holding in your hand the fruit of four years (and a little more) of work. What cannot be touched nor put easily in words is the personal development and growth which have run parallel to my growth as an astronomer. In spite of what one would think, the PhD is firstly a personal voyage, in the inner self. I here wish to thank all those special people who took part in this voyage, whether the whole or a part of it. People who, with their love, caring, support, have amplified the happiness in joyful times, and soothed the bitterness in harsh times. You are very special to me, and I will treasure our memories for a very long time: a Hubble time!

First of all, I am greatly grateful to my supervisor Gijs Nelemans. Gijs, many thanks for your moral support; I still remember when you told me: "your worst enemy, in research, is yourself", referring to my at-times shy self-esteem. In that sentence I have found great strength, and a starting point to develop as a researcher. You are an example of modesty and ethical behaviour in science. Your ideas flow quickly: it was always so productive and inspiring to discuss science with you. Thank you for always finding time to meet me, even in your busiest days, and especially during the hectic times of writing up my thesis. From you I have also learnt the fruitfulness of combining theory with observations.

I wish to thank my non-official advisor Manuel Torres, who has been my mentor along the (sometimes bumpy) road walking the world of observations. With patience, you have guided me. I started absolutely from zero; when I first went to Paranal with you, I did not even know how a telescope worked not to mention what an observing run was. Thank you also for all the office-time laughs and anecdotes, which were a great way of releasing the tension when pipelines were running in hell :).

Peter Jonker, my co-advisor, many thanks to you as well. Your enthusiasm and pro-active approach to research are contagious. Thank you for involving me in the GBS survey: I have learnt a non-measurable lot thanks to this project.

My thesis reading committee: thank you for agreeing to evaluate my thesis.

Melvyn Davies: you introduced me to the topic of black hole formation in the first place, when I was

a master's student in Lund. From you I have learnt the importance of clarity and straight-forwardness when writing and presenting (I will never forget the "invert the triangle"). Scientifically, I have learnt greatly from you. Many thanks for those times when you were advising me on my career and for guiding me when I was writing my first research proposal.

Chris Belczynski: your out-of-the-box (and at times bold) thinking has been a great example to me. Thank you for hosting me at the Warsaw Observatory and for involving me in the LIGO paper.

Selma De Mink: thank you for inviting me to visit the astro department at UVA, when we discussed science and you gave me great advice on career-planning. You are a source of inspiration for women in science.

Many thanks to the Radboud University Astronomy Department. To our helpful secretaries and to all my colleagues for making ru-astro such a vibrant and pleasant place of work. Silvia (for our chats on binary evolution and much more), Ester (for our chatty coffee breaks), Emilio (for the laughs and the support), Martha (for the fun and the wonderful surprise good-bye party), Christiaan (for the musical exchanges), Laura and Antonio (for their homey Italian vibe), Marianne (for our scientific collaborations and memorable conference trips), Thomas (for your help with the CX1004 paper), Roque, Monika, Deanne & Rocco for looking after my Tiger when I was in Iceland, Samaya, Sander, Kars, Sweta, Svea, Sarka, Sjoert (for hosting me at JHU), Simone & Anna, and many many others (sorry if I am not mentioning directly all of you). I will cherish many fond memories spent first on the third floor (in the unforgettable Jungle Office) and afterwards on the second.

I wish to thank Gijs, the LKBF and the NOVA for funding my travels and the printing of my thesis; Pim and Rudo for translating into Dutch the Summary of my thesis; Martin van den Akker for providing the thesis template; many thanks to my current boss Hagai Perets as well, for allowing me to finish up my thesis during the first months at Technion.

And now a list of special friends follows.

Annika: friends are the family one can choose, and you are like a sister to me. Thank you for our coffee breaks at university when stress was high. For all our dinners and sauna-evenings after work. But most of all, for your loving care, wise suggestions, and English expressions ;).

Pim: we have been office mates from the very first day and for each and every day later on. Not only I have found a colleague, I have found a very good friend, and a companion of running races and triathlon courses, which kept body and mind healthy.

Lalla: a special friend for a very long time, and a dear companion to Icelandic dreams. It is always so fruitful and soothing to discuss with you on the most diverse topics, from particle physics to literature, from travels to work/life balance.

Magda: I have always thought there is a special connection between the Poles and the Italians, and you are the best example of this. Thank you for all the laughs, the visits at Vossendijk, and the roller-skating.

David: we met for the first time in Boston at the X-ray conference, then in the following September I pleasantly found you as one of my colleagues. You have been an unforgettable coffee-break buddy for a whole three years. I will cherish our all-round conversations for long, from jets to stock markets, from Danish movies to politics.

Andrey: thank you for all our scientific discussions, especially on statistics :). I hope we will continue to work together, and to exchange literature suggestions and much more.

Jaap: thank you for the musical nights in Amsterdam.

Chiara: from Lund till today, a dear friend.

Alexey: thank you for all the adventures, cheesecakes, and Jim Jarmusch movies.

Laura L: humor is the salt of life! Thank you also for delighting my visits to SRON and to Utrecht.

Alice: it is a special entanglement that we have.

Rudo: you have always supported me with your energy and optimism.

Gabriel: thank you for taking such a loving care of the Tiger during my first months in Israel; you have a big heart.

Ann: thank you for making me feel at home and all the tasty food when visiting Estonia during the Xmas holidays in 2014.

Little Sophia: you shine like a star! Playing with you is a balm for the spirit.

Last but not least, thousands of warm thanks to my family. To my brothers, Luca & Andrea, for their caring and "supervision" at a distance. Little Marianna: my heart melts when I see you. Valeria, thank you for your care. My parents, Maria and Giuliano: thank you for all your visits to the Netherlands, like that time you left as soon as you knew I was sick in bed with chicken pox. But most of all, thank you for your ever-present support and for giving me the independence I have always looked for: if I never was fearful of the unknown, it is greatly thanks to you.

Ringraziamenti

Avete tra le mani il frutto di quattro anni (e qualcosa di piú) di lavoro. Quello che non é tangibile e che non é facile da mettere nero su bianco é lo sviluppo e la crescita personali che sono andati di pari passo con la mia crescita come astronoma. A differenza di quanto uno possa pensare, il dottorato é innanzitutto un viaggio personale, all'interno di se stessi. Ora desidero ringraziare tutte quelle persone speciali che hanno preso parte in questo viaggio, che sia il viaggio intero, o che sia una piccola parte di esso. Sono persone che, con il loro amore, premura e sostegno, hanno amplificato la felicitá nei momenti di gioia, e hanno smussato l'asprezza nei momenti di difficoltá. Siete molto speciali per me, e faró tesoro dei nostri ricordi per un tempo lunghissimo: un tempo lungo come il tempo di Hubble!

Innanzitutto, sono immensamente grata al mio relatore Gijs Nelemans. Gijs, mille grazie per il tuo supporto morale; mi ricordo ancora quando mi dissi: "nella ricerca il tuo piú grande nemico sei te stessa", riferendoti alla mia piccola autostima. In quella frase ho attinto molto forza, ed é stata un punto di partenza per crescere come ricercatrice. Sei un esempio di modestia e comportamento etico nella scienza. Le tue idee fluiscono veloci: é stato sempre cosí produttivo discutere del mio progetto con te. Grazie per essere sempre riuscito a trovare tempo per me, anche quando eri impegnatissimo, e soprattutto durante gli ultimi mesi frenetici quando stavo scrivendo la tesi. Da te ho imparato anche il beneficio di combinare la teoria con le osservazioni.

Desidero ringraziare il mio relatore non-ufficiale Manuel Torres, che é stato la mia guida mentre camminavo il sentiero (spesso dissestato) del mondo dell'astronomia osservativa. Mi hai sempre guidato con molta pazienza. Io sono partita completamente da zero; la prima volta che andai a Paranal con te, non sapevo neanche come funzionasse un telescopio, per non parlare di cosa fosse un blocco osservativo. Grazie anche per tutte le risate e gli aneddoti in ufficio, che sono stati un grande modo di allentare la tensione quando le *pipelines* ci tormentavano.

Peter Jonker, il mio co-relatore, molte grazie anche a te. Il tuo entusiasmo e approccio intraprendente alla ricerca sono contagiosi. Grazie anche per avermi coinvolto nella GBS *survey*: ho imparato tantissimo grazie a questo progetto.

RINGRAZIAMENTI

Alla mia commissione di lettura: grazie per aver accettato di valutare la mia tesi.

Melvyn Davies: sei stato tu ad introdurmi all'argomento della formazione dei buchi neri, quando ero una studentessa di Laurea Specialistica a Lund. Da te ho imparato l'importanza dell'essere chiari e diretti nello scrivere e presentare (non dimenticheró mai il tuo insegnamento: "inverti il triangolo"). Scientificamente, ho imparato tantissimo da te. Molte grazie anche per quei momenti in cui mi consigliavi sulla mia carriera futura e per quando mi hai guidato durante la stesura del mio primo progetto di ricerca.

Chris Belczynski: il tuo modo di pensare fuori dagli schemi (e talvolta ardito) é stato di grande esempio per me. Grazie di avermi invitato all'Osservatorio di Varsavia e di avermi coinvolto nell'articolo sulle onde gravitazionali.

Selma De Mink: grazie per avermi invitato a visitare il tuo gruppo di ricerca ad Amsterdam, quando abbiamo discusso di scienza e quando mi hai dato ottimi consigli su come pianificare la mia carriera futura. Sei un fantastica fonte di ispirazione per le donne nella scienza.

Molte grazie al Dipartimento di Astronomia dell'Universitá di Nijmegen. Alle nostre segretarie e a tutti i miei colleghi per aver reso il nostro dipartimento un posto piacevolissimo e vibrante dove lavorare. A Silvia (per le discussioni sull'evoluzione delle binarie e molto altro ancora), Martha (per le risate e per aver organizzato quell'adorabile festa a sorpresa prima che io partissi per l'Israele), Ester (per le pause caffé chiacchierine), Emilio (per il supporto), Kars, Samaya, Christiaan (per gli scambi musicali), Laura e Antonio (per avermi fatto sentire italiana e a casa), Thomas (per l'aiuto con l'articolo su CX1004), Sarka, Sjoert (per avermi ospitato quano ero in visita al JHU a Baltimora), Marianne (per la nostra collaborazione scientifica e per le memorabili conferenze), Roque, Svea, Simone & Anna, Monika, Sander, Deanne & Rocco per esservi presi cura della mia tigre quando ero in Islanda, e molti molti altri (mi spiace se non riesco a menzionare direttamente ciascuno di voi). Conserveró nel cuore i ricordi dei momenti passati prima al terzo piano (nell'indimenticabile ufficio-giungla) e poi al secondo.

Voglio ringraziare Gijs, l'LKBF e la NOVA per finanziare i miei viaggi di lavoro e la stampa della tesi; Rudo e Pim per aver tradotto in olandese il mio riepilogo; Martin van den Akker per aver fornito il modello della tesi; grazie anche al mio attuale capo Hagai Perets per avermi permesso di lavorare alla tesi durante i primi mesi al Technion.

Ed ora una lista di amici speciali.

Annika: gli amici sono la famiglia acquisita, e tu sei come una sorella per me. Grazie per tutte le pause caffé in universitá quando lo stress era elevato. Per tutte le cene e le serate alla sauna dopo il lavoro. Ma soprattutto, grazie per la tua amorevole premura, i saggi consigli, e le tue espressioni caratteristiche :).

Pim: siamo stati compagni di ufficio fin dal primo giorno a Nijmegen e per ogni giorno successivo. Ma in te non ho trovato solo un collega, ho trovato un carissimo amico, e un compagno di gare di corsa e

corsi di triatlon, che hanno mantenuto corpo e mente sani.

Lalla: un'amica speciale da tantissimo, e una cara compagna dei miei sogni islandesi. É sempre cosí fruttuoso e calmante discutere con te sugli argomenti piú disparati, dalla fisica delle particelle alla letteratura, dai viaggi al bilancio tra vita e lavoro.

Magda: ho sempre pensato che ci sia una connessione particolare tra polacchi e italiani, e tu sei il migliore esempio di questo. Grazie per tutte le risate e le visite a Vossendijk.

David: ci siamo incontrati per la prima volta a Boston alla conferenza sulle binarie X, poi nel settembre successivo ho avuto il piacere di scoprirti tra i miei colleghi. Sei stato un caro compagno delle mie pause caffé per tre anni interi. Conserveró nel cuore le nostre conversazioni a tutto tondo, dai jets ai mercati azionari, dai film danesi alla politica.

Andrey: grazie per tutte le nostre discussioni scientifiche, specialmente di statistica :). Spero che continueremo a lavorare assieme, e anche a scambiarci consigli su libri e molto altro ancora.

Jaap: grazie per le serate musicali ad Amsterdam.

Chiara: da Lund fino ad oggi, una cara amica.

Alexey: grazie per le avventure, le torte, e i film di Jim Jarmusch.

Laura L: l'umorismo é il sale della vita! Grazie anche per allietare le mie visite all'SRON e ad Utrecht.

Alice: é una correlazione di cuore e cervello quella che abbiamo.

Rudo: mi hai sempre supportato con la tua energia e ottimismo.

Gabriel: grazie per esserti preso cura della tigre durante i primi mesi che ero in Israele; hai un cuore grande.

Ann: grazie per avermi fatto sentire a casa e per tutto il cibo delizioso quando ero in visita in Estonia durante le vacanze di Natale nel 2014.

Piccola Sophia: brilli come una stella! Giocare con te é un balsamo per l'anima.

E per finire, un flusso caloroso di grazie per la mia famiglia. Ai miei fratelli, Luca e Andrea, per la loro premura e attenzione anche a distanza. Piccola Marianna: il mio cuore si scioglie quando ti vedo. Valeria, grazie per l'affetto. Ai miei genitori, Maria e Giuliano: grazie per tutte le vostre visite in Olanda, come quella volta che siete partiti immediatamente al sapere che ero a letto ammalata con la varicella. Ma soprattutto, grazie per tutto il supporto e per avermi concesso l'indipendenza che ho sempre cercato:

se non sono mai stata timorosa dell'ignoto, é grazie a voi. Vi voglio bene.

We shall not cease from exploration
And the end of all our exploring
Will be to arrive where we started
And know the place for the first time.
- T.S. Eliot -